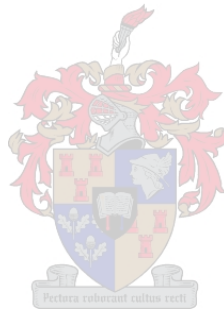


Four Quadrant Axial Flow Compressor Performance

by

Andrew Gill

Doctor of Philosophy in Faculty of Engineering at Stellenbosch University



Department of Mechanical and Mechatronics Engineering,
University of Stellenbosch,
Private Bag X1, Matieland 7602, South Africa.

Supervisors:

Professor T.W. von Backström Professor T.M. Harms

December 2011

Declaration

By submitting this report electronically, I declare that the entirety of the work contained therein is my own, original work, that I am the sole author thereof (save to the extent explicitly otherwise stated), that reproduction and publication thereof by Stellenbosch University will not infringe any third party rights and that I have not previously in its entirety or in part submitted it for obtaining any qualification.

Date:

Copyright © 2011 Stellenbosch University
All rights reserved.

Contents

Declaration	i
Contents	ii
1 Introduction	3
1.1 Introduction	3
1.2 Background and motivation	3
1.3 Aim of this dissertation	4
1.4 Four-quadrant mapping fundamentals	5
1.5 Organisation of this dissertation	7
2 Previous Research	8
2.1 Introduction	8
2.2 The second quadrant investigation of Gamache and Greitzer	9
2.3 The second quadrant two-dimensional model of Gallar <i>et al.</i>	10
2.4 The reversed-flow blockage-mixing method of Longley	11
2.5 The third quadrant investigation of Cyrus	12
2.6 The fourth quadrant investigation of Cyrus	13
2.7 The four-quadrant axial flow turbine investigation of Bammert and Zehner	14
2.8 Conclusion	16
3 Experimental Facility	17
3.1 Introduction	17
3.2 Compressor test-bench	17
3.3 Auxiliary fan	20
3.4 Instrumentation and data capture	20
3.4.1 Instrumentation for performance mapping	20
3.4.2 Inter-blade row flow field investigation	21
4 Numerical Simulation Techniques	24
4.1 Introduction	24
4.2 Solver and differencing schemes	24
4.3 Meshing scheme, grid convergence, and convergence of the iterations	24
4.4 Inlet and outlet boundary conditions	25
4.5 Steady-state simulation	26
4.6 Unsteady flow simulation	26
4.7 Turbulence modelling	27
4.8 Summary	28

5	Four-Quadrant Overall Performance Maps	30
5.1	Introduction	30
5.2	Results and discussion	30
5.2.1	First quadrant operation for positive rotation	31
5.2.2	Second quadrant operation for positive rotation	32
5.2.3	Fourth quadrant operation for positive rotation	32
5.2.4	Second quadrant operation for negative rotation	33
5.2.5	Third quadrant operation for negative rotation	33
5.2.6	Fourth quadrant operation for negative rotation	34
5.3	Zero-rotation S-curves	34
5.4	Summary	40
6	First quadrant: positive rotation	45
6.1	Introduction	45
6.2	Experimental results	46
6.2.1	Time-averaged velocity profiles	46
6.2.2	Time dependent results	50
6.3	Numerical results	60
6.4	Summary	65
7	Fourth quadrant: positive rotation	67
7.1	Introduction	67
7.2	Experimental results	67
7.2.1	Time-averaged velocity profiles	67
7.2.2	Time dependent results	73
7.3	Numerical results	79
7.4	Discussion	83
7.5	Summary	86
8	Second quadrant: positive rotation	87
8.1	Introduction	87
8.2	Experimental results	87
8.2.1	Time-averaged velocity profiles	87
8.2.2	Time dependent results	89
8.3	Numerical results	94
8.4	Numerical modelling the MIT compressor of Gamache and Greitzer	98
8.5	Conclusion	103
9	Third quadrant: negative rotation	105
9.1	Introduction	105
9.2	Experimental results	105
9.2.1	Time-averaged velocity profiles	105
9.2.2	Time dependent results	109
9.3	Numerical results	113
9.4	Discussion	122
9.5	Summary	124

10 Second quadrant: negative rotation	125
10.1 Introduction	125
10.2 Experimental results	125
10.2.1 Time-averaged velocity profiles	125
10.2.2 Time dependent results	131
10.3 Numerical results	133
10.4 Discussion	142
10.5 Summary	142
11 Fourth quadrant: negative rotation	144
11.1 Introduction	144
11.2 Experimental results	144
11.2.1 Time-averaged velocity profiles	144
11.2.2 Time dependent results	145
11.3 Numerical results	149
11.4 Summary	153
12 Conclusions	155
12.1 Summary of results	155
12.2 Further work	159
List of References	162
A Instrument calibrations curves	165
A.1 Pressure transducers	165
A.2 Turbine anemometer	165
A.3 Torque load cell	165
A.4 Inclined single sensor hot film probe	166
A.5 Two-sensor hot film X-probe	166
B Solution method for hot film X-probe velocity vector	168
C Testing procedure checklist	170
D CFD convergence, grid sensitivity and turbulence model sensitivity	171
D.1 Grid convergence and turbulence model sensitivity	171
D.2 Convergence of the iterations	172
D.3 Turbulence model sensitivity	172
E CFD grid quality	178
E.1 Design flow direction mesh	178
E.2 Reversed flow direction mesh	184
F MIT compressor geometry reconstruction data	190
G Brief explanation of non-linear harmonic method	192

Abstract

The aims of this thesis are to identify all possible modes of operation for a multi-stage axial flow compressor; then to characterise the performance, attempt to numerically model operation, and determine the main flow field features for each mode.

Four quadrant axial flow compressor operation occurs when the direction of flow through the compressor or the sign of the pressure difference across the compressor reverses, or any combination of these. Depending on the direction of rotation of the compressor, six modes of operation are possible in the four quadrants of the performance map. The rotor rotates in the design direction for three modes, and in the opposite direction for the other three. The stationary-rotor pressure characteristic is S-shaped and passes through the second and fourth quadrants.

A three-stage axial flow compressor operating in the incompressible flow regime was used for the experimental investigation. Flow through the compressor was reversed or augmented by means of an auxiliary axial flow fan. Compressor performance was measured by means of static pressure tapings, a turbine anemometer calibrated to measure forward and reversed volumetric flow and a load cell for torque measurement. The inter-blade row flow fields were measured with pneumatic probes and 50 μm cylindrical hot film probes.

Three dimensional single blade-passage Navier-Stokes simulations were performed using the Numeca FineTurbo package. Steady state simulations used a mixing plane approach. A non-linear harmonic approximation was used for time-unsteady simulations.

Unstalled first quadrant operation was unremarkable, and good agreement was obtained between experimental and numerical data. A single stall cell was detected experimentally during stalled operation, which was not modelled numerically.

In the fourth quadrant for positive rotation, (windmilling), the compressor acts as an inefficient turbine. Flow separates from the pressure surface of the blade, rendering the steady-state mixing plane approach unsuitable.

The performance characteristic curves for second quadrant for positive rotation, are discontinuous with those of first quadrant operation. The temperature rise in the working fluid is significantly higher than at design point. Periodic flow structures occurring across two blade passages were detected at all flow coefficients investigated, invalidating numerical modelling assumptions. Better agreement was obtained between experimental and numerical data from a case found in literature.

If the compressor operates as a compressor in reverse (third quadrant operation), significant separation occurs on the pressure surface of all blades, and flow conditions resemble severe first quadrant stall. Separation becomes less severe at larger flow rates, allowing numerical simulation, though this is sensitive to the initial flow field.

In the the part of the second quadrant, where the compressor rotates in reverse, it operates as a turbine. The blade angles and the direction of curvature match the flow angles and turning well, leading to high turbine efficiencies. Numerical simulations yielded good agreement with measured results, but were again sensitive to the initial flow field.

Fourth quadrant operation with negative rotation occurs when flow is forced through the compressor in the design direction. Large separation bubbles are attached to the pressure surfaces

of rotor and stator blades, so virtually all throughflow occurs near the hub and casing.

Opsomming

Die doelwitte van hierdie tesis is om al die moontlike werkmodusse vir 'n bestaande multi-stadium aksiaalvloeï kompressor uit te ken; om dan die gedrag te gekarakteriseer, 'n poging aan te wend om die werking numeries te modelleer, en die belangrikste vloeiveldkenmerke vir elke modus te bepaal.

Vier-kwadrant aksiaalvloeï kompressor werking vind plaas as die rigting van die vloeï deur die kompressor, of die teken van die drukverskil oor die kompressor omkeer, of enige kombinasie daarvan. Afhangende van die rigting van rotasie van die kompressor is ses operasionele modusse moontlik in die vier kwadrante van die kompressorkaart. Die rotor draai in die ontwerprigting vir drie van die modes, en in die teenoorgestelde rigting vir die ander drie. Die stilstaande-rotor drukkarakteristiek is S-vormig gaan deur die tweede en vierde kwadrante.

'n Drie-stadium onsamedrukbare vloeï aksiaalvloeï kompressor is vir die eksperimentele ondersoek gebruik. Vloeï deur die kompressor is omgekeer of aangehelp deur middel van 'n aksiaalvloeï hulpwaaier. Kompressor werking is gemeet deur middel van statiese druk meetpunte in die omhulsel, 'n turbine anemometer wat gekalibreer is om vorentoe en omgekeerde volumetriese vloeï te meet, en 'n lassel vir wringmoment meting. Interlemryvloeïvelde is opgemeet met pneumatiese sensors en 50- μ m silindriese warm film sensors.

Drie-dimensionele Navier-Stokes simulاسies is uitgevoer vir 'n enkele lem van elke lemry, met behulp van die Numeca FineTurbo sagtewarepakket. 'n Mengvlakbenadering is gebruik vir bestendige toestand simulاسies, terwyl 'n nie-linere harmoniese benadering gebruik is vir die tyd-afhanklike simulاسies.

Ongestaakte eerste kwadrant werking was alledaags, en goeie ooreenkoms is gevind tussen die eksperimentele en numeriese data. 'n Enkele staak-sel is eksperimenteel ontdek tydens gestaakte werking. Gestaakte werking is nie numeries gemodelleer nie.

In die vierde kwadrant vir positiewe rotasie, ("windmeulwerking"), werk die kompressor as 'n ondoeltreffende turbine. Vloeï-wegbreking op die lem drukoppervlaktes maak die bestendige toestand mengvlakbenadering ongeskik.

In die kenlyn vir tweede kwadrant positiewe rotasie, is daar 'n diskontinuiteit in die prestasie karakteristiekrommes vir die eerste en tweede kwadrant werking. Die temperatuurstyging in die werk- vloeïstof is beduidend hoër as by die ontwerp punt. Periodiese vloeïstrukture wat oor twee lemme plaasvind is gevind by alle vloeï koëffisiënte wat ondersoek is, en dit maak die numeriese modellering aannames ongeldig. Beter ooreenkoms tussen die eksperimentele en numeriese data is verkry met 'n geval wat uit die literatuur gevind is.

Indien die kompressor werk as 'n kompressor in omgekeerde (derde kwadrant weking), vind beduidende wegbreking op die drukoppervlak van al die lemme plaas, wat lyk soos ernstige gestaakte eerste kwadrant werking. Die vloeïskeiding raak minder ernstig by 'n groter vloeïtempo, wat numeriese nabootsing toelaat, maar die nabootsing is sensitief vir die aanvanklike vloeïveld.

In die tweede kwadrant, by omgekeerde rotasie, werk die kompressor as 'n turbine. Die lemhoeke en die rigting van lemkromming stem ooreen met die vloeïhoeke en verwringing, wat lei tot hoër turbine doeltreffendheid. Numeriese nabootsing stem goed ooreen met gemete resultate, maar is weereens sensitief vir die keuse van die aanvanklike vloeïveld.

Vierde kwadrant werking met negatiewe rotasie vind plaas wanneer die lug gedwing word

om deur die kompressor in die ontwerprigting te vloei. Groot skeidingborrels sit vas aan die drukoppervlaktes van alle lemme, sodat meeste deurvloei naby die naaf en die omhulsel plaas vind.

Acknowledgement

I would like to thank my supervisors Professor T.W. von Backström and Professor T.M. Harms for all they have done for me academically and personally. My gratitude to and admiration for these two men cannot be adequately expressed in a small number of words.

My completion of this PhD was also heavily dependent on the hard work of the technical staff: Cobus and Ferdie Zietsman, Calvin and Graeme Hammerse, Anton van den Berg in the workshops, and Clive, Shiyaam and Mauritia and many others for general help, and the ladies on the fifth floor for taking care of all the paperwork. Also thanks to Wessel from the E-and-E department and Kevin from the Mechatronics lab for the hot film probe repairs.

Thanks are also due to the CSIR and the NRF for providing the funding for this project.

Thanks to Numeca International, for providing simulation software on very generous licensing terms, and also to Thomas Hildebrandt of that organisation, for his friendly assistance.

Thanks to Cyrus Vaclav for digging up a 20-year old conference paper for me.

Thanks to Glen Snedden and Dwain Dunn of the CSIR, and Anthony Gannon of the Naval postgraduate School for their advice and assistance with experimental work.

Thanks to my former officemates and good friends Tom Fluri and Michael Kuhn for their help over the years, as well as their friendship and good company.

Thanks also to a number of students who I collaborated with over the years: Lauren, Mike, Danie, Marie, Nico, Christiaan, Ross, Viljoen, Gert Raubenheimer and Jaco, who worked on the compressor with me, and Andrew de Wet, for hours of help with computer problems.

Thanks to my brother Patrick, and Fabian, Marco, Jonathan, Robert and many other friends for encouraging me and helping me through more than a few scrapes along the way.

Thanks to my parents and family for always encouraging me.

And finally, thanks to my wife and very best friend Tania for all she has done for me, for her love and patience, and for the interest which she has always shown in my research.

Nomenclature

Greek symbols

α	Relative flow angle
β	Blade stagger angle
Δ	Difference between inlet and outlet condition
Γ	Circulation
ϕ	Flow coefficient; C_z/U
ψ	Pressure rise coefficient
ρ	Density
τ	Torque coefficient

Roman symbols

A_c	Compressor annulus cross-sectional flow area
b	Blockage factor
C	Absolute velocity
C_p	Constant pressure thermal coefficient for gas
d	Compressor blade tip diameter
h	Enthalpy
K	S-curve loss coefficient
K_ϕ	Non-dimensionalised S-curve loss coefficient
N	Rotational speed of rotor
P	Pressure
Q	Volumetric flow rate
r	Radius
s	Blade pitch
S	Entropy
T	Torque, Temperature
t	Time
U	Blade tip speed
$U(r)$	Local blade speed at radius r
u	Velocity component parallel with X -axis
v	Velocity component parallel with Y -axis
V	Absolute flow velocity, volume
W	Flow velocity relative to rotor blade

Subscripts

θ	Circumferential component
0	Stagnation condition
1	Upstream of blade cascade
2	Second quadrant (S-curve), or downstream of blade cascade
4	Fourth quadrant (S-curve)
design	Property occurring during design-point operation
hub	Property or condition at compressor hub
R1	Axial position at compressor inlet under design conditions
R1	Axial position between first stage rotor and first stage stator
S1	Axial position between first stage stator and second stage rotor
R2	Axial position between second stage rotor and second stage stator
S2	Axial position between second stage stator and third stage rotor
R3	Axial position between third stage rotor and third stage stator
S3	Axial position of compressor outlet under design conditions
TS	Total-to-static
SS	Static-to-static
r	Radial component
<i>tip</i>	Property or condition at compressor blade tips or near compressor casing
z	Axial component

Chapter 1

Introduction

1.1 Introduction

This chapter provides the background and motivation for the investigation of four quadrant axial flow compressor operation. The goals of the project are listed and explained. The fundamentals of four quadrant compressor operation are presented and the approach to the investigation is described.

1.2 Background and motivation

Four quadrant axial flow compressor operation occurs when the direction of flow through the compressor, the direction of rotor rotation or the sign of the pressure difference between the outlet and inlet reverses, or when any combination of these reverses occurs. This causes the performance characteristic curve to enter a quadrant other than the first quadrant on a pressure rise to flow rate or torque to flow rate compressor map. Such operation is uncommon and differs significantly from the normal operating condition of the compressor, and may be the result of malfunction of the system of which the compressor is a part. Under such conditions, there is a danger of blade breakage due to the unusual loading experienced by the blades. There is also danger to any devices connected to the compressor due to the unusual shaft torque and rotational speeds which may occur.

The investigation of four quadrant compressor performance was initiated by a request by the University of the Northwest, in Potchefstroom, South Africa, as part of their research for the Pebble Bed Modular Reactor project, in order to allow modelling of disaster scenarios. While reviewing literature early in the project, it was realised that no attempt had been made to identify and investigate all the possible modes of four-quadrant axial flow compressor operation.

Although the field of four quadrant compressor operation has been neglected, there are numerous areas of application for such research. Axial flow compressors are principally used in gas turbine engines, and in this application, windmilling (fourth quadrant operation) and surge, (which may lead to reverse flow and second quadrant operation) are common occurrences. Windmilling is particularly significant in turbo-ramjet engines under development at present for high-speed supersonic aircraft [Suder et al., 2010], as the low pressure fan experiences windmilling during the ramjet-phase of operation, at which throughflow velocities are highest.

In process-applications and power-generation schemes, compressors may operate in the

CHAPTER 1. INTRODUCTION

above-mentioned modes, and in others. Valve failure upstream or downstream of the compressor may result in surge and reverse flow, and ultimately turbine-like operation with rotation in either direction, depending on sign of the pressure difference across the machine. Human error can cause the compressor to be run with rotation in the opposite of the design direction. Failure of the drive-system, or breakage of the drive shaft, which also occurs in aircraft engines [Gallar et al., 2010], may also result in second quadrant operation.

It was thus decided to attempt to identify the different modes of axial compressor operation in the four quadrants of the performance map, obtain non-dimensional performance characteristics for all modes, and experimentally and numerically determine the principle features of the flow field within the machine under the various possible conditions.

The most detailed study of compressor operation beyond the first quadrant was that of Gamache and Greitzer [1990], which was restricted to second quadrant (reverse flow) operation for positive rotor rotation. This mode of operation was investigated exhaustively. Third and fourth quadrant operation for axial fans and single axial flow compressor stages have been investigated (Cyrus [2004] and Cyrus [1990]), but these neglect the blade-row interactions which occur between stages in multi-stage compressors. In addition, no attempts had been made to model four-quadrant compressor operation or performance numerically until very recently; Gallar et al. [2010] and Suder et al. [2010] represent the first attempts known to the author other than this project. Finally, other than the investigation of Gamache and Greitzer, no attempts have been made to investigate the manner in which compressor operation transitioned between different modes of operation.

An attempt to experimentally determine performance and internal flow-field characteristics of an axial flow turbine for all four quadrants was performed by Bammert and Zehner [1978] and Bammert and Zehner [1980]. These studies addressed some of the issues above, in particular the consideration of multi-stage machines and attempting to systematically define the different modes of turbine operation within the four quadrants. The test program was ended due to a blade shedding event during testing, as a direct result of the unusual loading experienced by the turbine blades. This illustrates the potential dangers of four quadrant axial flow turbomachine operation.

Chapter 2 provides a more detailed review of all four quadrant turbomachinery research found in literature.

1.3 Aim of this dissertation

This dissertation seeks to contribute the following to the field of axial flow compressor research:

1. Provide a general classification system for all the different modes of operation possible in the four quadrants of the compressor performance map.
2. Provide a set of non-dimensional performance characteristics for all modes of operation identified for a compressor operating in the subsonic regime.
3. Determine for which modes of operation the flow field may be modelled acceptably by use of a single blade passage simulation with a Reynolds Averaged Navier-Stokes solver using a steady-state mixing plane approach, and the non linear harmonic approach to approximate unsteady flow, and determine when one approach is more appropriate than the other.

CHAPTER 1. INTRODUCTION

4. Provide insight into the flow structures within a multi-stage compressor for each possible mode of operation, and determine the effect of flow coefficient on these flow structures for each mode. This is restricted to operation in the subsonic incompressible flow regime, with low relative blade Mach numbers and Reynolds numbers.

1.4 Four-quadrant mapping fundamentals

Every axial flow compressor has a preferred (design) direction of rotation, a preferred flow direction, and a preferred pressure difference between the inlet and outlet of the machine (positive under near-design conditions).

The normal operation of a compressor is confined to the positive direction of rotation, and a performance characteristic is represented as a graph of a pressure rise versus a positive flow rate. Consequently, when plotted on a graph with both positive and negative flow and pressure coefficient values, such a characteristic occurs in the first quadrant of the graph.

Turbomachines can, however, be forced to operate at various combinations of direction of rotation, flow direction, and pressure rise. This means that they can, in principle, operate in each of the four quadrants of the general graph. There are 8 combinations (2^3) of positive and negative flow, pressure rise, and rotational speed, but there are only four quadrants, therefore more than one mode of operation must occur in some quadrants. To understand which combinations will occur in which quadrant, a non-rotating compressor (rotational speed $N = 0$) is considered. In the following discussion incompressible flow is assumed, to explain the concepts without adding unnecessary complications.

When the compressor rotor rotational speed $N = 0$, the compressor will do no work and a positive flow, Q , will result in a negative pressure rise, ΔP , since the exit pressure will be lower than the inlet pressure. The negative pressure rise increases in magnitude as $\Delta P_4 = K_4 \rho Q_4^2$, where Q is the average volumetric flow rate at the inlet to the first stage of the compressor. The subscripts denote that the compressor will work in the fourth quadrant, where the flow is positive and the pressure rise is negative. Consequently K_4 is a negative constant. Conversely, a negative flow will result in a positive pressure rise, such that $P_2 = K_2 \rho Q_2^2$, with K_2 a positive constant. Also note that $\Delta P = 0$ when $Q = 0$, for any value of K , thereby precluding operation in the first or third quadrant (except at the origin of the coordinate system). Thus a non-rotating compressor can operate only in the second and fourth quadrants and only along an S-shaped curve (rotated through 90 anti-clockwise, passing through the origin of the coordinate system) as shown in figure 1.1 The region above the zero-rotation S-curve can only be accessed under the condition of positive compressor rotation, as only then can the pressure of the fluid be increased at constant flow, or the flow be increased against a fixed pressure difference. When the rotor turns in the positive direction ($N > 0$), the compressor may operate in the first, second, or fourth quadrants. Similar arguments relate negative rotation to the area below the S-curve.

If the compressor rotates in the positive direction, it imparts energy to the flow, and the operating point will be above the zero-rotation S-curve. As the throughflow speed increases, the area of positive pressure rise will increase. This area, situated in the first quadrant, is the normal operating map of the compressor, but it includes the region where the compressor is stalled. The compressor cannot, however, operate in the third quadrant when $N > 0$. To operate there, the rotational speed must be negative. Conversely, the

CHAPTER 1. INTRODUCTION

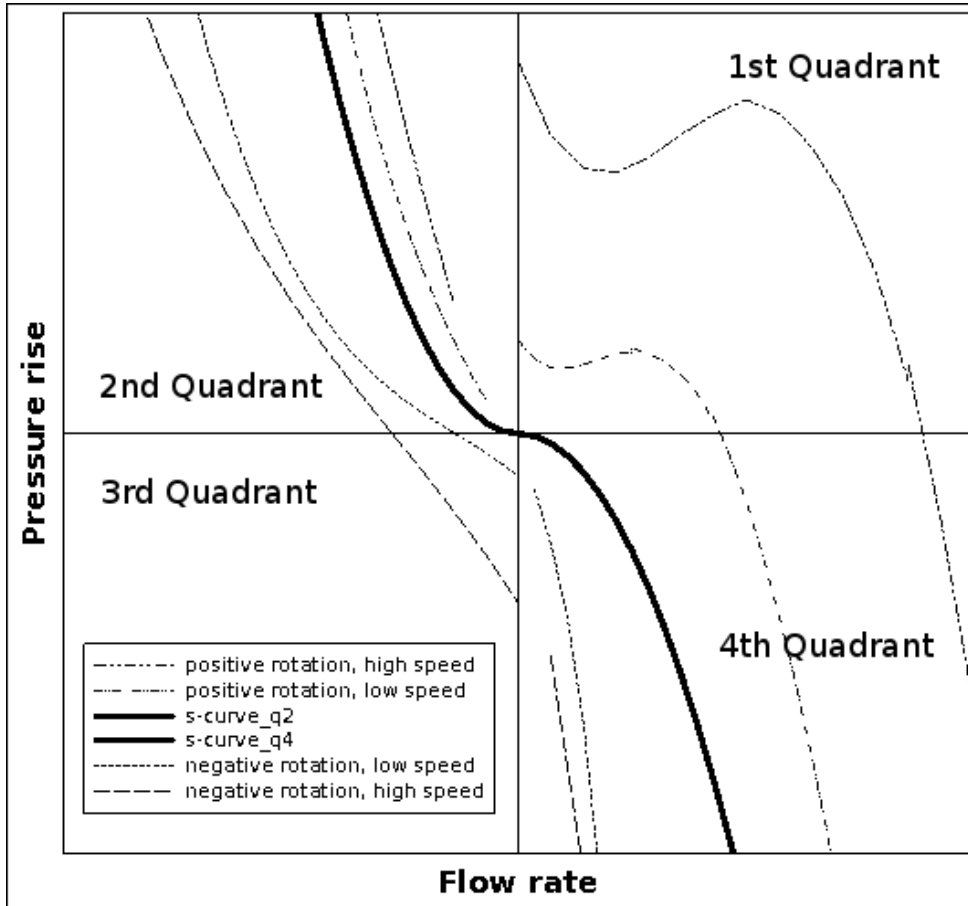


Figure 1.1: Generic Four Quadrant Compressor Map

compressor cannot operate in the first quadrant when $N < 0$. The preceding discussion can be summarized as follows.

1. Zero rotational speed in a compressor results in operation in either the second or the fourth quadrant along a line in the form of an S-curve rotated anti-clockwise through 90 and passing through the origin, as shown in 1.1
2. Positive rotational speed in a compressor results in operation in the first, second, or fourth quadrant in a region above the zero-speed S-curve.
3. Negative rotational speed in a compressor results in operation in the second, third, or fourth quadrant in a region below the zero-speed S-curve.

The S-curve divides the second and fourth quadrants into two parts each, thus the four quadrants can accommodate six operational modes. Third quadrant operation at positive rotor speed and first quadrant operation at negative rotor speed are not possible.

A notation scheme was developed to unambiguously denote the mode of operation of the compressor. The letters F , P , R and T indicate flow, pressure rise, rotation, and torque respectively, and each may be followed by a plus (+) or a minus (-) sign, indicating whether the particular running condition of the compressor is positive or negative. For example, $F+P+R+T+$ denotes the normal compressor mode of operation where flow, pressure rise, rotation and torque are positive. A positive torque is defined as one applied in the design

CHAPTER 1. INTRODUCTION

Table 1.1: Four Quadrant Compressor Operation Mode Notation

Quadrant	Running Condition	Description
1st Quadrant	F+P+R+T+W+	Normal operation (beyond stall included)
2nd Quadrant (above the S-curve)	F-P+R+T+W+	Compressor rotating in positive direction with positive pressure rise, but backflow occurs
2nd Quadrant (below S-curve)	F-P+R-T+W-	Compressor rotating backwards as a turbine under backflow conditions
3rd Quadrant	F-P-R-T-W+	Compressor rotating backwards as compressor under backflow conditions
4th Quadrant (below the S-curve)	F+P-R-T-W+	Compressor rotating backwards, sucking against axillary fans under positive flow
4th Quadrant (above the S-curve)	F+P-R+T-W-	Compressor rotating forwards as turbine

direction on the compressor by the input shaft, or one applied by the compressor to the input shaft in the opposite direction. If compressor characteristics are plotted for torque versus flow rate, the operating conditions in each of the four quadrants correspond exactly with those of the pressure-based compressor map. The torque characteristic curves are also a similar shape to the pressure characteristic curves for each mode of operation. As with the pressure map, the characteristics for locked-rotor operation occur in the second and fourth quadrants, each half being well approximated by half a parabola, thus forming an S-shaped curve which passes through the origin.

Shaft power (symbol W) could also be used as one of the primary running conditions. However, non-zero torque values occur at zero rotation speed, which is not the case for power. The sign of the power output running condition is defined as the product of the signs of R and T. According to this convention, power input to the compressor via the shaft has a positive sign, as is the convention for compressors, although this is the opposite of the usual thermodynamic convention, where the positive sign is reserved for work output.

Table 1.1 shows designations for all six modes of operation. Although it is redundant, the sign of W is also given in Table 1.1, as it is useful for determining whether the experimental setup for a given mode must allow for operation as a compressor or turbine. Note that all running condition indicators are positive in the first quadrant.

1.5 Organisation of this dissertation

This chapter has introduced the subject of four quadrant compressor operation, provided motivation for the investigation thereof, and described the nature of the problem. Chapter 2 contains a review of all previous work on the subject found in literature to date. A detailed description of the test compressor and the experimental techniques and measurement equipment used in the investigation is found in chapter 3. Chapter 4 describes the numerical techniques used in the investigation. Chapter 5 presents the performance maps for compressor operation for all modes of operation identified in all four quadrants, and some details relating to zero-rotation speed characteristics and operation. The remainder of the thesis deals with detailed flow field investigations of each mode of operation: chapters 6-8 cover the three modes of operation occurring for positive rotation of the rotor, while chapters 9-11 cover negative rotation operational modes. Finally, chapter 12 summarises the findings presented in the preceding chapters and describes possible future work in the field of four quadrant axial flow compressor operation.

Chapter 2

Previous Research

2.1 Introduction

First quadrant compressor operation has been exhaustively studied by a number of researchers for incompressible flow, subsonic and transonic compressible flow: Budinger and Thompson [1952] and Kovach and Sandercock [1954], to name a few examples. The phenomenon of stall and its effect on flow patterns within the compressor, which normally occurs at flow coefficients below that of the design-point of the machine, have also been extensively investigated, notably by McDougall et al. [1990], Day [1993] and Camp and Day [1998], and on the compressor used in the present investigation (albeit with modifications) by Lewis [1989]. The performance and flow field of the compressor used in this investigation was experimentally determined by Roos [1995]. Current axial compressor stall research appears to be primarily focused on the use of casing treatments for stall suppression [Houghton and Day, 2010], and improved methods of stability limit prediction and understanding of stall phenomena [Gannon et al., 2010].

Very little research has been conducted on four quadrant operation of axial flow compressors. The most common use of such machines is gas turbine engines, usually in aircraft, where operation beyond the first quadrant is rare in the extreme. Gamache and Greitzer [1990] mention that second quadrant operation has been known to occur during surge of compressors used in refrigeration and blast furnace installations. Gallar et al. [2010] observed that in the conditions following turbine shaft breakage in an aircraft engine, the compressor would experience surge and could enter second quadrant operation as a result. A method of predicting stage-performance was developed based on the data of Gamache and Greitzer [1990] and other historical data.

Cyrus [1990] observed fourth quadrant turbine-like operation in the final stages of compressors with a large number of stages, and consequently investigated this mode of operation for a single compressor stage. More recently, Suder et al. [2010] considered fourth quadrant turbine-like performance of a transonic axial flow fan for use in a Mach 4+ variable cycle turbofan ramjet engine, as the fan would windmill during the ramjet phase of operation. Performance maps extending into the fourth quadrant were obtained experimentally and through numerical simulation, but no detail was given of the flow structures observed within the fan during windmilling.

Axial flow fans are sometimes run in reverse so as to reverse the direction of flow in traffic tunnels. Such machines may have adjustable outlet guide vanes or stator blades to somewhat improve performance under such conditions. Cyrus [2004] describes the reverse flow performance characteristics of two single-stage axial flow fans with inlet and exit guide

CHAPTER 2. PREVIOUS RESEARCH

vanes, which may also be considered representative of single compressor stages.

2.2 The second quadrant investigation of Gamache and Greitzer

Gamache [1985] and Gamache and Greitzer [1990] describe an investigation of the second quadrant, positive rotation performance of a 3-stage, non-repeating axial flow compressor. The compressor had a casing diameter of 0.62 m and a hub-to-tip ratio of 0.88. The tests were conducted at rotational speeds of 1170, 1800 and 2400 RPM, equivalent to Reynolds numbers between 10^5 and 2×10^5 . Two different builds were investigated: the first with a reaction ratio of 0.64 and a second with a reaction ratio of 0.74. Steady-state and high-frequency time-dependent measurements were carried out. These included static pressure readings from tappings in the casing, total and static pressure readings using fast-response probes, and inclined hotwire readings. A fiber-optic pickup was used to determine the exact instantaneous position of the rotor. Measurements were taken at the compressor inlet, exit, and between all blade rows, at five radial stations, at 15, 30, 50, 70 and 85 % of the blade span, and eleven circumferential positions, spaced 0.6 degrees apart.

Results were presented in the form of non-dimensional total to static pressure and torque characteristics, static to static stage performance, time-averaged and high-response casing static pressure measurements and a time-dependent and a time-averaged inter-blade row velocity field.

For the purpose of determining the total-to-static pressure characteristics, the pressure coefficient was defined as follows:

$$\psi_{TS} = \frac{P_{outlet} - P_{0,inlet}}{1/2\rho U^2} \quad (2.1)$$

for axial flow in the design direction, and

$$\psi_{TS} = \frac{P_{0,outlet} - P_{inlet}}{1/2\rho U^2} \quad (2.2)$$

for reversed axial flow.

A significant discontinuity was observed between the first and second quadrant characteristics, for total-to-static pressure and torque coefficient characteristics, at low positive and negative mass flow rates. The transition between positive and negative mass flow rate also appears to mark a transition between a rotating stall and an annulus stalled condition. Pressure and torque coefficients increased rapidly and with increasingly negative gradient as the magnitude of the negative flow coefficient increased. Both pressure and torque characteristics in the second quadrant were virtually identical for all builds investigated, therefore it appears that second quadrant operation is relatively insensitive to reaction ratio for this particular compressor. This also holds true for the static stage characteristics obtained.

Casing static pressure measurements along the compressor suggest that, with the exception of the last stage (which functions as an inlet for reverse flow), most of the pressure drop occurring between the compressor outlet and inlet occurs across the stationary blade rows, namely the stators and inlet guide vanes. The magnitude of the pressure drop increases as the negative mass flow rate increases in magnitude, as has already been noted. Fast response static pressure measurements revealed a periodic pressure disturbance at a

CHAPTER 2. PREVIOUS RESEARCH

frequency dependent on the flow coefficient, somewhat higher than the blade passing frequency at moderate negative flow coefficients, and approaching that of the blade passing frequency as the magnitude of the flow coefficient increased.

Similar periodic disturbances were also detected in measurements of the inter-blade row flow field of the third rotor row. The upstream (trailing edge for reverse flow) measurements displayed fluctuations in axial velocity at the blade passing frequency for high negative flow coefficients. At more moderate flow coefficients, the disturbance in velocity had a frequency of half the blade passing frequency, suggesting that flow was blocked for every second blade passage. A disturbance of this frequency was also observed in the tangential flow component, and downstream of the rotor row (after the leading edge). A jet wake pattern was also detected downstream of the rotor row. The radial velocity component downstream was relatively large, approximately $C_r/U = 0.15$.

Time-averaged spanwise distributions for axial velocity were obtained upstream of each rotor and stator row. It was found that upstream of rotor rows, the axial velocity was highest near the hub, decreasing rapidly towards the casing, while upstream of stator rows the velocity component was largest near the casing. This was true for all flow coefficients investigated, although the gradient was most severe at low flow coefficients, where negative axial velocities were observed near the hub downstream of rotor rows, and least severe at high flow coefficients. It was suggested that this was caused by positive (tipwards) radial flow in rotor rows due to centrifugal acceleration, which in turn caused negative (hubward) flow within stator rows. Strong secondary flow circulation patterns occur in the space between rotor and stator rows.

Stagnation pressure radial distributions upstream of all rotor rows were found to be approximately constant, but those downstream tended to vary approximately linearly from hub to shroud, with highest pressures recorded near the shroud.

2.3 The second quadrant two-dimensional model of Gallar *et al.*

It will be recalled that Gallar *et al.* [2010] attempted to model second quadrant operation, in order to model the surging of an axial flow compressor following a shaft overspeed event and subsequent shaft breakage. Gallar *et al.* [2010] examined the work of Koff [1983], Gamache [1985] and Day [1994], and developed a semi-empirical two-dimensional model for the prediction of blade row performance. The model was based on that of Koff [1983], but incorporates compressibility effects. If the pressure change between the blade trailing and leading edges is known, the leading and trailing edge velocities can be calculated by means of equation 2.3:

$$\frac{p_2 - p_1}{\frac{1}{2}\rho_1 W_1^2} = 1 - (1 + k) \frac{\rho_2 W_2^2}{\rho_1 W_1^2} \quad (2.3)$$

The subscript 1 represents trailing edge conditions, 2 represents leading edge conditions, W the relative velocity, ρ the density and p the total pressure. The property k is the pressure loss coefficient, and is calculated by the following formula:

$$k = k_{coef} \sigma / \cos(\beta_1) \quad (2.4)$$

where k_{coef} is an empirically derived constant, σ is the blade row solidity, and β_1 is the trailing edge relative flow angle. Static temperature and pressure are calculated by consideration the momentum and energy balance equations.

CHAPTER 2. PREVIOUS RESEARCH

The value of k_{coef} was chosen to give the best fit to the blade row pressure rise data for both builds of Gamache and Greitzer [1990], and subsequently applied to the compressor of Day [1994] to yield a second-quadrant overall pressure rise characteristic for comparison with the experimental data. The model yielded reasonable agreement with Day's data over the range of investigation, although the exact shape of the characteristic was not captured.

2.4 The reversed-flow blockage-mixing method of Longley

Longley [2007] presents a blockage-mixing method for the estimation of reversed flow operation through an axial flow compressor during surge or other reversed flow operation, which was implemented as a time-accurate computational simulation. A distinction is made between short and long length scale flow features; the former of those which are of the same order of magnitude as the blade pitch such as wakes resulting from flow separation on blade surfaces, while those which are of a similar size to the circumference of the compressor annulus are referred to as long length scales.

Longley begins by considering a simplified cascade of flat plates and a large flow inlet angle. As these represent reversed flow cases, the relative flow angle is greater than 100° . The throughflow is assumed to form a series free-shear layers within the cascade. The resulting wake-jet structure is assumed to yield a velocity profile resembling a square wave due to the alternating wakes and jets.

The blockage is defined in equation 2.4:

$$b = 1 + \left| \frac{\sin(\alpha_2 - \beta)}{\cos \alpha_2} \right| \quad (2.5)$$

where the fraction of the blade pitch occupied by the jet is $1/b$. Skin friction is ignored and isentropic flow assumed. Expressions are then developed to describe the mixing of the jets and wakes as either a constant pressure or a constant area process:

$$\frac{\Delta p_0}{\Gamma_2 \rho \nu_2^2} = (b^2 - 1) \cos^2 \alpha_2 \quad (2.6)$$

(constant pressure)

$$\frac{\Delta p_0}{\Gamma_2 \rho \nu_2^2} = (b - 1)^2 \cos^2 \alpha_2 \quad (2.7)$$

(constant area).

For a more realistic case in which velocity profile across the wake-jet pattern is more complex than a square wave, the blockage factor is defined as the ratio of the momentum of the non-uniform flow to that which uniform flow through the blade row would have. Of course, this definition holds true for the simplified square-wave case, and can thus be used to convert the flow field into an equivalent "square wave" form, allowing the use of the simplified model.

In order to implement the model numerically, the velocities are averaged for a volume containing one blade pitch, in order to eliminate short length scale disturbances. These are represented in the momentum equation by the blockage factor b :

$$\int \rho u^2 dV / \int dV = \rho b \bar{u}^2 \quad (2.8)$$

CHAPTER 2. PREVIOUS RESEARCH

Where \bar{u} is the average velocity, V is the volume for the short length scale average. The energy equation is then derived similarly. Because kinetic energy flux is assumed to only be present in jets and not in the wakes, the kinetic energy term in the stagnation enthalpy is multiplied by the square of the blockage factor b :

$$\bar{h}_0 = c_p T + \frac{1}{2} b^2 (\bar{u}^2 + \bar{v}^2 + \bar{w}^2) \quad (2.9)$$

Where \bar{u} , \bar{v} and \bar{w}^2 are the three-dimensional velocity components. The definitions for continuity, momentum and energy are then substituted into the Euler equation, the solution of which describes only medium to long length scale phenomena, with the short length-scale phenomena being accounted for in the value of b . In order to solve the Euler equation numerically, body forces within blade passages and mixing out of short length scale phenomena such as wakes were derived. The equation used to describe mixing out of wakes was of particular interest for the present work, as it indicates the relationship between the entropy production rate DS/Dt and the blockage factor in the blade passages:

$$\rho T \frac{DS}{Dt} = \left(\frac{u |\bar{u}|}{\frac{1}{2}s} \right) \frac{1}{2} \rho (b - 1) \bar{\mathbf{u}}^2 \quad (2.10)$$

in which s is the blade pitch.

Longley [2007] then applied the method successfully to two compressor geometries for which data for reversed flow was available in literature, one of which was Gamache and Greitzer [1990], discussed earlier. The mean-line simulation performed on that compressor yielded reasonable agreement with experimentally determined post-stall performance characteristics, but under-predicted work input by approximately 15 % due to the large radial flows present (which to some extent invalidated the assumptions underlying a mean-line analysis).

In addition, the method was also applied to numerically simulate surge-cycle operation of a low-bypass ratio compressor such as would be used in a turbofan aircraft engine.

2.5 The third quadrant investigation of Cyrus

Cyrus [2004] describes an investigation into the third quadrant fan performance and flow structure. A simple theoretical model for reverse rotation, reverse flow axial fan operation was developed, based on two-dimensional cascade theory applied to an isolated rotor row. From this model, it was shown that in order to achieve the flow angles necessary for compressor-like operation, the axial velocity component must be smaller than for a corresponding first quadrant point of operation, and that the third quadrant performance of the machine will be considerably poorer than that of the first quadrant. Further, Cyrus noted that machines with larger rotor camber angles will suffer a larger degradation of performance in the third quadrant than those with smaller camber angles. Cyrus then presented an experimental investigation of the third quadrant operation of two axial flow fan stages, both having inlet guide vanes and adjustable outlet guide vanes. The experimental investigation consisted of the measurement of performance characteristics of a high pressure ratio and a medium pressure ratio stage, named A and B respectively by Cyrus, and area traverses conducted with five-hole conical probes at the stage inlet and outlet, and between all blade rows for each. Both made use of blades with NACA 65 thickness on circular arc camber lines with reinforced (thickened) trailing edges. The tip diameters

CHAPTER 2. PREVIOUS RESEARCH

of both fans were constant at 600 mm, and testing was conducted at 1500 rpm, with a maximum blade-tip relative Mach number of 0.35, and chord based rotor Reynolds numbers between 300 000 and 450 000. The hub-to-tip ratio of stage A was 0.7, and that of B was 0.55. The design pressure coefficient for stage A was approximately 0.72, while that of stage B was approximately 0.4, at flow coefficients of approximately 0.6 and 0.4 respectively.

The third quadrant pressure coefficient characteristics of the two stages reveal that the lower pressure ratio stage B suffers a smaller degradation of performance than stage A. Cyrus notes that this is in accordance with his theoretical findings, as stage A has the larger camber angles of the two.

2.6 The fourth quadrant investigation of Cyrus

Cyrus [1990] investigated the fourth quadrant turbine-like operation of a axial flow compressor stage in positive rotation. The investigation was concerned with the occurrence of this mode of operation at rotational and flow speeds considerably below design conditions, and low Mach numbers implying incompressible flow conditions, in the final stages of a compressor with a large number of stages. A single stage compressor with inlet and outlet guide vanes and constant hub and shroud diameters was used for the investigation. The blades used had a NACA-65 thickness distribution on circular arc camber lines. Tests were conducted at 2200 rpm, and the chord-based Reynolds number was between 3×10^5 and 3.8×10^5 . A five-hole conical probe was used to determine flow velocity, direction and pressure data, and a thermocouple was used to determine the temperature. An axial flow fan was used to augment the flow through the compressor to allow fourth quadrant operation. Torque was measured by means of a load cell on an arm attached to the stator of the electric motor driving the compressor. This was used to determine the efficiency of the compressor. For fourth quadrant operation, the definition of efficiency usually used for turbines, the inverse of compressor efficiency, was used.

For the purpose of comparison, the flow structure within the stage was investigated for design point operation, corresponding to a flow coefficient of 0.74, and fourth quadrant turbine operation, at a flow coefficient of 1.29. For design-point operation, the flow field downstream of the rotor was relatively uniform. Consequently, the loss coefficient across the rotor was well approximated by two-dimensional cascade correlations. For fourth quadrant operation, the loss coefficient increased sharply near midspan, decreasing towards the hub and tip, before increasing in the hub and shroud boundary layer areas. Negative angles of attack of a large magnitude (-14° or greater) were observed, indicating that the rotor blades were negatively stalled, and that separation had occurred on the pressure surfaces.

The design-point flow field downstream of the stator exhibited a large area of nearly uniform velocity between small, well-defined blade wakes. The stator is more heavily affected by secondary flows for design-point operation, particularly near the hub and casing. For fourth quadrant operation, a region of separated flow was evident on the pressure surfaces of the blades. An oil-trace flow visualisation revealed that the separated region began at the leading edge and extended for approximately 30 % of the chord length. Flow then reattached, and separated again towards the trailing edge. The flow structure was found to be highly three dimensional within the blade passage.

Cyrus noted that the deviation angles of both rotor and stator blades decreased slightly

CHAPTER 2. PREVIOUS RESEARCH

from design point to fourth quadrant operation. It was also noted that in order to apply the correlations of Lieblein [1959] the definition of the diffusion factor should be modified, as the maximum velocity occurs on the pressure rather than the suction surface of the blade. Lieblein's correlations were found to be less accurate for fourth quadrant than design-point operation, due to the large magnitude and three-dimensional nature of the secondary flows, deviates from the assumption of two-dimensional cascade flow on which these correlations are based.

2.7 The four-quadrant axial flow turbine investigation of Bammert and Zehner

Bammert and Zehner [1978] conducted a comprehensive mapping of performance operation of an axial flow turbine stage in all four quadrants. A similar study was partially completed for a seven-stage axial flow turbine [Bammert and Zehner, 1980]. The latter investigation was halted by destruction of the turbine blading due to a fatigue failure of a final stage blade during reverse flow tests. Both studies were motivated by the frequent operation of steam turbines in ships in reverse flow, positive rotation conditions, a condition which occurs when steam is introduced to brake and then reverse the propeller (and thus the vessel). The possibility of operation of industrial turbines outside of the first quadrant as a result of an accident, particularly in the nuclear industry, was also a motivating factor.

Bammert and Zehner [1978] identified seven parameters which vary in sign or direction according to the mode of operation, namely mass flow, rotational speed, torque, shaft power and pressure, temperature and enthalpy change between the machine inlet and outlet. Power is, of course, a function of torque and rotational speed, while enthalpy is a function of pressure and temperature. Bammert and Zehner [1978] used a performance map relating rotational speed to mass flow in order to define the four quadrants under investigation. Quadrant I is defined by the authors as the quadrant within which positive (normal design) mass flow and rotation occur. Quadrant II is defined as the condition occurring when backward mass flow coincides with positive rotation. Quadrant III contains all operating conditions in which mass flow and rotation are negative, or the reverse of normal operation, while in Quadrant IV, flow occurs in the positive direction, but rotation is reversed. Tests were also conducted to determine the torque and pressure rise characteristics for a rotational speed of zero, in which cases, the rotor was locked in position. Zero mass flow conditions were also investigated by closing appropriate valves.

For Bammert and Zehner [1978], a single stage air turbine with a maximum power rating of 1.4 MW was used. The turbine was braked or driven by a direct current machine. A compressor attached to a system of valves supplied appropriate inlet and outlet pressures, to allow positive and negative mass flows through the machine. A torsion shaft was used to measure torque developed by the turbine. Triple tube and wedge probes were mounted at the turbine inlet and outlet and between the guide vanes and rotor, in order to determine the angle of flow and the static and stagnation pressures. These probes were traversed across five radii. In addition, 18 tangential positions were investigated for a portion of the tests to take into account the effect of wakes. For other tests, the probes were positioned midway between wakes.

The relative power to relative mass flow and relative torque to relative mass flow characteristics for all four quadrants were obtained. It was found that even within Quadrant I, the turbine only generated power for a portion of the characteristic, and that if the mass

CHAPTER 2. PREVIOUS RESEARCH

flow was decreased sufficiently while the rotational speed was held constant, the turbine absorbed shaft power. The amount of power absorbed was of a similar order of magnitude to that generated under design conditions. It was discovered that the point at which the turbine no longer generated power corresponded to the point at which the circumferential velocity component downstream of the rotor was equal to that upstream of it. This was explained by constructing the velocity diagrams.

It was also shown that the turbine absorbed power when operating in Quadrant II. The power absorbed was found to be approximately linearly proportional to the mass flow, which is negative in this quadrant.

The velocity triangles of quadrants II and III were examined, and it was shown that the blade angles were less poorly mismatched for Quadrant III than Quadrant II. This allowed the turbine to supply a limited amount of power in a portion of Quadrant III, and caused the power dissipated over the rest of the operation range investigated to be smaller than that in Quadrant II for comparable magnitudes of rotation and mass flow.

When operating in Quadrant IV, the turbine was found to be capable of absorbing a large amount of power compared to other quadrants. The power was shown to increase sharply in a non-linear fashion in relation to the increase in mass flow rate for a constant rotational speed. This was shown to be due to the increasingly badly mismatched flow angles and blade metal angles, as the mass flow rate increased.

Bammert and Zehner [1980] presented a similar investigation, except that six additional repeating stages were added to the test machine. The stagnation temperature and pressure and static pressure between all stages was measured. The characteristics obtained followed similar trends to those observed in Bammert and Zehner [1978]. However, it was shown that it was not possible to extrapolate overall performance of the turbine by considering the first stage performance, and that each stage in the machine had to be analysed individually, and their respective solutions combined to yield an accurate estimate of four quadrant performance. This is due to the effect of upstream stages on the flow entering a stage, which generally has a negative effect with respect to matching the flow angles and blade metal angles. It was observed that at low mass flow rates, the first stage of the turbine operated as a turbine, while some subsequent stages operated as compressor stages, while for back flow at small flow rates and negative speeds, all stages operated as compressor stages.

The use of a rotational-speed-to-mass-flow performance map in defining four quadrant operation avoids the issue of non-dimensionalising the zero-speed performance characteristic, which in systems based on pressure-rise or shaft-torque maps would require division by the rotational speed, which is zero for this special case. However, the four quadrant performance maps thus obtained are difficult to relate to the pressure-rise, torque or power to flow rate performance maps which are usually used to quantify compressor performance. Some interpretation is also necessary in order to determine whether a turbomachine is acting predominately as a compressor, turbine or mixer at a given point on a characteristic, as more than one mode of operation is possible within some of the quadrants, as was observed by Bammert and Zehner [1978] and Bammert and Zehner [1980]. Unlike a system based on pressure-rise or shaft-torque characteristics, where the zero-rotation characteristic separates different modes within the second and fourth quadrant, as defined in chapter 1, the point of transition in the system described in Bammert and Zehner [1978] is unclear, and difficult to define. It is apparent that these limitations were apparent to Bammert and Zehner, as Bammert and Zehner [1978] and Bammert and Zehner [1980] include turbine performance maps relating pressure rise, torque and power to mass flow.

CHAPTER 2. PREVIOUS RESEARCH

In addition, multiple characteristics are necessary to represent different pressure rise, torque or operating power values, as these cannot be non-dimensionalised in terms of some function of rotational speed, as is common practise with compressors. This requires that data be obtained for a range of rotational speeds, which was not always possible for the test compressor, due to the limitations of the auxiliary fans and compressor power supply. The problem of non-dimensionalising zero-rotation characteristics may be addressed by defining the characteristic in terms of the limit value as the rotational speed tends towards zero. This is described in detail in chapter 5.

It was thus decided to develop the system for the definition of four quadrant axial flow compressor operation described in chapter 1, which is based primarily on the pressure-rise-to-flow-rate compressor map, but simplifies the conversion between choices of performance maps.

2.8 Conclusion

Summaries of the work found in literature on various aspects of four quadrant compressor, fan and turbine operation have been presented. A rigorous experimental investigation of one of the two possible modes of operation in the second quadrant, [Gamache and Greitzer, 1990], and an investigation of third quadrant operation and one possible mode of fourth quadrant operation ([Cyrus, 2004] and [Cyrus, 1990]) have been found. An attempt to model second quadrant operation using a two-dimensional semi-empirical technique [Gallar et al., 2010] was also found. No record of an investigation into second quadrant turbine-like operation, or fourth quadrant operation for negative rotation are known at this point. Further, the four quadrant axial flow turbine investigation of Bammert and Zehner [1980] suggests that the analysis of a single stage in an axial flow turbomachine may not yield full insight into the nature of the flow field or performance of an entire machine operating in the various possible modes in all four quadrants. Finally, no clear method of classification or identification for the modes of operation has been devised for axial flow compressors. An attempt was made for turbines in Bammert and Zehner [1978], but is deemed unsuitable for this project due to the fact that the system of classification developed is not easily related to the compressor performance maps commonly used.

Chapter 3

Experimental Facility

3.1 Introduction

This chapter describes the test compressor used in this investigation, the modifications which were necessary to the compressor to allow four quadrant operation, and the instrumentation used.

3.2 Compressor test-bench

The machine used for the four-quadrant investigation is a three-stage axial flow compressor manufactured by the Royston Fan Co. Ltd. The machine operates at a design speed of 3000 rpm, with a design mass flow rate of 2.7 kg/s, corresponding to a flow coefficient of 0.503, and a nominal total-to-total pressure ratio of 1.022. The entire operating range of the machine occurs within the subsonic incompressible regime, the first stage rotor having a relative blade-tip Mach-number of 0.2 when operating at design point. The relative rotor blade tip Reynolds number at design point is 1.5×10^5 , although some tests were conducted at a reduced speed, due to power limitations and safety concerns, leading to lower Reynolds numbers as low as 1.0×10^5 . The safety concerns were primarily due to the possibility of blade shedding, which occurred during the four quadrant turbine test of Bammert and Zehner [1980]. The compressor has constant hub and casing diameters of 300 mm and 420 mm. The entire hub rotates, including that section near the stator roots, with the exception of that portion upstream of the first stage rotor, and that downstream of the final stage rotor. The compressor has 43 rotor blades and 41 stator blades per stage. All stages are repeating and identical. The machine is fitted with NACA-65 blades on circular arc camber lines with the outflow from the stator blade rows in the axial direction. This is a commonly chosen alternative to the 50 % reaction ratio design according to Cumpsty [1989]. The reaction ratio of the compressor is approximately 0.82 at design point. The nominal blade length is 60 mm and the blade chords are 30 mm, with a maximum blade thickness 10 % of that value. The parameters defining the blades are given in table 3.1. The current set of blades was designed by Bernadé [1986] and fitted by Roos [1995]. Spacing between rotor and stator rows in each stage is 22 mm at the mean radius, which is identical to the inter-stage spacing. Rotor blades are fixed to the hub and stator blades are fixed to rings set into the casing. The mean rotor tip and stator hub gaps are listed in table 3.2. The machine has provision for mounting 36 inlet guide vanes on a fixed ring, but these were not fitted for initial four-quadrant performance tests. For later tests, a set of

CHAPTER 3. EXPERIMENTAL FACILITY

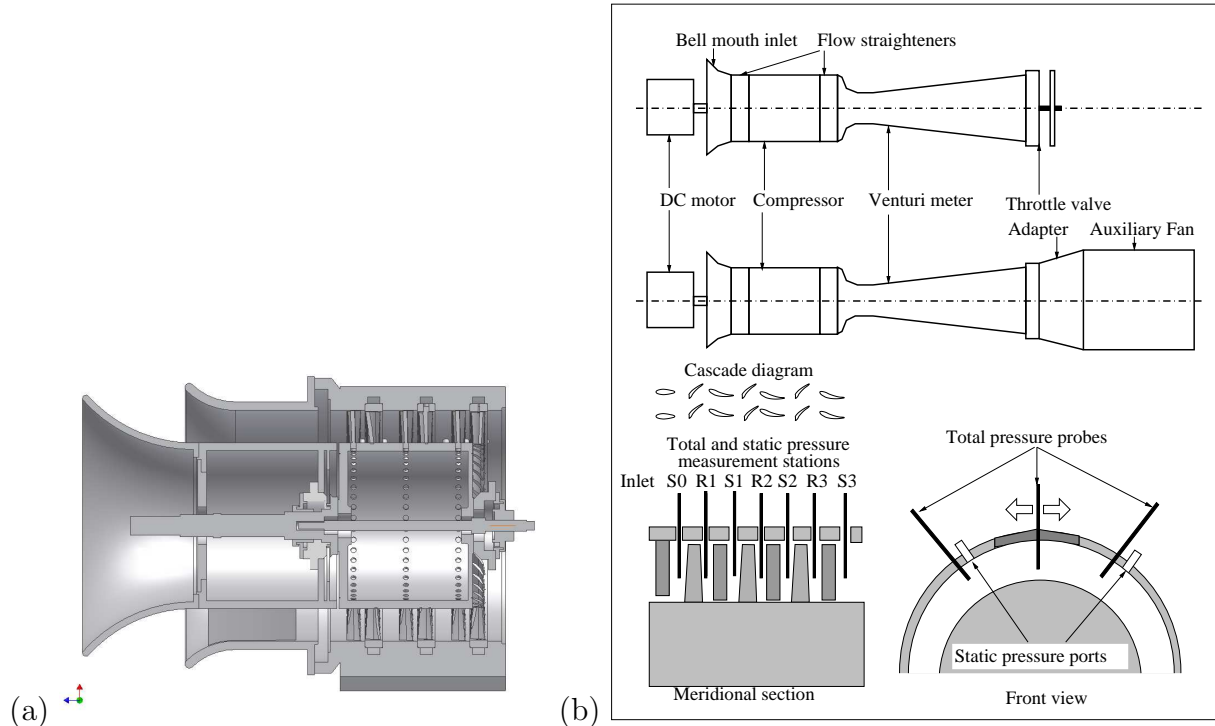


Figure 3.1: (a) A section through the compressor. (b) A schematic of the compressor with auxiliary fan

symmetrical inlet guide vanes with a NACA-65 thickness distribution was manufactured and fitted by Laubscher [2008]. These blades were aligned with the axis of the machine. Chord, span and maximum thickness to chord ratio of the inlet guide vanes is equal to that of the other blades.

The compressor is shown in section in figure 3.1.

The machine has two 11 mm diameter circular ports at each of seven axial positions labeled according to the blade row and stage number upstream of the station during first quadrant operation. Thus the first station, downstream of the IGVs is S0, the next, downstream of the first stage rotor row is R1, and so on, as shown in figure 3.1. These ports allow the insertion of instruments upstream or downstream of each rotor or stator blade row. When not in use, these ports are closed by means of plastic plugs the ends of which are flush with the inner casing wall. The rings on which the stator blades are mounted were originally able to rotate to allow investigation of the velocity wake downstream of stator blades via the ports. The stator rings were fixed in position after replacement of the blades, however, as rubbing could occur between the stator blades and the rotating hub. For this reason, slots were cut downstream of the first stage and stator stator rows (axial positions R1 and S1) to allow area traverses to be conducted for flow in the conventional and reversed directions. Both slots are in the same circumferential position, between the instrumentation ports, thus at an angle of 45° from those on either side. The slots are plugged with plastic inserts which end approximately flush with the inside of the casing when not in use.

The drive system consists of an 11 kW direct current motor with a thyristor control system. The motor cooling fan exhausts air through an attached duct fitted with an axially aligned honey comb grid to ensure that the cooling air is swirl-free and does not

CHAPTER 3. EXPERIMENTAL FACILITY

Table 3.1: Blade profile data for the Rofanco compressor

Blade section radial position (mm)	Blade profile stagger angle (degrees)	Blade profile camber angle (degrees)	Blade row solidity
Rotor			
150.0	38.00	31.04	1.3051
165.0	45.00	23.48	1.1864
180.0	49.40	17.93	1.0876
195.0	53.00	13.85	1.0039
210.0	56.10	10.90	0.9322
Stator			
150.0	20.38	46.28	1.3687
165.0	18.18	43.39	1.2443
180.0	16.61	41.05	1.1406
195.0	14.90	40.57	1.0529
210.0	14.32	40.00	0.9777

Table 3.2: Average rotor blade tip and stator blade hub gaps

Blade row	Gap (mm)
Rotor 1 (tip)	0.40
Stator 1 (hub)	0.68
Rotor 2 (tip)	0.38
Stator 2 (hub)	0.54
Rotor 3 (tip)	0.33
Stator 3 (hub)	0.50

exert a torque on the motor. The flow at the compressor exit is exhausted to 1.4 m duct of 0.42 m diameter, containing two flow straighteners, each 0.11 m long, with honeycomb cells 15 mm wide between opposite walls. The duct is in turn connected to a Venturi meter, which has an inlet diameter equal to the duct and a throat diameter of 0.25 /m. The inlet nozzle of the Venturi is 0.25 m long. The Venturi meter was not used for flow rate measurements, for reasons which will be described in the section on instrumentation. A 0.4 m long blunt-ended truncated cone with a base equal in diameter to the compressor hub and a conical angle of approximately 10° is fitted at the compressor outlet immediately downstream of the compressor hub. The base of the cone contains the rotor drive shaft outlet-end bearings and is mounted on six radial struts of a streamlined profile which are immediately downstream of the compressor outlet. For first third quadrant operation, and some third quadrant operating points at small negative flow coefficients, an adjustable disk throttle is fitted to a threaded spindle mounted on the venturi outlet by means of a three legged spider. This was replaced by an auxiliary fan mounted at the outlet of the venturi-meter, to augment or oppose the compressor in order to access all possible modes of operation.

CHAPTER 3. EXPERIMENTAL FACILITY

3.3 Auxiliary fan

The fan used for these tests was a 483 mm diameter two-stage, contra-rotating Woods axial flow fan, driven by two 4.1 kW induction motors. This fan was mounted at the venturi meter outlet, with two honeycomb flow straighteners in between the fan and compressor in order to remove swirl due to the fan. The speeds of both stages of the contra-rotating fan were variable by means of a single frequency control system at frequencies of up to 55 Hz, giving maximum fan speeds of 3170 rpm. A schematic illustration of the experimental setup is shown in figure 3.1.

3.4 Instrumentation and data capture

Two types of experimental investigation were conducted. The first consisted of the determination of overall performance maps relating non-dimensional flow, pressure, torque and efficiency coefficients for all six modes of operation. The second consisted of an investigation of the inter-blade row flow fields, including steady-state and time-dependent analyses.

3.4.1 Instrumentation for performance mapping

For the determination of performance maps, the following instrumentation was used. Two three-hole cobra probes were used to determine static and stagnation pressures at the compressor inlet and outlet. The inlet probe has a 5 mm long, 3 mm wide head, while the outlet probe had a head approximately 5 mm long and 5 mm wide. The probes were traversed across the compressor annulus and static and total pressures were determined at six equi-spaced radial positions, for the purposes of averaging across the annulus. Static pressure data was also obtained from tappings at the compressor inlet, immediately upstream of the first rotor row, and at the outlet, immediately downstream of the last stator row. This data was used for comparison and validation of that obtained from the probes.

Pressures from the probes and tappings were recorded by means of eight AutoTran model 860 pressure transducers.

Torque acting on the compressor was measured by means of an HBS 350 load-cell. The stated nominal load capacity of the load cell is 20 kg (196 N). The load-cell is attached to a 320 mm long arm mounted on the side of the compressor motor. The motor housing is mounted on air-bearings which are concentric to the compressor-shaft, allowing the motor to rotate due to the torque generated with very little friction. The combined linearity and hysteresis error for the load-cell was 0.03% of its rated output. The load-cell was connected to a HBM Scout-55 bridge-amplifier.

The volume flow rate at the compressor outlet was originally determined by means of the Venturi-meter. However, this device was found to yield inaccurate measurements at low flow rates, or during highly unsteady compressor operation, such as was encountered in some operational modes investigated. It was also necessary to reverse the venturi for reverse-flow cases. A turbine-type vaned anemometer with a diameter of 200 /mm was placed in the the 250 /mm venturi throat. The anemometer was found to give considerably more accurate measurements after being calibrated *in situ* for forward and reverse flow directions through the venturi throat.

Data was captured by means of an Agilent 34970A 22-channel data logger.

CHAPTER 3. EXPERIMENTAL FACILITY

3.4.2 Inter-blade row flow field investigation

The investigation of the flow field up and downstream of each blade row consisted of a number of radial traverses at the appropriate axial positions, via ports in the compressor casing, as well as area traverses downstream of a single stator row.

Steady-state flow measurements were performed by means of a five-hole conical aerodynamic probe, as described in Kirstein [2004]. The probe head, shown in figure 3.2 is approximately 1 mm in diameter, and 5 mm long. The resolution of the pitch and yaw angles is performed by iterative minimization of the difference between non-dimensionalised pitch and yaw pressure coefficients based on measured data, which are compared with data from bilinear interpolation from two-dimensional lookup-tables for these coefficients, compiled from calibration data. This method is based on that of Chue [1975]. A two-dimensional implementation of Powell's optimisation method using a golden section search, as described in Vanderplaats [2001], was used to perform this.

The pressure transducers used to measure pressures observed by the five-hole probe were identical to those used to determine four-quadrant overall compressor performance maps, as described above. Errors in stagnation and static pressures as determined by the probe are less than 4 Pa, while maximum errors in flow angles as determined by the probe do not exceed 2° , including mounting inaccuracies. Although the finite distance between the holes in such probes can result in inaccurate angular measurements, the most significant shear layers, namely the hub and casing boundary layers were almost an order of magnitude larger in scale than the probe head, thus there was no evidence of pitch angle error in these regions. In addition, it should be noted that any similar errors due to passing rotor blade wakes will be averaged out over multiple revolutions. For steady state investigations the sampling rate was 1000 samples per second per channel.

Time dependent measurements were performed by means of a TSI 1213-20 $50\ \mu\text{m}$ slanted cylindrical hot film sensor, connected to a TSI IFA 100 constant temperature thermal anemometer. In order to obtain three-dimensional time-dependent flow data, and rotated to a number of angles for each measurement. A triggering system based on a PM2-LL10 optical sensor and a stainless steel target attached to the rotor was used to provide a trigger signal for time dependent data, and give a time-dependent indication of rotational speed of the compressor.

The method of processing the hot-film data to yield time-dependent three-dimensional velocity data is based upon the method developed for rotating slant-wire sensors by Russ and Simon [1991]. Data for several complete revolutions was gathered with the slant-film sensor in eight angular positions, 15° apart, relative to a datum aligned with the axis of the machine. The sensitivity to the number of angular positions was initially investigated for four to ten positions in steps of 15° , and four to six positions in steps of 30° , resulting in the specified combination as the minimal number to ensure acceptable accuracy. Data was not captured with the probe in the datum position, as this results in an insoluble matrix when determining the velocity components. Average values are then obtained for the voltage for each time step, and each angular position. The averaging process eliminates non-repeating phenomena from the data, as these are related chiefly to flow turbulence in the measurement zone and signal noise. The exact number of data points per rotor revolution varied due to the 1-2 % variation in rotational speed. As a result, the number of data points for a rotation at the average speed was determined, and the averages were based on linearly interpolated values for each rotor position in each revolution. The cooling velocities based on the bridge voltages were then calculated, and these were then used to

CHAPTER 3. EXPERIMENTAL FACILITY



Figure 3.2: The three-hole cobra-probe and five-hole conical probe used in this investigation

calculate the velocity components for that rotor position by the method described by Russ and Simon [1991] for the determination of steady-state velocity components. This method also allowed the calculation of all six components of the Reynolds stress tensor. For this purpose, the root mean square values of the differences between the average and individual cooling velocities for a given probe angle were calculated for each rotor wheel position, and the results for all wheel positions were then averaged.

This eliminates variation in velocity due to blade-wakes, as inclusion of this would result in falsely high turbulent energy values. Unfortunately the linearisations used for this calculation are unsuitable for highly turbulent flow. Consequently the only credible results of this sort were obtained for first quadrant near design point operation. These are presented in chapter 6

For some cases, particularly those involving reversed flow and rotation in the second and third quadrant, the solution matrix for velocity components for the inclined cylindrical hot film sensor was found to become too ill-conditioned to yield acceptable accuracy for the tangential and radial velocity components. Spurious and unrealistically high radial velocities often resulted, sometimes exceeding all other velocity components by more than 200%. The tangential velocity components also did not compare well with those measured by means of the five-hole probe. As a result, some tests were conducted by means of a two-sensor cross-flow 'x'-probe, using 50 μm diameter film sensors offset from one another by 90°. This allowed instantaneous, simultaneous measurement of both axial and tangential velocity. This probe was thus not suitable for measurement when large radial velocity components were expected. However this represented the minority of cases investigated. Calculation of the axial and tangential velocity components was achieved by

CHAPTER 3. EXPERIMENTAL FACILITY

a two-dimensional equivalent of the method derived for three-component probes derived by Lekakis [1989]. The derivation of the solution method is given in appendix B. The time necessary for measurements was thus reduced by a factor of eight compared with the single sensor probe, and also allowed the recording of phenomena at frequencies other than multiples of the rotational frequency of the machine, such as rotating-stall cells in the first quadrant. However the x-probe only became available late in the testing program, and was thus not used for all cases.

Chapter 4

Numerical Simulation Techniques

4.1 Introduction

This chapter describes the methods of numerical modelling applied to the flow within a compressor operating in the six modes of operation identified. The choice of methods for particular cases is motivated. A three-dimensional finite-volume Navier-Stokes solver was used for all numerical modelling. Numeca FineTurbo version 8.7 [NUMECA, 2007] was used for all steady-state and time-dependent simulations. This package was chosen as it simplifies preprocessing and postprocessing for turbomachinery simulations.

4.2 Solver and differencing schemes

A multigrid solver was used, with three different grid levels. The solutions of coarser grids were used as initial conditions for finer grids. A central differencing scheme was applied for spatial discretisation. Merkle preconditioning [Choi and Merkle, 1993] was applied to accelerate the convergence of the iterations.

4.3 Meshing scheme, grid convergence, and convergence of the iterations

Convergence of the iterations was considered to be achieved when the normalised discrepancy between the mass flow at the boundaries corresponding to the compressor inlet and outlet did not exceed 4×10^{-4} and the variation in pressure ratio between inlet and outlet did not exceed 1×10^{-5} . This was chosen due to the limitations of the time and hardware available. This limit was found to give adequate agreement with experimental data, however. The use of a multigrid solver necessitated a structured grid approach. An H-O meshing strategy was used for grid generation for all blades. The mesh for forward flow cases is shown in figure 4.1.

Grid independence was demonstrated by comparing the solutions of three successively finer grids. Each finer grid had more cells by a factor of eight (2^3) than the one preceding it. These grids were generated to allow use of the multigrid solution scheme employed by the solver. A grid having approximately 2.8 million cells of the finest grid was investigated on three multigrid levels. This was the finest grid for which a solution could be obtained due to hardware constraints, as used for all subsequent simulations.

CHAPTER 4. NUMERICAL SIMULATION TECHNIQUES

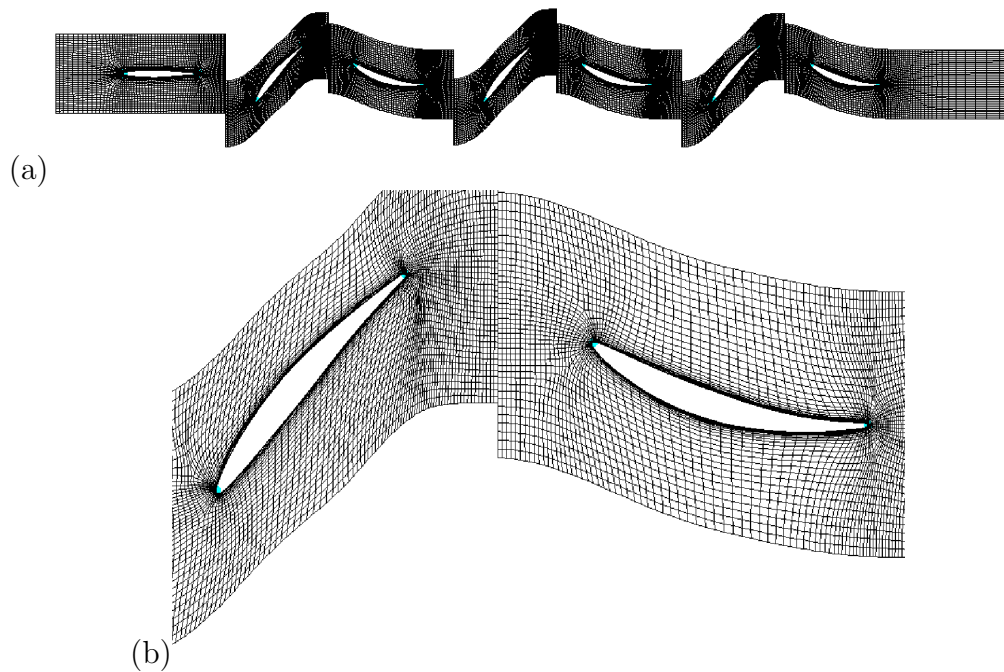


Figure 4.1: A section through the computational grid used for design-direction throughflow cases: (a) the entire compressor, (b) an enlarged view of the first stage mesh

Hub gaps on stator blades and tip gaps on rotor blades were modelled based on average values measured for the compressor (see table 3.2). The gaps for all blades were 13 cells wide, irrespective of the physical distance. This small number was dictated by hardware constraints, and is not expected to provide detailed information on the structure of leakage flows or vortices in these regions.

4.4 Inlet and outlet boundary conditions

The compressor used in this investigation is fitted with a bellmouth at the inlet. Boundary layers on the bellmouth are tripped to the turbulent condition by means of a ring of sandpaper glued to the bellmouth. From experimentally determined velocity profiles as a function of radius, it was determined that flow velocity upstream of the inlet guide vanes was essentially uniform except near the hub and the casing, where significant boundary layers developed. To simplify modelling, the bell mouth was not modelled. Instead, the measured velocity profile as a function of radius was applied as the inlet boundary condition.

The outlet boundary condition was approximated as a pressure boundary, based on the measured static pressure at the outlet casing. A simple radial equilibrium model was used to extrapolate the pressure at other radii, to allow the effect of swirl in the outlet flow on the static pressure. This model assumes a free vortex distribution at the outlet boundary condition.

CHAPTER 4. NUMERICAL SIMULATION TECHNIQUES

4.5 Steady-state simulation

For steady-state simulations, the computational domain was divided into stationary and moving reference frame regions or blocks surrounding stators and rotors respectively. A mixing-plane approach was applied at the interfaces between rotor and stator blocks. In this approach, the flow properties upstream of the mixing plane are averaged in the circumferential (azimuthal) direction downstream of the plane. Thus flow properties downstream of the mixing plane are a function solely of radius. This allows the use of rotor and stator blocks of different periodicity, which is necessary for this compressor, as there are 41 stator blades and 43 rotor blades per stage. This approach is most appropriate to flow conditions where blade wakes are small and well defined, and where there is little variation in flow properties in the azimuthal direction between successive blade wakes. Denton [2010] cautions that use of mixing planes when modelling axial flow compressor operation may lead to over-prediction of mixing-related losses. However he also states that this is most significant in cases involving Mach numbers close to or above unity.

For cases where separated flow yielded large blade wakes, a frozen rotor approach was considered and rejected, as a large number of frozen rotor simulations would be required to yield reasonable accuracy. Greater accuracy for a similar computational cost and run-time could, however be obtained using unsteady simulation techniques. Frozen rotor simulations were, however, of some use in the simulation of non-rotating (locked rotor) operation. It was necessary to alter the number of rotor and stator blades per row in order to ensure equal periodicity, as the frozen rotor approach replaces the mixing plane (which averages the upstream velocity profile circumferentially and thus does not require equal periodicity) with a simple internal boundary, in which flow leaving an upstream cell passes directly into a downstream neighbour. Thus the number of blades per rotor row was reduced by one, and the number of stator blades increased by one, so that each had an equal number of 42 blades.

4.6 Unsteady flow simulation

In turbomachinery, unsteady flow simulation is complicated by the presence of moving boundaries at the rotor-stator interfaces, through which rotor and stator wakes must pass. This is especially true in those cases where a high degree of separation occurs on a blade passage, as this increases the size and complexity of the wake.

For time-unsteady simulations, the non-linear harmonic approximation developed by He and Ning [1998] was used. The non-linear harmonic approximation assumes that the only significant circumferential variations in the flow-field surrounding a blade row occur at the frequencies at which a blade row passes or is passed by upstream and downstream blade rows. This allows a Fourier decomposition in terms of time to be applied to the flow field. The resulting unsteady (cyclically varying) Navier-Stokes equations are reformulated in the frequency domain and solved for each significant frequency and a finite number (N) of its harmonics, in addition to a time-averaged solution. Each sinusoidal component of the first N terms of the Fourier series is thus solved for, and the components are recombined into a time-series once all have converged. As N is small, typically between one and three [NUMECA, 2007], this method is computationally cheap compared with a time-marching solution. The solution is reconstructed in the time domain by injecting deterministic stresses representing the frequency component solutions into the steady-state solution. The resulting time-series solution represents one blade passing interval. More detail on the

CHAPTER 4. NUMERICAL SIMULATION TECHNIQUES

mathematics behind the method can be found in appendix G.

A sensitivity study revealed that a single blade passing perturbation frequency per blade-row, approximated by four Fourier-series terms, provided acceptable agreement with experimental results. The experimentally determined frequency spectra for velocity time traces downstream of rotor rows indicate that this is more than adequate for all cases under investigation, as no harmonics of the blade passing frequency beyond the fourth were distinguishable above the noise level for any of the operating points examined. The use of repeating stages in the test compressor justifies the choice of a single perturbation frequency per blade row. The assumption of a single blade passing perturbation frequency is not entirely accurate for the first stage, as there are 36 IGV blades, and not 41 (the number of stators in all stages). This leads to a corresponding increase in the number of blade wakes across the IGV-rotor interface for cases of forward flow. However, the wakes of the IGV blades are small and thin and decay rapidly, and were found to have negligible effect on downstream blade rows in forward flow cases. Indeed, it was determined experimentally that for first quadrant operation, the absence of all IGVs had no significant effect on the flow field. This, coupled with the excessive memory requirements for modelling two perturbation frequencies per blade row, justified the use of a single perturbation frequency. This did not affect reverse flow cases, as no data was extracted downstream of the IGVs for such cases.

Flow phenomena affecting multiple blade passages simultaneously require full-unsteady, time-marching treatment on more than a single blade passage. The package used, however, requires that the periodicity of the segments simulated be equal. The test-compressor, however, had 41 stator and 43 rotor blades per row. Prime numbers of blades were used in order to prevent problems with resonance and mechanical vibration. For this reason, the method of domain scaling would have to be applied, where the number of blades in some or all passages is altered and scaled geometrically in the numerical model so as to avoid this problem. However, this would introduce additional inaccuracies, for a questionable gain in accuracy and a considerably larger cost in terms of computation time.

4.7 Turbulence modelling

Although direct numerical simulation of turbulent flow is becoming more common, neither the time nor computational resources were available to make use of this approach. Eddy-viscosity turbulence models were thus used for all simulations.

Eddy-viscosity turbulence models are divided into high and low Reynolds number models, depending on whether flow conditions in wall-cells are treated as being in that part of the boundary layer best approximated by an empirically-determined logarithmic law of the wall, or a linear approximation representing the laminar sublayer [White, 1991]. High Reynolds number models thus require larger wall-cells than low Reynolds number models, so that the non-dimensional length-scales (y^+ values) in such cells are appropriate for their underlying assumption. Thus low Reynolds number turbulence models provide more detailed data for flow within the boundary layer, as a smaller portion thereof is approximated. The interaction of the boundary layers on the blades and end-walls of turbomachinery are of importance for this study, as they affect secondary flows. Thus low Reynolds number models are the more appropriate choice for this investigation, and the computational cost will be acceptable as the length-scales in the machine used for the investigation are relatively small.

CHAPTER 4. NUMERICAL SIMULATION TECHNIQUES

Low-Reynolds eddy-viscosity turbulence models were used for all simulations. For the steady-state simulations, the choice of the particular low-Reynolds number turbulence model was based upon a sensitivity study performed for a single blade passage of the test compressor operating near the design condition. The $k - \omega$ SST and Spalart-Allmaras [Spalart and Allmaras, 1992] models yielded the best agreement with experimental data. At near-design point operation ($\phi = 0.508$) the maximum difference recorded between the results of these models was 1.2 % of the mean value of the two models. For most of the span the difference was nearly an order of magnitude smaller.

A comparison of results for these two turbulence models at a flow coefficient of $\phi = 1.024$ (fourth quadrant turbine operation) was also conducted, in order to determine the variation in a case with moderate flow separation. This case yielded a maximum difference of less than 2.5 % at positions R1, R2 and R3. These turbulence models all require wall-cells within the laminar sublayer, corresponding to $y+$ values less than 10, ideally between 1 and 3. Average $y+$ values for all blades were 2.6 for a flow coefficient of $\phi = 0.665$, and 2.1 at $\phi = 1.024$. Maximum $y+$ values of approximately 8 were recorded in a single spanwise row of cells on each blade for fourth quadrant operation.

Celić and Hirschel [2006] evaluated a number of turbulence models for adverse flow conditions, including the Spalart-Allmaras and $k - \omega$ SST and a number of variations on these, and concluded that both would give acceptable agreement with experimental data compared with models such as the Baldwin-Lomax [Baldwin and Lomax, 1978], with the model yielding best agreement being highly dependent on the geometry and flow conditions. Given the negligible difference observed between $k - \omega$ SST and the Spalart-Allmaras models, the Spalart-Allmaras model was used due to its lower computational cost.

For time-dependent simulations utilising the non-linear harmonic approximation, the Spalart-Allmaras model was chosen, as this and Baldwin-Lomax models are the only options available in Numeca.

Spalart and Rumsey [2008] found that the Spalart-Allmaras and $k - \omega$ SST models were both similarly incapable of accurately predicting the relaminarisation or reattachment of separated flows in low Reynolds-number flow simulations. Both were also found to be relatively poor predictors of laminar-to-turbulent transition. However, despite the low blade-chord Reynolds numbers in the present work, the highly separated nature of the flow in many of the cases under investigation ensures that the flow field is turbulent. This is supported by Cumpsty [1989], who states that all flows in axial compressors at Reynolds numbers in excess of 30000 should be considered turbulent. Although a number of models have been developed to attempt to predict the point of transition from laminar to turbulent flow, Denton [2010] suggests that these are still unreliable, particularly in the range of Reynolds numbers in which this compressor operates, as the mechanism of transition to turbulent flow under such circumstances is a separation bubble, which is not appropriately dealt with by existing models. For this reason as well as the preceding argument, no attempt was made to model the point of transition, and flow was assumed to be fully turbulent over the entire chord of all blades.

4.8 Summary

Numerical modelling of four quadrant operation was restricted to three-dimensional solution for single blade passages of all stages in the machine. A steady-state approach utilising mixing planes between blade rows was used where appropriate, and the non-linear har-

CHAPTER 4. NUMERICAL SIMULATION TECHNIQUES

monic method to approximate unsteady operation. Frozen rotor simulations were used to simulate locked-rotor operation. Full unsteady simulation was not attempted due to the computational and time constraints, and the fact that this would have required domain scaling. The Spalart-Almaras turbulence model was selected, as it provided good agreement with experimental data and the $k-\omega$ SST model, at significantly lower computational cost to the latter. No attempt was made to model laminar-to-turbulent transition, due to the unreliability of existing models, and the fact that most modes of operation exhibited a large amount of turbulence in experimental investigations, justifying an assumption of fully turbulent flow throughout the compressor.

Chapter 5

Four-Quadrant Overall Performance Maps

5.1 Introduction

This chapter describes the determination of the steady-state performance of an axial flow compressor for all six modes of operation in all four quadrants. Static to static and total to static pressure and efficiency characteristics, and torque characteristics, are presented and discussed. Performance predictions obtained from numerical simulations are presented and compared with experimentally determined values. These results provide an overall view of the behaviour of the compressor in each mode, which is of use for the construction of a general four-quadrant compressor model, and as a reference for the detailed steady-state and time-dependent inter-blade row flow field investigation described in chapters 6-11. Some of the data in this chapter has been published in Gill et al. [2007a] and Gill et al. [2007b] as a part of this dissertation.

5.2 Results and discussion

The static pressure coefficient relates the change in static pressure between the compressor inlet and outlet (at the compressor casing, in the present investigation) to a reference dynamic pressure, based on the rotor blade tip speed. Static to static pressure coefficient ψ_{SS} is thus defined as follows:

$$\psi_{SS} = \frac{P_{S3} - P_{S0}}{1/2\rho U^2} \quad (5.1)$$

where S3 refers to the machine outlet and S0 the inlet during near-design operation, as shown in figure 3.1 (b). Static to static pressure rise coefficient and efficiency characteristics were determined at the beginning of the research project, because such measurements are simple and quick to perform, allowing a large number of measurements to be taken.

Total to static pressure coefficient and efficiency characteristics are more frequently used and arguably more meaningful for axial flow compressors as the wasted kinetic energy in the outlet flow is ignored. For this reason they were presented by Gamache and Greitzer [1990] for one of the possible modes of second quadrant operation, and for this work. As in Gamache [1985], the total to static pressure coefficient ψ_{TS} is defined as follows:

$$\psi_{TS} = \frac{P_{S3} - P_{0,S0}}{1/2\rho U^2} \quad (5.2)$$

CHAPTER 5. FOUR-QUADRANT OVERALL PERFORMANCE MAPS

for throughflow in the design direction, where S3 refers to the machine outlet and S0 the inlet during near-design (see figure 3.1 (b)).

For reversed throughflow operation, the flow enters the machine at the outlet (S3), and leaves at the inlet (S0), therefore, the total pressure P_0 is used at S3, and the static pressure P at S0. However, in order to keep the sign convention consistent with the static to static pressure coefficient, the condition at S0 is subtracted from S3, regardless of throughflow direction.

$$\psi_{TS} = \frac{P_{0,S3} - P_{S0}}{1/2\rho U^2} \quad (5.3)$$

The torque coefficient is less commonly used as a measure of compressor performance than the power coefficient, but is of more relevance here, as the direction and magnitude of shaft torque would have greater significance than shaft power in a disaster-scenario; especially when considering the possibility of mechanical failure of the drive shaft or related components. Bearing in mind that shaft power is the product of torque T and shaft angular velocity, the torque coefficient may be obtained by dividing the denominator and numerator of the power coefficient by the angular velocity of the shaft. Instead of raising the characteristic diameter (in this case d_{tip}) to the third power in the denominator, Gamache [1985] uses the product of the characteristic diameter and the annulus sectional area $A_c = \pi (r_{tip}^2 - r_{hub}^2)$. Thus following Gamache [1985], the torque coefficient τ is thus defined as:

$$\tau = \frac{T}{1/2\rho U^2 d_{tip} A_c} \quad (5.4)$$

The static to static compressor efficiency is defined as:

$$\eta_{SS} = \frac{Q (P_{S3} - P_{S0})}{2TU/d_{tip}} \quad (5.5)$$

The total to static compressor efficiency uses the same convention regarding the pressure difference as the total to static pressure coefficient, and is therefore defined as:

$$\eta_{TS} = \frac{Q (P_{S3} - P_{0,S0})}{2TU/d_{tip}} \quad (5.6)$$

for throughflow in the design direction, and

$$\eta_{TS} = \frac{Q (P_{0,S3} - P_{S0})}{2TU/d_{tip}} \quad (5.7)$$

for reversed throughflow, where Q is the volumetric flow rate. The turbine efficiencies for forward and reversed flow are the negative inverse of the above definitions.

The static to static and total to static pressure rise coefficient, torque coefficient and efficiency characteristics will now be discussed, quadrant by quadrant, for positive and negative rotation.

The non-dimensionalisation of locked-rotor (s-curve) operation will be described later in this chapter.

5.2.1 First quadrant operation for positive rotation

First quadrant compressor operation has been experimentally investigated previously for this machine by Roos [1995]. The static to static pressure coefficient characteristic is presented

CHAPTER 5. FOUR-QUADRANT OVERALL PERFORMANCE MAPS

in figure 5.1 (a), and the total to static pressure coefficient characteristic in figure 5.2 (a). Stall inception appears to occur at a flow coefficient of approximately 0.38 (figure 5.2 (a)). Most of the characteristic could be obtained by adjustment of the throttling valve on the compressor, however the auxiliary fan was necessary to access points with a high flow and low pressure coefficient, near the boundary of the fourth quadrant. The torque coefficient characteristic (figure 5.3 (a)) crosses the x-axis at a higher flow coefficient than the pressure rise coefficient. Between these two points the compressor runs at a negative efficiency. The peak total to static efficiency of the compressor is 66 % (figure 5.5 (a)), lower than that of axial flow compressors employed in aircraft engines or industrial applications. However, the numerically determined total to static efficiency values only exceed the experimentally determined values by approximately 6%, suggesting that the compressor does in fact operate at a low efficiency. The peak static to static efficiency determined was approximately 80 %, as shown in figure 5.4.

The characteristic determined for the first quadrant is of a similar form to that determined by Gamache and Greitzer [1990]. Hysteresis was observed by Gamache and Greitzer [1990] while entering and leaving stall; this phenomenon was not investigated during this work, although it had been previously investigated for this machine by Roos [1995].

5.2.2 Second quadrant operation for positive rotation

Second quadrant operation for positive rotation occurs when the pressure difference between the compressor outlet and inlet becomes so large that throughflow occurs in the reverse of the normal direction. This may occur intermittently during surge, or as result of industrial accidents. The unsteady nature of the reversed flow in this mode of operation resulted in unreliable stagnation pressure data at the compressor inlet (a problem also experienced by Gamache [1985]). The total-to-static pressure characteristic for this mode of operation (figure 5.2 (a)) is of a similar shape to that found by Gamache and Greitzer [1990], and also exhibits a discontinuity for low negative flow coefficients near the y-axis. This is a highly dissipative mode of operation, in which a maximum temperature increase of 10 K was observed in the working fluid. This equates to 3 kW of power dissipated in the form of heat, which is 60 % of the fluid power at design point. For comparison, the stagnation temperature rise across the machine when operating at design point is approximately 2.5 K. In the non-dimensional form $C_p \Delta T / U^2$, the temperature rise for second quadrant operation is 14.4, while at design point it is 0.58. In this mode of operation, where virtually all the fluid power is supplied by the auxiliary fan and most of the energy input is dissipated as heat, efficiency has little meaning, and the efficiency curve is consequently not plotted.

5.2.3 Fourth quadrant operation for positive rotation

Fourth quadrant operation above the S-curve represents a turbine-like mode of operation for the compressor, similar to that investigated in Cyrus [1990]. The mass flow rate and consequently the flow coefficient are considerably higher than those occurring in the first quadrant. As can be seen in figures 5.2 (a) and 5.3 (a), the pressure and torque coefficient characteristics join smoothly with those of the first quadrant. Static to static and total to static turbine efficiency, which are defined as the inverse of the respective compressor efficiencies, are presented in figures 5.4 (a) and 5.5 (a) respectively, as the compressor is generating shaft power in this mode. The compressor efficiency is zero where the pressure

CHAPTER 5. FOUR-QUADRANT OVERALL PERFORMANCE MAPS

rise is zero, and undefined where the shaft torque is zero, the zero-torque line forming an asymptote to the compressor efficiency. The turbine efficiency is zero at the zero torque line and asymptotic to the zero-pressure rise line. As the pressure rise coefficient characteristic curve crosses the zero-line at a lower flow coefficient than the torque coefficient, due to the frictional losses on the shaft bearings, there is a small region between the zero-pressure rise and zero-torque lines in which both are meaningfully defined, and in which both are negative. It was found convenient to use the definition of compressor efficiency for flow coefficients between zero and that at which compressor and turbine efficiency characteristics cross. This is shown diagrammatically in figure 5.6.

5.2.4 Second quadrant operation for negative rotation

Second quadrant operation below the S-curve is another turbine-like mode of operation; this time for reverse flow and rotation. The characteristics in figures 5.2 (b) and 5.3 (b) are very similar in shape to turbine characteristics, particularly if the pressure coefficient is plotted on the x-axis and the flow coefficient on the y, as is common practice with turbines. The direction of blade curvature is better suited to turbine operation than in fourth quadrant operation, however, yielding a total to static turbine efficiency of 55 %, as can be seen in figure 5.5 (b). The peak static to static efficiency value attained was approximately 75 %, as shown in figure 5.4 (b). The torque and efficiency values obtained from numerical modelling are higher than those determined experimentally. At a flow coefficient of approximately 0.6, the numerically determined total to static efficiency was approximately 70 %, while the experimental value was approximately 40 %. This was the largest difference between numerical and experimental total to static efficiency values. As for first and fourth quadrant operation for positive rotation, the flow coefficient at which the pressure rise is zero is closer to the origin (smaller in magnitude) than that at which the torque is zero. The zero-pressure rise and zero torque lines are once again the asymptotes to the turbine and compressor efficiency characteristics. This is shown left of the origin in figure 5.6.

5.2.5 Third quadrant operation for negative rotation

In third quadrant operation (F-P-N-T-W+), negative rotation, mass flow rate and pressure difference across the compressor were observed. In this mode the machine operates as a compressor running in the reverse of the normal direction Cyrus [2004]. However, the blades are curved in the wrong direction for such operation, and efficiency is thus lower than for first quadrant operation, as can be seen in figure 5.5 (b). The maximum total to static efficiency observed was less than 10 %. The flow coefficients at which zero torque and total to static pressure rise occur are -0.45 and -0.2 respectively. In comparison, for transition between first and fourth quadrant operation, zero torque occurs at a flow coefficient of approximately 0.7, while a zero total-to-static pressure rise occurs at a flow coefficient of 0.65. This results in rather large efficiencies at high negative mass flow rates just below those necessary for turbine operation. However, this is deceptive, as most of the fluid power in this mode is supplied by the auxiliary fan. However, torque must be applied to the compressor by the motor to maintain rotational speed, as can be seen in figure 5.3 (b).

CHAPTER 5. FOUR-QUADRANT OVERALL PERFORMANCE MAPS

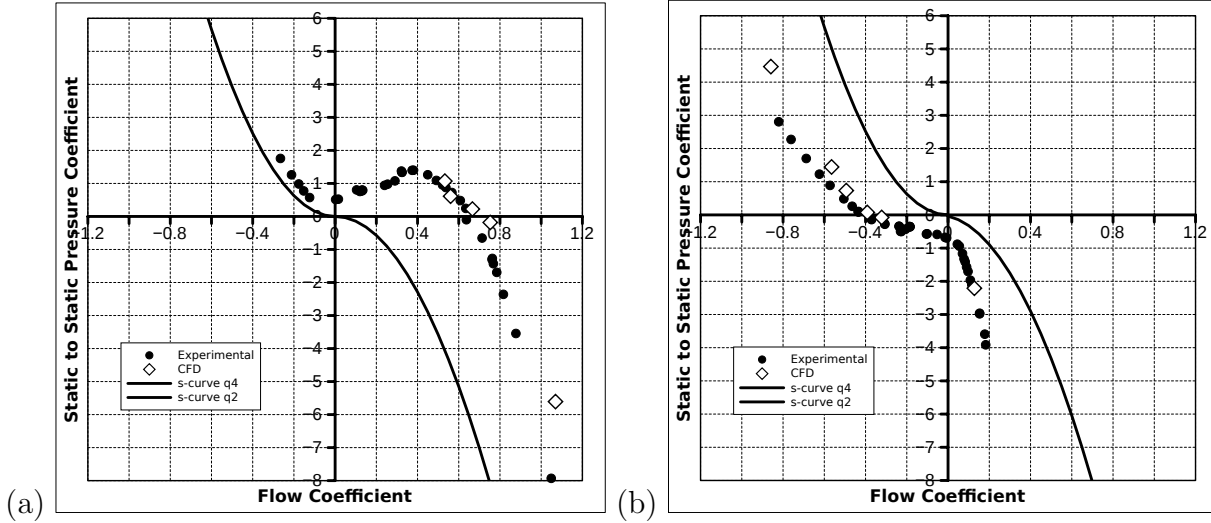


Figure 5.1: Four-quadrant static to static pressure coefficient compressor maps for (a) positive rotation and (b) negative rotation

5.2.6 Fourth quadrant operation for negative rotation

Fourth quadrant operation below the S-curve is a dissipative condition not unlike that occurring for second quadrant positive rotation, although the amount of power dissipated is less for this mode, with a maximum recorded temperature increase of 4 K, compared with 10 K observed for second quadrant, forward rotation operation. In the non-dimensional form $C_p \Delta T / U^2$, this yields a value of 3.7, compared with the second quadrant value of 14.4. The total to static pressure coefficient characteristic decreases sharply as a function of flow coefficient, as is shown in figure 5.2 (b), while the torque rises sharply (figure 5.3 (b)). A discontinuity was also found to occur at between this mode of operation and third quadrant operation. As for second quadrant positive rotation operation, efficiency is not plotted on figure 5.5 (b) for this mode, as it is not meaningful.

5.3 Zero-rotation S-curves

The zero-rotation (locked rotor) total to static and static to static pressure characteristics for a positive flow direction (fourth quadrant) and a negative flow direction (second quadrant) are shown in figures 5.1 and 5.2. The corresponding torque characteristics are shown in figure 5.3. The pressure characteristics obey the relationship $\Delta P = KQ^2$ where ΔP is the pressure rise, Q the volume flow rate, and K an empirically derived constant, which is positive in the second quadrant, and negative in the fourth. Non-dimensionalising non-rotating compressor characteristics in a meaningful way presents a challenge. The usual practise of non-dimensionalising pressure rise to the pressure coefficient $\psi = \Delta P / (1/2\rho U^2)$ and the flow rate to the flow coefficient $\phi = C_z / U$ fails, as the rotor blade tip speed U is zero. However, by defining the characteristic as the limit approached as $U \rightarrow 0$ a meaningful curve may be obtained. From the calculation of the limit:

$$\lim_{U \rightarrow 0} \frac{\psi}{\phi^2} = \frac{\Delta P A_c^2}{1/2\rho Q^2} \quad (5.8)$$

CHAPTER 5. FOUR-QUADRANT OVERALL PERFORMANCE MAPS

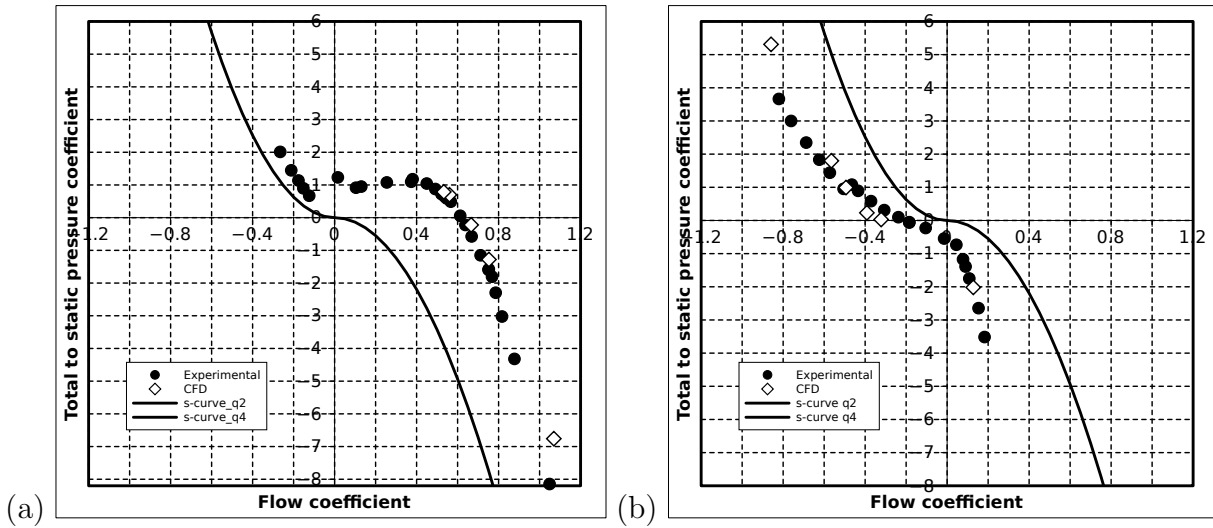


Figure 5.2: Four-quadrant total to static pressure coefficient compressor maps for (a) positive rotation and (b) negative rotation

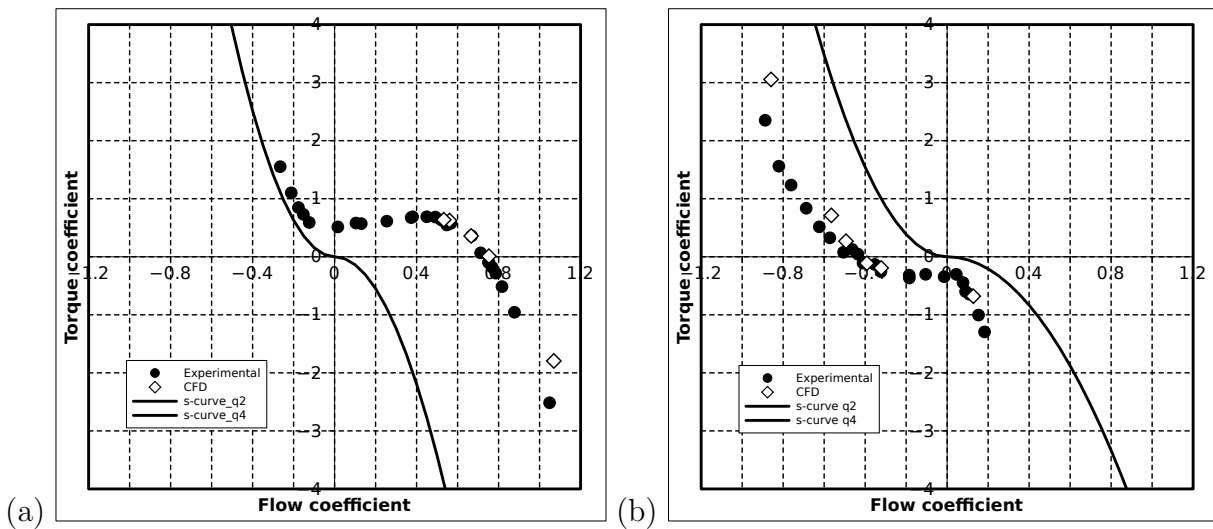


Figure 5.3: Four-quadrant torque coefficient compressor maps for (a) positive rotation and (b) negative rotation

CHAPTER 5. FOUR-QUADRANT OVERALL PERFORMANCE MAPS

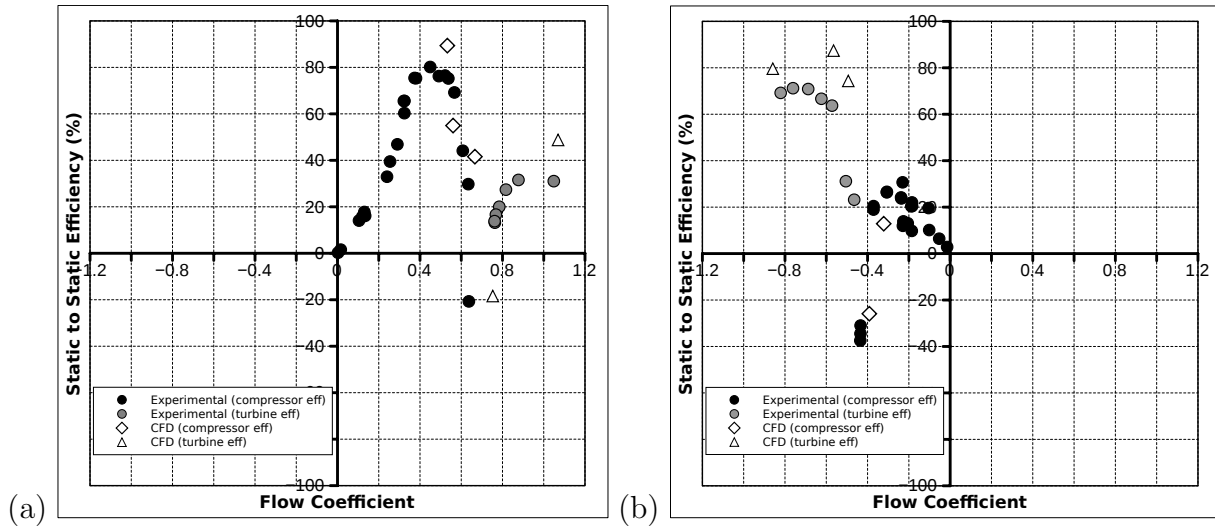


Figure 5.4: Four quadrant static to static efficiency maps for (a) positive rotation and (b) negative rotation

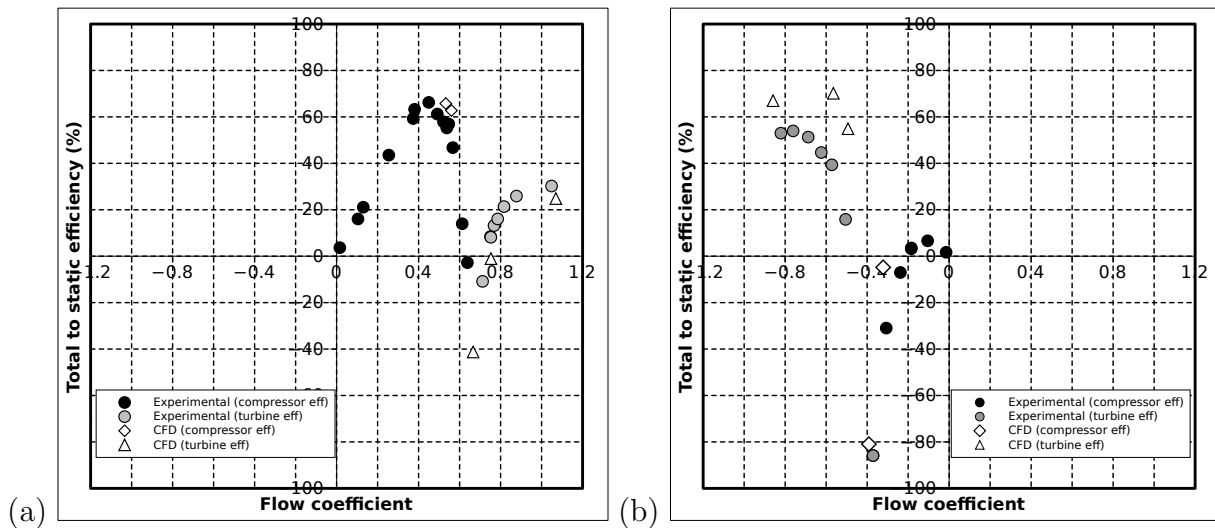


Figure 5.5: Four quadrant total to static efficiency maps for (a) positive rotation and (b) negative rotation

CHAPTER 5. FOUR-QUADRANT OVERALL PERFORMANCE MAPS

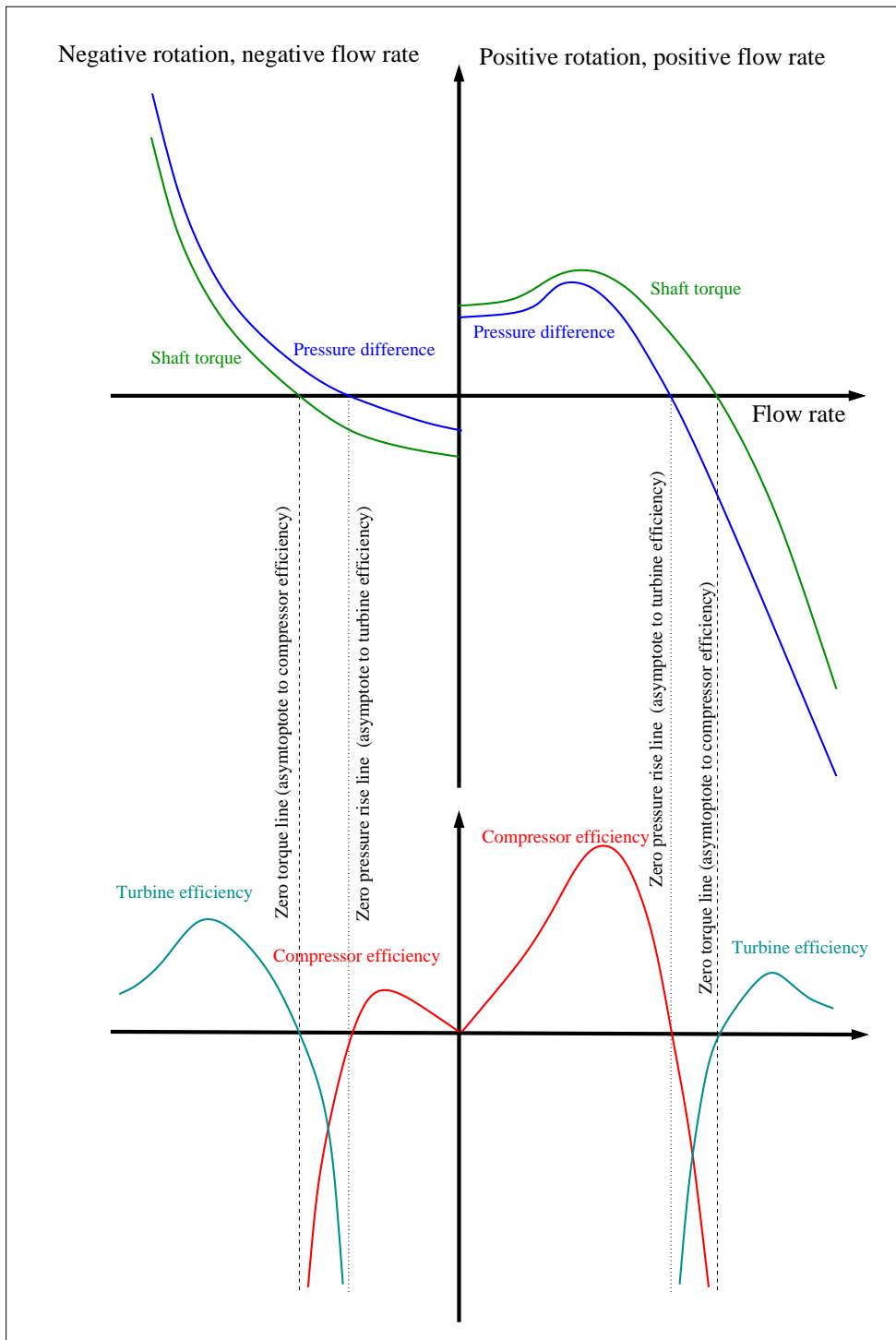


Figure 5.6: The relationship between zero pressure rise, zero torque and compressor and turbine efficiency characteristics

CHAPTER 5. FOUR-QUADRANT OVERALL PERFORMANCE MAPS

the constant K_ϕ is defined:

$$K_\phi = \frac{A_c^2}{1/2\rho} K \quad (5.9)$$

yielding the relationship

$$\psi = K_\phi \phi^2 \quad (5.10)$$

which is plotted in figures 5.1 and 5.2. The torque S-curves in figure 5.3 are obtained in a similar manner.

The effect of clocking, that is the exact position in which the rotor blades are locked relative to the upstream and downstream stators, was investigated by means of numerical simulations using a frozen rotor approach. This necessitated matching periodicity in rotor and stator blocks. For this reason, the number of rotor blades per row was decreased by one, and the number of stators per row increased by one, so that both equalled 42. As there are 43 rotor blades and 41 stators per stage in the physical compressor, the relative circumferential position of rotor blades to stator blades upstream and downstream varies with each blade. For this reason, three different angular positions of the rotor relative to the stator were investigated: for the first, which was chosen as the datum, the centres of the blade chord lines are directly in line for rotors and stators. For the second position, the rotors are offset by a quarter of the blade pitch, and for the third, the centre line of rotors are offset by half the blade pitch. The effect of variation in clocking angle between rotor rows or stator rows in different stages was not considered, however, as this was deemed beyond the scope of the present study. The inlet velocity profile was set as constant at 13.741 m/s for the clocking study.

The entropy increase on a constant radius surface at midspan during forward flow locked rotor operation is shown for three different angular positions of the rotor relative to stator rows in figure 5.7. For this and all subsequent figures showing numerical results, the net flow direction is from left to right, irrespective of whether the flow direction is reversed. Longley [2007] relates blockage to entropy generation in the non-dimensional form $\frac{T\Delta s}{u^2}$. For the sake of consistency in this document, the rotor tip speed U is used in the denominator when non-dimensionalising entropy plots. This leads to a problem for the case currently under investigation, where the rotor tip speed is zero. In order to render these results directly comparable with those in the following chapters, the rotor tip speed at design point is used to non-dimensionalise entropy for all locked-rotor cases.

For rotor rows at midspan and mid-chord, locally reversed flow occurs over approximately 18 % of the blade pitch due to the separation bubble attached to the pressure surfaces of blades, while for stator rows, reversed throughflow occurred across approximately 30 % of the blade pitch at midspan and mid-chord. Downstream of the first stage rotor trailing edge at midspan, the wake occupied 40 % of the blade pitch, while the wake downstream of the first stage stator was 65 % of the blade pitch at midspan.

Differences in size and shape of the separated areas may be observed for the three clocking positions. These regions are shown more in more detail in figure 5.8. This is most notable in separated regions attached to the first stage rotor and the final stage stator. The total to static pressure loss coefficient $K_{\phi TS}$ varies from a maximum of 21.0 when blade chord centres are aligned (figure 5.7(a)), to 18.3, when the chord centres are offset though a quarter of the blade pitch (figure 5.7(b)). The first case is 7.9 % higher than the mean value for the three cases, while the second is 6.7 % lower. The third case (figure 5.7(c)), in which the blade chord centres are offset by half the blade pitch, is only 1.7 % below the mean value, at 19.2.

 CHAPTER 5. FOUR-QUADRANT OVERALL PERFORMANCE MAPS

The variation of the static to static loss coefficient $K_{\phi SS}$ for the three cases follows the same trend and the percentage difference between each case and the mean is very close to the corresponding figure for the total to static loss coefficient, given above.

The variation observed may be explained by considering that flow through each blade passage consists of a large area of separated flow on the pressure surface, and relatively thin jet in which most of the through flow occurs. The position where this jet impinges upon the blade downstream, or the fact that it does not, affects the size and shape of the area of separated flow on the suction of the downstream blade. Thus separation is worst where the jet impinges on a downstream blade near the centre of its chord, as occurs between the first stage stator and the second stage rotor in figures 5.8(a), and least severe where it impinges on the blade on the leading edge, as in the first stage stator and second stage rotor in figure 5.8(b). For the test compressor, the position in which the inter-stator jets impinge on downstream rotors appears to have more affect on the size and shape of the separation bubbles on the rotor than the inter-rotor jets have on separation bubbles on downstream stator blades. This is probably due to the fact that the separation bubbles on rotor blades are smaller, thus the inter-rotor jets are larger and thus relatively weaker. This is probably dependent on the compressor geometry, more specifically, the degree of reaction, and the relative sizes of rotor and stator camber angles.

The entropy variation for reverse flow locked rotor operation is shown for three different angular rotor positions, relative to stator rows, in figure 5.9. There are separation bubbles on the suction surfaces of all blades. The separation bubbles on stators occupy approximately 60 % of the blade passage circumferential width at midspan, and those of rotors approximately 40 %. As was found for forward flow, the difference in size of the separated areas for the three different clocking positions appears small. The size of the separation bubbles, particularly those on the stator suction surfaces, appears to be smaller than those occurring in forward flow. The total to static pressure loss coefficient $K_{\phi TS}$ for each of the three cases differed from the average value by less than two percent, as did the static to static loss coefficient $K_{\phi SS}$. This lack of variation may be attributed to the smaller regions of separated flow, which lead to broader, less strong jets between the separated regions, and thus the separation of downstream blades is not as strongly affected by the position of blades upstream.

Figure 5.10 shows the flow field surrounding the third stage rotor and second stage stator for the three clocking positions investigated. Note that for reverse flow, the separation bubbles are attached to the suction surfaces of both rotors and stators, and that the variation of the flow field with change in clocking position is considerably smaller than for forward flow (figure 5.8). The wake downstream of both rotor and stator rows is approximately half the blade pitch in width at midspan, except downstream of the final stage stator, as the trailing edge is aligned with the flow direction.

Henceforth, all data presented for locked rotor operation was from the mid-span plane. This yields a good representation of flow at all radii, as axial velocity distributions downstream of rotors and stators for forward and backward flow are relatively flat, although velocities are slightly higher near the hub in both cases, due to the smaller stagger angles in this region. Figure 5.11 shows the meridionally-averaged flow paths for forward flow (subfigure (a)) and backward flow (subfigure (b)). For flow in the design direction, there is less radial flow than for reversed flow, and it may be disregarded for most purposes. For reversed flow, radial velocity components are small at the outlet, where flow enters the machine, but increase in size further downstream.

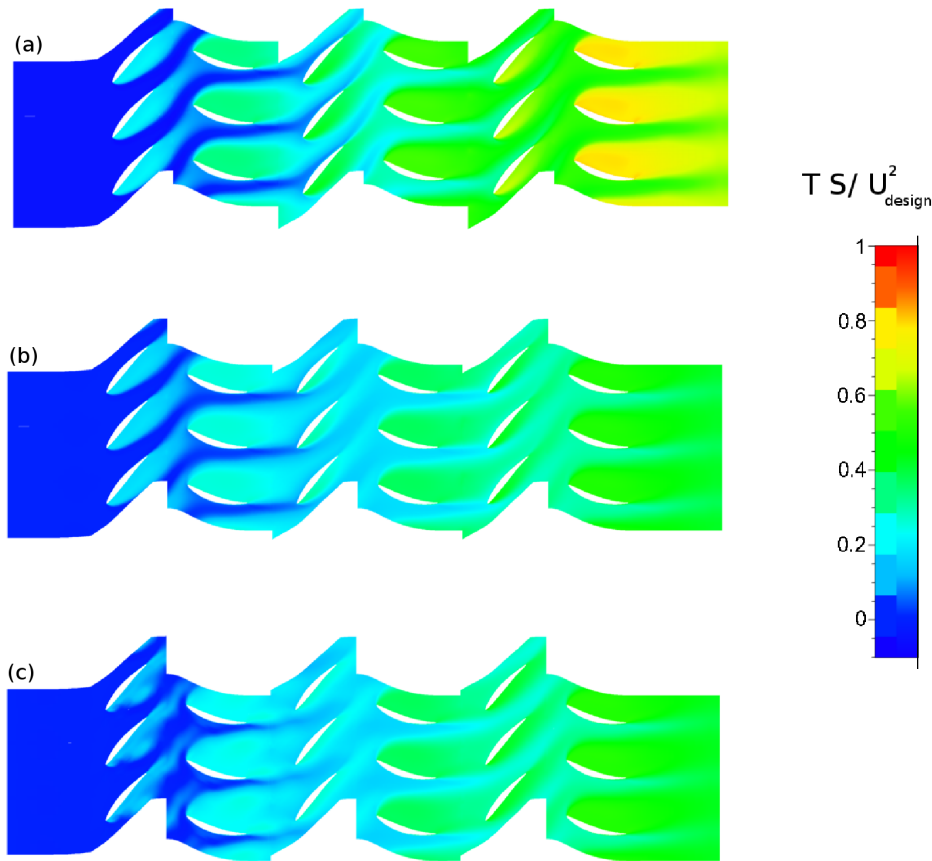


Figure 5.7: Entropy distribution for forward flow through compressor with locked rotor on midspan constant-radius surface for three clocking positions: (a) no offset; (b) offset by 0.25 blade pitch; (c) offset by 0.5 blade pitch

5.4 Summary

The non-dimensional characteristics for total to static and static to static pressure rise, torque and efficiency of a low speed axial flow compressor were experimentally determined for positive and negative rotation in for all four quadrants. The six possible modes of operation were accessed. Zero-speed S-curves for total to static pressure rise and torque were also determined. Performance data obtained from numerical modelling agree well with the experimental data in all modes.

Characteristics for first quadrant operation were of the shape expected for this type of machine.

Second quadrant positive rotation operation was a highly dissipative mode of operation, and the working fluid static temperature increased by as much as 10 K. In the non-dimensional form $C_p \Delta T / U^2$, the temperature rise for second quadrant operation is 14.4, while at design point it is 0.58. This mode of operation would thus be dangerous for machines operating at higher speeds.

In the second quadrant, negative rotation turbine mode, the test compressor displayed a static to static turbine efficiency of approximately 75 %, as the curvature of rotor and

CHAPTER 5. FOUR-QUADRANT OVERALL PERFORMANCE MAPS

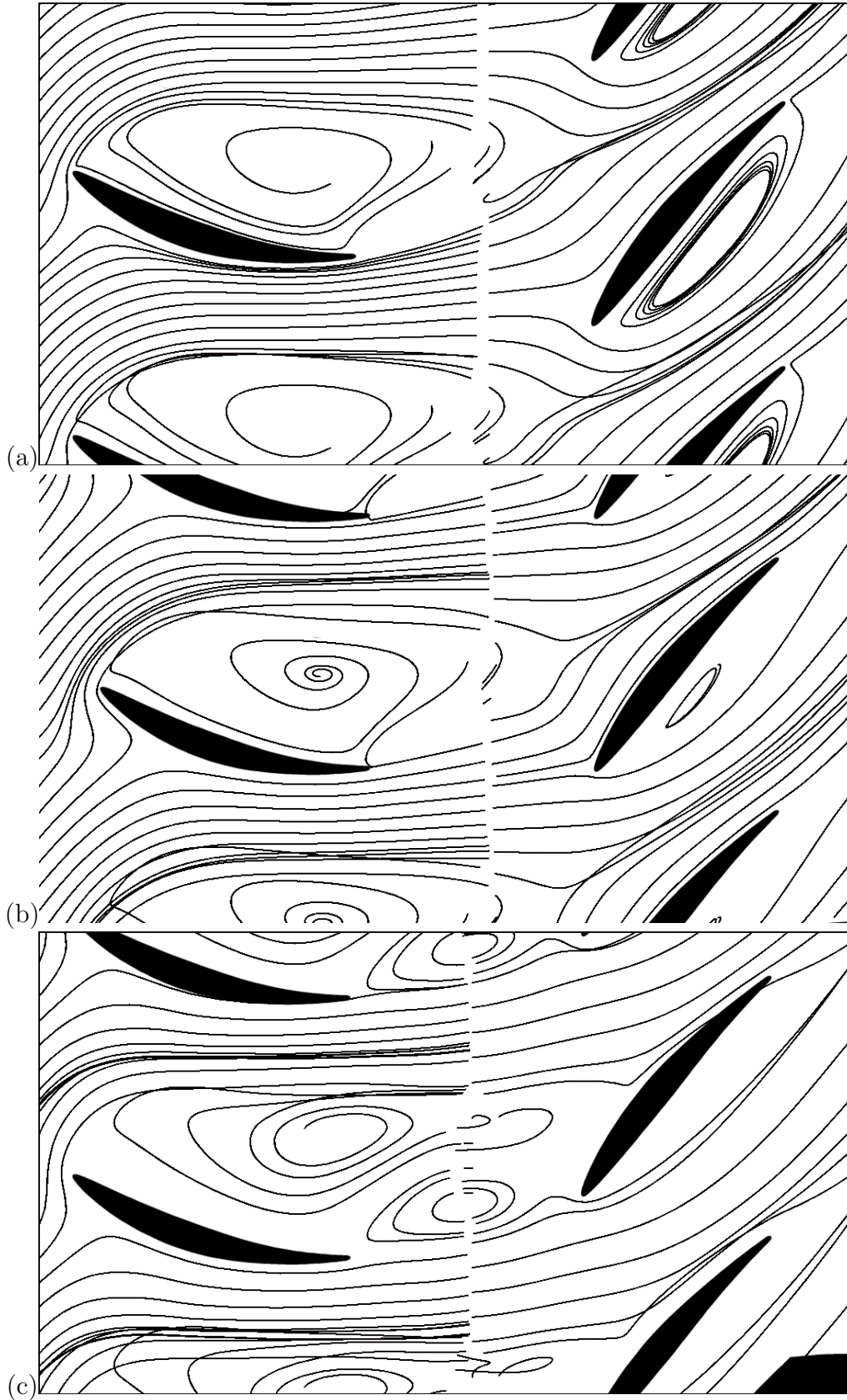


Figure 5.8: Streamlines surrounding first stage stator and second stage rotor for forward flow through compressor with locked rotor on midspan constant-radius surface for three clocking positions: (a) no offset; (b) offset by 0.25 blade pitch; (c) offset by 0.5 blade pitch

CHAPTER 5. FOUR-QUADRANT OVERALL PERFORMANCE MAPS

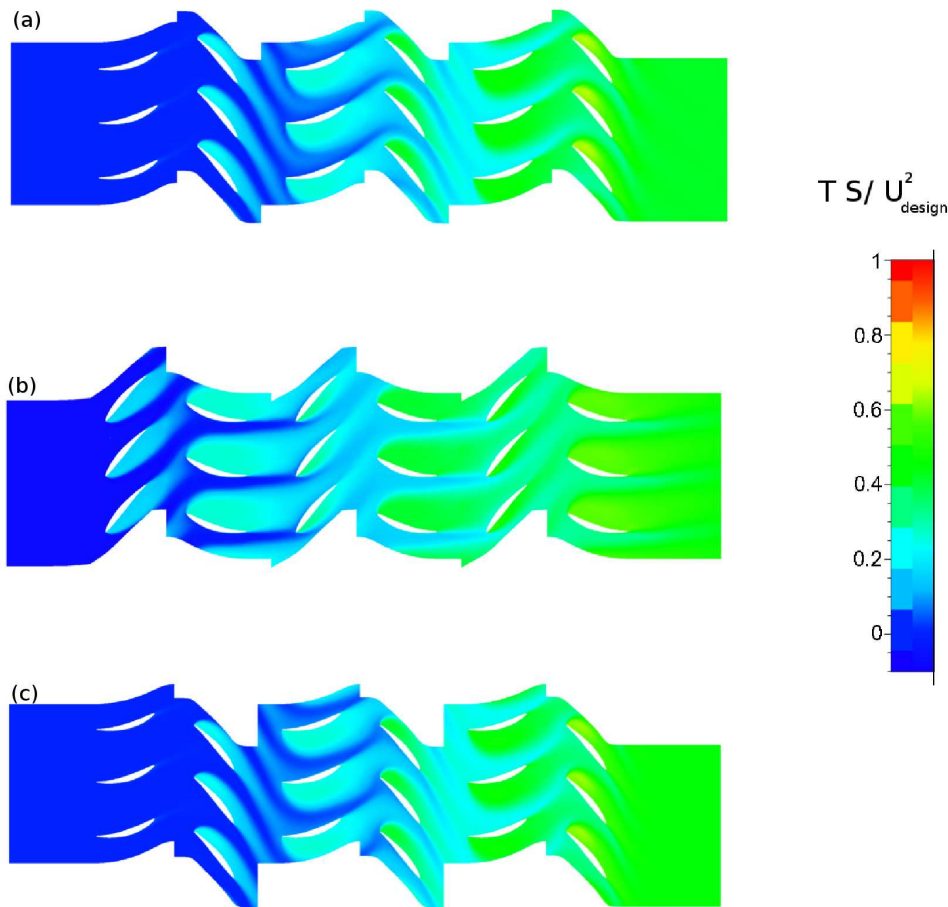


Figure 5.9: Entropy distribution for reversed flow through compressor with locked rotor on midspan constant-radius surface for three clocking positions: (a) no offset; (b) offset by 0.25 blade pitch; (c) offset by 0.5 blade pitch

stator blades was well matched to the relative flow angles.

In the fourth quadrant positive rotation mode of operation, the pressure and torque coefficients continue smoothly from those representing first quadrant operation. The fourth quadrant turbine efficiency was approximately 30 %, which is lower than that observed for second quadrant reverse rotation, due to the fact that the compressor blades are curved in the opposite direction to the direction of flow turning in this mode. Fourth quadrant negative rotational operation was dissipative in nature, but the temperature rise in the working fluid for this mode of operation was negligible.

Third quadrant operation represents a badly designed compressor with the blades curved in the wrong direction operating in reverse rotation and throughflow. Consequently the compressor is thought to operate in a stalled condition throughout this quadrant, yielding low efficiencies.

CHAPTER 5. FOUR-QUADRANT OVERALL PERFORMANCE MAPS

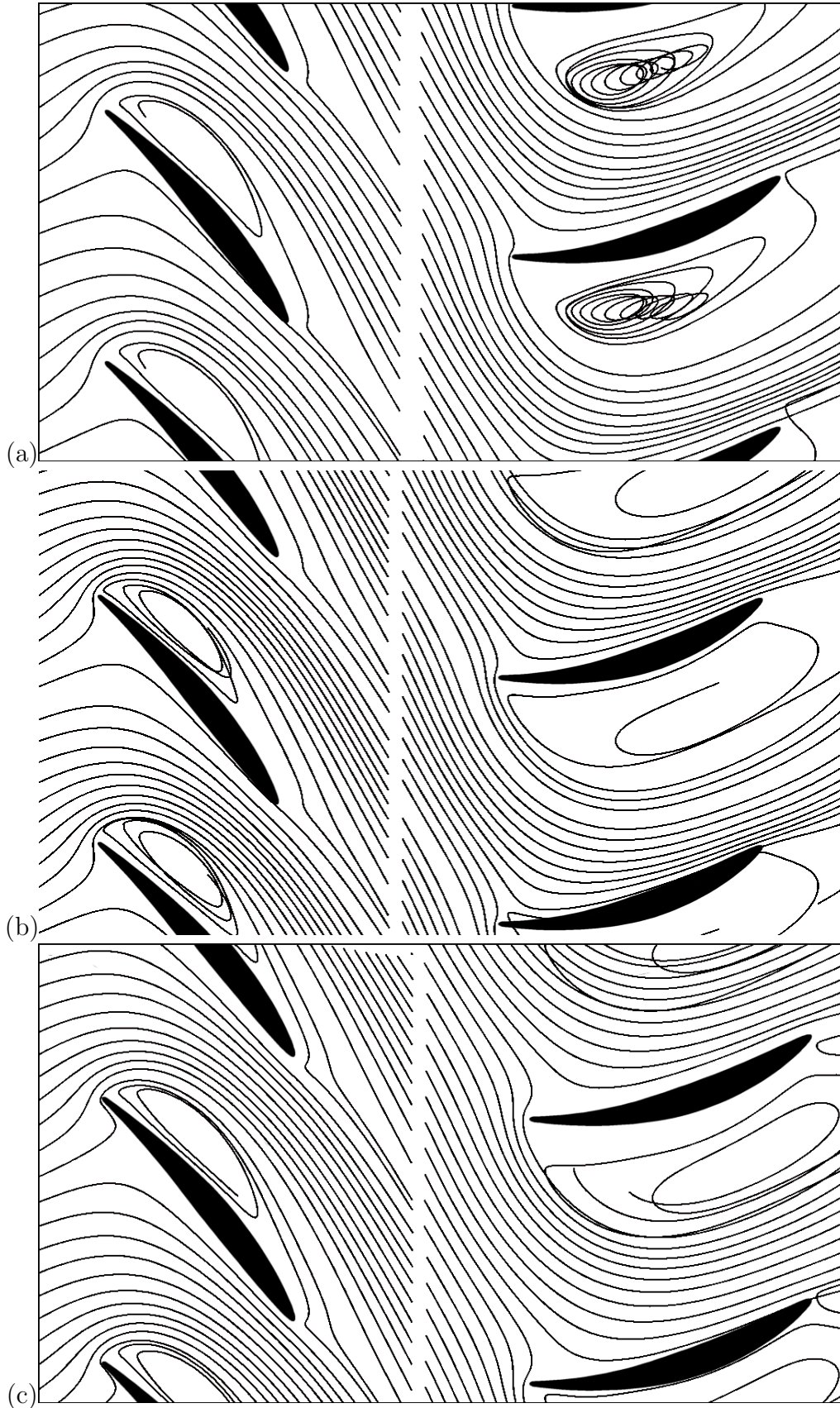


Figure 5.10: Streamlines surrounding third stage stator and second stage stator for reversed flow through compressor with locked rotor on midspan constant-radius surface for three clocking positions: (a) no offset; (b) offset by 0.25 blade pitch; (c) offset by 0.5 blade pitch

CHAPTER 5. FOUR-QUADRANT OVERALL PERFORMANCE MAPS

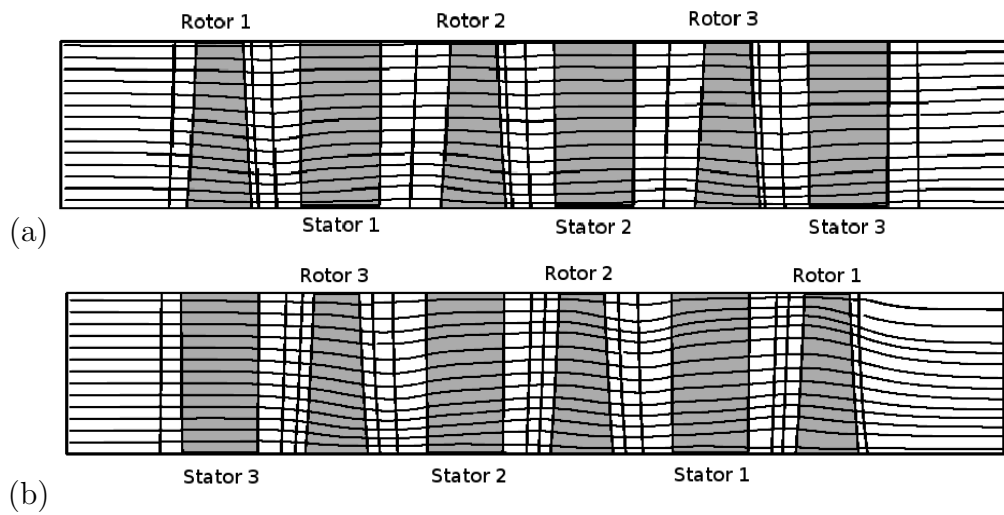


Figure 5.11: Meridionally averaged flow paths through the test compressor with locked rotor: (a) Forward flow, zero offset clocking position; (b) Reverse flow, zero offset clocking position.

Chapter 6

First quadrant: positive rotation

6.1 Introduction

As mentioned in chapter 2, first quadrant compressor operation has been exhaustively studied by a number of researchers for incompressible flow, subsonic and transonic compressible flow, and the phenomenon of stall and its effect on flow patterns within the compressor, as well as methods of stall suppression have also been extensively investigated. It will be recalled that the performance and flow field of the compressor used in this investigation was experimentally determined by Roos [1995], while the stall properties for the test compressor (albeit with modifications) were investigated by Lewis [1989].

The purpose of investigating the flow field under first quadrant operating conditions is threefold:

1. To characterise the performance of the compressor in the first quadrant.
2. To serve as a source of data for validation and verification of results obtained by means of computational fluid dynamics simulations.
3. To serve as a basis for comparison with the flow fields observed in other modes of operation.
4. To justify the experimental techniques used, by comparison with historical data and comparison between different measurement techniques.

Three points representative of first quadrant operation were investigated, namely a high-flow coefficient condition, with the throttle valve fully opened, with a rotor-tip based flow coefficient $\phi = 0.568$, near-design point operation ($\phi = 0.508$), and stalled operation ($\phi = 0.279$). Due to ageing of components in the thirty year old power electronics which controlled the rotational speed of the DC motor, it was not possible to run the compressor at full speed, thus all tests were conducted at 97 % of design speed. The power electronics have since been replaced. Operational points at pressure rise coefficients close to zero will be dealt with in chapter 7, with the discussion of fourth quadrant, positive rotation operation.

CHAPTER 6. FIRST QUADRANT: POSITIVE ROTATION

6.2 Experimental results

6.2.1 Time-averaged velocity profiles

Time averaged velocity profiles were obtained by means of a five-hole probe and by time-averaging of hot-film velocity measurements. Velocity distributions as a function of radius were obtained at the compressor inlet, and downstream of each rotor row (measurement stations S0, R1, R2 and R3) shown in figure 3.1. The axial and tangential velocity profiles thus determined are shown for the three flow coefficients under investigation, representing stalled operation, design point operation and the maximum mass flow rate attainable without use of an auxiliary fan.

Figures 6.1 and 6.2 show the spanwise distribution of the axial and tangential velocity components respectively at design point. Figures 6.3 and 6.4 show the corresponding velocity distributions for the maximum flow coefficient attainable without the use of auxiliary

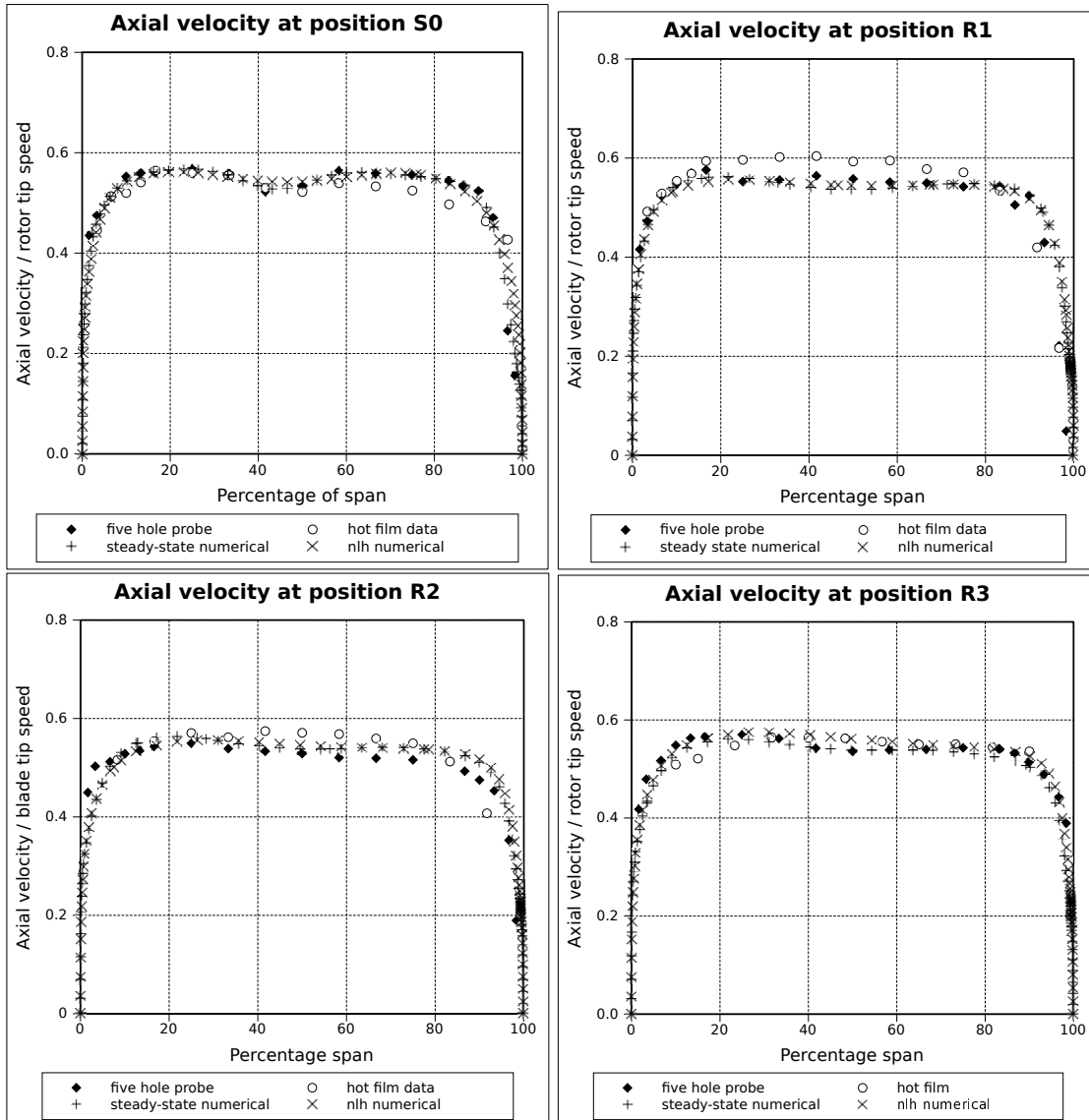


Figure 6.1: Axial velocity components as a function of radius at $\phi = 0.508$ (design point)

CHAPTER 6. FIRST QUADRANT: POSITIVE ROTATION

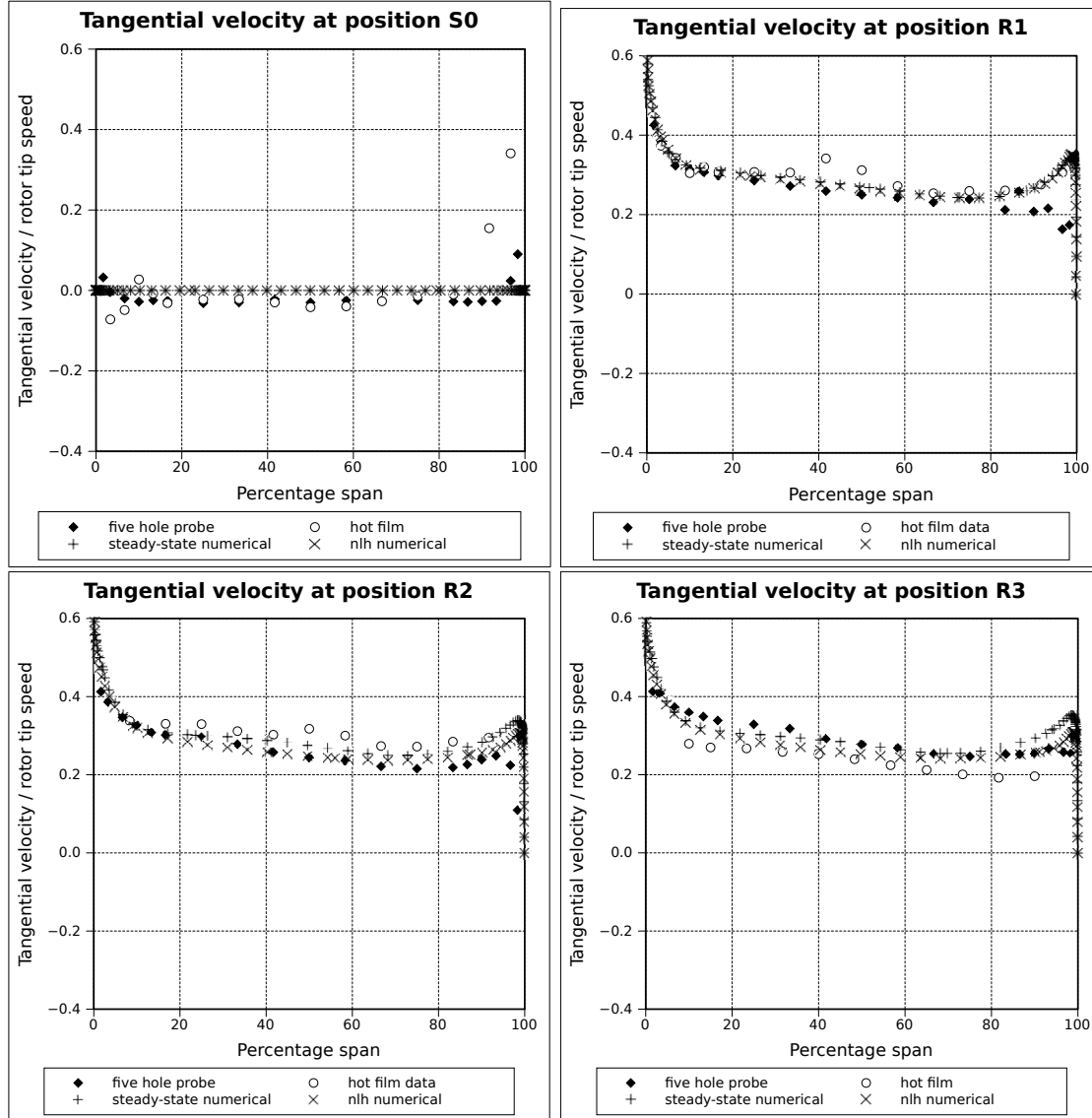


Figure 6.2: Tangential velocity components as a function of radius at $\phi = 0.508$ (design point)

fans. The radial velocity components are less than 5 % of the axial velocity at all axial positions and radii, and are thus negligible, and not shown.

The results obtained from radial traverses with time averaged hot film and five-hole probe agree well with one another. The spanwise distribution of the axial velocity profiles at design point (figure 6.1) is unremarkable, exhibiting well-defined hub and casing boundary layers, each approximately 20 % of the span, and the velocity in the remaining, central area is approximately uniform. Integration of the axial velocity components over the annulus for design-point operation (figure 6.1), and high flow coefficient (figure 6.3) at axial positions S0, R1, R2 and R3 yields a maximum difference of 2 % compared with the average volumetric flow as measured by the turbine anemometer, assuming axisymmetric flow.

A comparison was made between velocity profiles obtained before and after the installation of the inlet guide vanes. The IGVs were fitted in an attempt to ensure axial flow downstream of station S0, although it was later shown that they were unnecessary. It

CHAPTER 6. FIRST QUADRANT: POSITIVE ROTATION

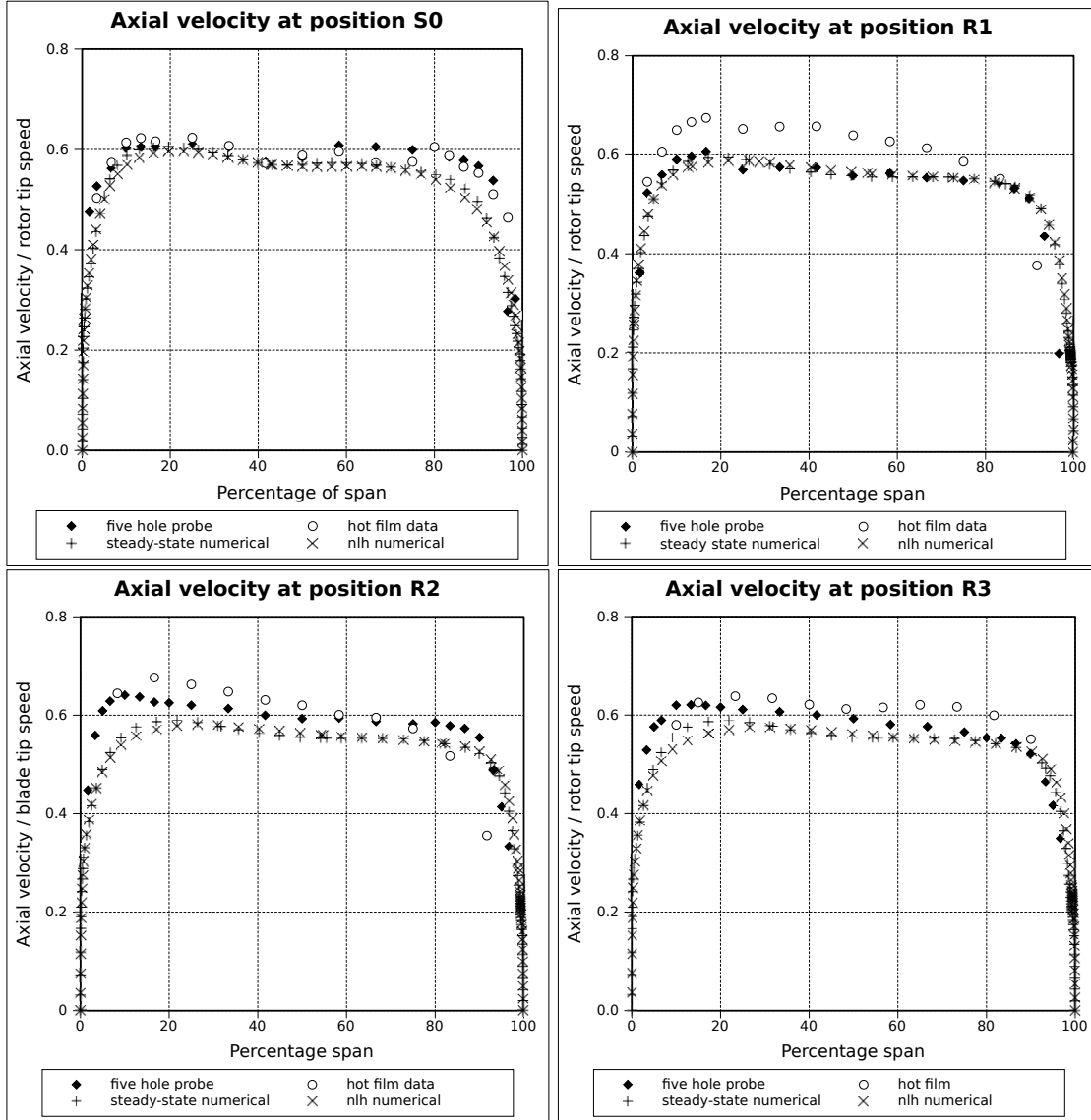


Figure 6.3: Axial velocity components as a function of radius at $\phi = 0.568$

was shown that the IGVs do not affect the flow field measurably during first quadrant operation.

At a flow coefficient of 0.568 (6.3), the hub boundary layer decreases in thickness to approximately 10 % of blade span. This change is evident at the compressor inlet (station S0), thus it appears that the hub boundary layer has undergone transition due to the higher flow velocities. The axial velocity decreases approximately 10 % from hub to tip downstream of all rotor rows.

The tangential velocity components (figures 6.2 and 6.4) conform approximately to a free vortex distribution beyond the hub and casing boundary layers, as the blading was designed for free vortex operation. Consequentially, the fluid work is evenly distributed along the span; figure 6.5(a) shows that the load coefficient $U(r)C_\theta(r)/U^2$ varies by approximately 5.9 % for the portion of the annulus between hub and casing boundary layers. The diffusion factor for the first stage rotor at design-point (figure 6.5 varies from approximately 0.4 near the hub to approximately 0.3 near the tip; at midspan it is 0.32. This

CHAPTER 6. FIRST QUADRANT: POSITIVE ROTATION

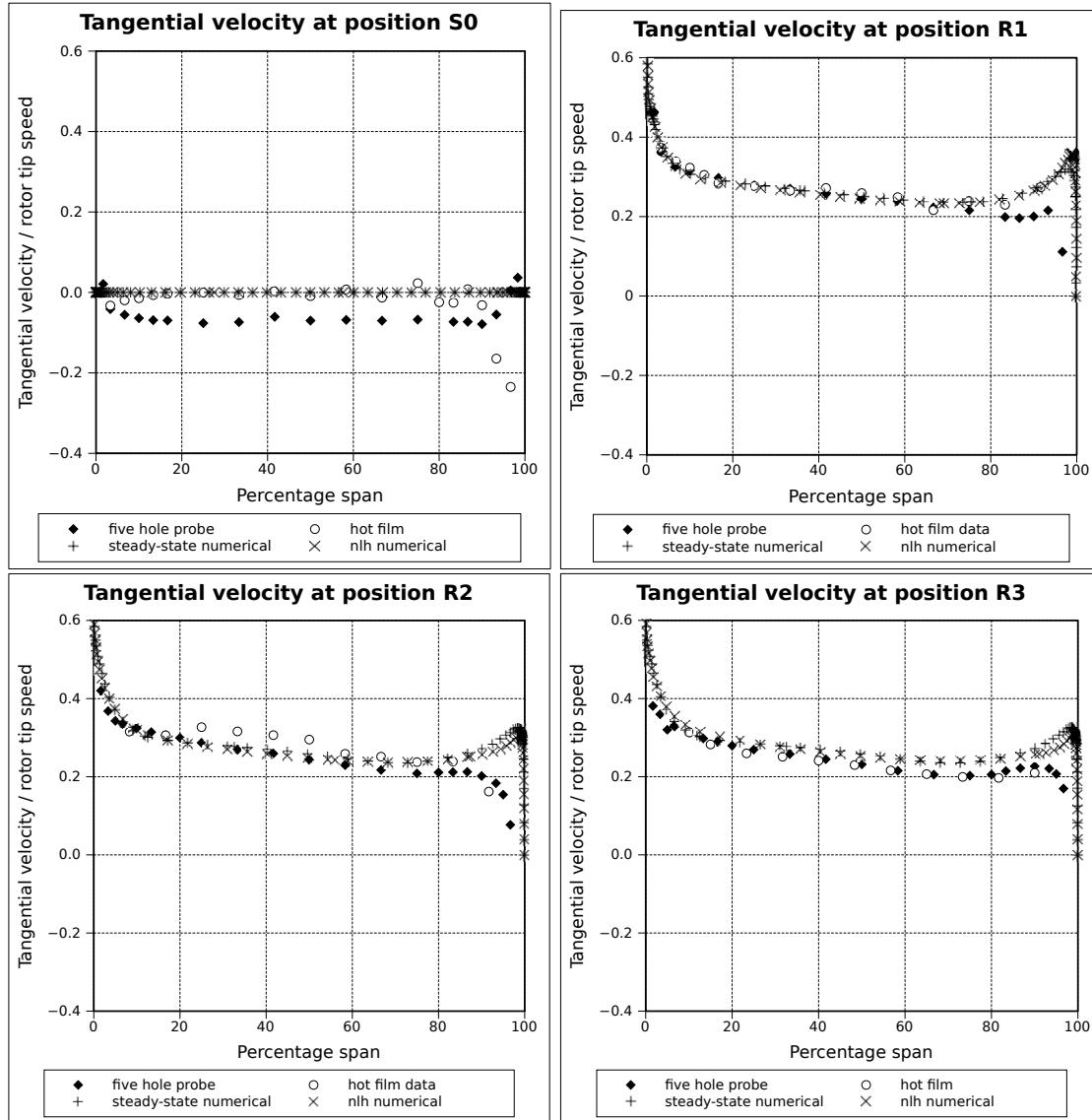


Figure 6.4: Tangential velocity components as a function of radius at $\phi = 0.568$

is somewhat lower than the value of 0.45 given by Cumpsty [1989] as "a typical design choice". The result of this is that less flow turning occurs in the rotors than in the stator rows, as will be seen later in this chapter.

The velocity profiles obtained are similar to those of Roos [1995], although the flow coefficients investigated are not identical.

Experimentally determined velocity profiles for stalled operation are shown in figures 6.6 and 6.7. Agreement between five-hole probe and hot film data for stalled operation were poor for axial velocity profiles (figure 6.6), but somewhat better for circumferential velocity profiles (figure 6.7). The volume flow rate determined by integration of axial velocity profiles disagreed with that measured by the turbine anemometer by more than 30 % downstream of the rotor rows. Stalled operation is unsteady, and not axisymmetric, which may be responsible for these discrepancies. It should also be noted that the velocity profiles obtained during stall represent a fictitious average of stalled and unstalled blade passages. Flow velocities in the unstalled blade passages are, of course, larger than the

CHAPTER 6. FIRST QUADRANT: POSITIVE ROTATION

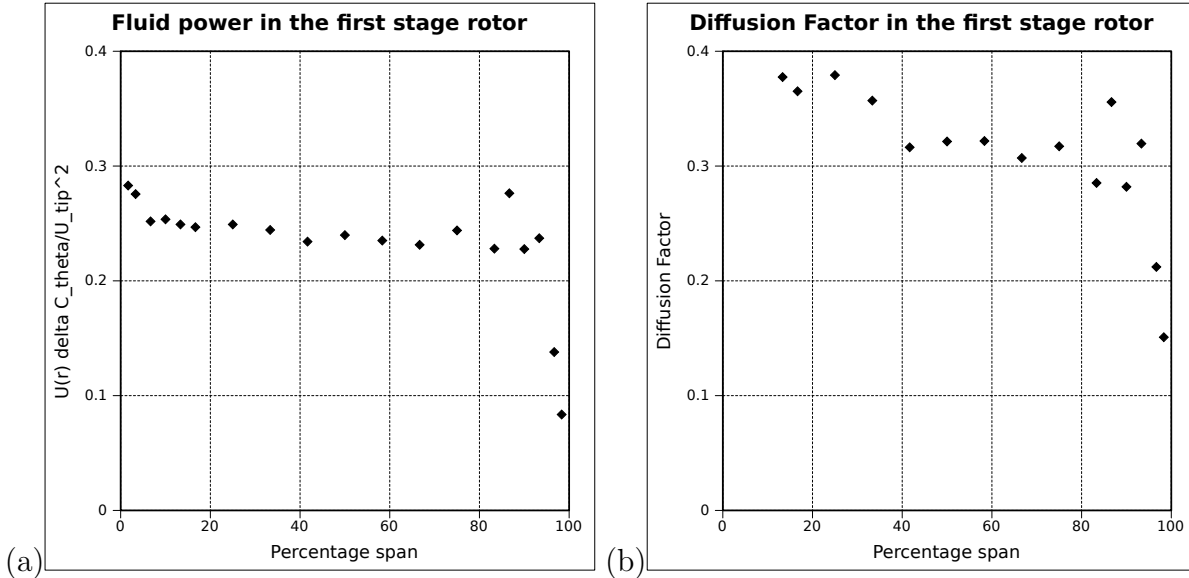


Figure 6.5: (a) Local load coefficient (b) Diffusion factor for the first stage rotor as a function of radius at design point $\phi = 0.508$

velocities indicated by the time-averaged data, while those within the stall cell are lower. This will be discussed in more detail in the section on time-dependent results. The reasons for the lack of numerical results for the stalled case will be discussed in the section on numerical results.

6.2.2 Time dependent results

Time dependent flow field variations may be divided into those which are cyclic in nature, usually related to the rotational speed or blade passing frequency of the rotor row adjacent to the measurement position, and those which are non-repeating or random in nature, which are usually related to turbulence, and variations in environmental conditions. A special case of the first type of disturbance is the rotating stall cell. Analysis of rotating stall is complicated by the fact that the stall cells rotate at a different speed to the machine rotor.

Cyclic flow field variations linked to the rotation of the machine rotor are dealt with by a phase-locking averaging scheme: the flow-conditions for a number of rotor positions are averaged over many rotations, thus eliminating random velocity fluctuations. The end result is the cyclic velocity variation for a single “ideal” rotor revolution. This approach works well for unstalled first quadrant operation, yielding clearly defined wakes for each of the 43 rotor blades, as shown in figure 6.8. The average difference between minimum velocity in the rotor blade wakes, and the maximum velocity in the jets is approximately 10 % of the mean velocity. The instantaneous velocity drops below the time-averaged velocity for approximately 35 % of each blade passing interval, indicating that the jets are dominant over the wakes. Also note that the blade wakes are sharp, while the jets are rounded in profile. These observations suggest that flow around the blades is not separated, thus the blockage observed is probably due to blade boundary layers. It will be shown in later chapters that flow separation on blades would cause wakes to occupy a larger percentage of each blade passage, and have a more rounded profile.

CHAPTER 6. FIRST QUADRANT: POSITIVE ROTATION

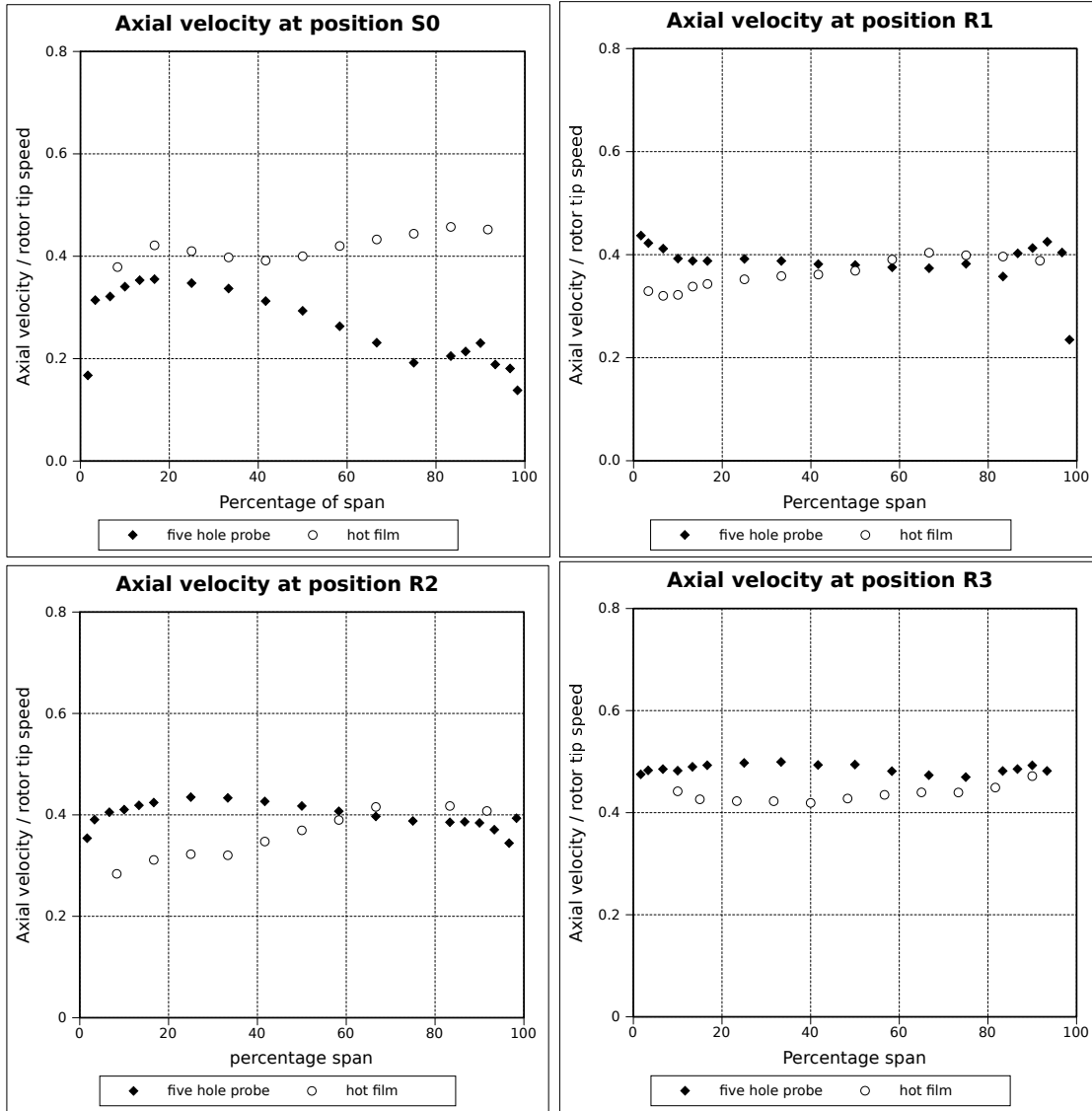


Figure 6.6: Axial velocity components as a function of radius at $\phi = 0.279$ (stalled operation)

The averaging scheme used to obtain the idealised revolutions shown above fails for stalled operation, as cyclic variations occur at a frequency unrelated to the rotational speed of the machine. However, use of a two-sensor cylindrical hot-film x-probe allowed the determination of the axial velocity component in real-time. Figure 6.9 shows the resulting time trace over 14 revolutions downstream of the third rotor row. A repeating pattern with a period of approximately two and a half revolutions can be observed. This appears to be due to a single rotating stall cell, such as was observed by Lewis [1989] in his investigation of the test compressor. The repeating stall cell pattern in the time trace is similar to that observed following the onset of stall as observed by Camp and Day [1998].

A Fast Fourier Transform (FFT) was applied to time-series velocity data obtained downstream of each rotor row, in order to obtain frequency spectra. This yields information regarding the size and shape of any cyclic or repeating disturbances which occur in the time series. In unstalled cases, the blade passing frequency and its harmonics may be expected to dominate, while in stalled operation, the presence of stall cells may be determined from the existence of a spike. It may also be deduced whether one or several stall cells are

CHAPTER 6. FIRST QUADRANT: POSITIVE ROTATION

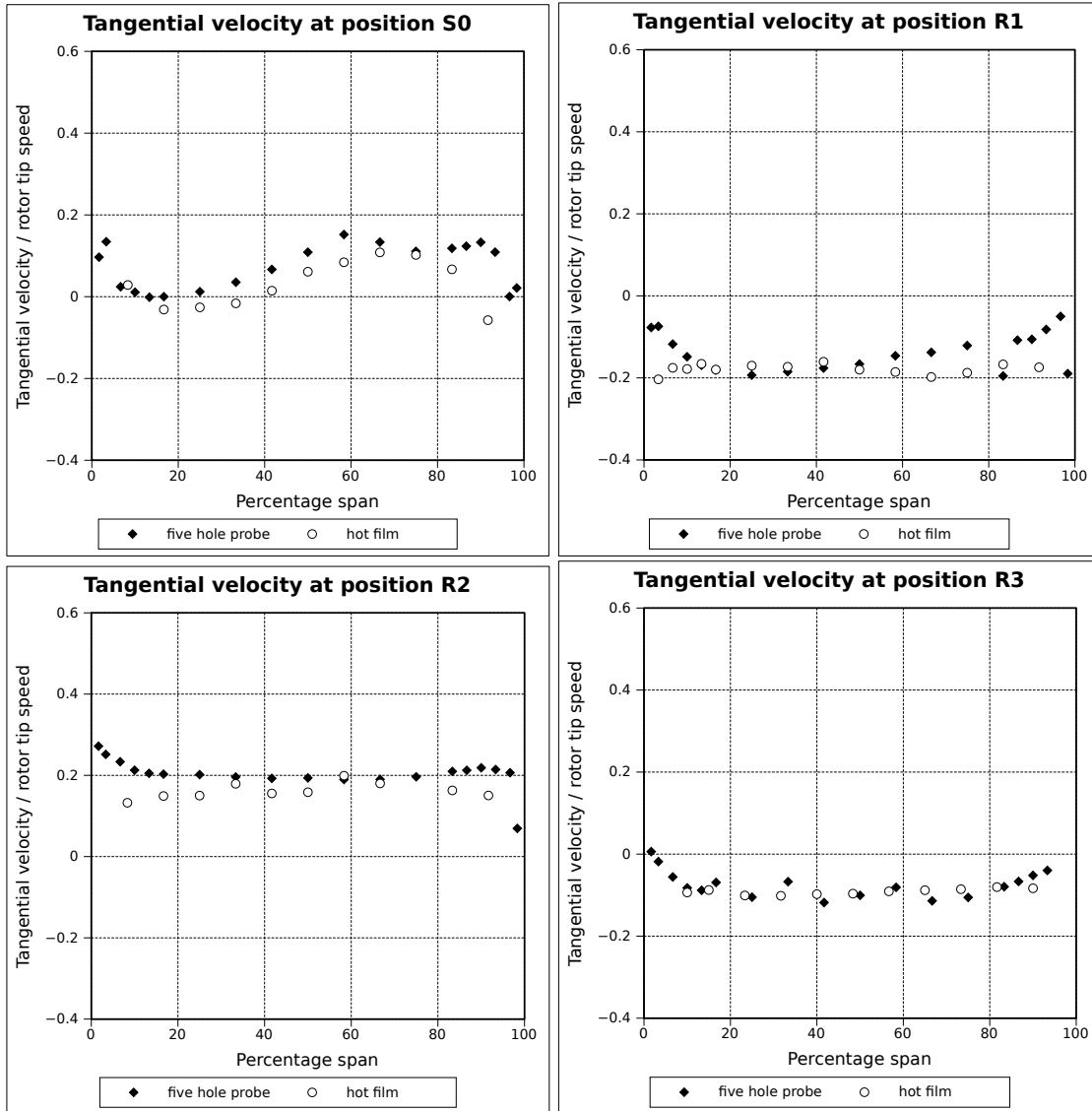


Figure 6.7: Tangential velocity components as a function of radius at $\phi = 0.279$ (stalled operation)

present, depending whether the frequency is below or above the compressor rotational frequency respectively.

The frequency domain data is also important as it allows the detection of cyclic disturbances at frequencies other than multiples of the blade passing frequency. Such disturbances would invalidate the phase-lock averaging scheme employed to process hot film anemometer data, and also numerical modelling results, both steady-state and unsteady results, if they are of the same order of magnitude as the cyclic variations caused by rotor wakes. As the latter are obtained using the non linear harmonic approximation, which requires that an appropriate number of harmonics of the blade passing frequency are modelled, this information is also useful in ensuring efficient use of computational resources in modelling. It should be noted that the raw cooling velocity was used for these investigations, as the phase-lock averaging scheme used to obtain three dimensional velocity vectors for average revolutions would effectively filter out or corrupt any disturbances not

CHAPTER 6. FIRST QUADRANT: POSITIVE ROTATION

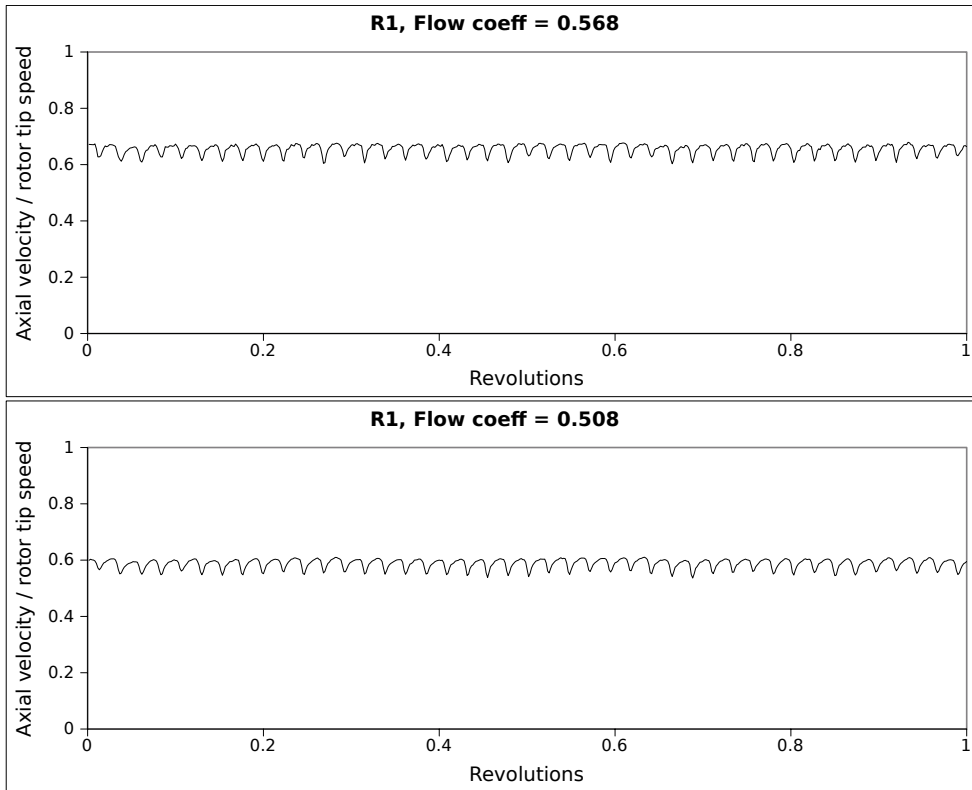


Figure 6.8: Time-traces for axial velocity component over one revolution at mid-span

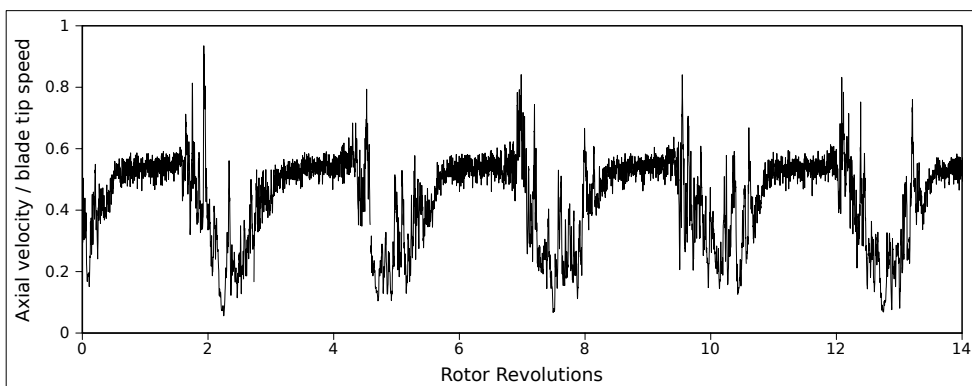


Figure 6.9: Time-trace for axial velocity component at mid-span at position R3 showing stall-related disturbances

CHAPTER 6. FIRST QUADRANT: POSITIVE ROTATION

related to the rotational frequency of the compressor. The x-probe hot film sensor was used for measurements at position R3 for all flow coefficients, and as it yielded two true velocity components independent of the averaging scheme, the axial velocity was used for frequency domain analysis for this station.

Figure 6.10 shows the frequency spectra of the velocity time trace at midspan downstream of each rotor row for design point operation. All the velocity spectra above the noise level occur at multiples of the blade passing frequency or the rotational frequency of the machine, although the latter less than 10 % of the blade passing frequency component amplitude, and are thus almost negligible. This indicates that virtually all cyclic variation in velocity is caused by the wakes of the passing rotor blades. The number of harmonics of the blade passing frequency indicates that the wake-jet pattern is relatively complex, in this case taking the form of the truncated sawtooth pattern observed in figure 6.8. This information is important as it indicates that the phase-locked averaging scheme used to determine the time traces in figure 6.8 is valid. It is also of significance to the numerical simulations, as the non-linear harmonic approximation assumes that all cyclic variation occurs at multiples of the blade passing frequency, which is, for practical purposes, the case. The size of the spikes provides an indication of the amplitude of the velocity variation due to the passing wakes. The largest spike, in this case the one at the blade passing frequency, provides a relatively good indication of this because the magnitude of the its harmonics decay rapidly. The second harmonics at positions R1 and R2 are both approximately 20 % of the amplitude of the fundamental, while the third harmonics are approximately 16 % thereof.

In figure 6.10, the amplitude at blade passing frequency and its harmonics at position R2 are double those at R1. This indicates that the difference between velocities in the wakes and the jets between them is approximately twice as large downstream of the second stage rotor than the first stage, indicating that the second stage rotor wakes are stronger than those in the first. The amplitudes at position R3 are fourfold larger than at position 1, but it should be remembered that this data is based on the true velocity determined by means of the x-probe, while the data at position 1 and 2 is based on the cooling velocity from the single sensor inclined hot film probe. The cooling velocity may be equal to or up to 25 % smaller than the true velocity to a varying degree dependent on the angle of flow relative to the sensor at any instant, thus the actual increase in the velocity variation between wakes and jets from R2 to R3 may be smaller than is suggested by the figure.

The frequency domain data for a flow coefficient of 0.568 (figure 6.11) is similar to that for design point operation. The blade passing frequency is dominant, followed by its second and third harmonic. All amplitudes are smaller than for design point operation, however, by approximately 50 % in the case of the first stage blade passing frequency and 20 % for the third stage.

An area traverse downstream of the first stage stator row (axial position S1) was performed for design-point operation. A time-series for a single blade passing interval is shown in figure 6.12. The wakes of two stator blades are visible in all time-steps. The wakes of upstream stator blades are well-defined, occupying a maximum of approximately 40 % of the blade pitch at approximately 60 % span, approximately half this value at 40 % of the blade span, and they vary by less than 5 % of the blade span in size in any direction as a function of rotor position, although some "breathing" is observed relating to the movement of the upstream rotor blades. The upstream rotor wake is not evident, however, and appears to have dissipated due to mixing in the stator blade passage. An area of relatively uniform high-velocity flow occurs between stator wakes, with the highest velocities occur-

CHAPTER 6. FIRST QUADRANT: POSITIVE ROTATION

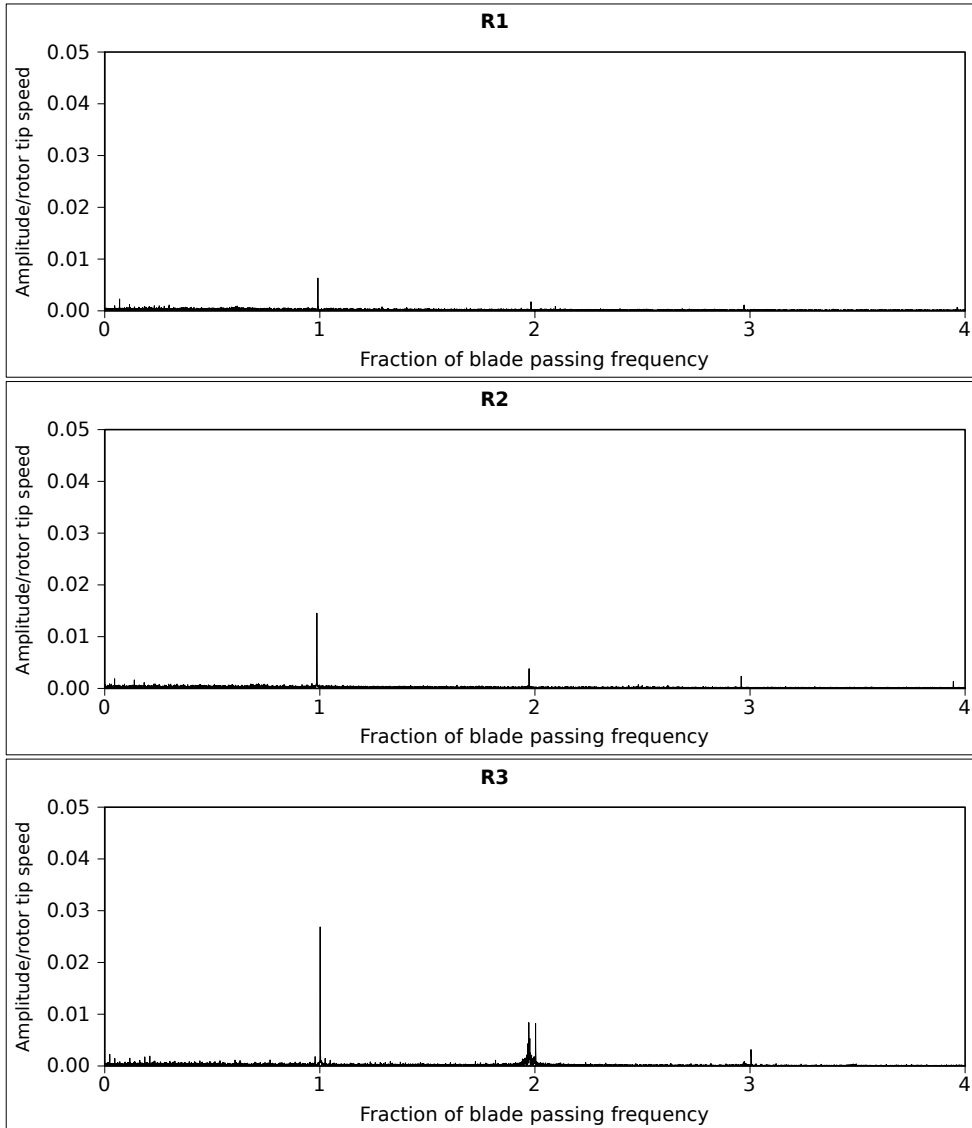


Figure 6.10: Frequency domain of cooling velocity variation at design point ($\phi = 0.508$) at mid-span

ring between 25 and 50 % of the span (label A in figure 6.12). The lowest velocities in the core of the wake appear to be approximately 80 % of the maximum velocity occurring between wakes (label B). The casing boundary layer occurs from 80 to 100 % of the blade span (label C). It was not possible to insert the probe to the depth necessary to allow measurement of the hub boundary layer.

The large area of approximately uniform velocity between wakes and the small difference between the velocity in the wakes and that between them imply that downstream rotor blades spend between 20 and 40 % of each blade passing interval in the upstream stator wake, and the remainder of the time they receive nearly uniform flow. Further, the velocity in the wake is less than 20 % lower than that in the jet. This implies that the use of mixing planes between stator and rotor rows in numerical modelling is a reasonable approximation for this mode of operation. This does not, however, invalidate the concerns of Denton [2010] that mixing planes cause artificial losses not present in the physical flow, although the low Mach numbers in the test compressor (of the order of 0.2) preclude the

CHAPTER 6. FIRST QUADRANT: POSITIVE ROTATION

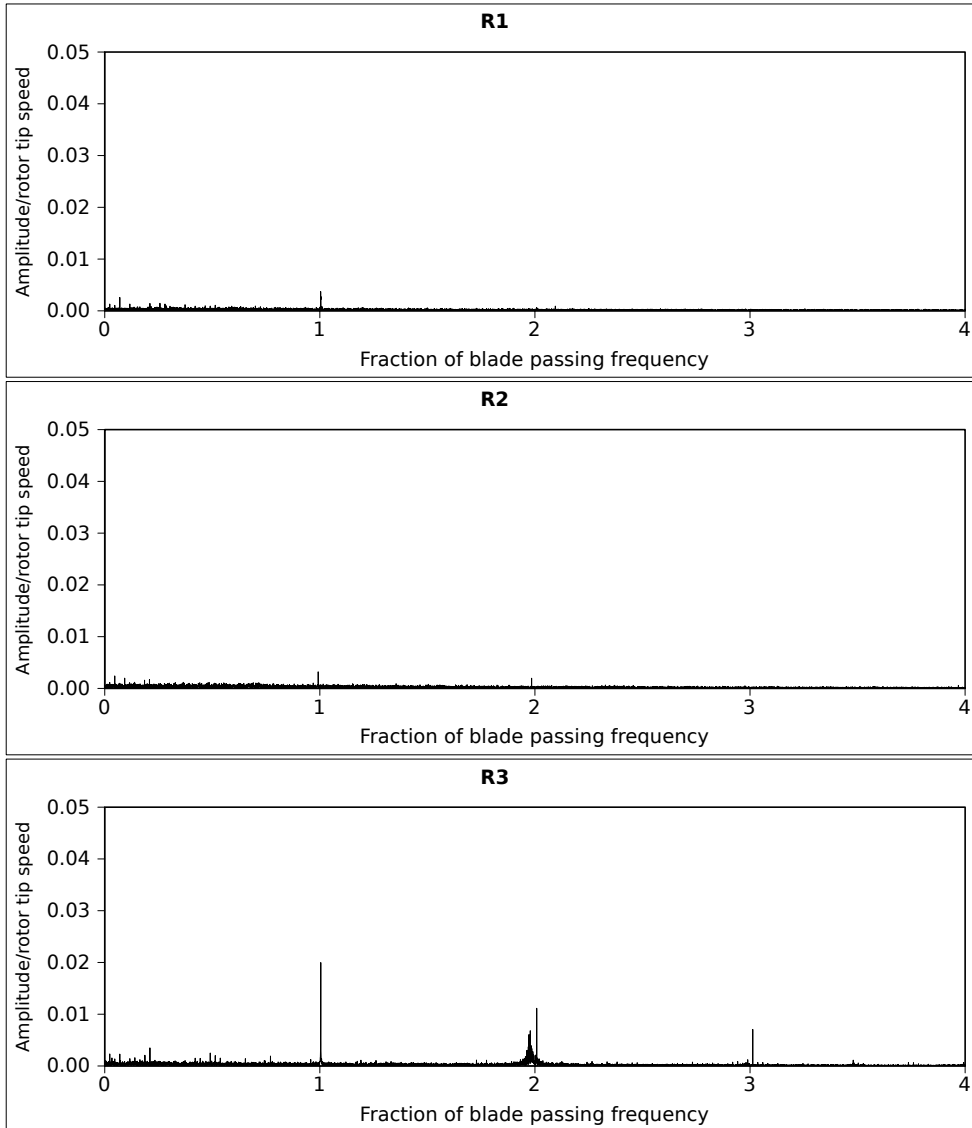


Figure 6.11: Frequency domain of axial velocity variation at maximum flow rate ($\phi = 0.568$) at mid-span

existence of shocks or other compressible flow phenomena which would further exacerbate this.

Due to the well-ordered nature of flow at near-design point operation, the linearised method of Russ and Simon [1991] for calculating the Reynolds stress tensor components could be successfully applied as described in chapter 3. This was applied for a flow coefficient of 0.508 downstream at position R1 and S1. For position S1, a radial trace positioned approximately mid-way between two stator wakes was used for this calculation. The three diagonal components of the tensor ($\overline{u'_z u'_z}$, $\overline{u'_\theta u'_\theta}$ and $\overline{u'_r u'_r}$) were used to calculate the three-dimensional turbulence intensity as a percentage of the time-averaged flow velocity, while the non-diagonal terms ($\overline{u'_z u'_\theta}$, $\overline{u'_r u'_\theta}$ and $\overline{u'_z u'_r}$) are presented as calculated. Turbulence intensities are shown as a function of percentage span in figure 6.13, while the non-diagonal Reynolds stress tensor components are shown in figure 6.14. The large turbulence value is due to the presence of a fine mesh in the compressor inlet a short distance upstream of the hot film probe. It is interesting to note that the local minimum occurring near 40 % span

CHAPTER 6. FIRST QUADRANT: POSITIVE ROTATION

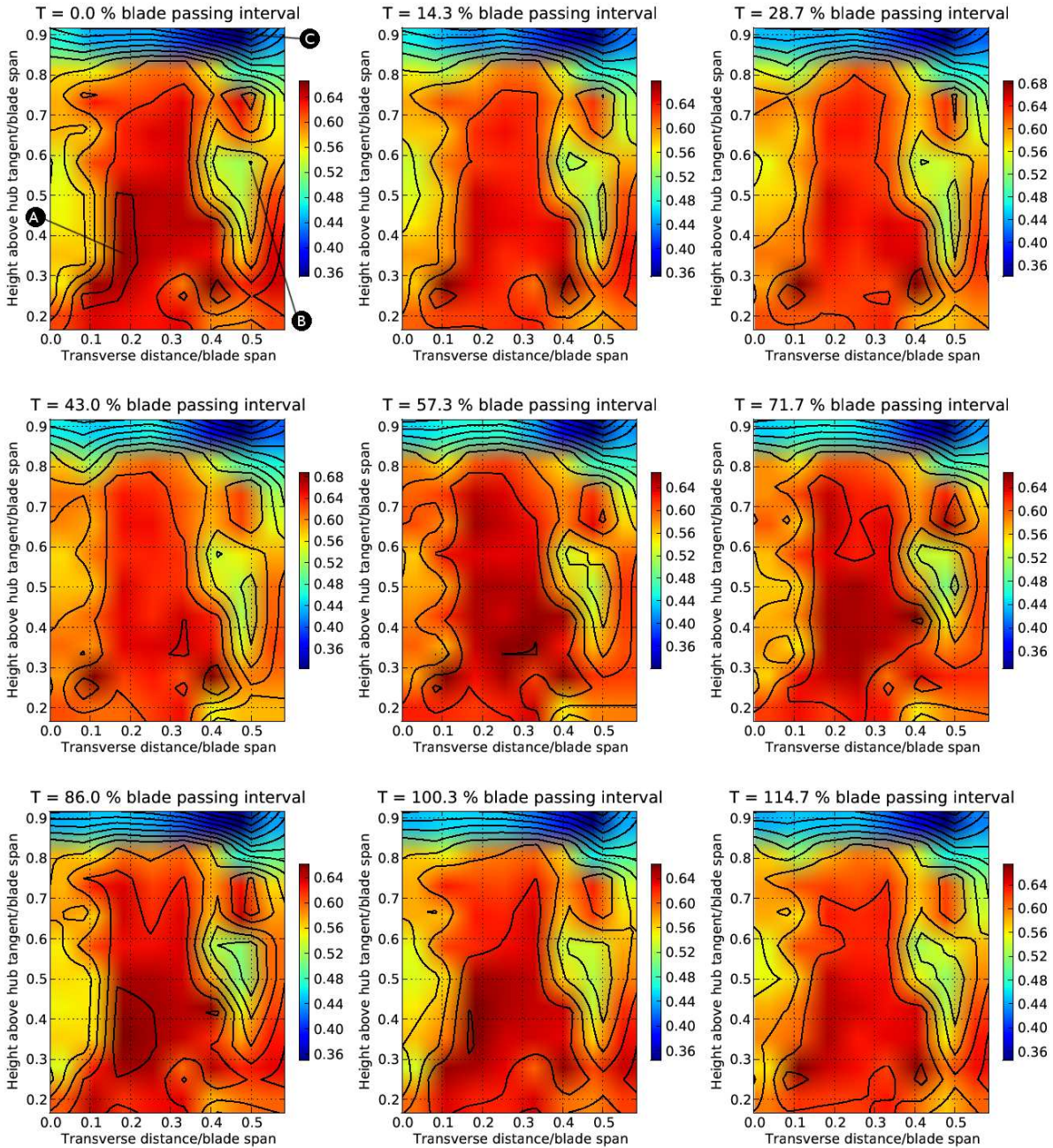


Figure 6.12: Time series of axial velocity contours at position S1 at $\phi = 0.508$

CHAPTER 6. FIRST QUADRANT: POSITIVE ROTATION

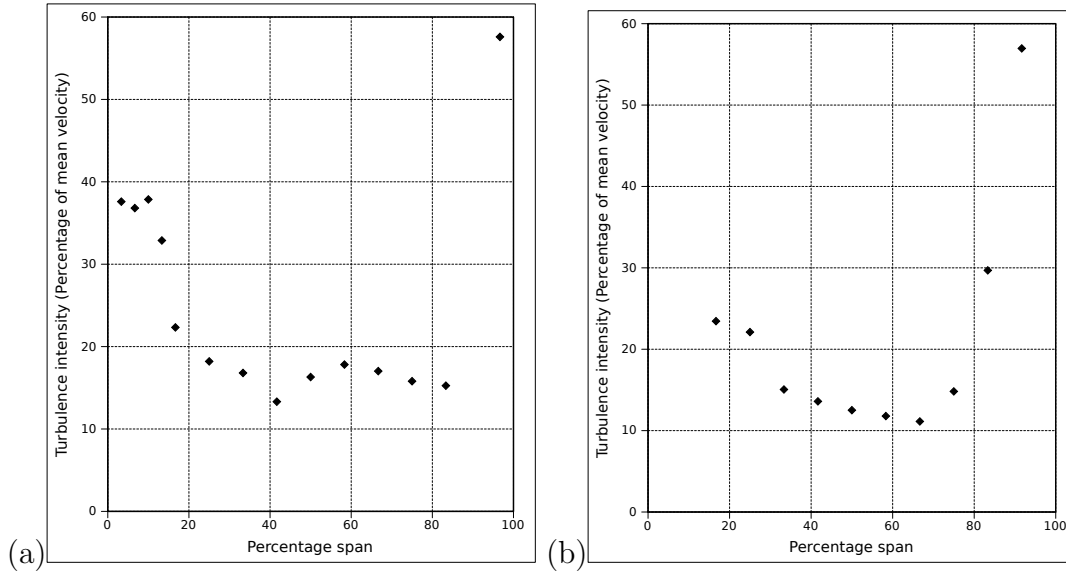


Figure 6.13: Turbulence intensity as a function of percentage span at near design-point operation ($\phi = 0.508$) at (a) R1 and (b) S1

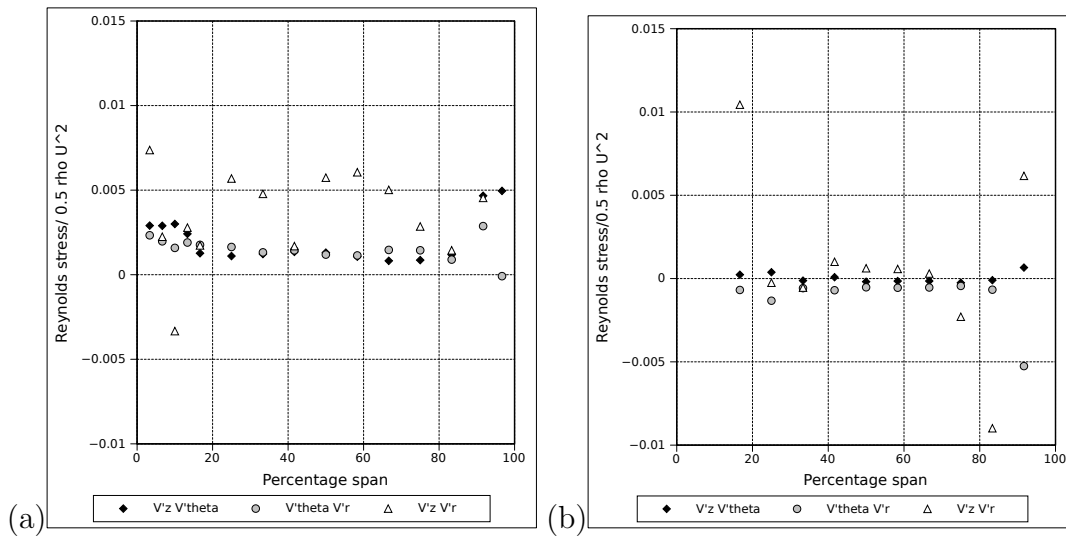


Figure 6.14: Reynolds stress components as a function of percentage span at near design-point operation ($\phi = 0.508$) at (a) R1 and (b) S1

in the axial velocity profile at R1 (figure 6.1) corresponds with a similar local minimum in the turbulence intensity (figure 6.13).

An attempt was made to obtain Reynolds stresses for operating points in other quadrants, but the linearising assumptions in the method [Russ and Simon, 1991] are inappropriate for the highly turbulent, time-unsteady conditions encountered, and thus results, particularly turbulent intensity, were spuriously large. For this reason they were not included.

For stalled operation, shown in figure 6.15, the blade passing frequency component and its second and third harmonic may be identified, having magnitudes more than 200 % above the noise level. Their amplitudes are approximately 20 % and 10 % of the amplitude of the

CHAPTER 6. FIRST QUADRANT: POSITIVE ROTATION

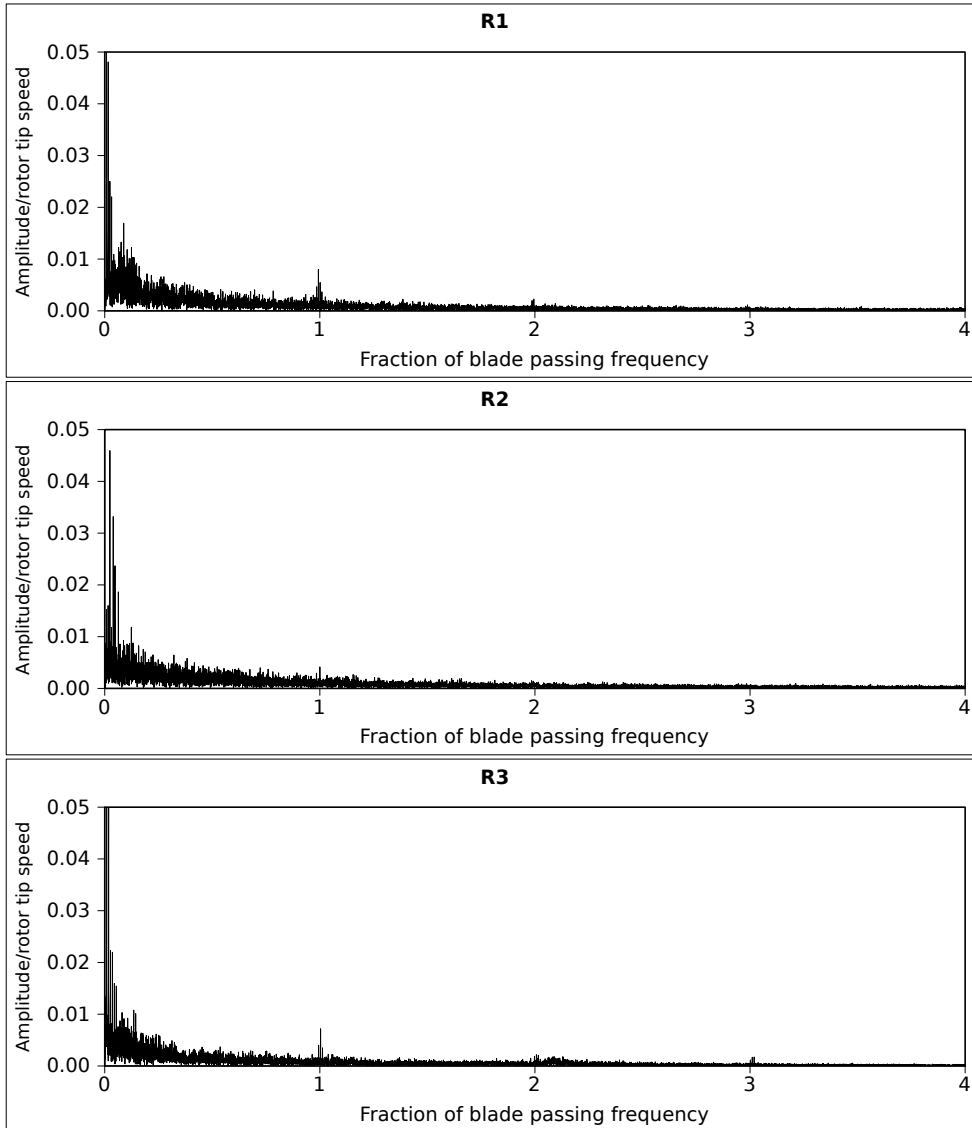


Figure 6.15: Frequency domain of cooling velocity variation at stall $\phi = 0.279$ at mid-span

blade passing frequency component, respectively. All blade passing-related phenomena are somewhat overshadowed by a large number of frequency components at frequencies below the blade passing frequency, the largest of which are more than 200 % the amplitude of the blade passing frequency component. These are related to the stall cells present in the machine. For stalled operation frequency domain data in a higher pressure ratio and Mach number compressor, the reader is directed to Gannon et al. [2010], in which an investigation of a transonic axial flow fan is presented.

In order to examine the frequency components relating to the presence of stall cells at less than the blade passing frequency, the data for position R3 in figure 6.15 is replotted in figure 6.16, with all frequencies expressed as a fraction of the rotational frequency of the machine. The rotational frequency of the stall cell can now be clearly determined as approximately 40 % of the rotational frequency, in agreement with the period indicated in figure 6.9. All harmonics of this frequency up to and including the sixth harmonic have an amplitude of over 200 % of that of background noise. This provides an indication of the complexity of the shape of the stall cell and of the flow structures within.

CHAPTER 6. FIRST QUADRANT: POSITIVE ROTATION

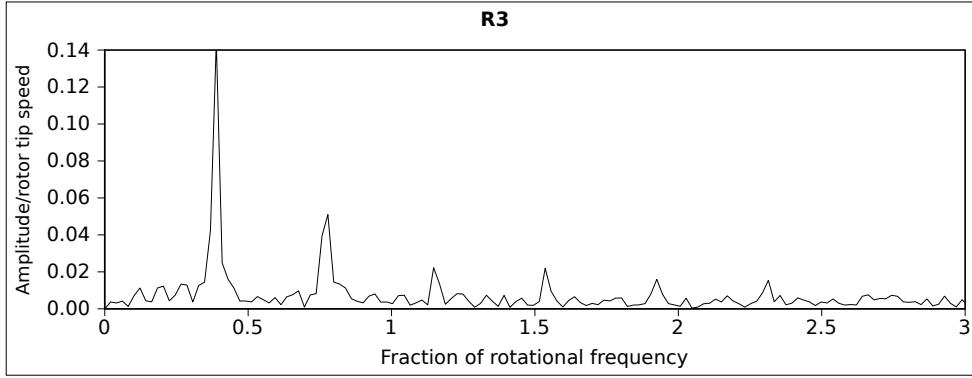


Figure 6.16: Frequency domain of cooling velocity variation at stall at mid-span, with frequencies normalised to the rotational frequency of the compressor

No attempt was made to determine the nature of stall inception, as this has been extensively covered in studies to be found in literature, such as that of Camp and Day [1998].

6.3 Numerical results

Numerical modelling was applied to two of the three operational points investigated: design point operation ($\phi = 0.508$) and the maximum flow coefficient attainable without use of auxiliary fans ($\phi = 0.568$). The numerical velocity profile at the inlet (position S0) is the inlet boundary condition, as specified based on five-hole probe data. It can be seen in figures 6.1-6.4 that steady-state simulation data obtained using mixing-planes between blade rows agree well with experimental data for the design point and high flow coefficient cases. This is unsurprising, as the velocity time traces downstream of rotor blades (figure 6.8) and the area traverse downstream of the stator at design-point (figure 6.12) reveal that time-dependent effects and circumferential variation of the flow field due to blade wakes are relatively small, as already discussed. However, the circumferential averaging across mixing planes precludes the use of the steady-state results in understanding the interaction between wakes and downstream blade rows. The time-dependent results, however, provide this information, and agree as well, if not better, with experimental data than the steady state simulation results.

The time-series of midspan entropy contour plots for design point operation are shown in figure 6.17, and clearly show the shapes of rotor and stator wakes. Note that three adjacent blade passages are shown by duplicating the computational domain, which consisted of a single blade passage, in order to make the results more comprehensible and the effect of the periodic boundary conditions clear. Flow occurs from the left to the right of the image.

In figure 6.17, the wakes of upstream blade rows pass through downstream blade passages and emerge from these still recognisable and distinct though somewhat distorted due to the circulation around the blades which they impinge on. However, the experimental area traverse results downstream of the first stage stator (figure 6.12) indicate that the wakes of upstream rotor blades are mixed out within the rotor, and do not emerge from the stator blade passage in a recognisable form. To illustrate this, a time series of the numerical data for the axial velocity component in the plane of station S1 is shown in figure 6.18. This may be compared with the experimentally determined time-series shown

CHAPTER 6. FIRST QUADRANT: POSITIVE ROTATION

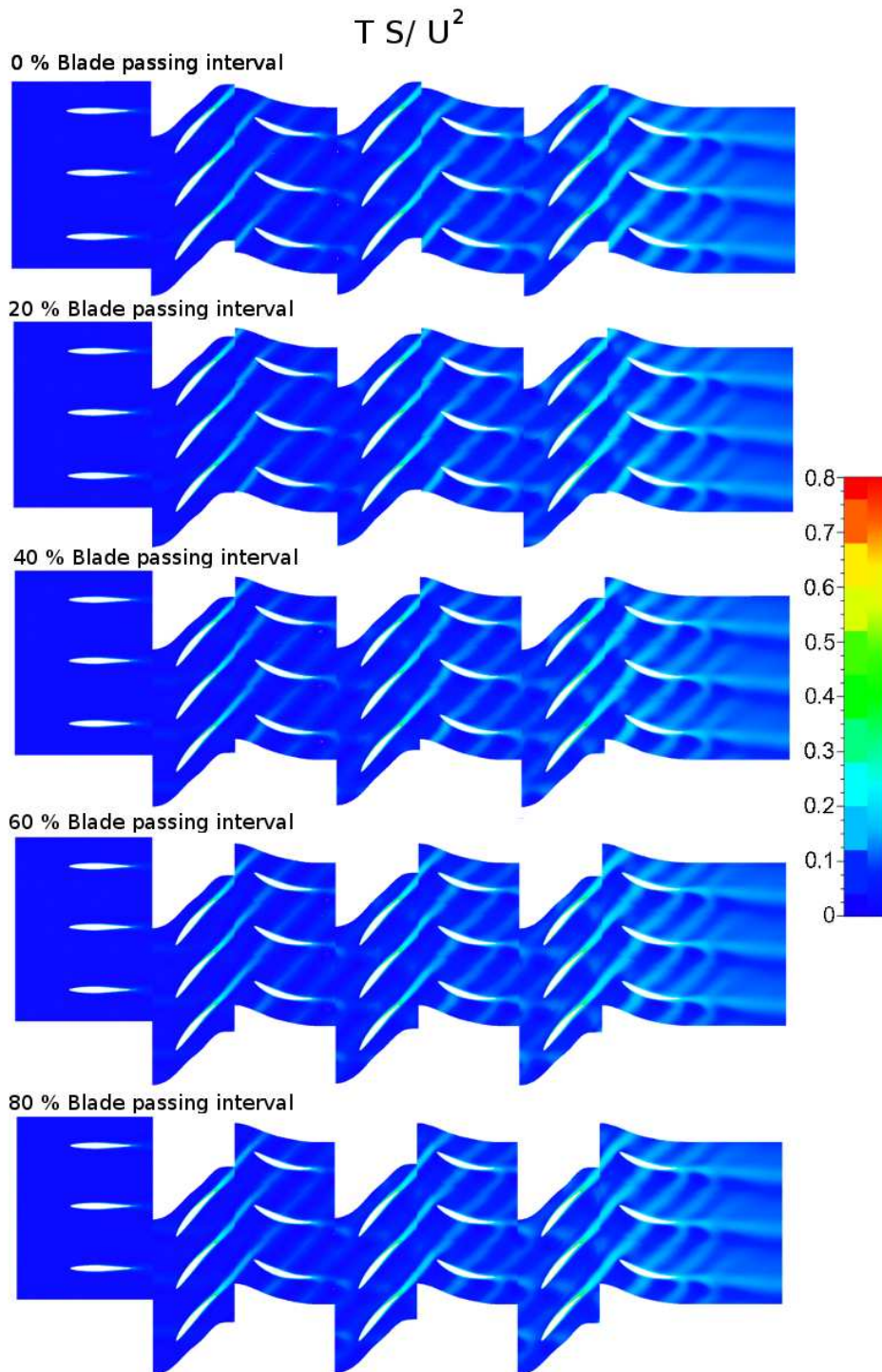


Figure 6.17: Time-series entropy distribution, normalised relative to inlet, on constant radius surface at midspan at design flow coefficient $\phi = 0.508$

CHAPTER 6. FIRST QUADRANT: POSITIVE ROTATION

in figure 6.12. The approximate size and shape of the rectangular area investigated in the experimental area-traverse is indicated by the black rectangle in the first frame. It can be seen that the stator wakes in the experimental data are slightly less clearly defined, but occupy similar positions. The upstream rotor wake may also be identified in the numerical data, moving across the flow field from right to left, while this is not apparent in the experimental data shown in figure 6.12. It thus appears that the numerical model predicts less mixing of the flow than in fact occurs.

It will be seen that the wakes of the IGVs are not perfectly transmitted across the IGV-rotor interface. This is due to the fact that a single rotor-stator interaction frequency was assumed for all blade rows, as the compressor has repeating stages. Thus the number of stators upstream and downstream of each rotor row is equal. However, in practice, this is not true of the first stage, as there are only 36 inlet guide vanes, where as there are 41 stator blades per stage. The result is that the the IGV-rotor interface incorrectly transfers the wakes of 41 IGVs to the flow field surrounding the rotor. The effect of this error is negligible, however, as the wakes do not exceed approximately 10 % of the blade pitch at midspan in width, and decay within one chord length. The instantaneous position at which the IGV wake impinges upon the blade does not appear to affect the flow field surrounding the downstream rotor. The pressure drop across the symmetrical IGVs is of the order of 10 Pa, approximately 0.5 % of the overall pressure rise at design point, thus this inaccuracy does not affect performance predictions.

For the sake of completeness in establishing a basis for comparison with other modes of operation, figure 6.19 shows the streamlines surrounding the first stage rotor and stator blades on a constant radius surface at 50 % of the blade span, operating at design-point. Unsurprisingly, no separation is evident on either the rotor or stator blade, nor at any other radius within the blade rows. The remaining stages are similar, and are omitted here for the sake of brevity.

The numerically approximated streamlines (referred to as "vector lines" by the post-processing software) are obtained by numerically fitting curves to be tangential to the velocity vectors of one time step of the numerical solution for the flow field. The use of the term "streamline" may seem questionable, as the flow in question is three dimensional in nature. However, in this case (and many of the cases in the chapters to follow) the radial component is less than 5 % of the in-plane velocity components across most of the area shown, thus much of the flow is essentially two-dimensional in nature, justifying the use of this term. In those cases where three-dimensional phenomena such as vortices occur, the "streamlines" may appear to cross, and the term is no longer strictly appropriate, but will be used for the sake of consistency and brevity. Note that in all such diagrams in this document, the surface on which the streamlines are approximated is rendered transparent.

The velocity triangles for the first stage for all three flow coefficients investigated are shown in figure 6.20. All diagrams are approximately to scale; velocity data for these diagrams is a combination of experimental and numerical data, as experimental data are not available at position S1 for the largest flow coefficient, and numerical data was not available for the stalled case. The velocity triangle diagrams for flow coefficients 0.568 and 0.508 (design point) (shown in subfigures (a) and (b) respectively) are similar due to the small change in flow coefficient (approximately 12 %), and the corresponding small change in flow angles (approximately 2.5°). Note that the change in flow angles between the leading and trailing edge of the rotor is small (approximately 11.6° at midspan for design point operation) compared with that for the stator (approximately 24.2°). The stalled case (subfigure (c)) shows the expected increase in incidence angles on the leading edge of both

CHAPTER 6. FIRST QUADRANT: POSITIVE ROTATION

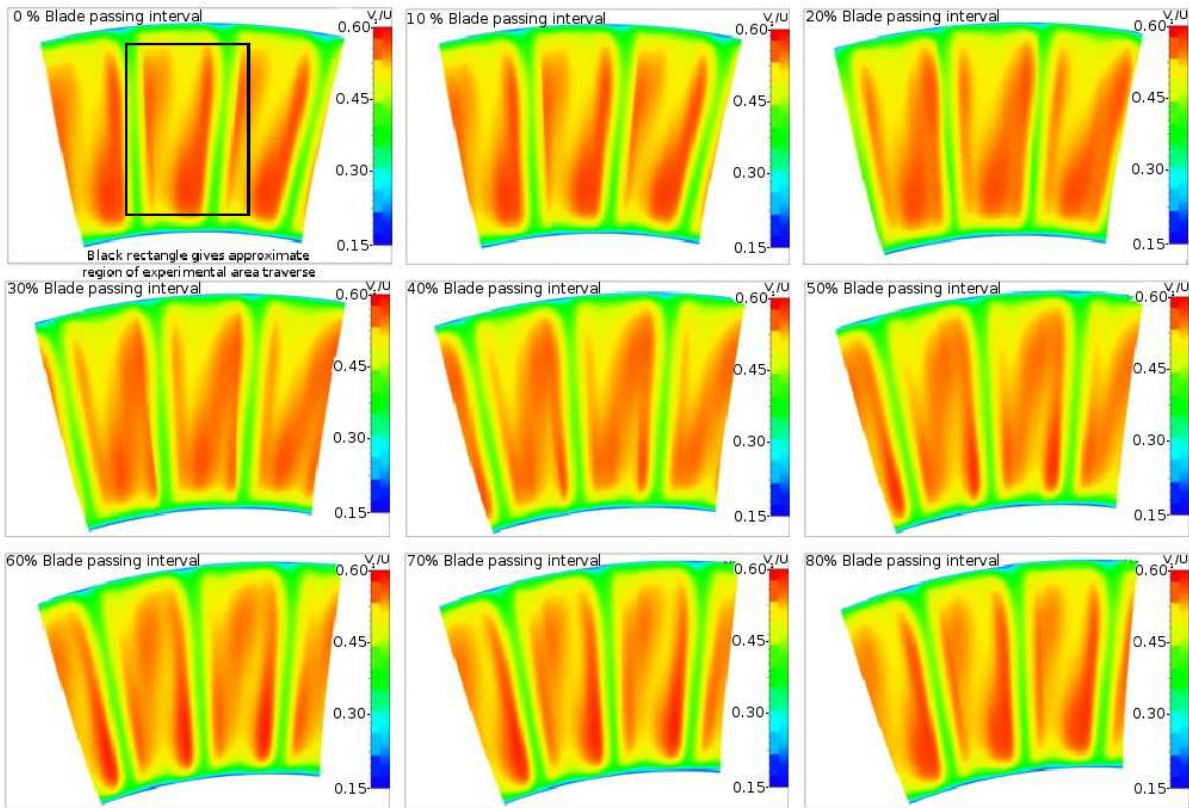


Figure 6.18: Time series of axial velocity contours at position S1 at $\phi = 0.508$

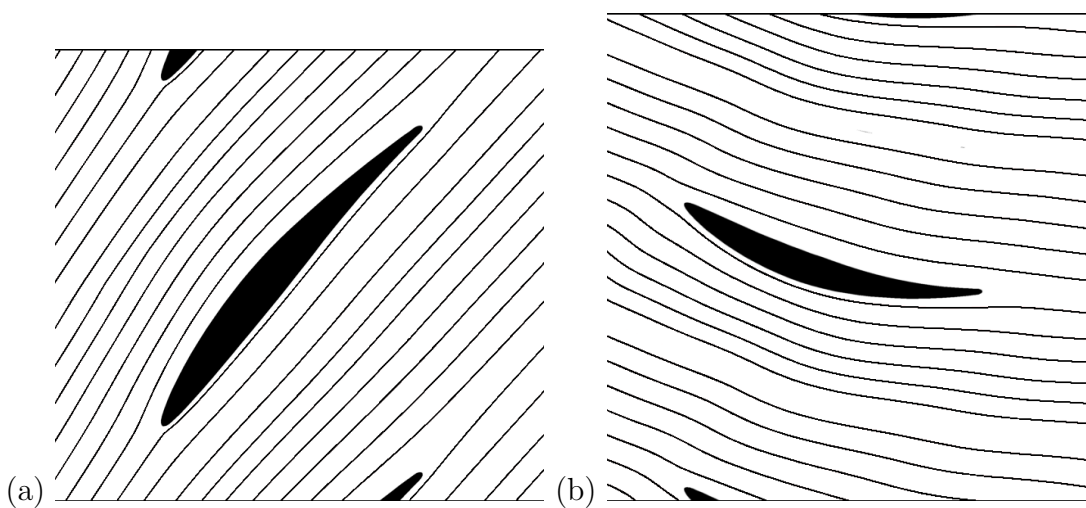


Figure 6.19: Streamlines surrounding (a) first stage rotor and (b) first stage stator blades at 50% of blade span; $\phi = 0.508$

CHAPTER 6. FIRST QUADRANT: POSITIVE ROTATION

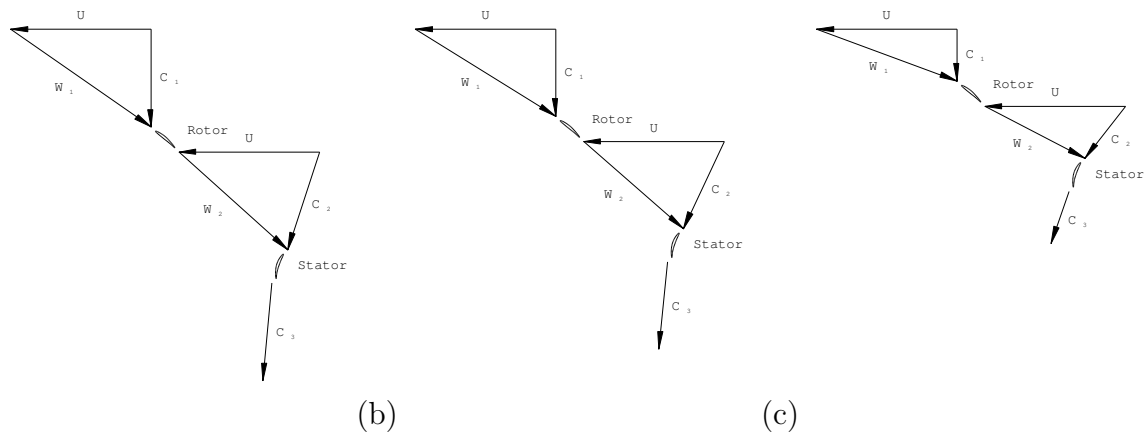


Figure 6.20: Velocity triangles for first stage at 50 % of blade span: (a) $\phi = 0.568$ (b) $\phi = 0.508$ (c) $\phi = 0.279$

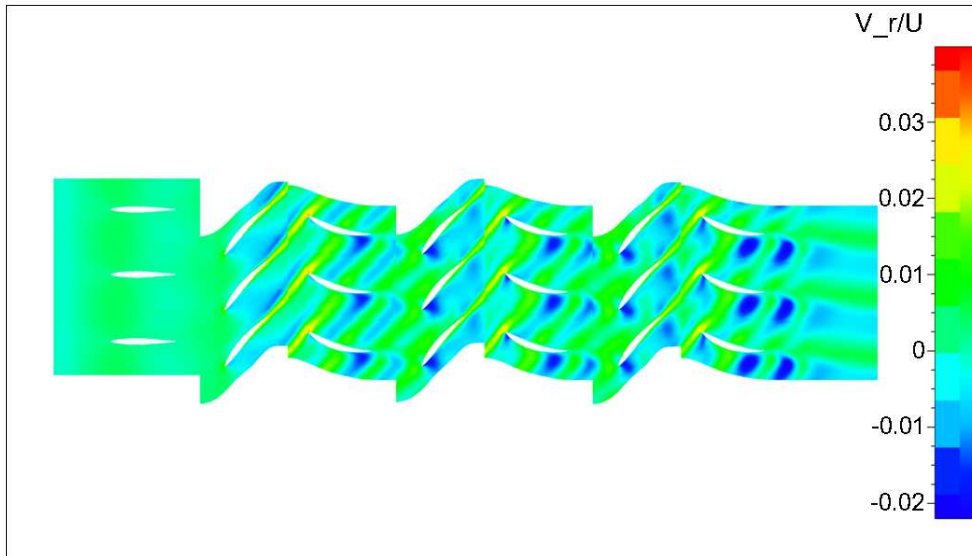


Figure 6.21: Radial velocity distribution on constant radius surface at midspan at design flow coefficient $\phi = 0.508$

rotor and stator blades, and the effect of flow separation on the deviation angles at the trailing edges of rotor and stator blades.

At design point, the simulation agrees with the experimental finding that radial flows are negligible at virtually all points in the flow field. This is illustrated on the constant radius surface at midspan, in figure 6.21. The maximum positive (tipward) flow occurs in the rotor wakes, particularly when these pass over the leading edge of a downstream stator row. Nonetheless, this maximum value represents less than 5 % of the absolute flow velocity magnitude. There is a parallel area of negative (hubward) radial flow parallel to the wake, attached to the pressure surface of the leading edges of both rotors and stators and extending across the blade passage; in the case of the stators making contact with the suction surface at the trailing edge.

CHAPTER 6. FIRST QUADRANT: POSITIVE ROTATION

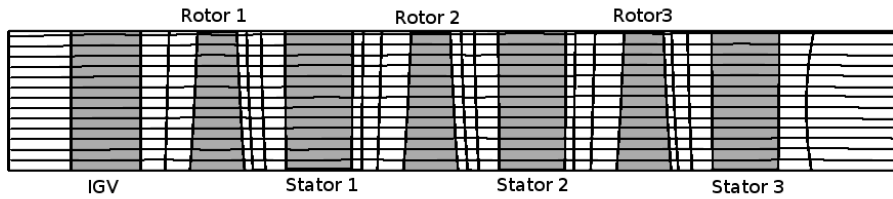


Figure 6.22: Circumferentially averaged flow paths at design flow coefficient $\phi = 0.508$

The circumferential average of the radial velocity component is very close to zero at all points within the compressor, as is shown in figure 6.22.

In the stalled case (figures 6.6 and 6.7), the presence of stall-cells, which are non-axisymmetric phenomena, invalidate the assumptions implied by the solution of a single blade passage. For this reason no numerical results representing stalled operation are presented. The detailed numerical simulation of stalled operation of an axial flow compressor is a subject of ongoing research for many other researchers, and requires considerably more computational resources than are available, and is beyond the scope of this work. An example the computational resources required is provided by Wilke and Kau [2004], who presented a numerical investigation of the effect of endwall treatment on near-stall operation of an axial compressor rotor using an earlier version of the numerical solver used for this research. The number of cells for the rotor mesh used, excluding the end-wall casing mesh, was stated as 10^6 . This represents approximately three times the number of cells per blade row in this investigation. In addition, the time-unsteady nature of stalled operation requires a time-marching or other appropriate time-unsteady solution method. Similar difficulties were encountered in attempting to simulate second quadrant, positive rotation operation, described in chapter 8, and third quadrant, negative rotation operation close to the origin of the compressor map, as described in chapter 9.

6.4 Summary

The time-averaged velocity profiles measured downstream of the rotor using two different measurement techniques agree well with one another and with historical data. Experimental data agree with both steady state and unsteady numerical simulations. For this mode of operation, the solution obtained using the non-linear harmonic method differs from the steady state solution by less than 5 % downstream of the third stage rotor, and thus does not offer a significant improvement over a mixing-plane approach. This is because the wakes caused by upstream blades are a small percentage of the blade pitch. Both simulation approaches used are unsuitable for simulation of stalled operation.

The methods of investigation chosen have been validated against one another, and agree closely with one another for unstalled operation. The data obtained serves as a basis for comparison with more exotic modes of operation, in order to highlight the features of the flow fields under these conditions.

The flow-field downstream of the first stage stator showed a thin, well-defined wake, and exhibited some “breathing” at the blade passing frequency of the upstream rotor row. The wakes of rotor blades were clearly identifiable in velocity time-traces, and were thin and sharp. Rotating stall cells were observed in velocity time-traces for stalled operating

CHAPTER 6. FIRST QUADRANT: POSITIVE ROTATION

conditions.

Chapter 7

Fourth quadrant: positive rotation

7.1 Introduction

Axial flow compressors are designed to operate within certain flow coefficient ranges. When the flow coefficient is increased beyond a certain point by forcing additional flow through the machine, then the pressure change across the compressor decreases, and eventually changes sign. When this has occurred, the compressor acts as a poorly designed turbine, as the blades are curved in the opposite direction to the flow turning, and experience negative incidence stall. The flow-coefficient versus pressure coefficient characteristic curve extends into a different quadrant on the compressor map, namely the fourth quadrant. The overall fourth quadrant performance characteristics of the compressor used in this investigation have been presented in chapter 5. This chapter describes the flow structures observed under fourth quadrant operating conditions. Three flow coefficients were investigated, namely 0.665, 0.747 and 1.024. Due to the limitations of the auxiliary fans, the compressor rotational speed was reduced to 60 %, 46 % and 25 % of design speed respectively, to achieve these operating points. Some of the experimental and numerical data in this chapter was published in Gill et al. [2010] as a part of this dissertation.

7.2 Experimental results

7.2.1 Time-averaged velocity profiles

Time averaged velocity profiles were obtained by means of a five-hole probe and by time-averaging of hot-film probe velocity measurements. Velocity distributions as a function of radius were obtained at the compressor inlet and downstream of each rotor row (measurement stations S0, R1, R2 and R3 in figure 3.1). These are shown in figures 7.1-7.6.

The flow field downstream of the IGVs (station S0) is very nearly axial, as shown by the negligible tangential velocities in figures 7.2, 7.4 and 7.6, and approximately uniform as shown in figures 7.1, 7.3 and 7.5.

It was determined that the wakes of the zero camber angle IGVs are of similar thickness to the maximum blade thickness, and decay within one chord length. In addition, the axial velocity profile at this position changes by less than 2 % if the IGVs are removed, thus this is a reasonable representation of the velocity profile at the compressor inlet. A small decrease in velocity occurs near midspan in all cases. For all cases, the hub wall boundary layer occupies approximately 10 % of the span, and the casing boundary layer approximately 20 %.

CHAPTER 7. FOURTH QUADRANT: POSITIVE ROTATION

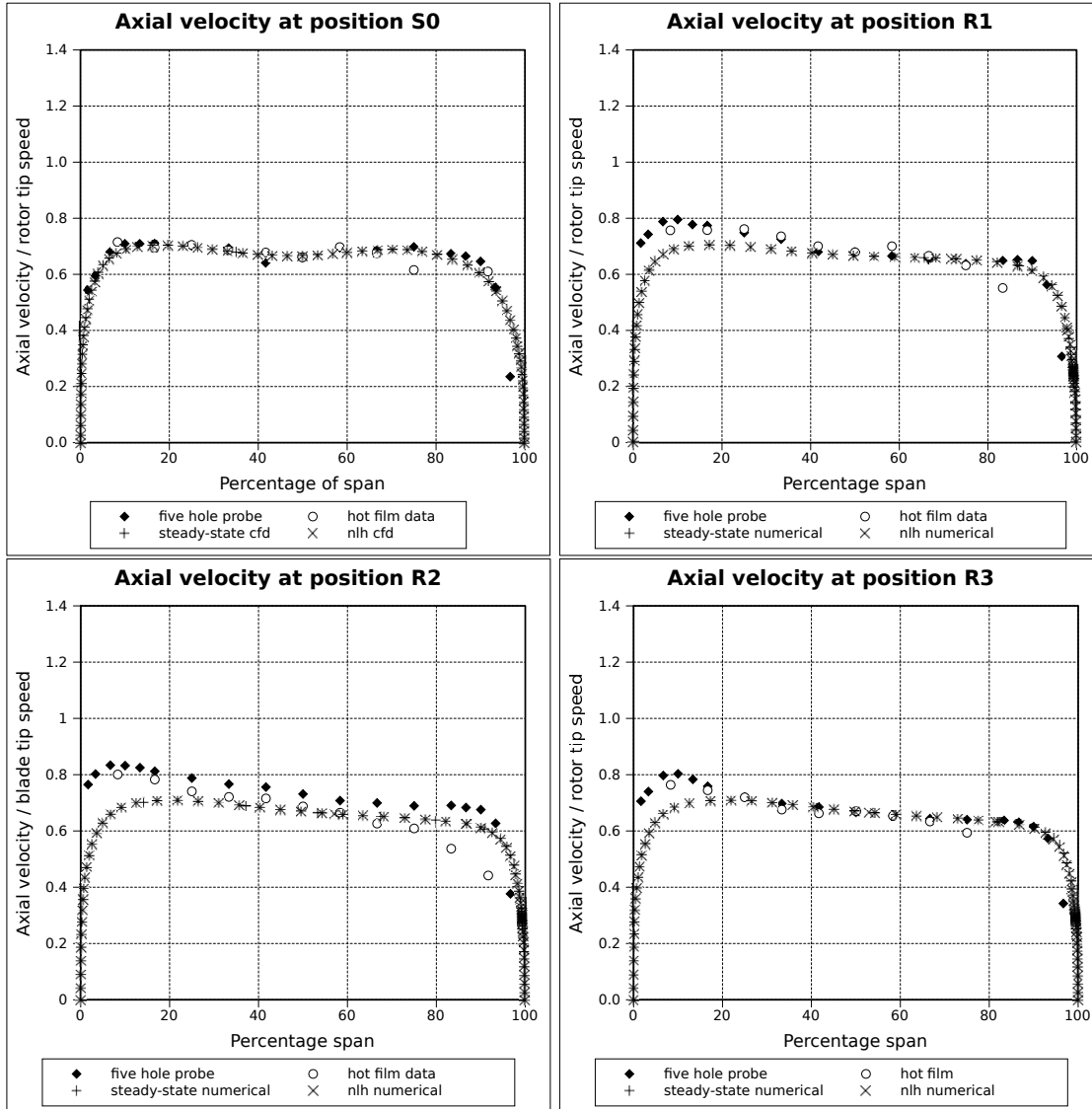


Figure 7.1: Axial velocity components as a function of radius at $\phi = 0.665$

The radial velocity component in the positions investigated was approximately 5 % of the absolute velocity magnitude, and thus negligible. The oil-trace flow visualisation of Cyrus [1990] in the stator blade passage indicated the presence of radial flows in the within the blade passage (at least in the blade boundary layer), but not near the trailing edge of the blades, where the radial velocity component became negligible.

In all tests, the circumferential position of the probe was approximately midway between the nearest upstream stator blade trailing edges. The circumferential positioning is important because the stator wakes are so large that they affect flow at the trailing edge of the downstream rotor row, as will be demonstrated in the discussion of the time dependent area traverse and the numerical results.

The axial velocity decreases from hub to tip, as was observed by Cyrus [1990]. At flow coefficients of 0.665 and 0.747, (figures 7.1 and 7.3 respectively), the axial velocity varies approximately linearly with the span in the region between the two boundary layers, decreasing by approximately 21 and 25 % from hub to tip respectively. The velocity profiles at R2 and R3 are less linear than that of R1. When the flow coefficient is increased to

CHAPTER 7. FOURTH QUADRANT: POSITIVE ROTATION

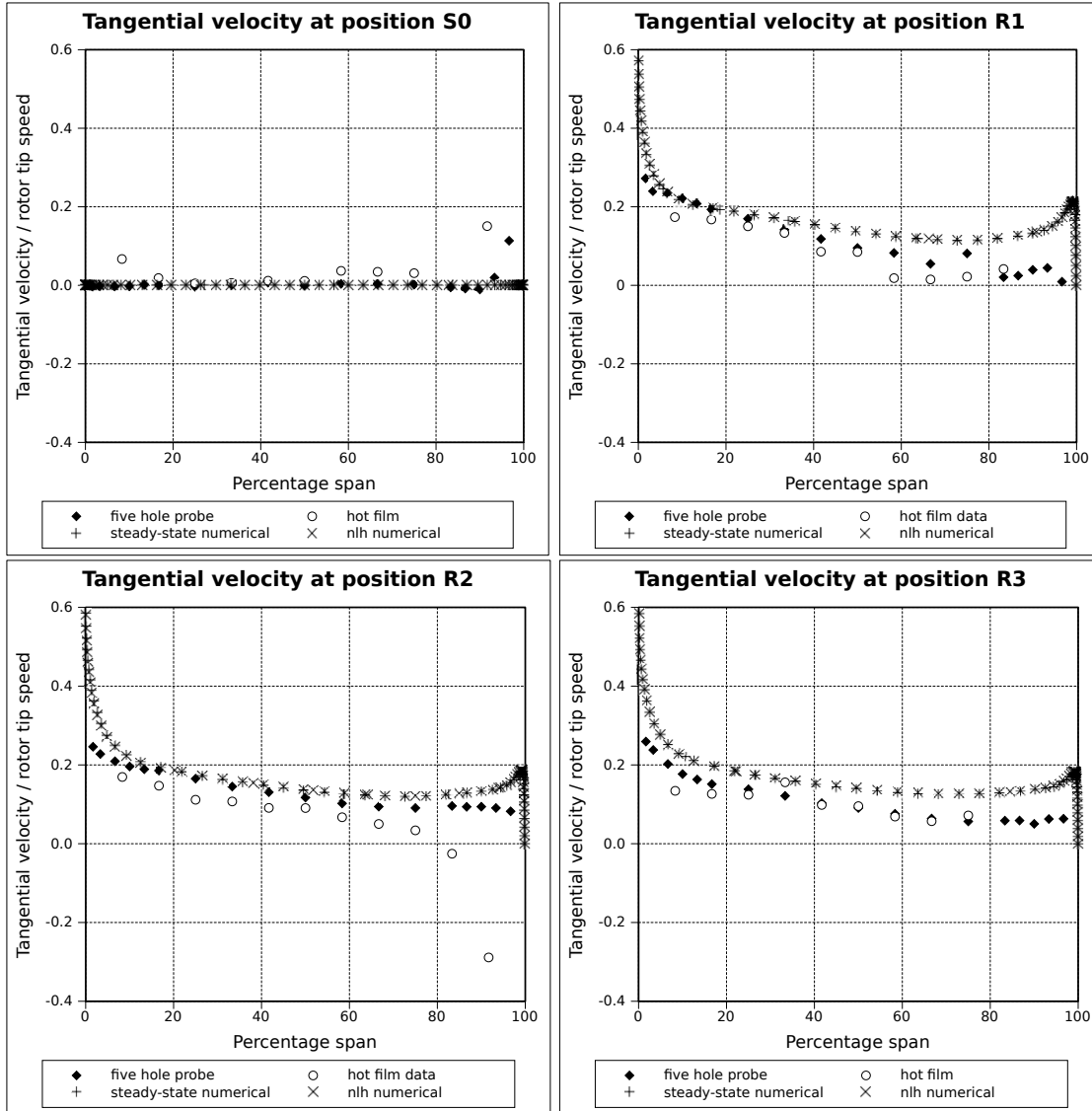


Figure 7.2: Tangential velocity components as a function of radius at $\phi = 0.665$

1.024, (figure 7.5), the axial velocity decreases by 30 % from hub to midspan, then remains approximately constant to the end-wall boundary layer. Regions of high axial velocity form near the hub of the machine. These are most pronounced at higher flow coefficients, and are also more clearly defined at positions R2 and R3 than R1, where they are small and indistinct. These regions of high axial velocity appear to be non-axisymmetric phenomena, as the experimental area traverse and numerical results indicate that a circumferentially localised increase in axial velocity occurs near the hub between stator wakes in a position which coincide with the placement of the sensors, and have a measurable effect at the trailing edge of the downstream rotor row. These regions of higher axial velocity will be discussed with the time-dependent area traverse results.

The tangential velocity component decreases from hub to casing for all cases. At a flow coefficient of 0.665, (figure 7.2), the tangential velocity component near the blade tips is nearly zero, indicating that the flow is approximately axial in this region. The direction of the tangential component changes near midspan at a flow coefficient of 0.747 (figure 7.4) and is reversed across the entire span at a flow coefficient of 1.024 (figure 7.6).

CHAPTER 7. FOURTH QUADRANT: POSITIVE ROTATION

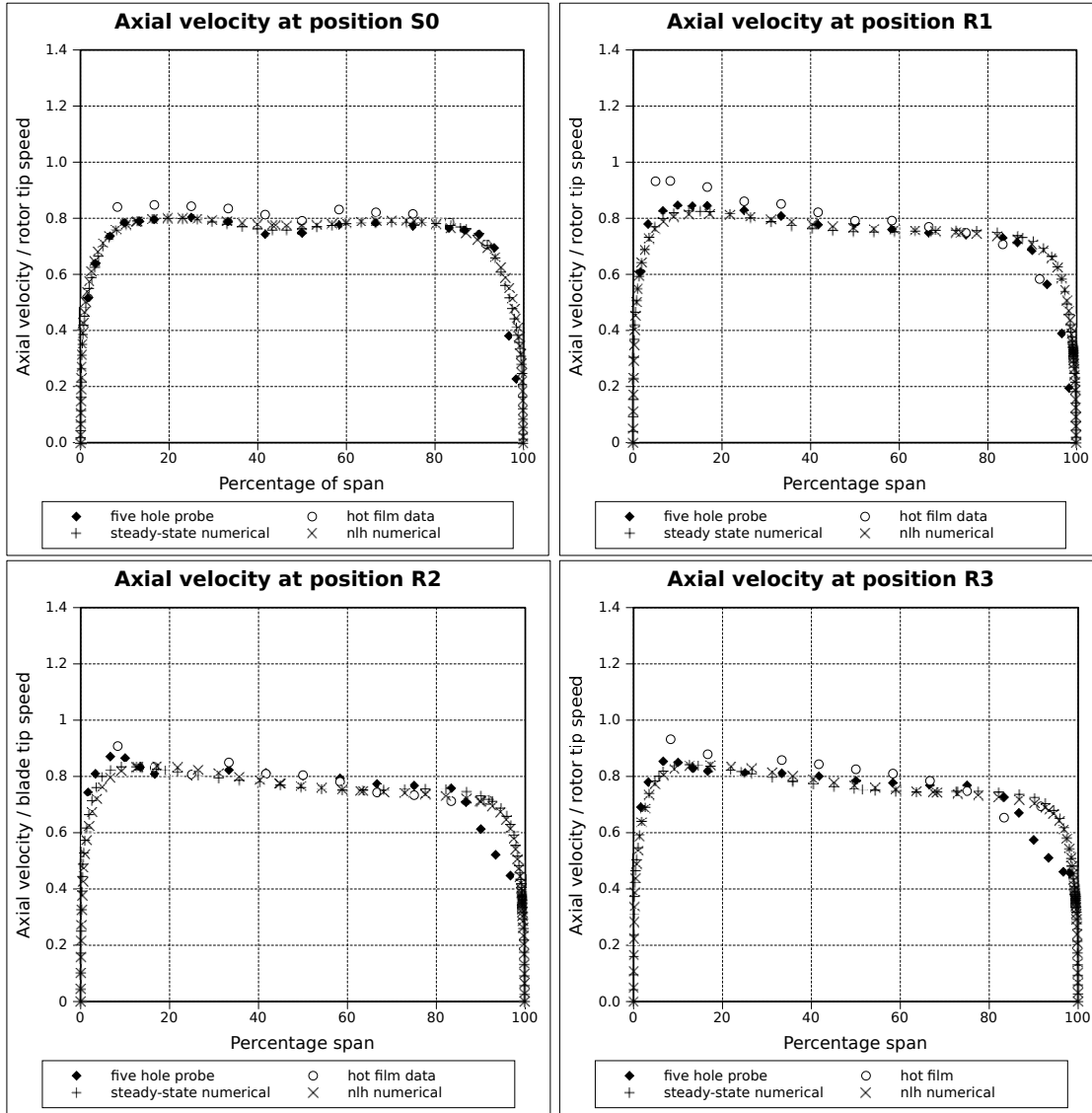


Figure 7.3: Axial velocity components as a function of radius at $\phi = 0.747$

The decrease in axial velocity downstream of the first stage rotor (position R1) may be explained by calculating the fluid work per unit radial length extracted from the flow as a function of radius:

$$W = U(r) \cdot (C_{\theta R1}(r) - C_{\theta S0}(r)) \quad (7.1)$$

The fluid work per unit mass for the first stage rotor, non-dimensionalised as the load coefficient $U(r)\Delta C_{\theta}(r)/U^2$ is plotted as a function of radius in figure 7.7. In this figure, a positive sign indicates that work is performed on the fluid by the rotor blades, indicating compressor-like operation, while a negative sign indicates energy extracted from the fluid, or turbine-like operation at a given radius. At a flow coefficient of 0.665 the first stage rotor is still performing work. At a flow coefficient of 0.747, the portion of the blade from approximately 60 % of the blade span to the casing is acting as a turbine, while at 1.024 the entire first stage rotor blade is functioning as a turbine.

At all three flow coefficients, either less energy is added to the fluid or more is removed from the fluid in the tip region. This is because the hub-to-tip ratio of the test compressor

CHAPTER 7. FOURTH QUADRANT: POSITIVE ROTATION

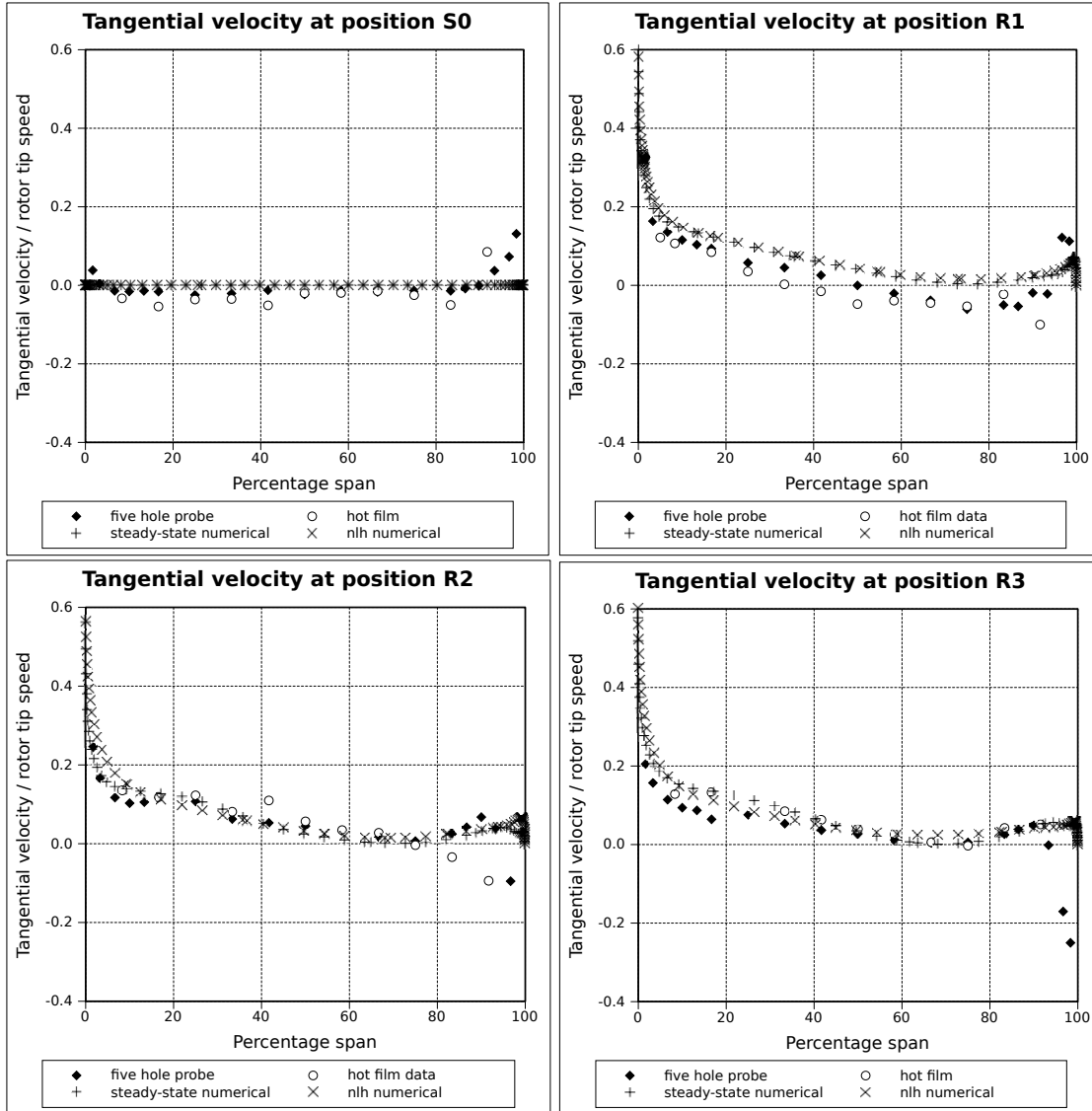


Figure 7.4: Tangential velocity components as a function of radius at $\phi = 0.747$

is 0.71, thus the blade speed at the tip (U_{tip}) is 40 % higher than that at the hub U_{hub} . The absolute swirl velocity downstream of the rotor $C_{\theta R1}$ varies with flow coefficient. However, the relative flow angle at R1 is relatively independent upon the negative angle of incidence at the rotor leading edge. This is because deviation angle is not heavily dependent on inlet flow angle for small changes in incidence for either axial flow compressors [Cumpsty, 1989] or axial flow turbines [Dixon, 1978]. However, it will be shown later that this is not true for the stator rows under this mode of operation.

The difference in angle of incidence between design point and an arbitrary fourth quadrant positive rotation case may be expressed solely in terms of the local blade flow coefficient, simplifying calculation. Consider the two velocity triangles at the first stage rotor leading edge (position S0) as shown in figure 7.9. The absolute velocity is assumed to be perfectly axial, and of equal magnitude for design and fourth quadrant operation, C_z . In other words, the difference in flow coefficient between the two cases illustrated is due solely to the difference in the rotor speed U . By application of the cosine rule, it is possible to express the difference in relative inlet flow angles between the design and fourth quadrant

CHAPTER 7. FOURTH QUADRANT: POSITIVE ROTATION

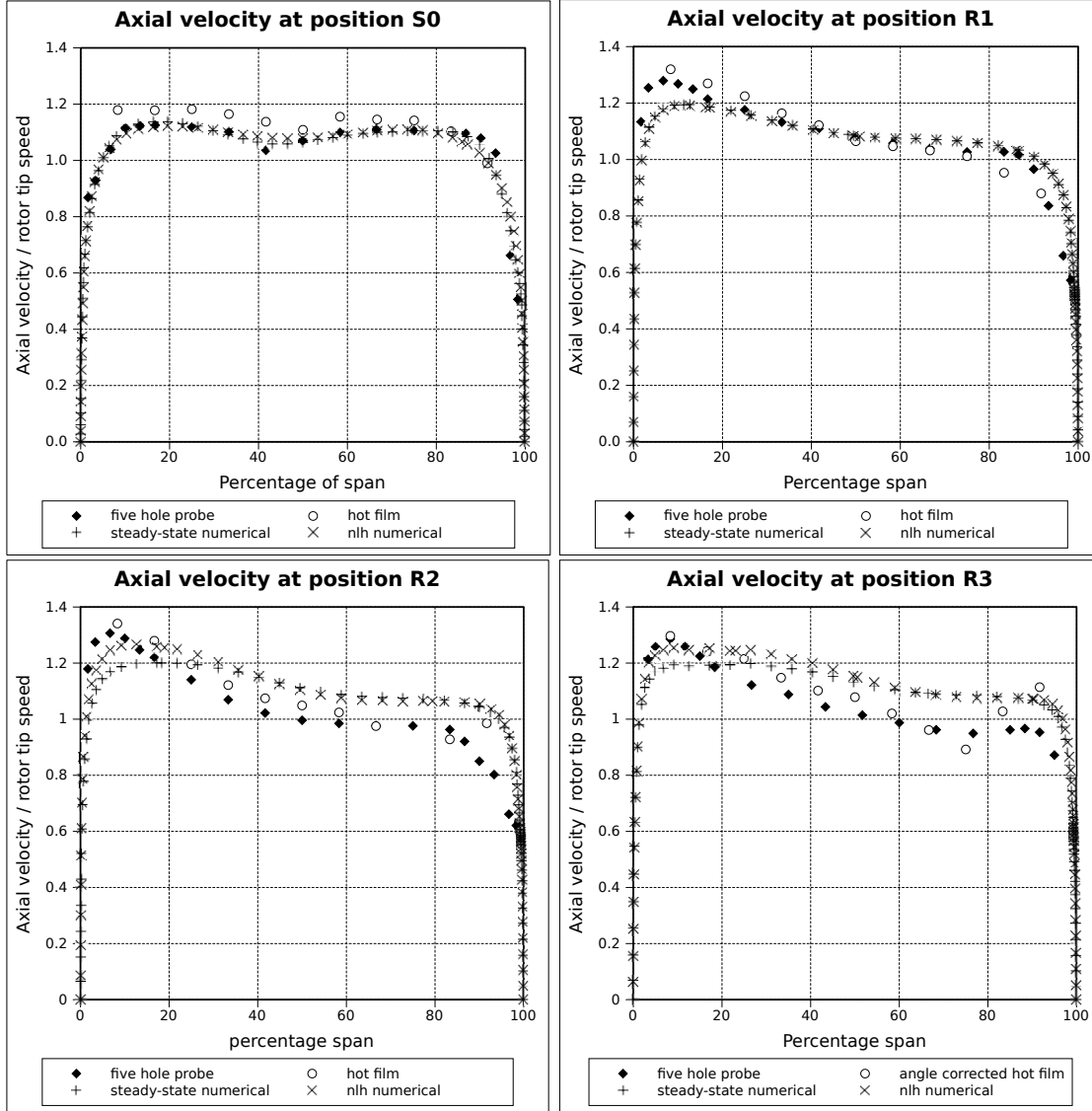


Figure 7.5: Axial velocity components as a function of radius at $\phi = 1.024$

cases, $\alpha - \alpha_{design}$ in terms of C_z , the local blade speed $U(r)$, and thus in terms of the local flow coefficient based on the local blade speed $\phi(r)$:

$$\begin{aligned} \alpha - \alpha_{design} &= -\arccos \left(\frac{U(r)^2 + C_z \cdot C_{z,design}}{\sqrt{(C_z^2 + U(r)^2) (C_{z,design}^2 + U(r)^2)}} \right) \\ &= -\arccos \left(\frac{1 + \phi(r) \cdot \phi_{design}(r)}{\sqrt{(\phi_{design}(r)^2 + 1) (\phi(r)^2 + 1)}} \right) \end{aligned} \quad (7.2)$$

The values for equation 7.2 are plotted for the three flow coefficients under consideration in figure 7.8 (a). The data points in the boundary layer region are omitted in order to more clearly show the midspan trends. Comparison with figure 7.8 (b) shows that for fourth quadrant operation, an increase in the negative angle of incidence leads to a larger flow turning angle, due to the effect of separation on the flow field. Nonetheless, the difference

CHAPTER 7. FOURTH QUADRANT: POSITIVE ROTATION

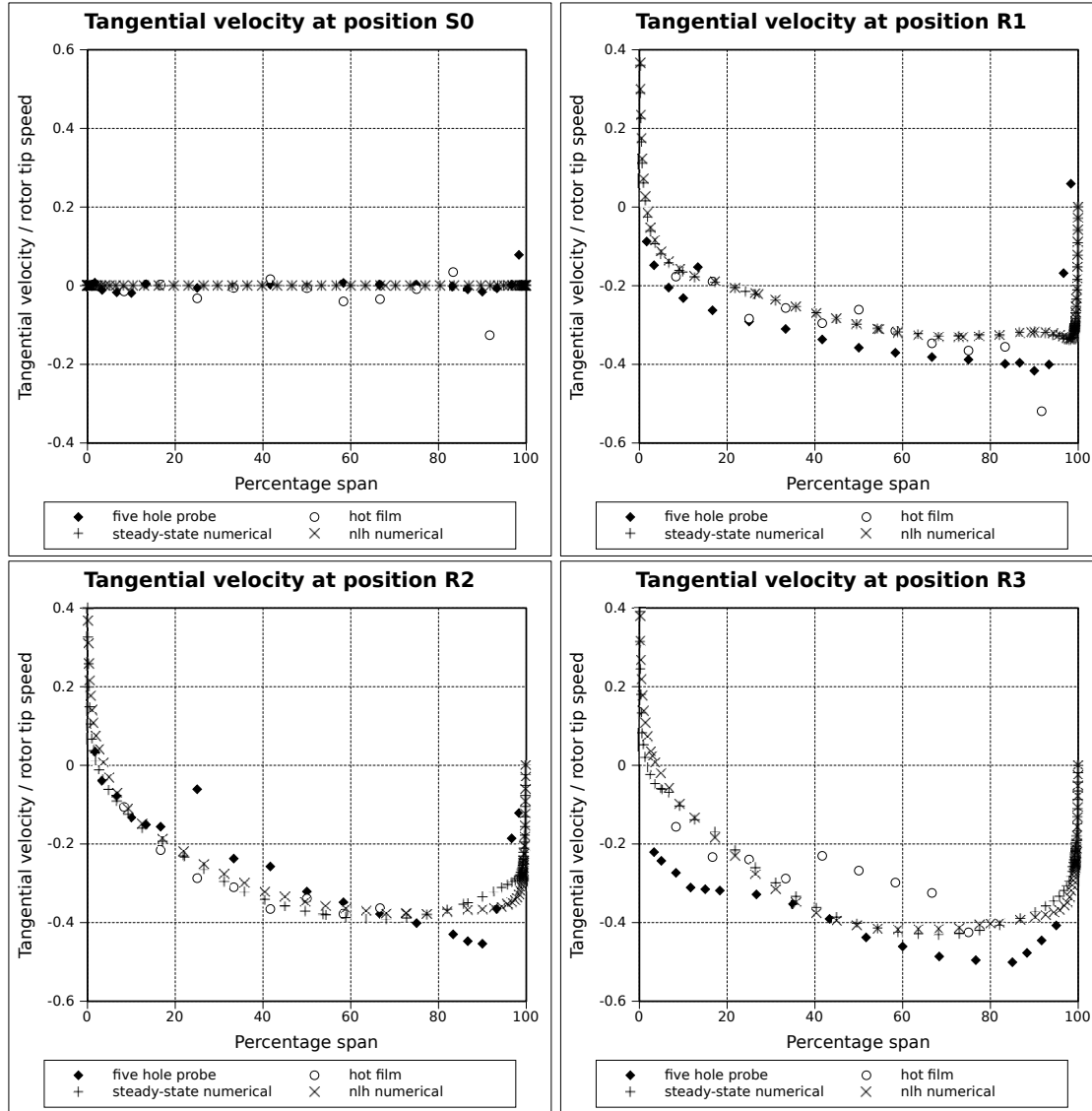


Figure 7.6: Tangential velocity components as a function of radius at $\phi = 1.024$

in incidence angle does not cause a sufficiently large difference in flow turning to offset the difference in blade speed between hub and tip. For second and third stage rotors, the situation is complicated by non-uniform velocity profiles at the blade leading edge due to upstream blade rows, and radial flows present within the rotor blade passages. These will be discussed later in this chapter.

7.2.2 Time dependent results

The axial velocity component time-traces at position R1 are presented in figure 7.10 at flow coefficients of 0.665, 0.747 and 1.024. The wakes are clearly visible in all cases. At a flow coefficient of 0.665, the first stage rotor wakes are approximately 35 % of the blade pitch in width, based on the fraction of the blade passing interval for which the axial velocity is less than the mean value. This is similar to the value for design point operation. The average minimum value in the wakes is approximately 5.4 % lower than the mean velocity, while the average maximum value is 2.9 % above it. At flow coefficients of 0.747 and

CHAPTER 7. FOURTH QUADRANT: POSITIVE ROTATION

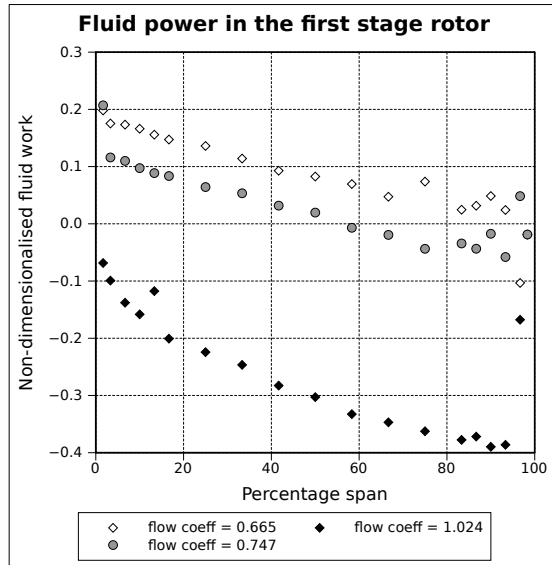


Figure 7.7: Non-dimensionalised fluid work as a function of radius for the first stage rotor

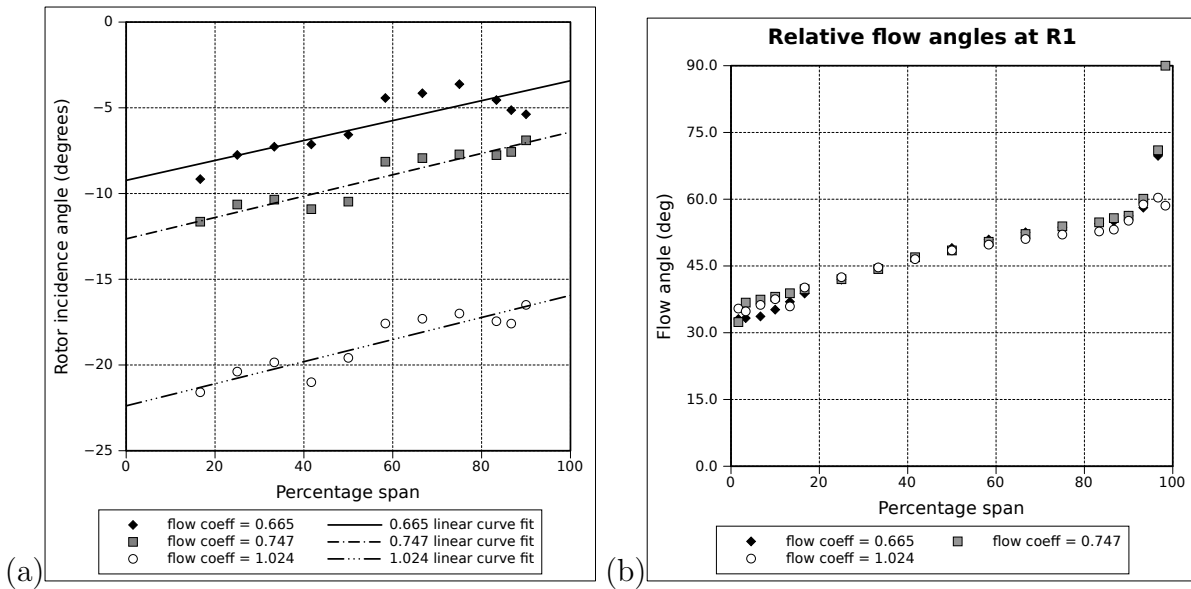


Figure 7.8: (a) Rotor incidence angle at S0 and (b) relative blade outlet angle at S1 as a function of radius for the first stage rotor

CHAPTER 7. FOURTH QUADRANT: POSITIVE ROTATION

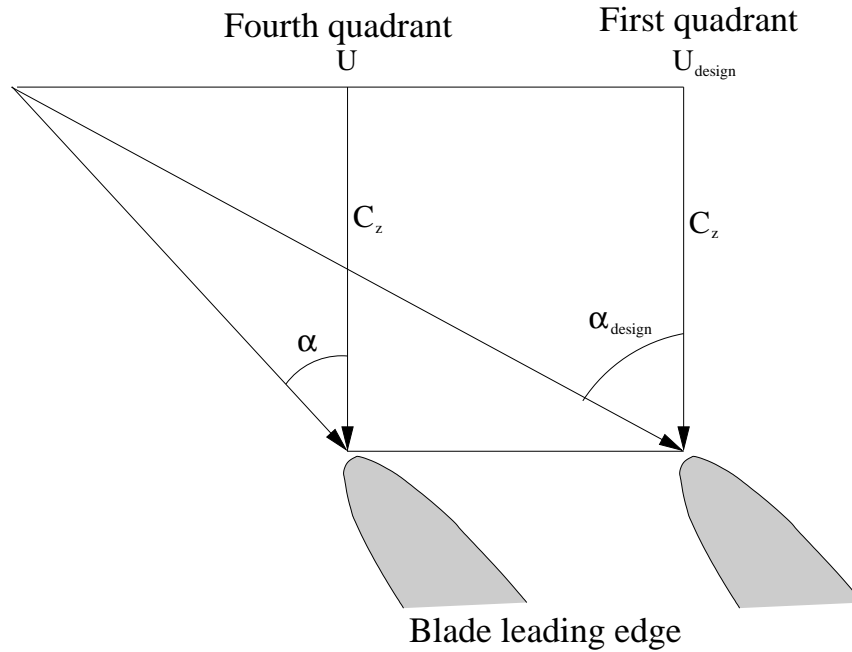


Figure 7.9: Velocity triangles at station S0 for design point and fourth quadrant operation for equal axial absolute velocities C_z

1.024, the first stage rotor wakes occupy approximately 40 % and 50 % of the blade pitch respectively, becoming broader as the flow coefficient (and thus degree of separation on the blades) increases, due to the increasingly severe negative incidence stall on all blades.

The averaging scheme used to eliminate non-repeating flow phenomena also distorts the effect of cyclic disturbances not occurring at a multiple of the rotor rotational speed. The presence of such phenomena can be detected by applying a fast Fourier transform to the unprocessed cooling velocity time-series data for a single sensor angle. The number of harmonics of the blade passing frequency visible above the noise level also provides an indication of the rotor wake shape and size. This information is also useful in choosing the number of terms in the Fourier series used to approximate the flow-field on the inter-blade-row boundaries in unsteady non-linear harmonic numerical modelling.

Figures 7.11-7.13 show the frequency domain at midspan at the three flow coefficients under investigation, downstream of the first and final rotor rows. The components occurring at the blade passing frequency and their harmonics are dominant. Thus the averaging scheme applied to the hot-film data is acceptable, and the non-linear harmonic approximation is valid. The amplitude of the harmonic components increases with the stage number. At a flow coefficient of 0.665 (figure 7.11), the fundamental amplitude is approximately twice the first stage rotor amplitude at position R2, and thrice the value at position R3. This relationship also holds true for the flow coefficients 0.747 (figure 7.12) and 1.024 (figure 7.13) at position R2, although the the amplitude of the blade passing frequency does not increase from R2 to R3. This increase in amplitude is due to the greater variation of velocity downstream of the later rotor rows, which are affected by the large, separated wakes of all preceding blade rows.

At flow coefficients of $\phi = 0.665$ (figure 7.11) and $\phi = 0.747$ (figure 7.12), the fundamental and second and third harmonics of the blade passing frequency may be identified above background noise at positions R1, R2 and R3. At the highest flow coefficient,

CHAPTER 7. FOURTH QUADRANT: POSITIVE ROTATION

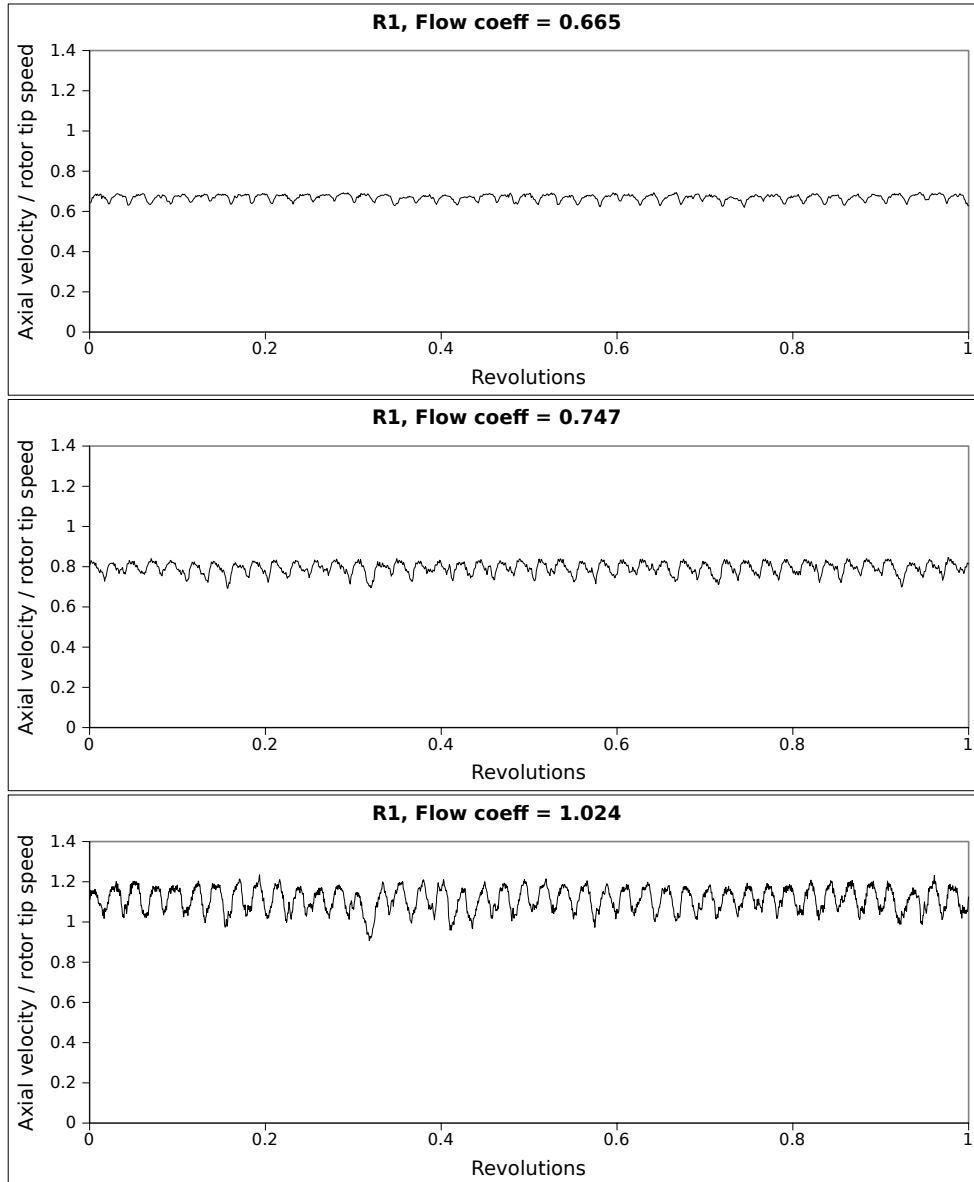


Figure 7.10: Time-traces for axial velocity components at midspan over one revolution

$\phi = 1.024$ (figure 7.13), the second and third harmonics are only clearly visible at position R1, while only the blade passing frequency is significant above the noise level at R2 and R3. This indicates that the velocity variation is approximately sinusoidal downstream of the second and third rotor rows. This is an indication of severe flow separation on these blade rows, as the wakes occupy approximately half the blade passage, as has already been established. Flow separation is not as severe on the first stage rotor row, as the inlet guide vanes upstream are aligned with the flow and no separation occurs upstream of the first stage rotor row. This in turn causes less severe separation to occur on the first stage than on subsequent stages.

An area traverse downstream of the first stage stator row was performed at a flow coefficient of 0.747. The resulting time-series of axial-velocity contours is shown in figure 7.14. The traverse represents a rectangular area which coincides largely with a single blade passage, with some overlap. The dominant features are a blade wake with a maximum

CHAPTER 7. FOURTH QUADRANT: POSITIVE ROTATION

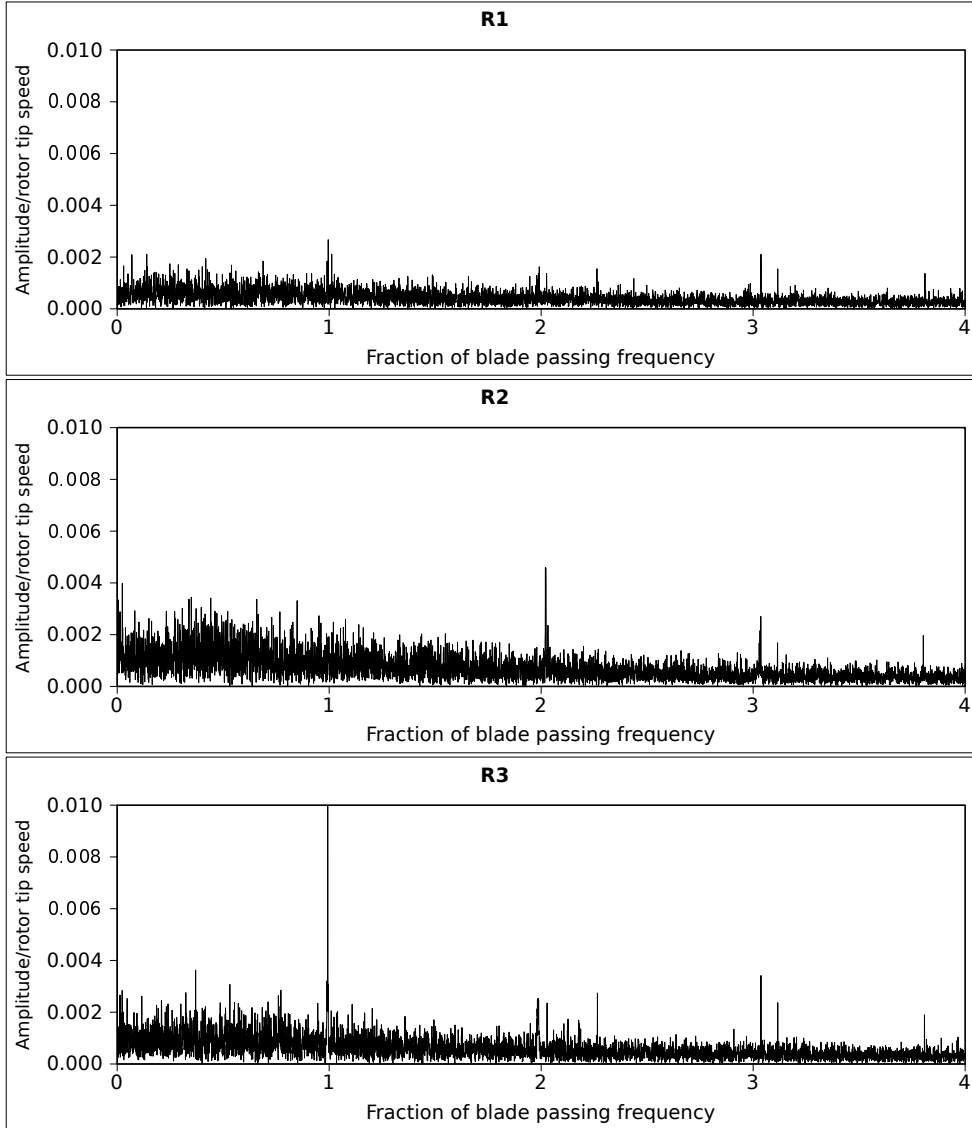


Figure 7.11: Frequency domain of cooling velocity variation at $\phi = 0.665$ at mid-span

breadth of approximately 50 % of the local blade pitch at approximately 65 % of the blade span, and a jet between the wakes with a maximum velocity at 20 % of the blade span, also approximately 50 % of the local blade pitch. The stator wake is smallest, and the average velocity is highest near the hub because the stator blade leading edge metal angles are less badly mismatched to the angle of incidence, thus separation is less severe in this region than near the casing. The thickness and position of the wake and jets vary with the rotor position, as a result to the variation in flow angle due to the wakes and jets of upstream rotor blades passing the blade.

The wake increases in breadth as the distance from the hub increases. The highest velocities occur near the hub in the inter-wake jet at all time steps (label A). The maximum axial velocity in this jet varies between 180 and 186 % of the minimum value occurring in the wake. This local maximum in the inter-wake jet is thought to cause the high axial velocities measured near the hub in the time-averaged radial traverses at positions R2 and R3. It will also be remembered that the average axial velocity downstream of rotor blade rows is highest near the hub and decreases towards the tip. Thus, during fourth

CHAPTER 7. FOURTH QUADRANT: POSITIVE ROTATION

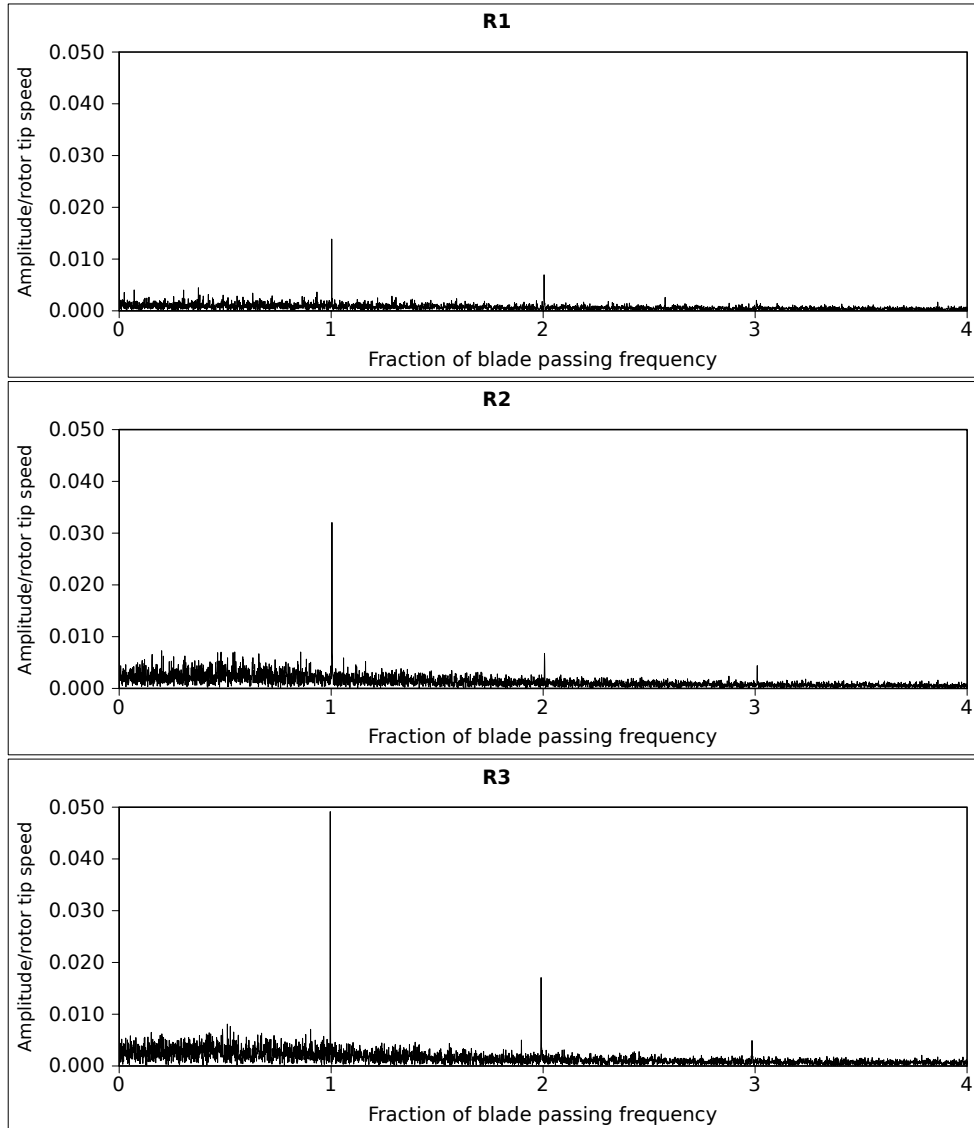


Figure 7.12: Frequency domain of cooling velocity variation at $\phi = 0.747$ at mid-span

quadrant turbine-like operation, most flow through the test compressor occurs near the hub, and comparatively little near the shroud for all blade rows. This tendency becomes more pronounced as the flow coefficient increases.

An area of highly retarded flow occurs between approximately half span and three quarter span. This region grows and merges with two smaller regions of retarded flow at a lower radius, but at the same tangential position. The wake is smallest at the beginning of the time-trace, and reaches it's maximum size (approximately 60 % of the local blade pitch) at 70 % of the span and approximately 68.8 % of the blade passing interval (label B). At this radius the axial velocity in the wake is approximately 54 % of the average flow velocity, the minimum axial velocity occurring in the area examined. The axial velocity in the wake is slightly higher at 80 % of the span nearest the casing, reaching a local maximum of 75 % the mean velocity before the end-wall boundary layer (label C). A smaller region of retarded flow is visible to the right of the stator tip, though average flow velocities near the tip are only 20 % below the maximum velocity in the jet (label D). This may represent a tip-vortex or tip leakage jet.

CHAPTER 7. FOURTH QUADRANT: POSITIVE ROTATION

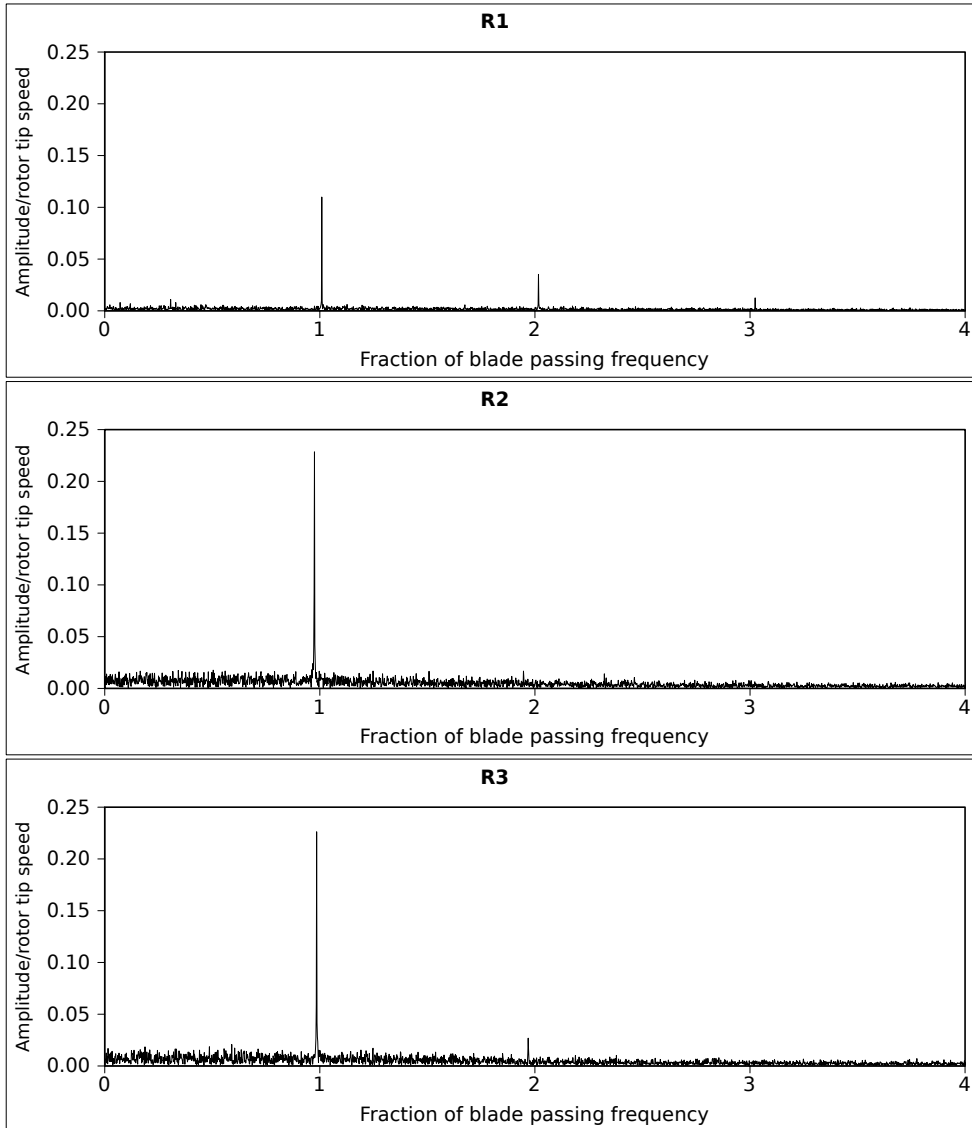


Figure 7.13: Frequency domain of cooling velocity variation at $\phi = 1.024$ at mid-span

7.3 Numerical results

Figures 7.1-7.6 show the circumferentially-averaged results of the steady-state simulations utilising a mixing plane assumption between blade rows, as well as the time-averaged, circumferentially-averaged non-linear harmonic results. The validity of the mixing plane assumption begins to erode due to the large wakes downstream of blades experiencing significant flow separation on the pressure surface. However, the method still provides reasonable agreement at a flow coefficient of $\phi = 0.747$ (figures 7.3 and 7.4). The areas of high axial velocity evident near the hub are less well defined in the numerical than the experimental results because the results presented are averaged circumferentially as well as in time, while the experimental data represent a fixed circumferential position. Examination of the axial velocity variation along a radial line at an appropriate circumferential position yielded better agreement with experimental results.

In order to illustrate the rotor-stator wake-interaction and the areas of separated flow, a contour plot of entropy at midspan, for operation at a flow coefficient of $\phi = 1.024$,

CHAPTER 7. FOURTH QUADRANT: POSITIVE ROTATION

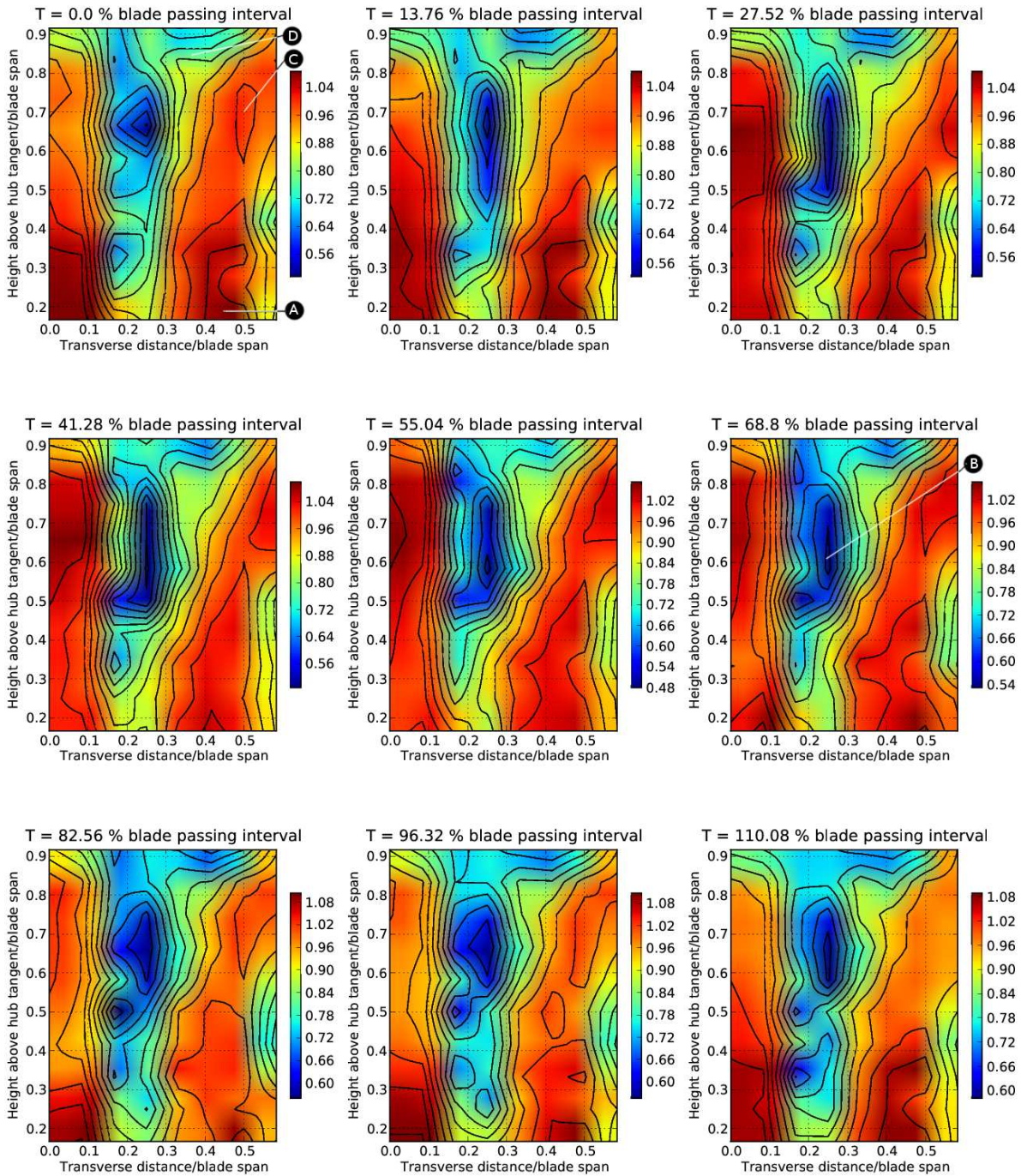


Figure 7.14: Time series of axial velocity contours at position S1 at $\phi = 0.747$

is shown in the dimensionless form Ts/U^2 , in figure 7.15. The non-dimensional entropy increase from inlet to outlet is approximately 2.2, which is approximately 25 times larger than for design-point operation (see figure 6.17). The stage entropy rise is approximately equal for all stages, with the rotor contributing approximately 30 % of the entropy increase per stage. The entropy in the middle of the recirculation zone in the first stage stator row is five times larger than that in the jet between the separated regions, while in the third stage the cumulative entropy has risen to such a degree that entropy in the separation

 CHAPTER 7. FOURTH QUADRANT: POSITIVE ROTATION

bubble in the stator row is only 70 % higher than in the jet.

Flow separation occurs on the pressure surface of all stators. The separated regions are turbulent and the flow is disordered, thus entropy increases in these regions. The disordering effect of an upstream stator wake passing over a rotor blade leading edge is also evident, particularly at the pressure surface of the third stage rotor between 0 and 40 % of the blade passing interval.

The area of separated flow around the first stage stator is shown in figure 7.16. The separation becomes more pronounced as the flow coefficient increases. No significant separation is evident for the lowest flow coefficient ($\phi = 0.665$). The pressure difference across the machine is close to zero at this flow coefficient. Two recirculation zones occur at mid-span at $\phi = 1.024$ for all stators. A similar structure was observed in the oil-streak flow visualisation of Cyrus [1990] in a stator blade passage. The second region is smaller and downstream of the first, and appears to indicate vortex shedding, which may contribute to the variation with time of the size and shape of the stator wakes observed in the experimental area traverse. The Strouhal number of the stator blade is 0.86, assuming that the frequency of vortex shedding is related to the blade passing frequency of the upstream rotor row, and using the chord and velocity at midspan.

Separation on stator blades is most severe near the casing, and least severe near the hub. This may be seen in the numerical results in figure 7.17, and is also suggested by the results of the experimental area traverse at station S1 (figure 7.14), where the wakes were shown to be thickest near the casing. The recirculation zone on the pressure surface of stators is widest at the trailing edge, and is 37 % of the blade pitch in circumferential width for the third stage rotor at midspan at a flow coefficient of 1.024.

Rotor blade rows experience separation most severely near the hub. The rotors of the second and third stages experience more severe separation than the first stage rotor due to the effects of upstream blade rows. This is particularly clear in the final stage rotor at a flow coefficient of $\phi = 1.024$. Figure 7.18 shows the relative velocity flow field at 10 %, 50 % and 90 % of full span. Note the clearly defined area of separation and recirculating flow on the pressure surface at 10 % of full span, and the more orderly flow at the larger radii. Unlike the stator row, in which the recirculation zone is largest near the trailing edge, the recirculation zone in rotor rows is largest perpendicular to the blade at mid-chord. This corresponds to a greatest circumferential extent of the separated region approximately 65 % of the axial distance from the leading edge to the trailing edge of the blades, at which point the circumferential width of the recirculation zone is approximately 35 % of the blade pitch at 10 % of the blade span. The circumferential width of the recirculation zone at the rotor trailing edge is only 15 % of the blade pitch at the same radius.

It was mentioned earlier that no radial velocity components larger than 5 % of the absolute velocity magnitude were detected experimentally between blade rows, but that radial flows were observed within blade rows by Cyrus [1990]. The numerical results agree with this, as can be seen in the contour plot of the radial velocity component shown in figure 7.19. With the exception of the first stage rotor, relatively large positive (radially outward) radial velocity components occur on the suction surfaces of the blades, while negative (inward) components occur near the centre of the blade passages. The first stage rotor is the only blade row to receive orderly axial flow due to the absence of separation on upstream blades. The magnitude of all radial velocity components increases with the blade row number. This is caused by the increasingly bad mismatch between blade leading edge metal angle and flow angle due to flow separation on upstream blade rows, and will be discussed in more detail in the next section.

CHAPTER 7. FOURTH QUADRANT: POSITIVE ROTATION

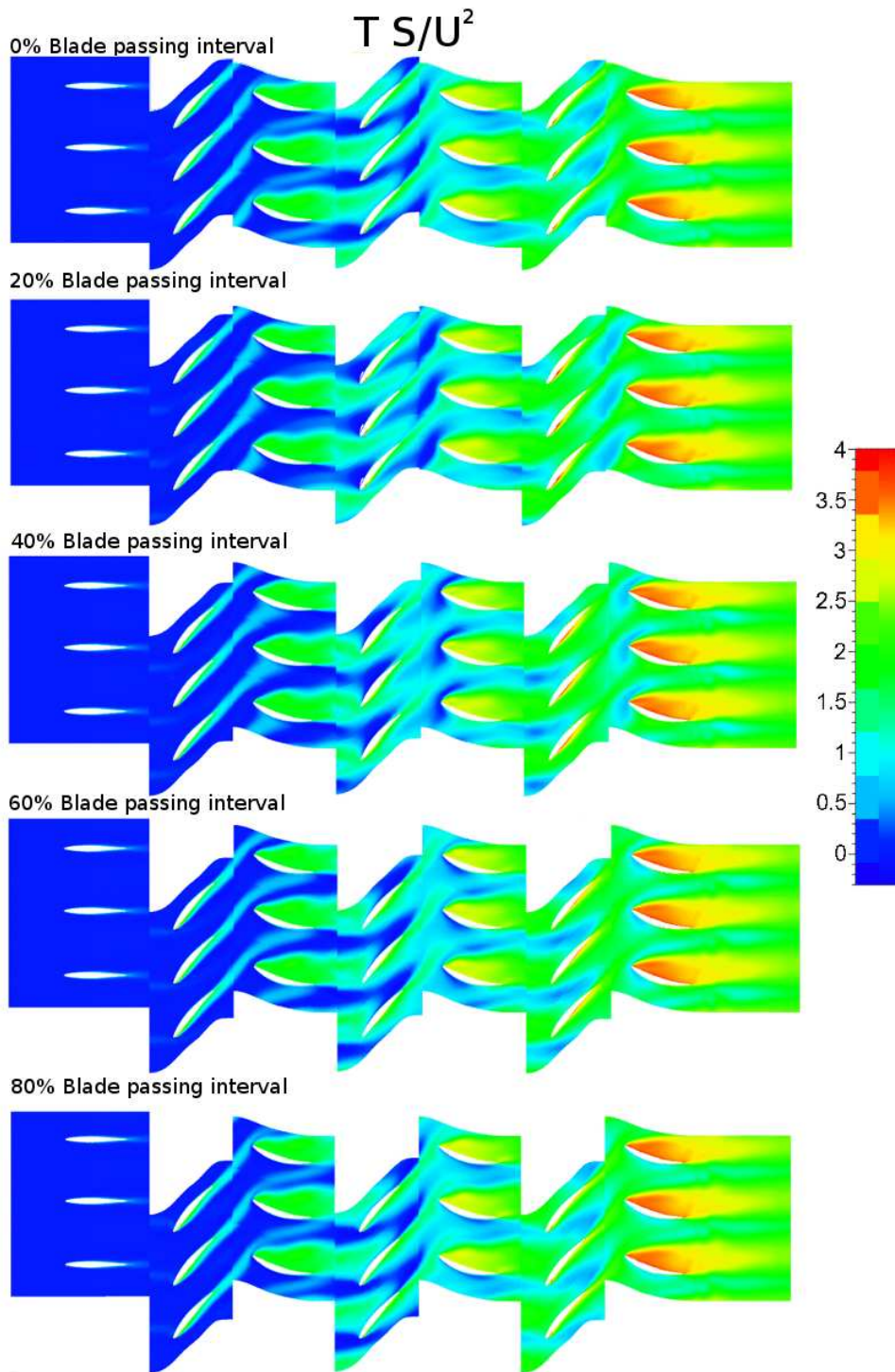


Figure 7.15: Time-series entropy distribution, normalised relative to inlet, on constant radius surface at midspan; $\phi = 1.024$

CHAPTER 7. FOURTH QUADRANT: POSITIVE ROTATION

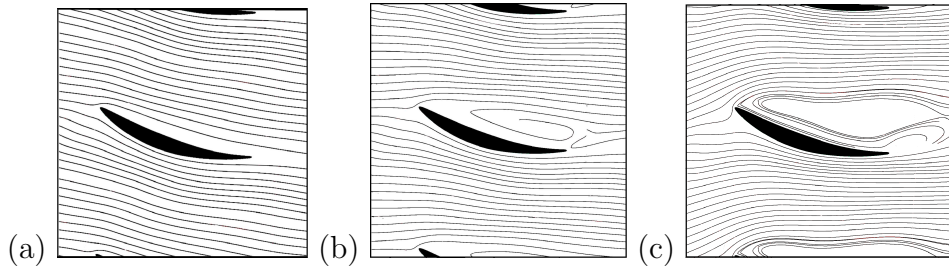


Figure 7.16: Streamlines surrounding first stage stator at (a) $\phi = 0.665$, (b) $\phi = 0.747$ and (c) $\phi = 1.024$, at mid span

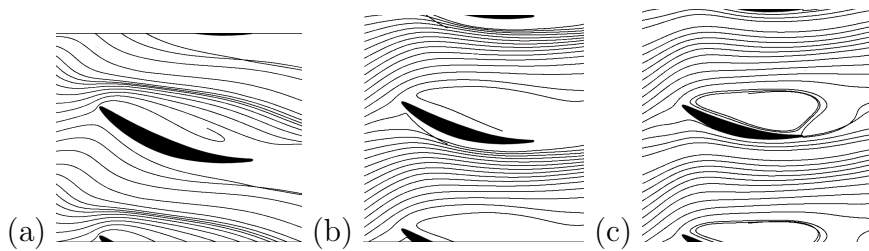


Figure 7.17: Relative velocity streamlines surrounding final stage stator at $\phi = 1.024$, at (a) 10 %, (b) 50 % and (c) 90 % of full span

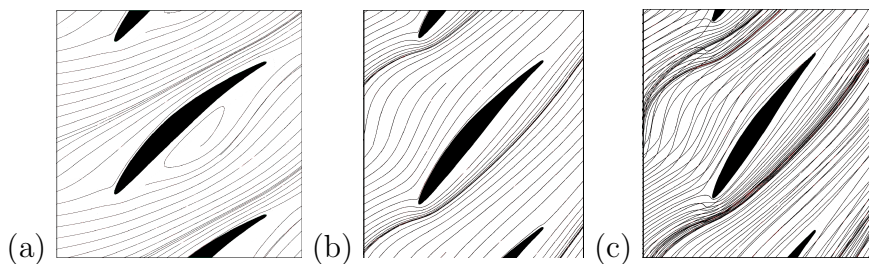


Figure 7.18: Relative velocity streamlines surrounding final stage rotor at $\phi = 1.024$, at (a) 10 %, (b) 50 % and (c) 90 % of full span

The circumferentially averaged radial velocity is close to zero at all points within the compressor, but are progressively larger in later stages, as is shown in figure 7.20. Note the undulations in the streamlines in second and third stage blade rows. These indicate net average tipward radial flows in rotor rows and net average hubward flows in stator rows, particularly from the hub to approximately midspan. The magnitude of the radial components increase with the stage number.

7.4 Discussion

It has been shown that in general, during fourth quadrant turbine-like operation of the test compressor, in all blade passages, flow velocities near the hub are 10 -20 % higher than those at the casing. It has also been shown that flow separation in rotor rows is greatest near the hub. Despite this, flow velocities downstream of rotor rows are highest near the

CHAPTER 7. FOURTH QUADRANT: POSITIVE ROTATION

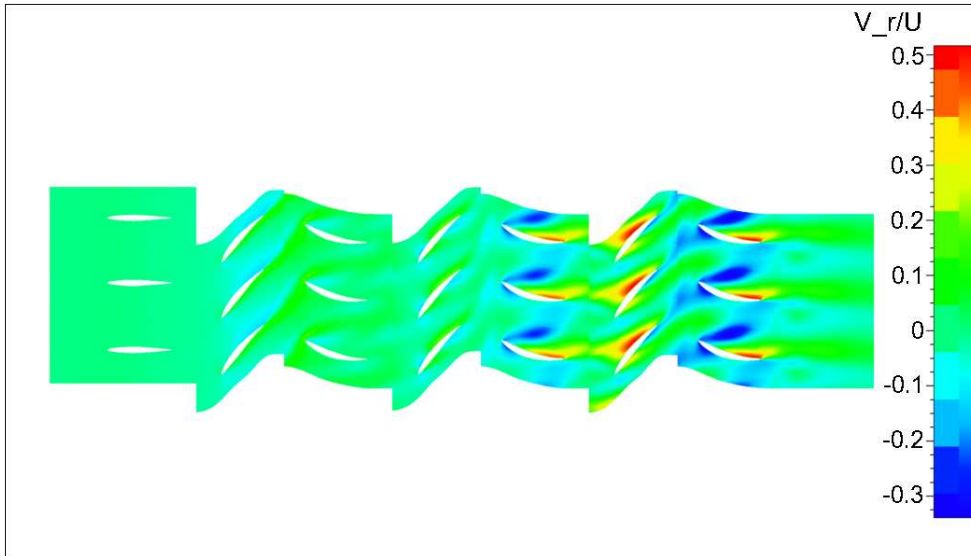


Figure 7.19: Radial velocity component magnitude on a constant radius plane at halfspan, at a flow coefficient of $\phi = 1.024$,

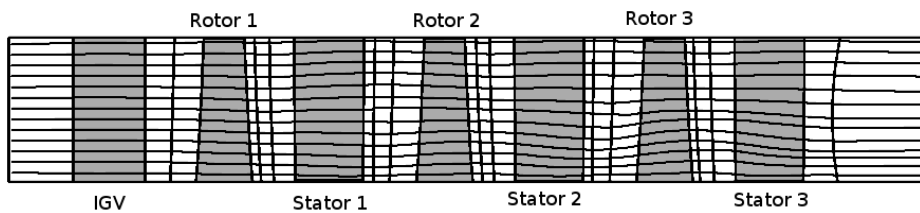


Figure 7.20: Circumferentially averaged flow paths at $\phi = 1.028$

hub and decrease towards the tip due to the greater amount of energy extracted from the flow at larger radii, as was explained earlier. Finally, it has been shown that in stator rows, blockage is greatest near the casing due to flow separation in that region, which extend across a greater fraction of the span, and a greater percentage of the blade pitch than the separation bubbles on rotor blades.

The comparatively mild flow separation on the rotor, and highly separated flow on the stator is the reverse of the situation reported by Cyrus [1990]. The lower reaction-ratio of the compressor stage investigated by Cyrus is probably responsible for this, as the stator blades of the lower reaction-ratio are less badly aligned with the flow. The fact that the stator camber angles are larger than those of the rotor for the test compressor may also partially account for this, as the midspan camber angles of the compressor stage used in Cyrus [1990] were approximately equal.

The velocity triangles for the first stage for all three flow coefficients investigated are shown in figure 7.21. Note that the flow angle downstream of the stator decreases with an increase in flow coefficient, and changes sign between flow coefficients of 0.747 (subfigure (b)) and 1.024 (subfigure (c)). The change in sign of the absolute flow angle downstream of the rotor occurs at a lower flow coefficient, between 0.665 (subfigure (a)) and 0.747 (sub-

CHAPTER 7. FOURTH QUADRANT: POSITIVE ROTATION

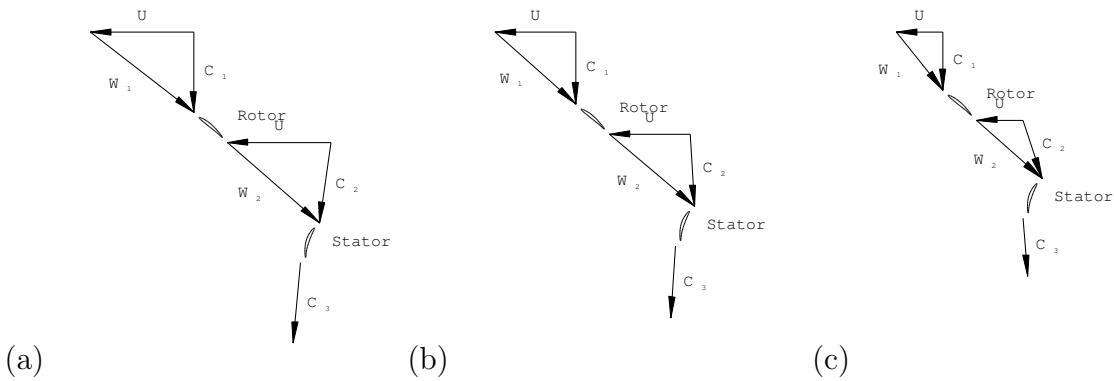


Figure 7.21: Velocity triangles for first stage at 50 % of blade span: (a) $\phi = 0.665$ (b) $\phi = 0.747$ (c) $\phi = 1.024$

figure (b)); however the relative flow angle remains approximately constant. The stronger dependence of deviation angle in the stator than in the rotor is due to the fact that the difference between the flow angle and leading edge stator blade metal angle is larger than for the rotor, with the result that separation on the stator is more severe, as has already been shown. When severe separation occurs on a blade, the resulting recirculation zone affects the direction of flow at the blade trailing edge, effectively altering the blade shape. Cumpsty [1989] comments that “When a blade stalls the most serious effect is usually that the deviation rises to a high level...” (p.168).

Because separation is more severe in stator rows than in rotor rows, the difference in axial velocity between the hub and casing regions is greater in the former than the latter. This implies that, for continuity to be satisfied, hubward radial flows must occur in stator blade passages. In effect, most of the flow moves hubward in order to avoid the separation bubble near the tip. These radial flows are evident as the dark blue regions of hubward radial flow in the middle of the second and third stage stator blade passages in figure 7.19, and are also responsible for the net hubward tendency observable in these stages in figure 7.20. The increase in axial velocity near the hub in stator blade passages also has the effect of raising the local flow coefficient in this region for the downstream rotor rows. This decreases the angle of incidence of the rotor blades, deepening the negative incidence stall, and leading to more severe separation on the downstream rotor in the near-hub region. In addition, the lower net axial velocities near the casing decrease the local flow coefficient, which is why separation in this region is less severe. This leads to tipward radial flows in rotor blade passages, which may also be observed in figures 7.19 and 7.20. Continuing with this line of reasoning, and considering the stator row downstream of the rotor row under consideration, separation in the tip region will be still more severe due to the relatively higher local flow coefficient, leading to a larger difference in velocity between the hub and the tip region, which will in turn lead to still worse separation in the hub region of the rotor row downstream of that stator. Because of this, the radial velocity components within blade passages increase in magnitude with stage number, as shown in figure 7.20. This also accounts for the increasingly severe separation with stage number.

CHAPTER 7. FOURTH QUADRANT: POSITIVE ROTATION

7.5 Summary

The flow field in a compressor operating at flow coefficients up to approximately twice the design point value, in the fourth quadrant positive rotation, or turbine-like regime, has been investigated experimentally and numerically. Flow is dominated by large areas of separated flow near the pressure surfaces of the blades. For the compressor examined, separation was more severe on the stator rows than the rotor rows; however, on comparison with the findings of Cyrus [1990], this appears to be dependent on the reaction ratio of the machine under investigation. Radial velocity components are negligible in flow in the inter-blade row regions. Axial and tangential velocity components vary in the span-wise direction in inter-blade row regions. In particular, the axial velocity decreases from hub to casing, and a jet occurs near the hub for very high flow coefficients. Radial flows occur within blade passages, and increase in magnitude with stage number. The degree of flow separation increases with the number of blade rows, as the wakes of upstream blade rows exacerbate separation on downstream blades. Separation on rotor blades is most severe near the hub, while separation on stator blades is most severe near the casing. This caused the tipward and hubward radial flows observed in rotor and stator blade passages respectively. For both rotor and stator rows, most throughflow occurs near the hub, and this trend becomes more marked at higher flow coefficients.

Examination of data in the frequency domain indicated that flow is dominated by cyclic phenomena at the blade passing frequency due to the wakes.

Numerical modelling of single blade passages for all stages with a Navier-Stokes solver, with circumferential averaging on planes between rotor and stator blade-rows, yields reasonable agreement with experimental data for lower fourth quadrant flow coefficients. However, the large, time-unsteady wakes occurring at higher flow coefficients render such a modelling approach questionable. The non-linear harmonic approximation provides an improvement in agreement with experimental data from midspan to the casing. The disagreement between numerical and experimental data near the hub is the result of circumferential averaging of numerical data, and the circumferential variation in the flow field downstream of blade rows due to wakes.

Chapter 8

Second quadrant: positive rotation

8.1 Introduction

This chapter describes the flow structures observed under second quadrant operating conditions, for positive rotation. In this mode of operation, the compressor dissipates power, as the direction of rotation remains positive but with flow through the machine reversed, leading to a bad mismatch between blade metal angles and relative flow angles. The result is a "mixer-like" mode of operation dominated by large tangential velocity components at the flow coefficients investigated.

Three flow coefficients were investigated: $\phi = -0.132$, $\phi = -0.200$, $\phi = -0.340$. The investigation of Gamache and Greitzer [1990] on a three-stage subsonic compressor operating under this mode has been discussed in an earlier chapter. Numerical simulation results are presented for the compressor used by Gamache and Greitzer [1990]. For brevity, the compressor used for that investigation will be referred to as the MIT compressor, as the second quadrant research was conducted upon it at that establishment.

The flow coefficients investigated by Gamache and Greitzer [1990] extended over a range between $\phi = -0.05$ and $\phi = -0.21$. In this chapter, and all subsequent chapters describing reversed flow directions (negative flow coefficients), a positive axial velocity implies that the velocity has the same direction as the mean flow through the machine, i.e. it is reversed from the design direction. In the same way, the tangential velocity is defined as positive when swirl occurs in the opposite direction to that occurring downstream of the rotor blades under design conditions, or the opposite of the rotor blade rotation direction for first quadrant operation.

8.2 Experimental results

8.2.1 Time-averaged velocity profiles

In the present study, time averaged results were obtained by means of a five-hole probe and by time-averaging of hot-film probe velocity measurements. Velocity distributions as a function of radius were obtained at the compressor inlet and downstream of each rotor row (measurement stations S3, S2, S1 and S0 in figure 3.1). These are shown in figures 8.1-8.6.

At a flow coefficient of -0.132, the radial average circumferential velocities at positions S2, S1 and S0 (figure 8.2) are approximately five times the magnitude of the average axial velocity. Similarly, the average tangential velocities at flow coefficients of -0.200 (figure 8.4) and -0.340 (figure 8.6) are also approximately five times the magnitude of the average axial

CHAPTER 8. SECOND QUADRANT: POSITIVE ROTATION

velocities. The tangential velocity component is thus dominant over the axial velocity component at all flow coefficients investigated. For this reason, the datum for the five-hole probe and the hot film probes was offset through 90° relative to the axis of the machine, to coincide with this velocity component, except at position S3, where flow entered the machine. The scatter observable in the time-averaged axial velocity profiles obtained from hot film measurements, particularly in figures 8.3 and 8.5, is due to the unsteady nature of operation in this mode. The disagreement between axial velocity data from five-hole probe and hot film measurements is most marked at station S0 (downstream of the first stage rotor; the final stage to receive flow under this mode of operation). Obtaining repeatable measurements at this axial station and flow coefficient proved troublesome. Velocity measurements at the outlet (position S3) were also troublesome, which was surprising, as the flow enters the machine here under this mode of operation, and should thus be axial due to upstream flow straighteners. This may be as a result of localised reversed flows due to recirculation zones in blade rows further downstream (that is, downstream according to the mean throughflow direction). Evidence of such localised reversed flows may be seen in figure 8.1, and will be discussed in the next paragraph. The most consistent results were obtained when the five hole probe was aligned with the machine axis, that is the angle offset was 0° . However, the velocity readings thus obtained at S3 were relatively insensitive to probe alignment, and thus both the velocity magnitude and directions obtained at this location may be erroneous.

It would appear from hot film results (discussed in the next section) that flow in this region is highly unsteady, which may explain the difficulty experienced with the five-hole probe for these measurements. As the Venturi meter was reversed, the possibility that wall separation occurring in the venturi nozzle, which would function as a diffuser with an inappropriately wide conical angle of approximately 35° , was causing this unsteadiness. However, this possibility was rejected for three reasons. Firstly, the length to inlet-diameter ratio of the resulting diffuser is low (1.0), which will lead to a relatively small separation region. Secondly, the duct between the venturi and the compressor outlet (station S3) being approximately 3.5 times its diameter, over which length it is reasonable to assume that most of the effects of separation will have mixed out. Thirdly, there are two honeycomb flow straighteners in this region, each with an associated pressure drop between 2 and 4 Pa depending on the flow coefficient, representing a combined pressure drop of 50 - 70 % of the dynamic pressure in the duct. One of the flow straighteners is less than one diameter from the venturi inlet. The presence of the flow straighteners, with their associated pressure drop, promote the dissipation of non-uniform flow features related to the separation in the Venturi. At a flow coefficient of -0.132, the discrepancy between the volumetric flow rate as measured by the turbine anemometer and the value determined at position S3 by integration of the measured velocity profile is 1.9 %; however at a flow coefficient of -0.200, the discrepancy at S3 increased to 7.5 %, while at a flow coefficient of -0.34, the discrepancy had risen to nearly 60 %.

At a flow coefficient of -0.132, the axial velocity profile downstream of the final stage rotor (position S2 in figure 8.1), both hot film and five hole probe measurements show an area of locally reversed flow near the hub. Most of the throughflow appears to occur near midspan, where the velocity is positive and at a maximum. The velocity decreases towards zero towards the tip from midspan. The reversed velocity near the hub was also observed by Gamache and Greitzer [1990], although at a flow coefficient with a smaller magnitude (that is, closer to zero). However, it cannot be conclusively stated to be present downstream of the second and first stage rotor rows (positions S1 and S0), as hot film and

CHAPTER 8. SECOND QUADRANT: POSITIVE ROTATION

five hole probe measurements differ near the hub at these axial positions. In addition, the maximum negative velocity measured in these regions was not as large in magnitude as that observed at S2. As with the final stage rotor, however, most of the through flow occurs near midspan. It should be noted that the discrepancy between the volumetric flow rate obtained by integrating the axial velocity profile at S2 differed from the value measured by the turbine-anemometer by approximately 100 %. This is probably due to large circumferential variation in the flow field. The discrepancy at higher flow coefficients was also large, being of the order of 50 to 60 %.

The tangential velocity component at positions S3, S2 and S1 is similar for all stages. The velocity increases sharply from hub to approximately midspan, and less so from midspan to the casing.

At a flow coefficient of -0.200, the axial velocity downstream increases slightly from the hub to a maximum value at approximately 40 % of the span, before decreasing, finally increasing again near the tip. This is shown in figure 8.3. At station S1, the axial velocity component appears to decrease below zero and changes direction between approximately 70 and 90 %. At S2 and S0, the minimum velocity does not change sign, but approaches zero, reaching very low positive values at approximately 80 %.

The tangential velocity components downstream of the three rotor rows (figure 8.4) increase sharply from the hub to approximately 40 % of the blade span, beyond which they are approximately constant to the blade tips. There is very little difference between the velocity profiles at stations S2, S1 and S0.

The presence of a local maximum and a sharp change of gradient at 40 % of blade span in both the axial and tangential velocity components indicates that the flow field downstream of each of the rotor rows appears to be divided radially at this radius, with different mechanisms occurring hubward and tipward.

At a flow coefficient of -0.340, the spanwise distribution of the axial velocity components at positions S2, S1 and S0, shown in figure 8.5, are similar to those occurring at a flow coefficient of -0.200. The local maximum occurs at approximately 30 % of span instead of 40 %, and there is a small area of reversed flow near the tip downstream of all rotors. There is also a sharper increase in axial velocity from the hub to the local maximum at 30 %, and a sharp increase in velocity between the area of reversed flow and the blade tip in all positions investigated. There is a large discrepancy between data derived from the five-hole and hot film probes at position S0; however based on the appearance of the velocity profiles at positions S2 and S1, it would appear that the five-hole probe data is closer to reality. The tangential velocity components (figure 8.6 likewise resemble those occurring at a flow coefficient of -0.200, with a sharp increase in velocity to approximately 30 % of the blade span from the hub, and an approximately flat distribution for the remainder of the blade.

The overall similarity between the flow field at flow coefficients of -0.200 and -0.340 suggests that the basic flow mechanisms are similar within this range of flow coefficients.

8.2.2 Time dependent results

Time traces of axial velocity at midspan downstream of the third stage rotor are shown in figure 8.7. At a flow coefficient of -0.132, blade wakes are evident, but in general every second wake appears to be smaller than those preceding and following it. A similar phenomenon was observed by Gamache and Greitzer [1990] at a similar flow coefficient. This is apparently due to the flow passing through "every second blade passage". The fact

CHAPTER 8. SECOND QUADRANT: POSITIVE ROTATION

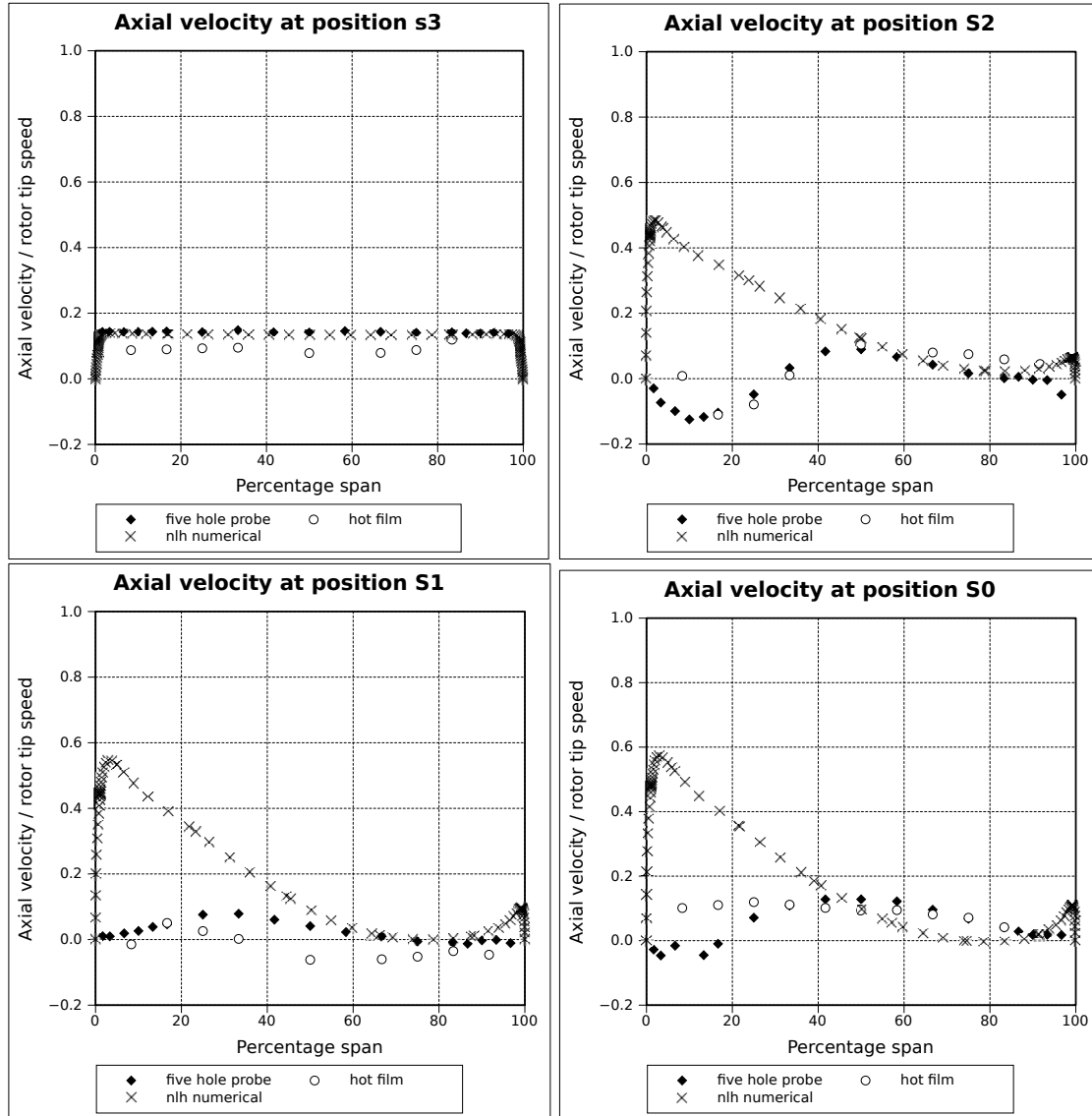


Figure 8.1: Axial velocity components as a function of radius at $\phi = -0.132$

that there are an odd number of blades accounts for the slight deviation from the pattern observable.

It will also be noted that the time trace becomes more noisy as the flow coefficient increases. This is also evident in the work of Gamache and Greitzer [1990]. It is due to the increased turbulence due to the mixer-like operation of the compressor in this mode.

In the frequency domain, the blade passing frequency is not evident at a flow coefficient of -0.132 (figure 8.8) except at station S0, downstream of the first stage rotor. However, there is a noticeable spike at slightly less than half (approximately 40 %) of the blade passing frequency, corresponding approximately to the "every second rotor" flow phenomenon described previously. There is also a spike at approximately a quarter of the blade passing frequency. The amplitude of the 25 % component is five times that of the 40 % component at station S2, but only three times larger at station S1. The amplitude of the disturbances at 40 % and 25 % of the blade passing frequency are 68 % and 70 % larger than the amplitude at the blade passing frequency at S0 respectively. The presence of flow phenomena at

CHAPTER 8. SECOND QUADRANT: POSITIVE ROTATION

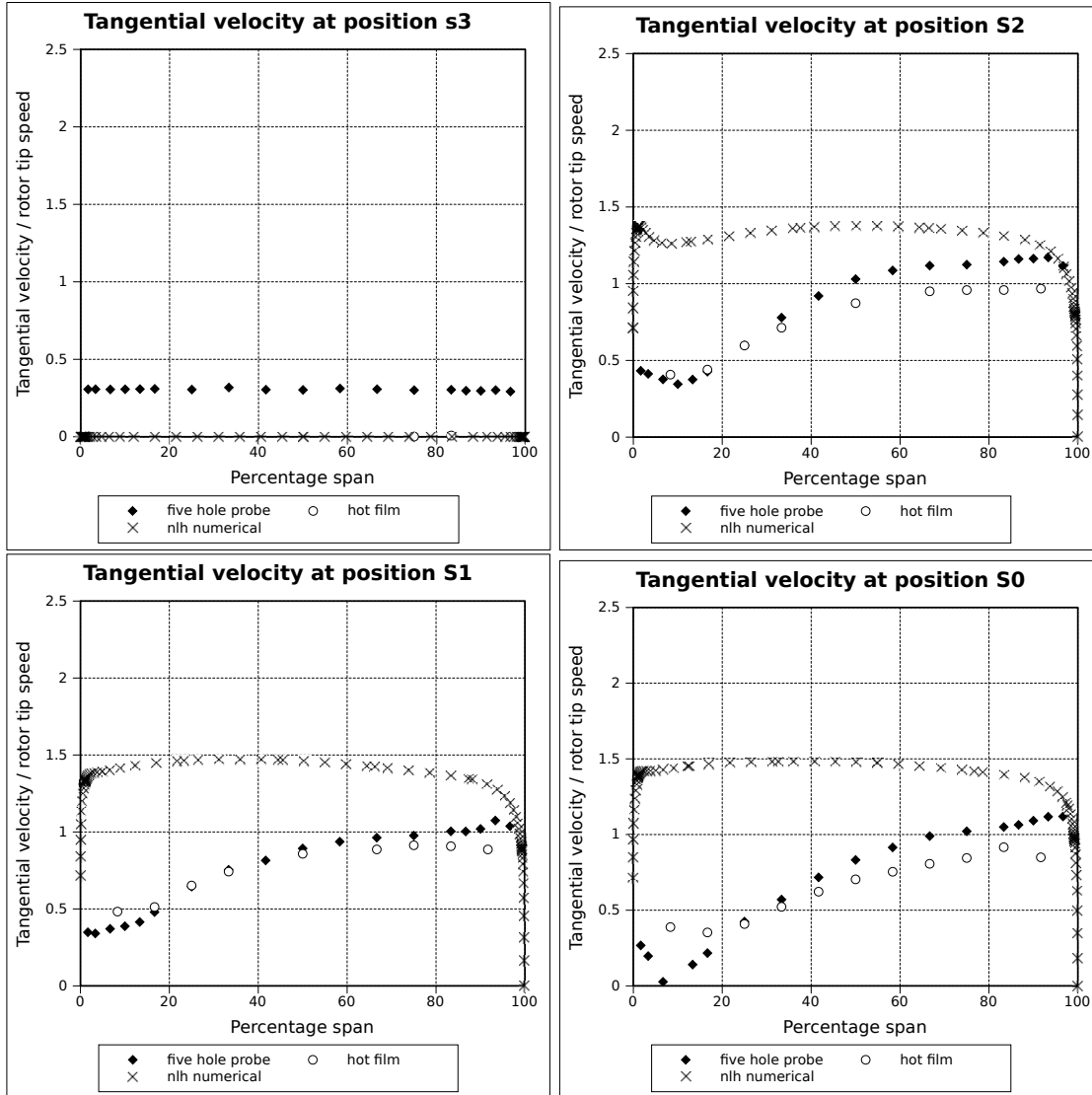


Figure 8.2: Tangential velocity components as a function of radius at $\phi = -0.132$

frequencies lower than the blade passing frequency invalidates a fundamental assumption of the single blade passage numerical simulations, namely that the flow fields in all blade passages in a given rotor row are similar.

The frequency spectra at a flow coefficient of -0.200 (figure 8.9) resemble those at the smaller flow coefficient in all of the above regards, except that no blade passing frequency component is visible at position S0.

At a flow coefficient of -0.340 (figure 8.10), the blade passing frequency and its second harmonic are evident downstream of all rotors. However, the amplitudes of the disturbance at 40 % the blade passing frequency is roughly equal that of the amplitude of the blade passing frequency component, while the 25 % component amplitude is twice the size of the blade passing frequency amplitude at S2, and thrice the size at S1. The differences between the results for S0 and the other two positions are due to the fact that the two-sensor x-probe was used for the former, allowing the use of the true velocity, while the cooling velocity was used for the frequency domains of S1 and S2.

A time-series of the area traverse conducted downstream of the first stage stator (po-

CHAPTER 8. SECOND QUADRANT: POSITIVE ROTATION

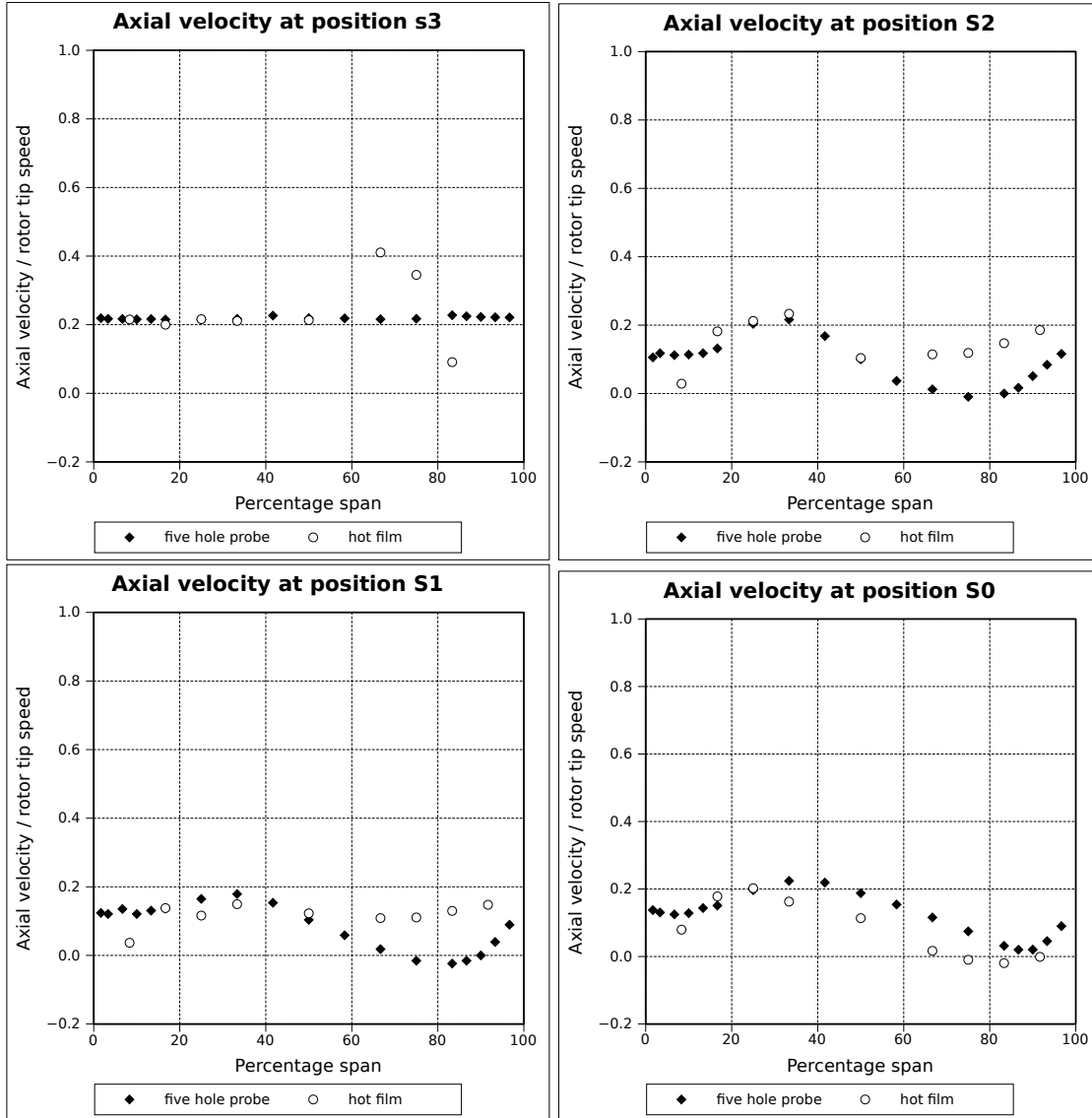


Figure 8.3: Axial velocity components as a function of radius at $\phi = -0.200$

sition R1) is shown in figure 8.11. The time series shows two rotor blade passing intervals because of the existence of cyclic phenomena at half the blade passing frequency. It can be seen that the principle features of the flow field are similar at 0.0 % and 205.1 % of the blade passing interval, despite the considerable variation evident between these time-steps, confirming that cyclic phenomena with a period half that of the rotor blade passing frequency dominate the flow field.

The magnitude of the maximum axial velocity occurs at 30 % of the span (label A). The area of high velocity in which this occurs extends from 20 to 65 % of the span, and is 70 % of the local stator blade pitch on average, varying in circumferential width in time by approximately 20 % of the blade pitch. These high axial velocity areas appear to account of the bulk of the throughflow, exceeding the average axial velocity by at least 32 %, and the maximum velocity varies in time by 23.5 % of the average axial velocity. The circumferential position at which the maximum axial velocity occurs appears to sweep across the flow field over the interval of twice the rotor blade passing period. When the

CHAPTER 8. SECOND QUADRANT: POSITIVE ROTATION

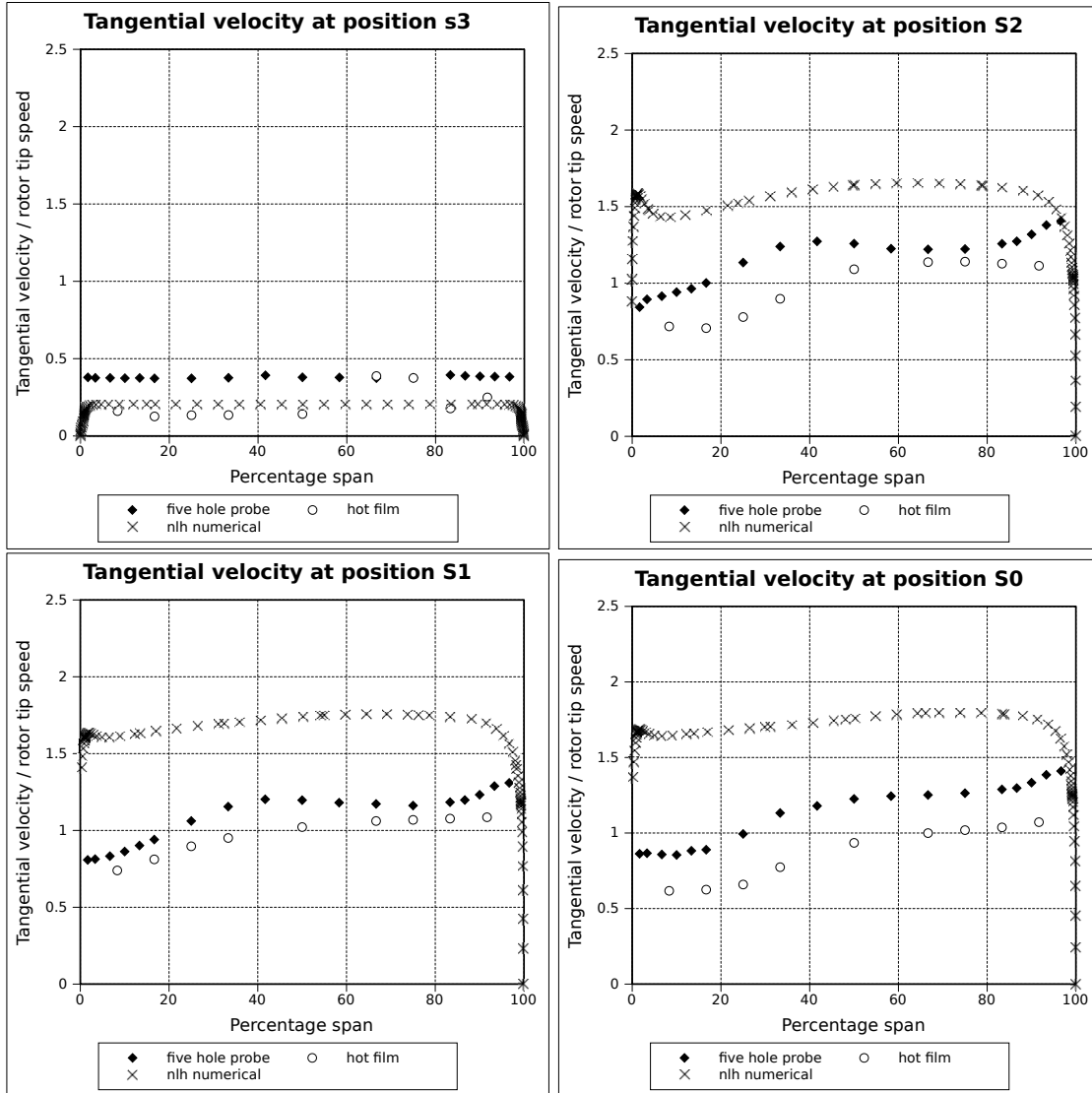


Figure 8.4: Tangential velocity components as a function of radius at $\phi = -0.200$

area moves so far to the left of the plots as to move out of the area under consideration, another enters from the right. Bearing in mind the suggestion of Gamache and Greitzer [1990] that second quadrant flow may occur through every second rotor blade passage, the movement of these jets appears to correspond with similar phenomena from the upstream rotor row, and thus appear to be direct evidence for this phenomenon.

Immediately above this high velocity area is a region of very low velocity, with a minimum value close to zero, which also fluctuates in size with time (label B). The small white areas present in the contour plots (label C) indicate regions where the velocity could not be resolved. This is probably as a result of the flow angle relative to the datum of the sensor being outside the wedge of acceptance of the hot film sensor, and thus represent either areas of reversed flow, as were observed at approximately the same radii downstream of all rotor rows at this flow coefficient, or large radial flows which invalidate the assumption of two-dimensional flow for the x-probe. In either case, the flow structure which is probably responsible for these is the same: immediately above the low velocity area is an area of high velocity of similar circumferential width (label D). Again bearing in mind the suggestions

CHAPTER 8. SECOND QUADRANT: POSITIVE ROTATION

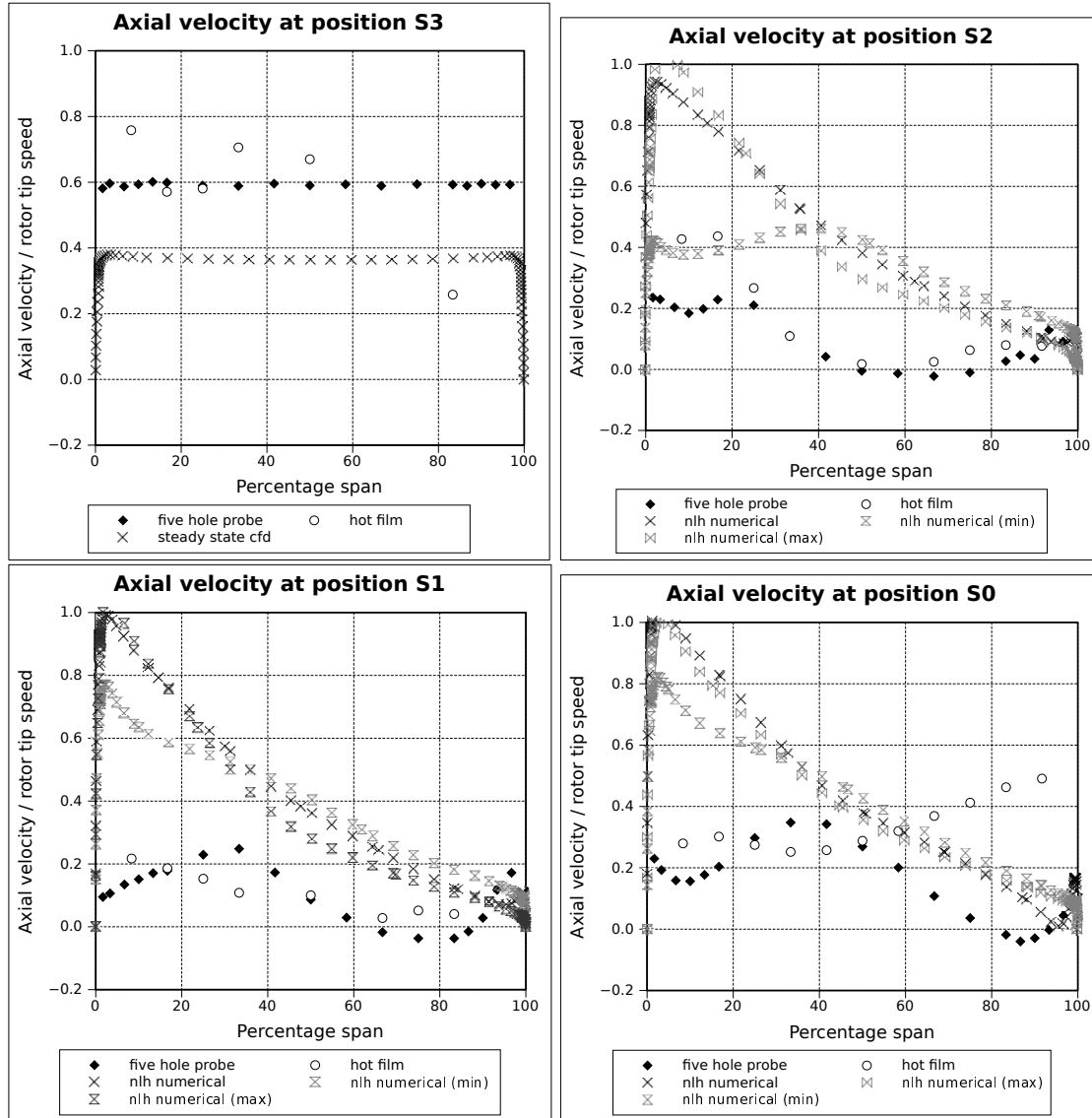


Figure 8.5: Axial velocity components as a function of radius at $\phi = -0.340$

of Gamache and Greitzer [1990], it would appear that these two combined represent a section through an area of recirculating flow located near the casing at the stator trailing edge, with an axis of rotation perpendicular to the meridional plane. Further evidence for this will be advanced later in this chapter, based on the numerical simulation of second quadrant operation of the compressor used in the investigation of Gamache and Greitzer [1990].

8.3 Numerical results

The numerically determined velocity profiles downstream of the rotors are compared to experimental results in figures 8.1-8.6. Due to uncertainties regarding the accuracy of the measured velocity profiles at the machine outlet, where flow enters in this mode of operation, an average velocity based on the upstream volumetric flow measurement was imposed as the computational inlet boundary condition.

CHAPTER 8. SECOND QUADRANT: POSITIVE ROTATION

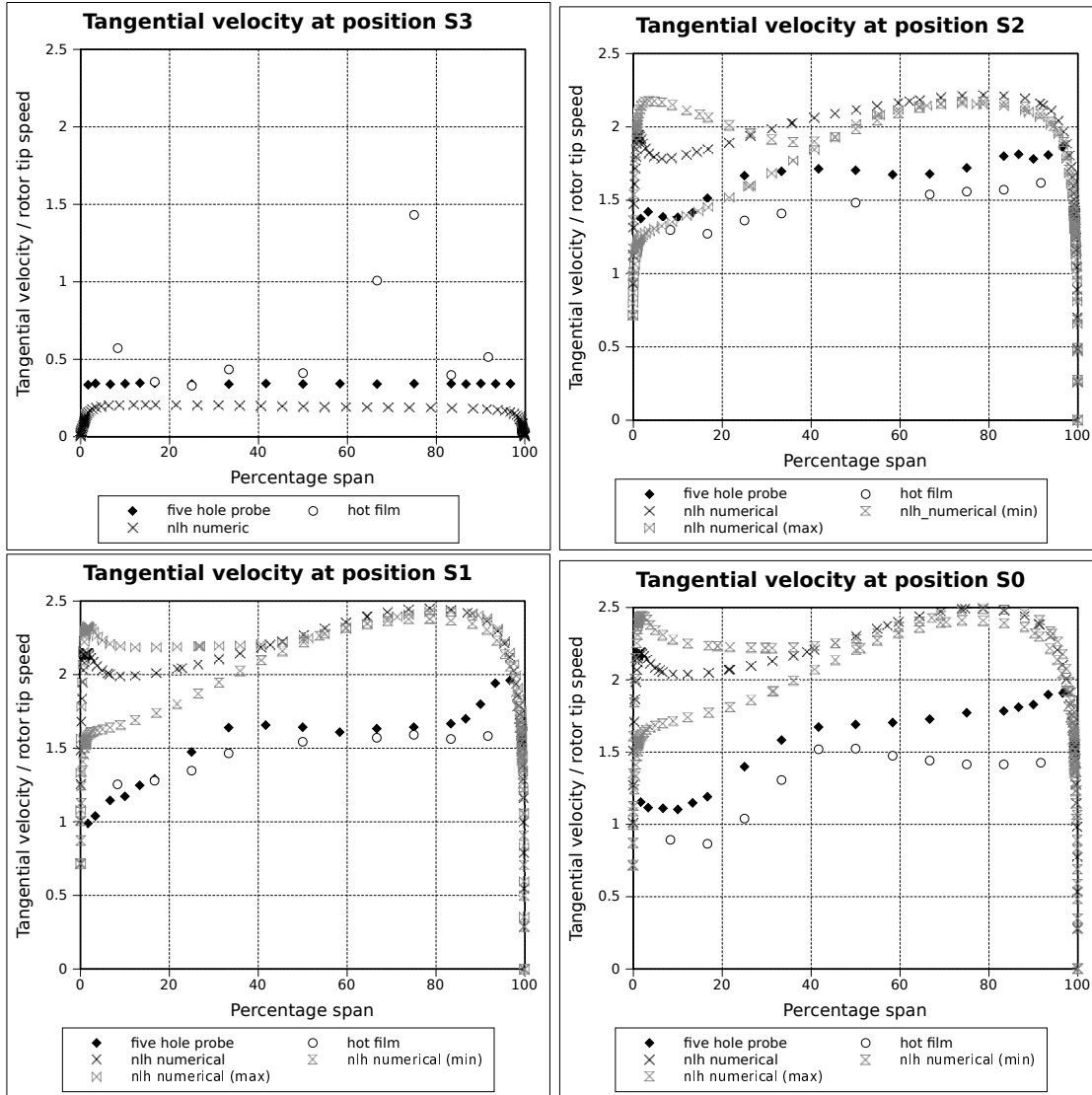


Figure 8.6: Tangential velocity components as a function of radius at $\phi = -0.340$

At a flow coefficient of -0.132, there is reasonable agreement between the experimentally and numerically determined axial velocity profiles downstream of rotor rows for the region between midspan and the casing, as shown in figure 8.1. The differences between the results from the hub to midspan, however, are approximately three times the average axial velocity. In addition, the numerical and experimental results for the tangential velocity profiles differ by a factor of three near the hub (figure 8.2).

At a flow coefficient of -0.200, (figure 8.3), the circumferentially averaged axial velocity profiles differ from the measured velocity profile at the hub by 100 % at station S2, and 150 % at stations S1 and S0. The discrepancy is smallest downstream of the final stage rotor because there are no upstream stages to disrupt the flow. Examination of the numerical velocity distribution at various circumferential positions within the blade passage shows variation of 30 % of the minimum value near the hub at station S2, and approximately 150 % at S1 and S0. However, this circumferential variation does not account for the difference between experimental and numerical results, as at the circumferential position yielding closest agreement with the experimental velocity profiles, the discrepancies are

CHAPTER 8. SECOND QUADRANT: POSITIVE ROTATION

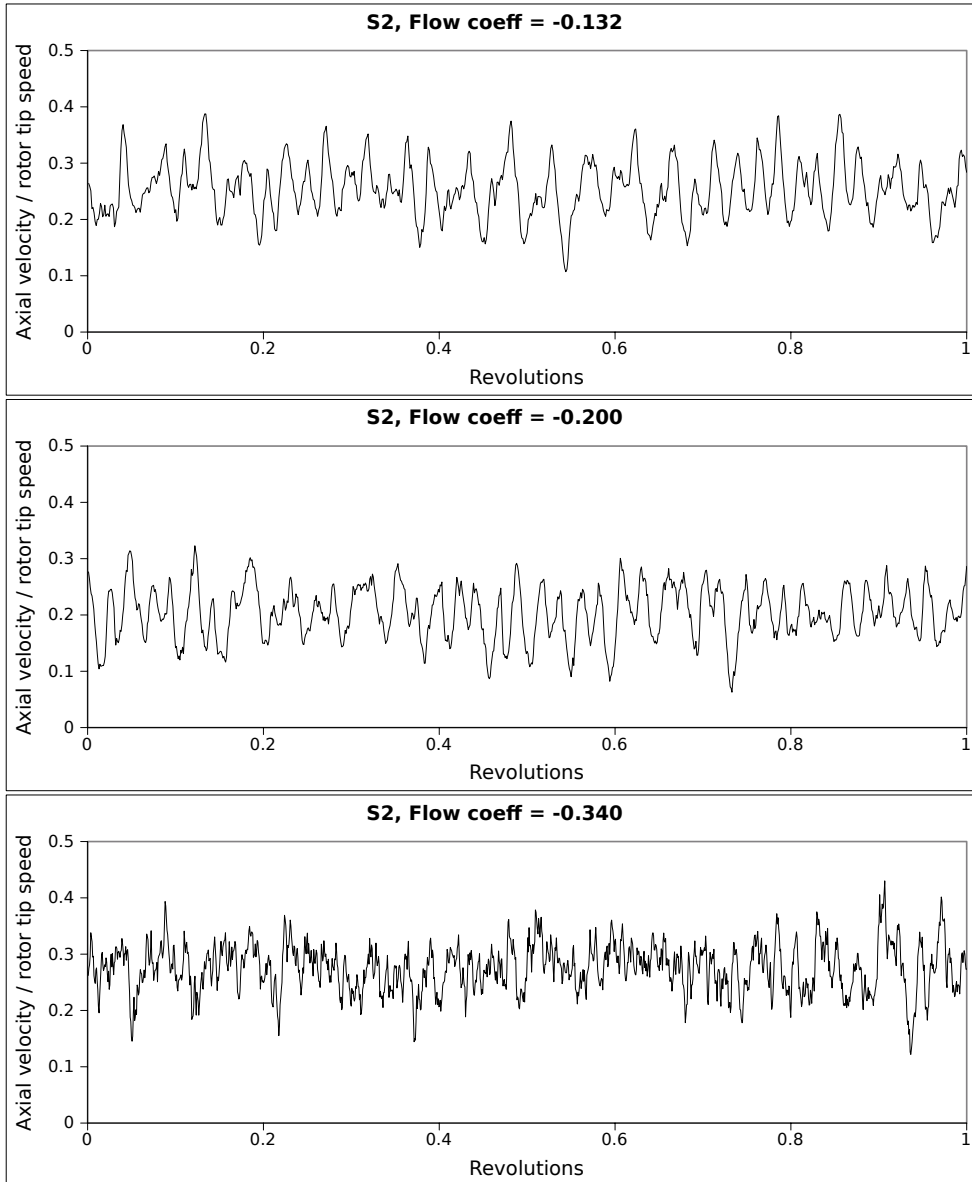


Figure 8.7: Time-traces for axial velocity components at midspan over one revolution

more than 100 % of the experimentally determined values for most of the area under consideration.

At a flow coefficient of -0.340, neither the axial velocity profiles (figure 8.5) nor the tangential velocity profiles (figure 8.6) agree well with the experimental data at any radius.

The failure of the numerical data to agree with the experimental data may be explained by the existence of flow phenomena spanning more than one blade passage. as indicated by the spikes in the frequency domain plots at frequencies below the blade passing frequency (figures 8.8-8.10). Some similar phenomena were detected by Gamache and Greitzer [1990], specifically a variation in velocity with a period of approximately two blade passages, and disturbances relating to an "annulus-stalled" condition at flow coefficients closer zero. It is thus reasonable to assume that the simulation of a single blade passage is inappropriate for the numerical modelling of this mode of operation for the test compressor. The method outlined in Longley [2007] would be more appropriate, but the implementation of

CHAPTER 8. SECOND QUADRANT: POSITIVE ROTATION

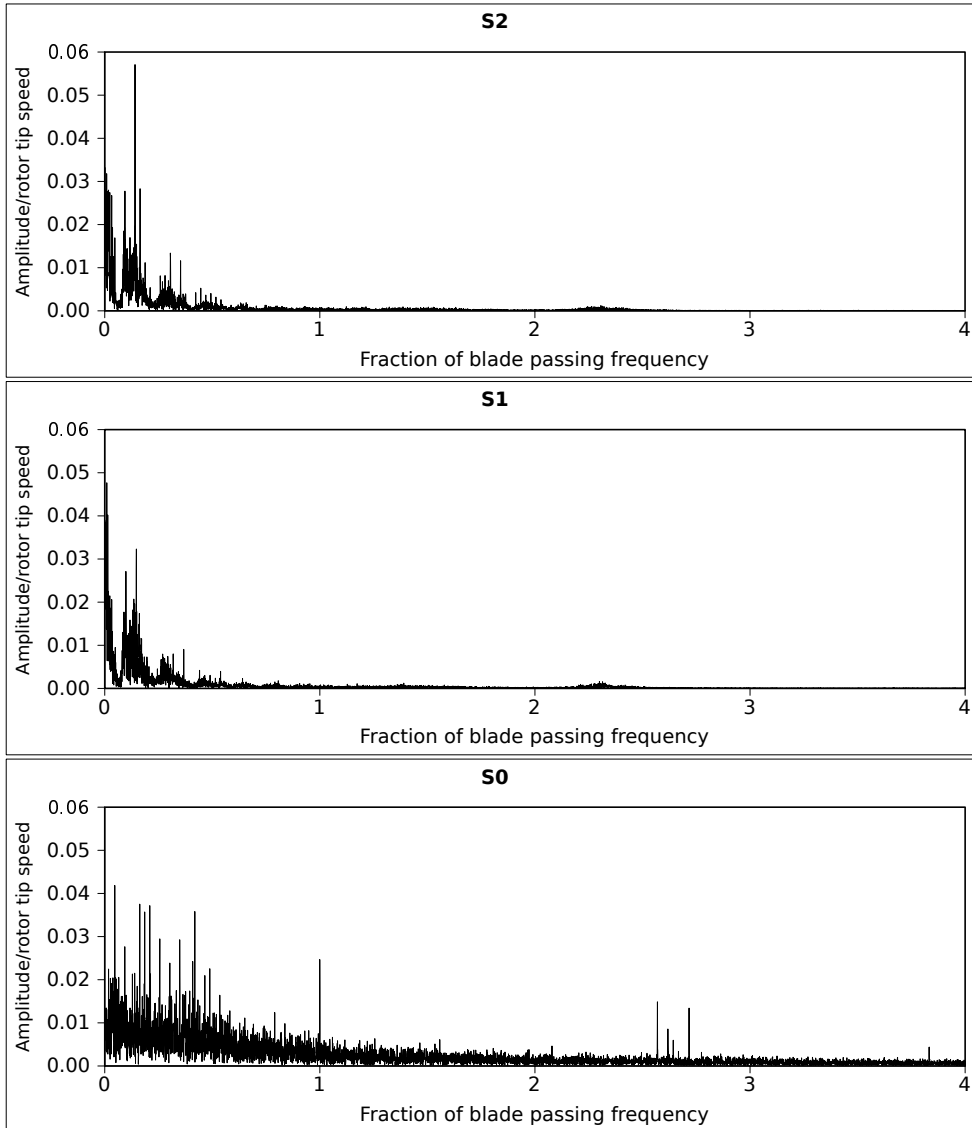


Figure 8.8: Frequency domain of cooling velocity variation at $\phi = -0.132$ at mid span

a numerical solver for this purpose is beyond the scope of this dissertation.

The compressor used in Gamache and Greitzer [1990] also exhibited flow phenomena which spanned more than one blade passage at some flow coefficients, but the range of flow coefficients at which such phenomena were was smaller than that for the test compressor used in the present study, with the result that for large negative flow coefficients, such phenomena no longer dominate those at the blade passing frequency. There was thus a possibility of reasonable agreement between numerical and published experimental data for operation at an appropriate choice of flow coefficient. For this reason, an attempt was made to numerically model that compressor. This is described next.

CHAPTER 8. SECOND QUADRANT: POSITIVE ROTATION

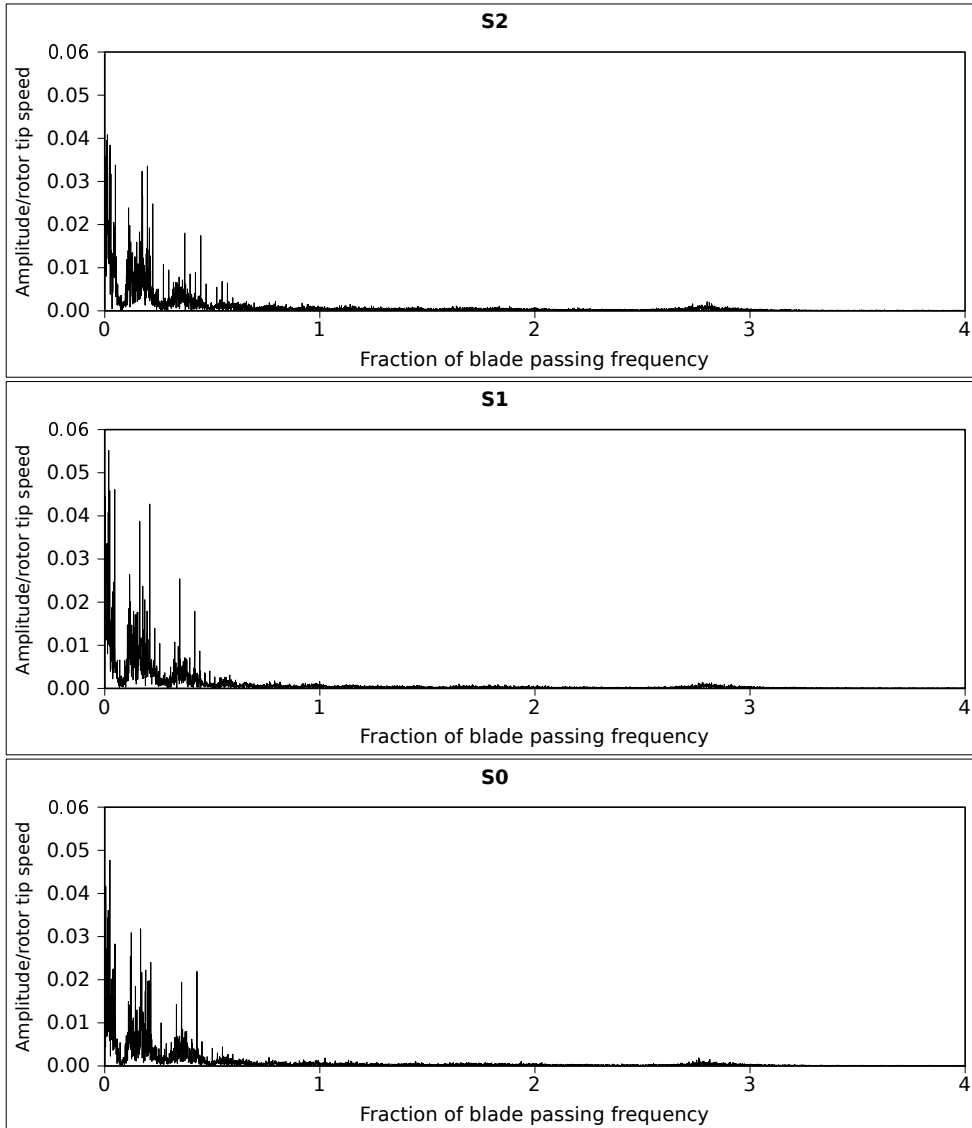


Figure 8.9: Frequency domain of cooling velocity variation at $\phi = -0.200$ at mid span

8.4 Numerical modelling the MIT compressor of Gamache and Greitzer

As experimental second quadrant data is available for the compressor of Gamache and Greitzer [1990] an attempt was made to model operation for this compressor numerically. A single flow coefficient of second quadrant operation was modelled ($\phi = -0.12$), using the non-linear harmonic approximation to model unsteady flow, for the compressor build with a reaction ratio of 0.64 and a hub-to-tip ratio of 0.88. Only midspan blade geometry data was available (Table 8.1), and this was incomplete, as the blade profiles used were not specified. The geometry was thus approximated by applying a free vortex design based on midspan data, and using NACA-65 blade thickness distributions on circular arc camber lines. This results in a compressor geometry which may differ from the machine under consideration to an unknown degree, thus a first quadrant simulation of operation under design conditions was performed, to show that the approximation yielded reasonably

CHAPTER 8. SECOND QUADRANT: POSITIVE ROTATION

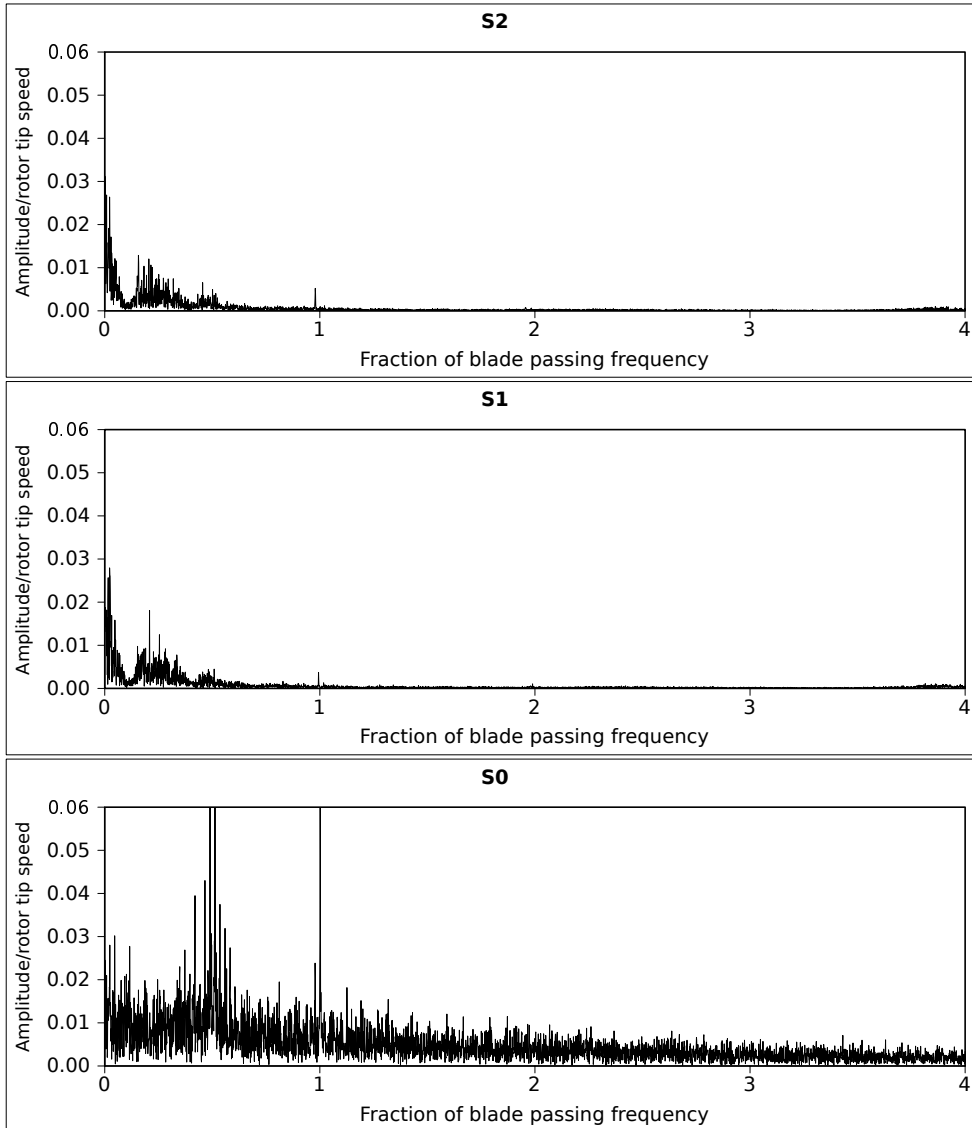


Figure 8.10: Frequency domain of cooling velocity variation at $\phi = -0.340$ at mid span

accurate performance data.

Axial, tangential and radial velocity profiles downstream of the second stage stator (position 6) and downstream of the third stage rotor (position 7 as defined by Gamache and Greitzer [1990]) are shown in figure 8.13. Agreement between the numerical model and the experimental data of Gamache and Greitzer [1990] appears reasonable for the axial and tangential velocity components, and is noticeably better for position 6 than position 7. Agreement between simulation results and the experimental data is worst for the tangential velocity profile at position 7, although the simulation results show a similar trend to experimental data. However, the small number of experimental data points limits the extent to which meaningful comparisons can be made. The better agreement between numerical and experimental results may be attributed to the fact that, according to the findings of Gamache and Greitzer [1990], at this flow coefficient flow patterns repeat once per blade passage in the circumferential direction, not once for every two blade passages, as was found for the Rofanco test compressor, and for the MIT compressor at negative flow coefficients closer to zero.

CHAPTER 8. SECOND QUADRANT: POSITIVE ROTATION

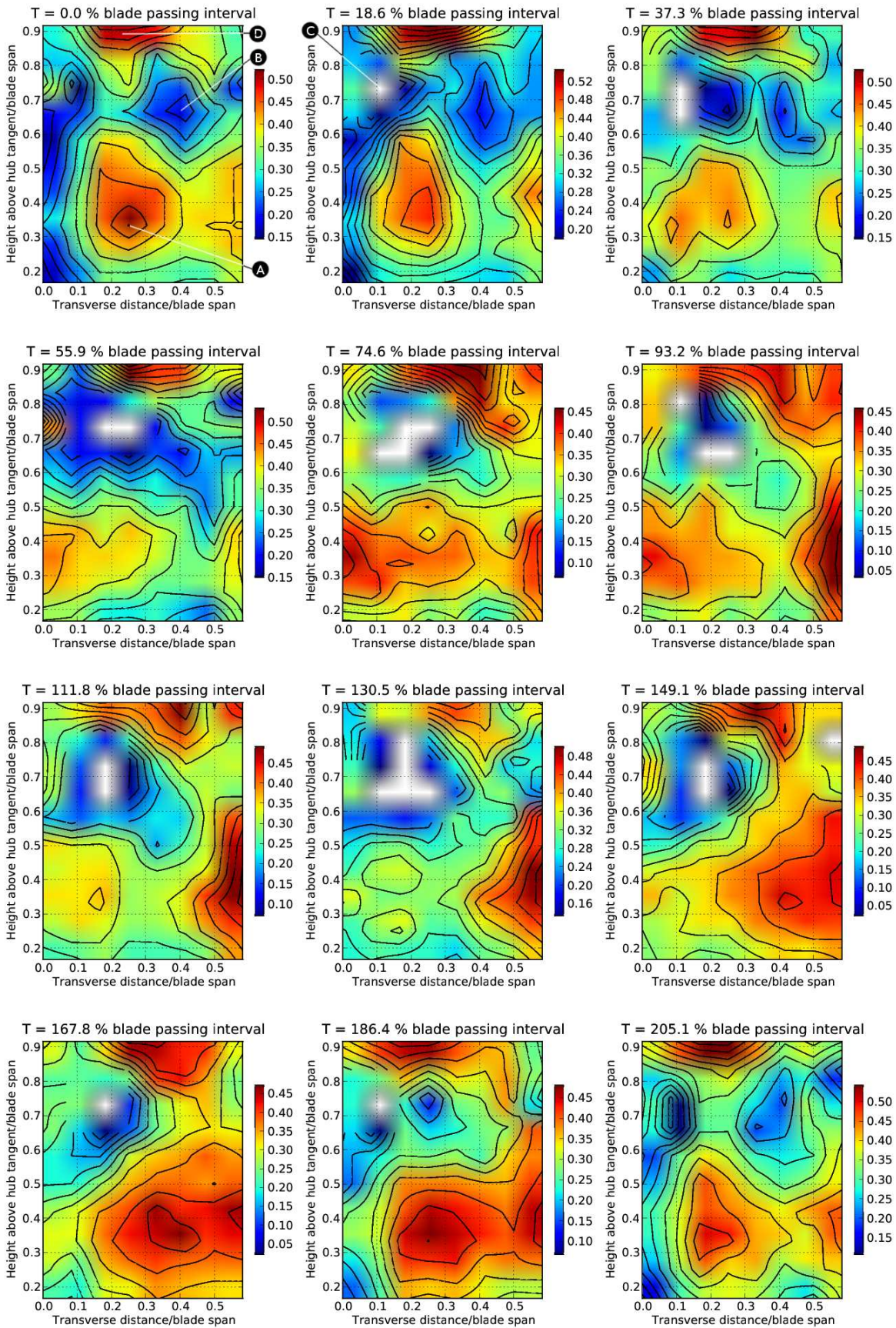


Figure 8.11: Time series of axial velocity contours at position R1 at $\phi = -0.340$

CHAPTER 8. SECOND QUADRANT: POSITIVE ROTATION

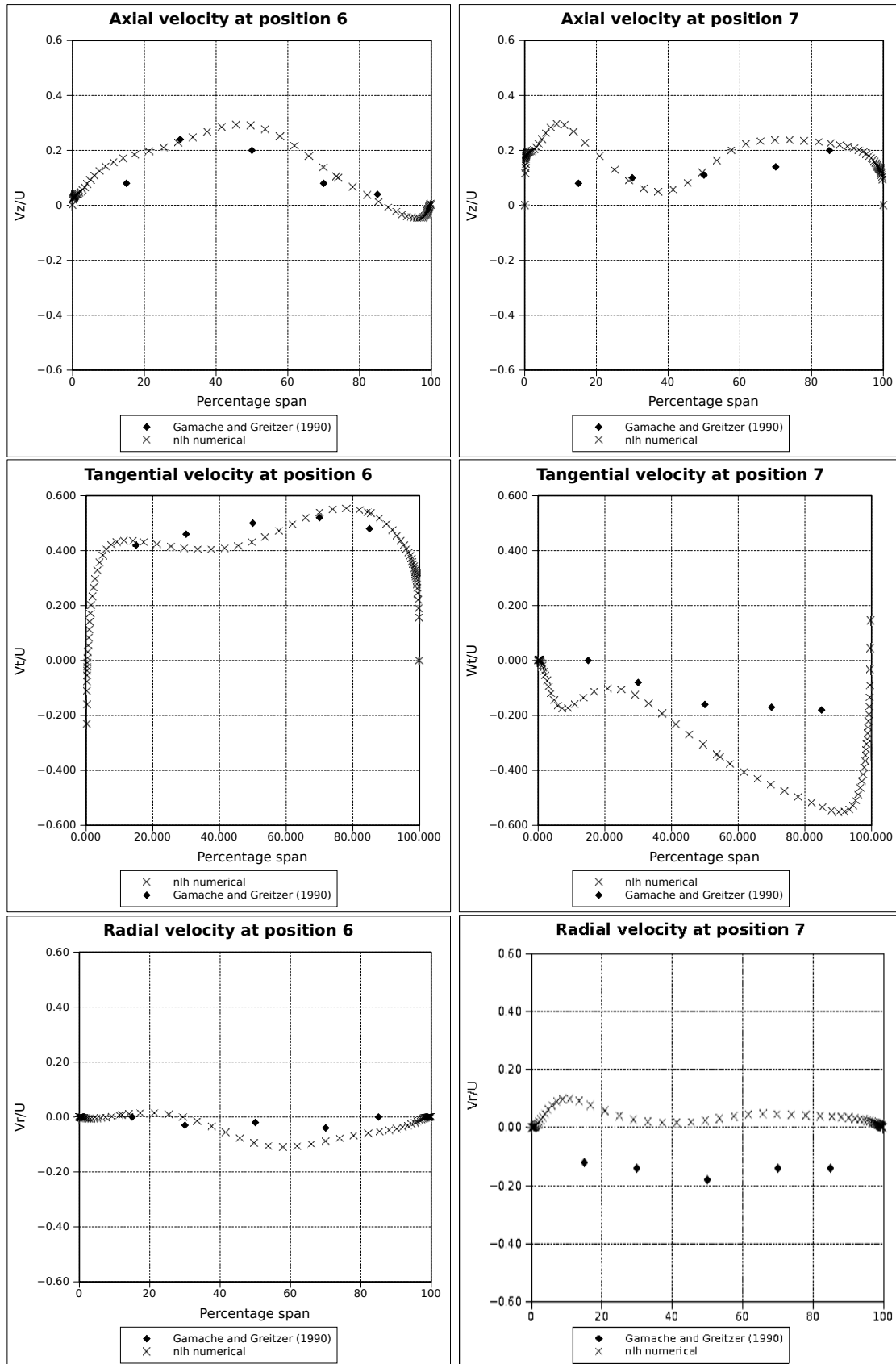


Figure 8.12: Velocity components as a function of radius at $\phi = -0.12$

CHAPTER 8. SECOND QUADRANT: POSITIVE ROTATION

Table 8.1: Geometry data for the MIT compressor [Gamache and Greitzer, 1990]

Midspan data						
	Stage number	Number of blades	Chord (m)	Camber angle (deg)	Stagger angle (deg)	
IGV		124	0.021	11.0	8.1	
Rotor	1	54	0.045	17.0	37.8	Tip Gap (mm) 0.965
	2	55	0.044	18.0	38.5	0.940
	3	49	0.051	20.0	39.6	0.889
Stator	1	85	0.031	27.0	21.0	Hub Gap (mm) 0.813
	2	88	0.031	25.0	23.0	0.940
	3	90	0.031	53.0	15.5	0.864

Gamache and Greitzer [1990] suggested that radial flow in rotor rows was in the tipward direction, while that in stator rows was hubward. They also suggested that secondary flows surrounding blade rows were circulating in the meridional plane. At the flow coefficients closest to zero, some reversed flow was detected near the hub, suggesting that the circulation was strongest at low flow coefficients.

Figure 8.13 shows a meridional section of the MIT compressor, with streamlines representing the circumferentially averaged flow paths. Flow is from left to right in the diagram. The diagram shows areas of circulation near the trailing edges of rotor blade tips. These appear to cause the tipward radial flow observed in rotor rows by Gamache and Greitzer [1990], as the blockage caused by these regions disappears downstream of the rotor trailing edge. Similar separated regions near the hub, at the trailing edge roots of stators, cause the hubward radial velocities observed in stator rows. The flow must thus "climb over" the obstructions caused by recirculation zones on the hub in rotor blade passages, and "dive under" the recirculation zones near the tip in stator blade passages. There are small regions of circulating flow attached to the hub near the trailing edges of rotor blades, but these do not affect the downstream flow to the same degree as the other separated regions owing to their small size (perhaps 20 % the diameter of those at the casing), and the much larger and thus dominant effects of the large circulating region at the rotor tips. The numerical results thus support the findings of Gamache and Greitzer [1990] regarding radial flows and circulation occurring within blade passages at this operating condition. Note that the flow field repeats over rotor-stator pairs, as was observed by Gamache and Greitzer [1990].

The flow fields surrounding the blades also appear to agree with those suggested by Gamache and Greitzer [1990], as is shown in figure 8.14. Flow surrounding the final stage stator (subfigure (a)) is relatively orderly. However, large separated areas containing recirculating flows occur on the suction surface of the final stage stator (subfigure (b)) and the stator of the penultimate stage (subfigure (c)), with all axial flow occurring in a thin layer on the pressure surface.

Thus, although there are some uncertainties regarding the exact geometry of the MIT compressor, and some discrepancies between experimental and numerical results, many of

CHAPTER 8. SECOND QUADRANT: POSITIVE ROTATION

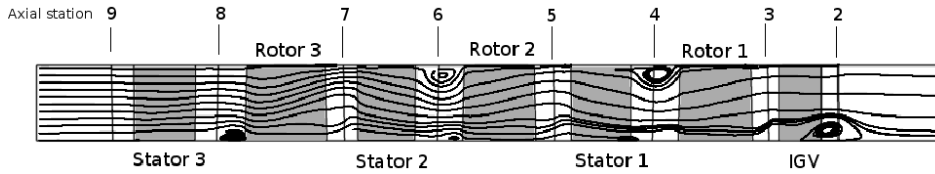


Figure 8.13: Meridional view of MIT compressor showing circumferentially averaged flow paths and areas of separation and recirculation on the hub and shroud

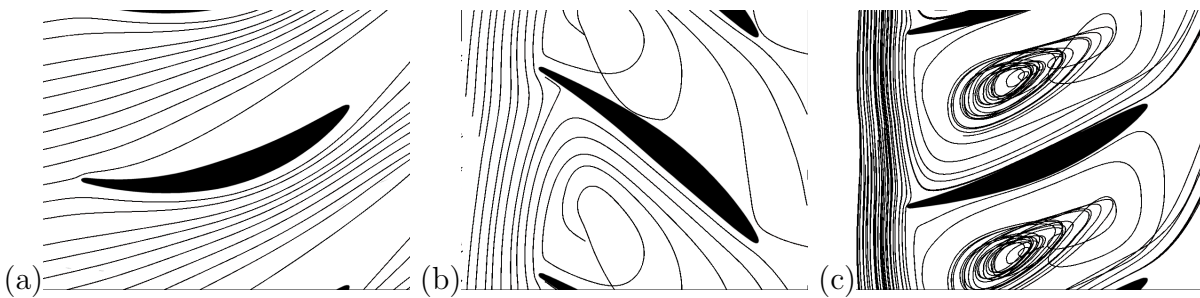


Figure 8.14: Streamlines at $\phi = -0.12$ at midspan surrounding: (a) third stage stator (absolute) (b) third stage rotor (relative) (c) second stage stator (absolute)

the significant flow features of second quadrant operation that were detected by Gamache and Greitzer [1990] were identified in the numerical results.

8.5 Conclusion

Second quadrant operation with positive rotation has been investigated experimentally for the test compressor and numerically for both the test compressor and that of Gamache and Greitzer [1990]. The experimental investigation revealed highly unsteady flow within the compressor, with the flow fields downstream of all rotor rows dominated by the tangential velocity component. Time dependent measurements revealed the existence of cyclic disturbances affecting more than one blade passage at a time, similar to those described by Gamache and Greitzer [1990] at some flow coefficients. Direct evidence for such phenomena was found downstream of the first stage stator, in the form of jets sweeping across the flow field with a period of approximately twice the blade passing interval of the rotor.

These render the numerical modelling approach used, namely the modelling of a single blade passage, invalid, and as a result numerical simulation results for the test compressor did not agree well with experimental results. The attempt to numerically model the compressor of Gamache and Greitzer [1990] was more successful, as numerical results agreed relatively well with the published experimental results, and, in addition, correctly captured the existence of hubward and tipward radial flows within stator and rotor rows respectively, as detected by Gamache and Greitzer [1990].

Experimental evidence was also found for the existence of areas of recirculating flow at the hub in rotor rows and at the casing in stator rows for the test compressor. This also supported the findings of Gamache and Greitzer [1990]. In addition, a numerical

CHAPTER 8. SECOND QUADRANT: POSITIVE ROTATION

simulation based on a reconstruction of the compressor of Gamache and Greitzer [1990] illustrated the existence of recirculating flows in the same regions, and further, confirmed the suggestions by those authors that these recirculation zones cause the hubward and tipward radial flows observed in stator and rotor rows respectively.

Chapter 9

Third quadrant: negative rotation

9.1 Introduction

This chapter describes the flow structures observed under third quadrant operating conditions. In this mode of operation, the compressor rotates in the reverse of the design direction, and flow through the machine is reversed. The pressure of the gas leaving the machine at the inlet (station S0) is higher than that of gas entering the machine at the outlet (station S3). The compressor thus operates as a compressor acting in reverse, although the pressure rise and efficiency obtained from this machine during such operation have been shown to be low. Cyrus [2004] investigated single stage fan operation in the third quadrant, as has already been discussed. However, much of this work does not allow for direct comparison, as reversible (variable stagger) stator blades were used.

Operation was investigated at three flow coefficients, namely -0.220, -0.314 and -0.369. The range of third quadrant operation possible for the test compressor is small, extending from the origin of the compressor map to a flow coefficient of approximately -0.4 based on the static to static pressure or torque coefficient maps (figures 5.1 and 5.3, and only -0.25 based on the total to static pressure coefficient map (figure 5.2). Thus the latter two flow coefficients are on the border between third and second quadrant operation. All tests were conducted at 80 % of design speed due to safety concerns, as this mode of operation is analogous to severe first quadrant stall, a condition which places large cyclic loading on the compressor blading. In this chapter, as in the second quadrant mode discussed in chapter 8, a positive axial velocity implies that the velocity has the same direction as the mean flow through the machine, i.e. it is reversed from the normal direction. In the same way, the tangential velocity is defined as positive when swirl occurs in the opposite direction to the direction of movement of the rotor blades under design conditions.

9.2 Experimental results

9.2.1 Time-averaged velocity profiles

Time averaged velocity profiles were obtained by means of a five-hole probe and by time-averaging of hot-film probe velocity measurements. Velocity distributions as a function of radius were obtained at the compressor inlet and downstream of each rotor row (measurement stations S3, S2, S1 and S0 in figure 3.1). These are shown in figures 9.1-9.6.

At a flow coefficient of -0.220 , the spanwise distributions of the axial velocity component downstream of each rotor row show large, well-defined velocity gradients. The

CHAPTER 9. THIRD QUADRANT: NEGATIVE ROTATION

maximum axial velocity (approximately 200 % the average axial velocity) occurs near the blade tip, while the minimum value, near the hub, is only 50 % of the mean value. This is shown in figure 9.1. The velocity profiles are approximately linear from 40 % to 100 % of the blade span, and would pass through the origin if the velocity profile did not increase near the hub at position S2, or flatten out near the hub at positions S1 and S0. The gradients are approximately equal for all rotor blade rows, as all stages have identical geometry. The variation in the profiles near the hub and casing is due to the fact that the flow entering the final rotor is more orderly and enters at a different angle, as the trailing edge angles being axial at all spans and thus aligned with the flow, and there being no blade row upstream to distort the flow. It is thus reasonable to expect that the flow follows the stator blade curvature, and that no areas of recirculating flow exist in this blade passage. This will be shown to be the case in the section dealing with the numerical results.

Downstream of the third stage rotor (station S2), the axial velocity is very low near the hub because the blade metal angles in this region are more poorly matched to the flow angles than at the tip, due to the direction of blade twist. This means that most of the flow must pass through the tip region. The fact that the gradient is continuous for most of the span suggests that there is no sudden change in flow conditions at any span, but rather a gradual one across the entire span. Given that flow is known to be heavily separated under this operating condition, this suggests that some degree of flow separation is present over the entire blade span, although the size of the separated area, and thus the blockage, varies continuously from hub to tip. This condition is thus similar to severely stalled first quadrant operation, although with flow and rotation directions and pressure difference between outlet and inlet all reversed.

The tangential velocity (figure 9.2) is of a similar average magnitude for all stages. However, at position S2 there is considerable variation across the span in comparison with S1 and S0, with a decrease in tangential velocity from hub to casing. This is due to the fact that flow around the final stage stator, which is immediately upstream of the rotor row in question, is more orderly than that of downstream stators. The velocity profiles at S1 and S0 are similar to one another, and are nearly uniform, with slightly higher velocities occurring near the hub and casing boundary layers. The spanwise variation of the tangential velocity downstream of the third stage rotor (position S2) matches a free vortex distribution quite well for most of the span, with the result that the work performed on the fluid is approximately constant from the hub to 80 % of the blade span. This will be shown later in this section. The circumferential velocity profile at positions S1 and S0 further downstream conforms to a free vortex distribution for the third of the span closest to the hub.

At a flow coefficient of -0.314 (figure 9.3), the axial velocity is approximately constant from hub to tip. This indicates that, unlike the smaller flow coefficient, the degree of blockage due to separation across the blade span is approximately equal for all radii. There is a small jet occupying the 10 % of the span nearest the hub downstream of each rotor blade. In the jet, axial velocities are approximately 10 % higher than the average value. The velocity increases from the near the hub to the casing: at S2, the maximum velocity at 80 % is 15 % larger than the average value. This is because more work is being performed on the flow near the casing than the hub, as will be shown later in this section. Downstream of the final stage rotor (position S2), the axial velocity decreases to zero from 70 % of blade span to the casing. This appears to be due to flow conditions at the outlet (position S3), (where flow enters the machine), and does not appear in downstream stages (S1 and S0).

CHAPTER 9. THIRD QUADRANT: NEGATIVE ROTATION

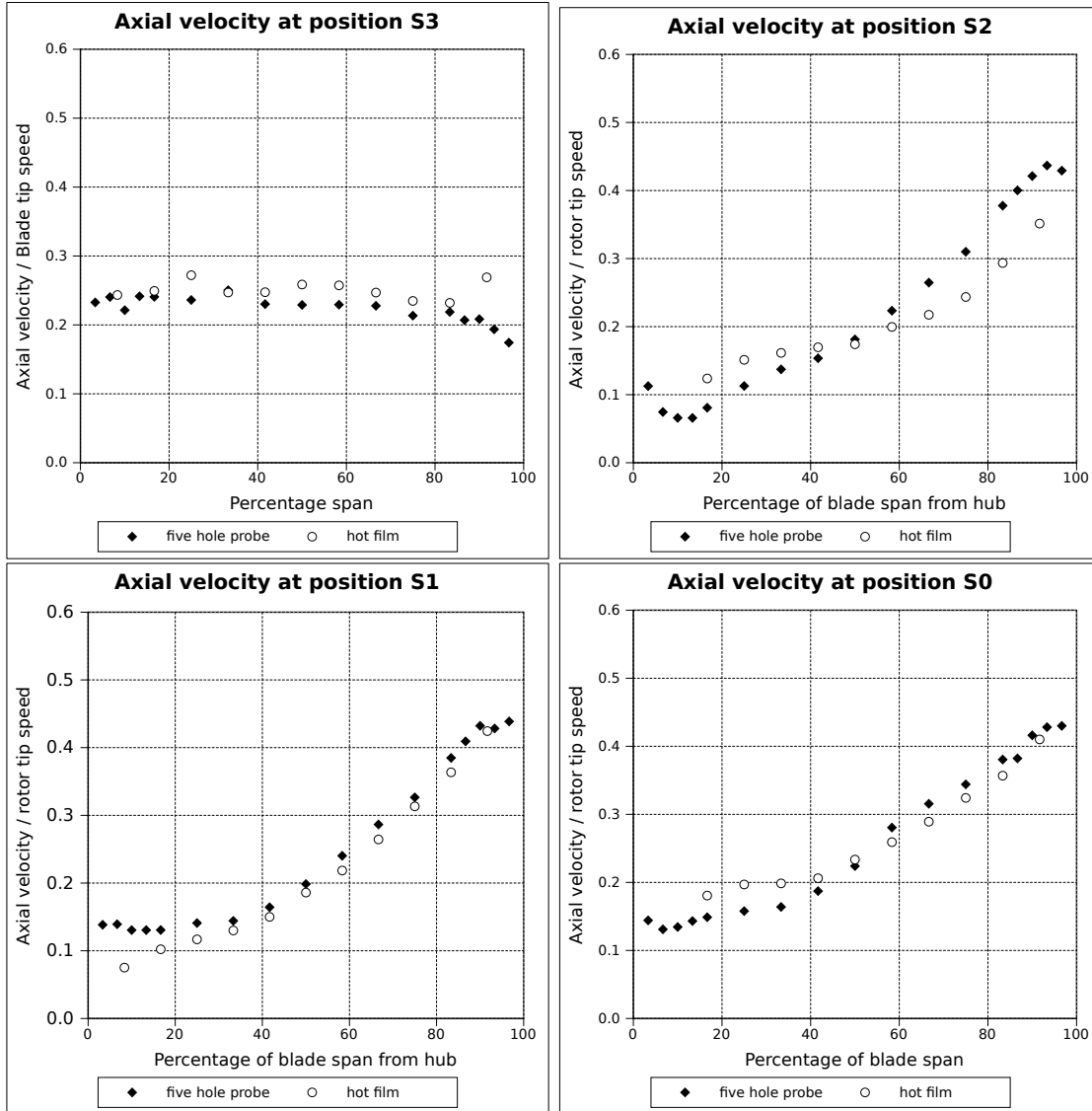


Figure 9.1: Axial velocity components as a function of radius at $\phi = -0.220$

The tangential velocity downstream of the third stage rotor (position S2, figure 9.4) increases in magnitude by 50 % from the minimum magnitude at midspan to the tip. From the hub to midspan, the tangential velocity follows a free vortex distribution. For downstream rotor rows (positions S1 and S0), the free-vortex distribution extends only a third of the span from the hub.

At the largest flow coefficient of -0.369 (figure 9.5), the axial velocity is highest for the 20 % of the span nearest the hub and the casing, and is somewhat lower, and approximately uniform for the central portion of the span. The circumferential velocity (figure 9.6) increases from hub to tip, with a relatively uniform gradient for all rotor blade rows.

Examination of figures 9.2, 9.4 and 9.6 show that for the three flow coefficients investigated, the average tangential velocity downstream of all rotor rows decreases with an increase in the magnitude of the flow coefficient. In other words, for third quadrant operation, the further from the origin of the compressor map the operating point occurs, the smaller the average tangential velocity will be.

Figure 9.7 shows the load coefficient ($U(r)\Delta C_\theta(r)$), which indicates the distribution of

CHAPTER 9. THIRD QUADRANT: NEGATIVE ROTATION

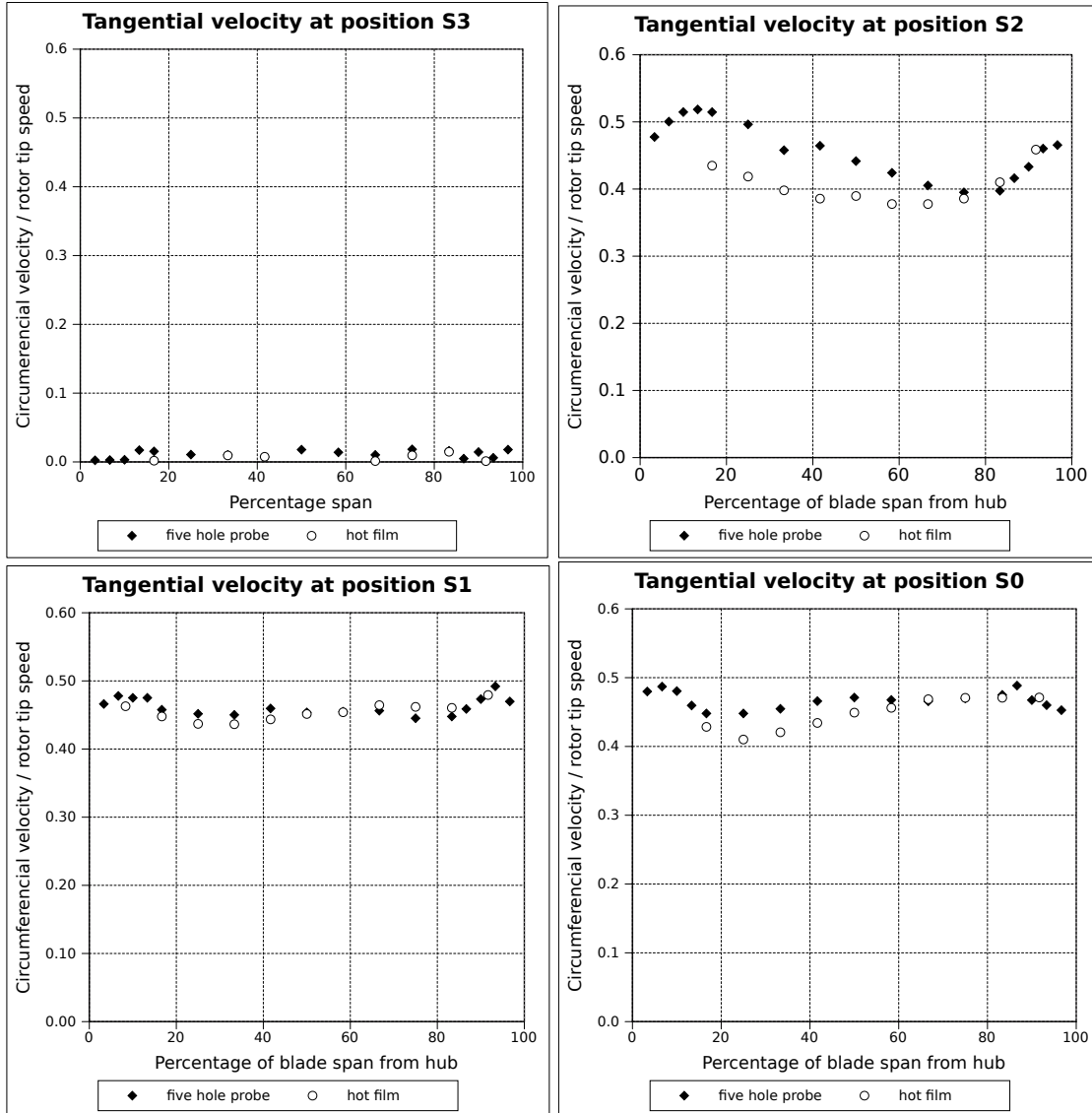


Figure 9.2: Tangential velocity components as a function of radius at $\phi = -0.220$

the work performed on the fluid by the third stage rotor as a function of radius. For a flow coefficient of -0.220 , from 10 to 70 % of the span, the work is approximately uniformly distributed, because the tangential velocity profile conforms closely to a free vortex distribution. From 70 to 100 % the work performed increases, reaching double the midspan value. For a flow coefficient of -0.314 , the work performed on the fluid in the region near the hub is 40 % of the value for a similar radius at a flow coefficient of -0.220 . The value for fluid work near the tip is similar for both flow coefficients, however. At a flow coefficient of -0.369 , the fluid work from the hub to 25 % of the span is negative, indicating that this portion of the rotor is acting as a turbine.

At all flow coefficients investigated, the work input is lower near the hub than the tip. The local blade speed at the hub is 30 % lower than the value at the tip. However, the smallest decrease in work from hub to tip occurs at a flow coefficient of -0.220 , and is 50 %, implying that the linear increase in blade speed cannot alone account for the difference in fluid work between hub and tip. A portion of this must thus be caused by the change

CHAPTER 9. THIRD QUADRANT: NEGATIVE ROTATION

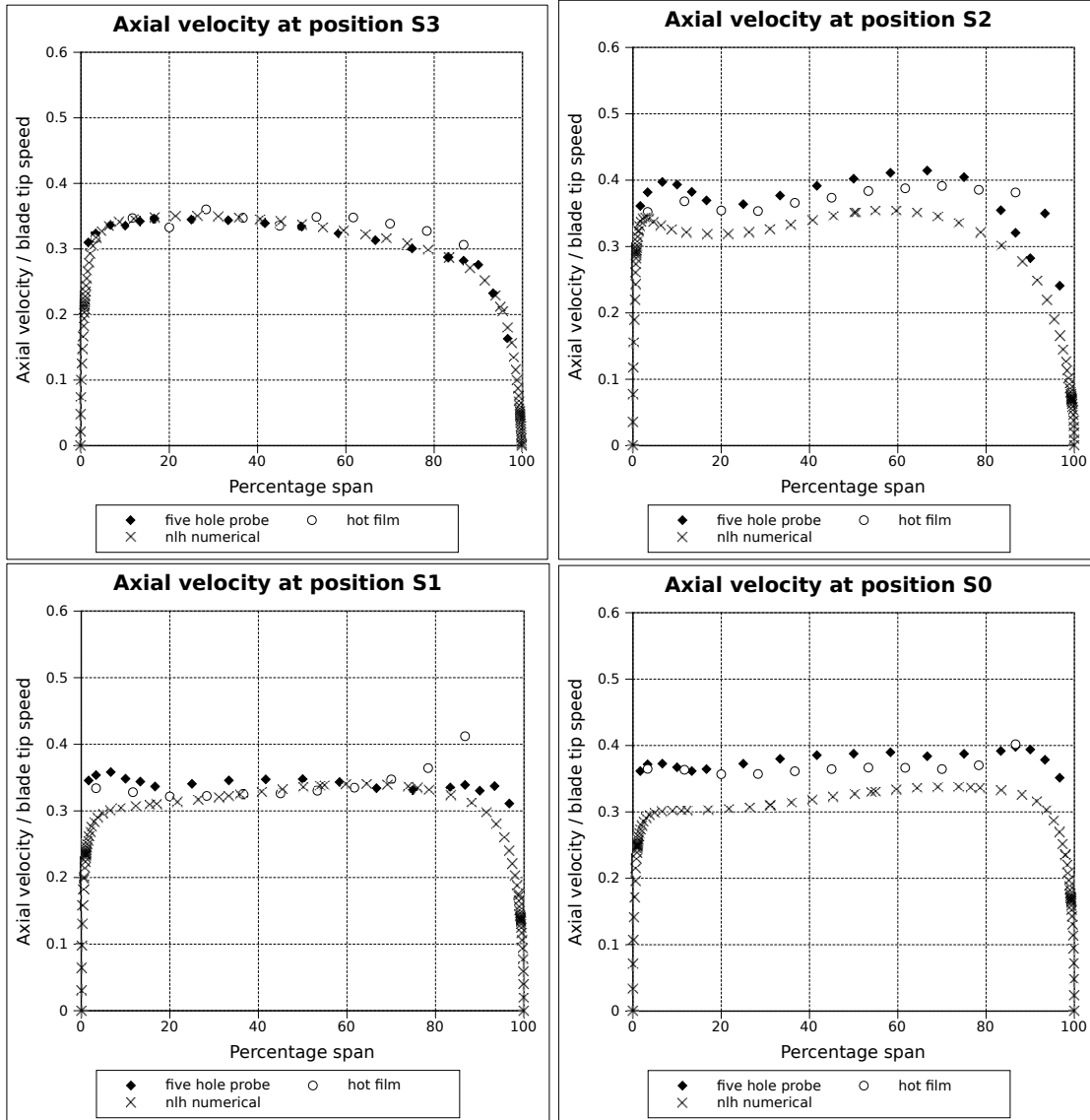


Figure 9.3: Axial velocity components as a function of radius at $\phi = -0.314$

in swirl velocity being smaller near the hub than the tip, implying that less flow turning occurs near the hub than the tip. Relative flow angles upstream of rotor rows are larger than the blade metal trailing edge angles (which function as leading edges for this reversed flow case). Also, transition from third quadrant to second quadrant turbine-like operation begins at the hub. This is the reverse of the situation for the transition from first to fourth quadrant turbine-like operation that have been discussed in chapter 7.

9.2.2 Time dependent results

Time dependent velocity data were obtained by means of a two-sensor hot film x-probe. Figure 9.8 shows the time-traces for axial velocity at midspan, at position S2, downstream of the final stage rotor row. Flow at the lowest flow coefficient can be seen to be highly disordered, with little evidence of any repeating pattern of wakes and jets. This is due to the large degree of separation on the rotor blades at this flow coefficient, which causes the

CHAPTER 9. THIRD QUADRANT: NEGATIVE ROTATION

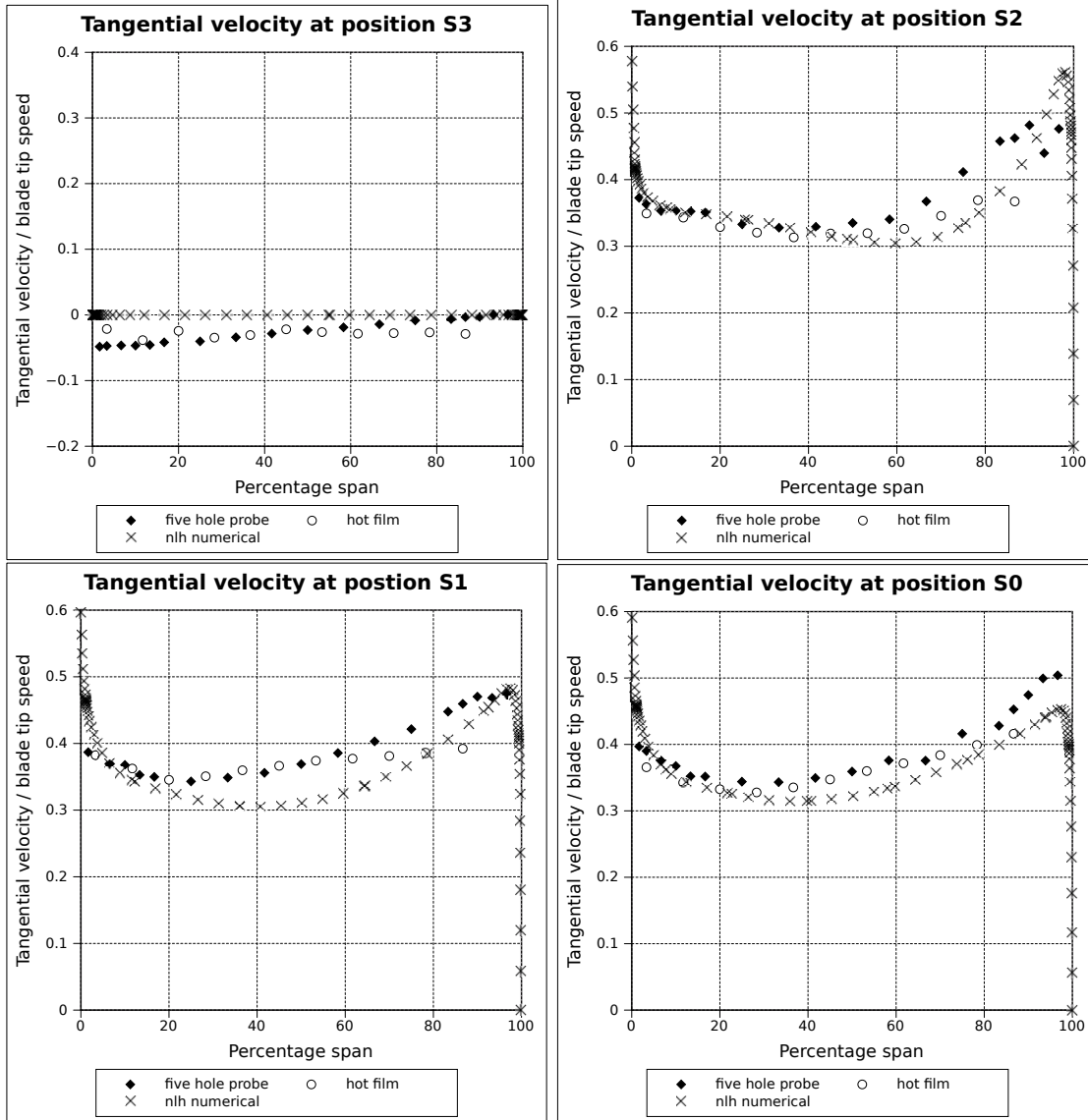


Figure 9.4: Tangential velocity components as a function of radius at $\phi = -0.314$

compressor to operate in a state not unlike severe first-quadrant stalled operation. As the flow coefficient increases, the flow angles become less severely mismatched as operation becomes less like that of a stalled compressor, and closer to second-quadrant turbine-like operation. Consequently, the flow becomes less disordered, and a wake-jet pattern begins to emerge from the chaos, growing stronger with increasing distance of the operating point from the origin of the compressor map.

The time-series data, when shown in the frequency domain, reflect this change clearly. At a flow coefficient of -0.220 (figure 9.9), the frequency domain exhibits a considerable amount of activity at frequencies below the blade passing frequency, in particular at 10 % of the blade passing frequency. The amplitude at this frequency is approximately four times the size of the blade passing frequency at position S2. The blade passing frequency amplitude at S2 is only about 50 % greater than the noise level, making it difficult to resolve accurately. At position S1 the blade passing frequency cannot be resolved with certainty, and the amplitude of the flow phenomenon at one tenth of the blade passing

CHAPTER 9. THIRD QUADRANT: NEGATIVE ROTATION

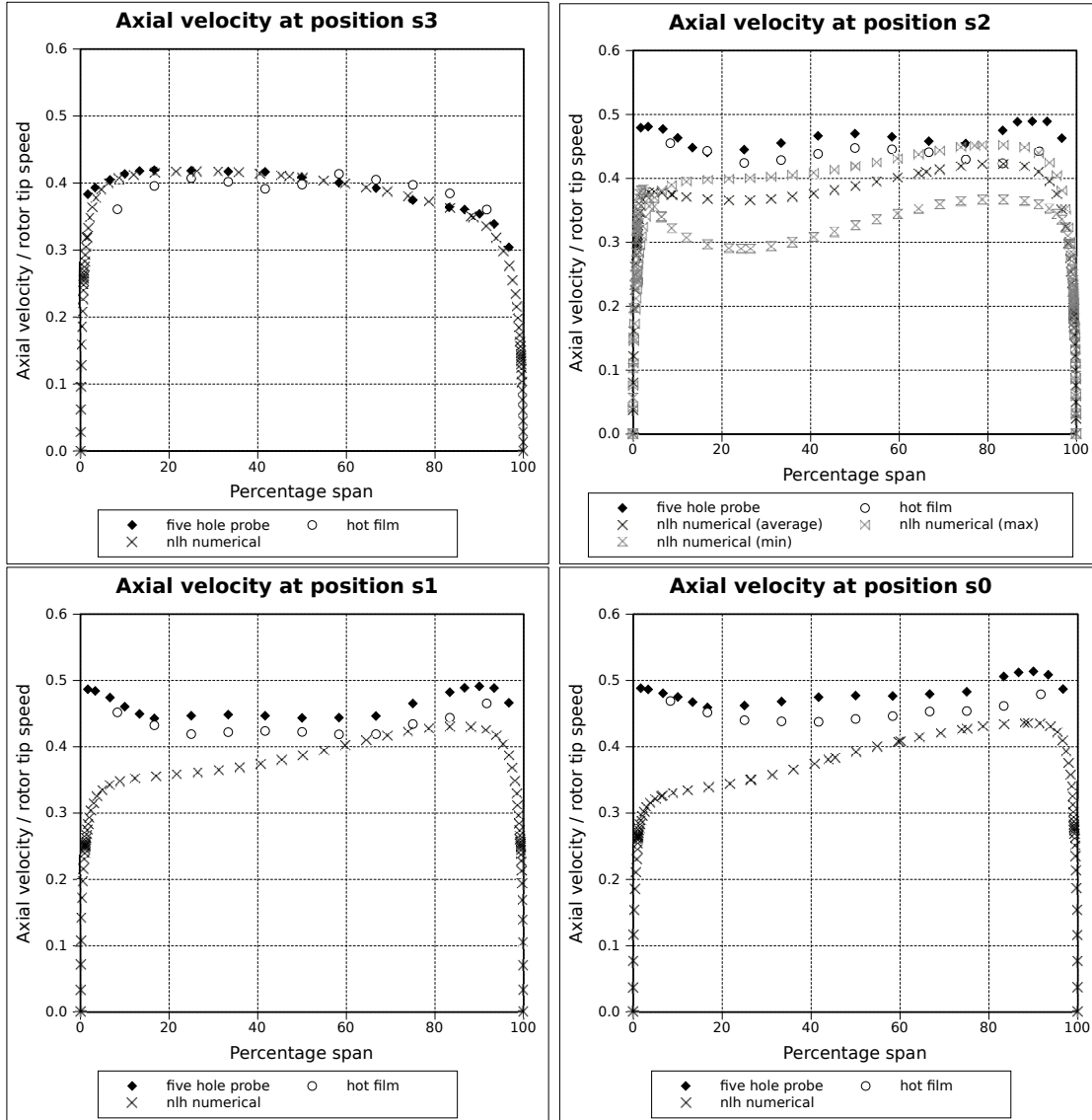


Figure 9.5: Axial velocity components as a function of radius at $\phi = -0.369$

frequency decreases by 27 %. It is possible that the phenomena at 10 % of the blade passing frequency at stations S2 and S1 represent a large rotating stall cell. At position S0 the blade passing frequency amplitude exceeds the noise level by more than 100 %, and the spike at 10 % cannot be readily identified. There are, however, spikes at one quarter and half the blade passing frequency, both indicating amplitudes approximately 150 % that of the blade passing frequency. No harmonics of the blade passing frequency are evident, indicating that the wake-jet pattern is approximately sinusoidal, thus the wakes are approximately half the width of the local blade pitch.

At a flow coefficient of -0.314 (figure 9.10), the blade passing frequency component begins to dominate, although there is still a considerable amount of activity at lower frequencies; particularly at one tenth of the blade passing frequency, as was observed at $\phi = -0.220$. There is also a phenomenon at approximately 240 % the blade passing frequency. This is thought to be related to vortices which originate in the separated region extending from the hub to midspan, and which are shed downstream of the rotor

CHAPTER 9. THIRD QUADRANT: NEGATIVE ROTATION

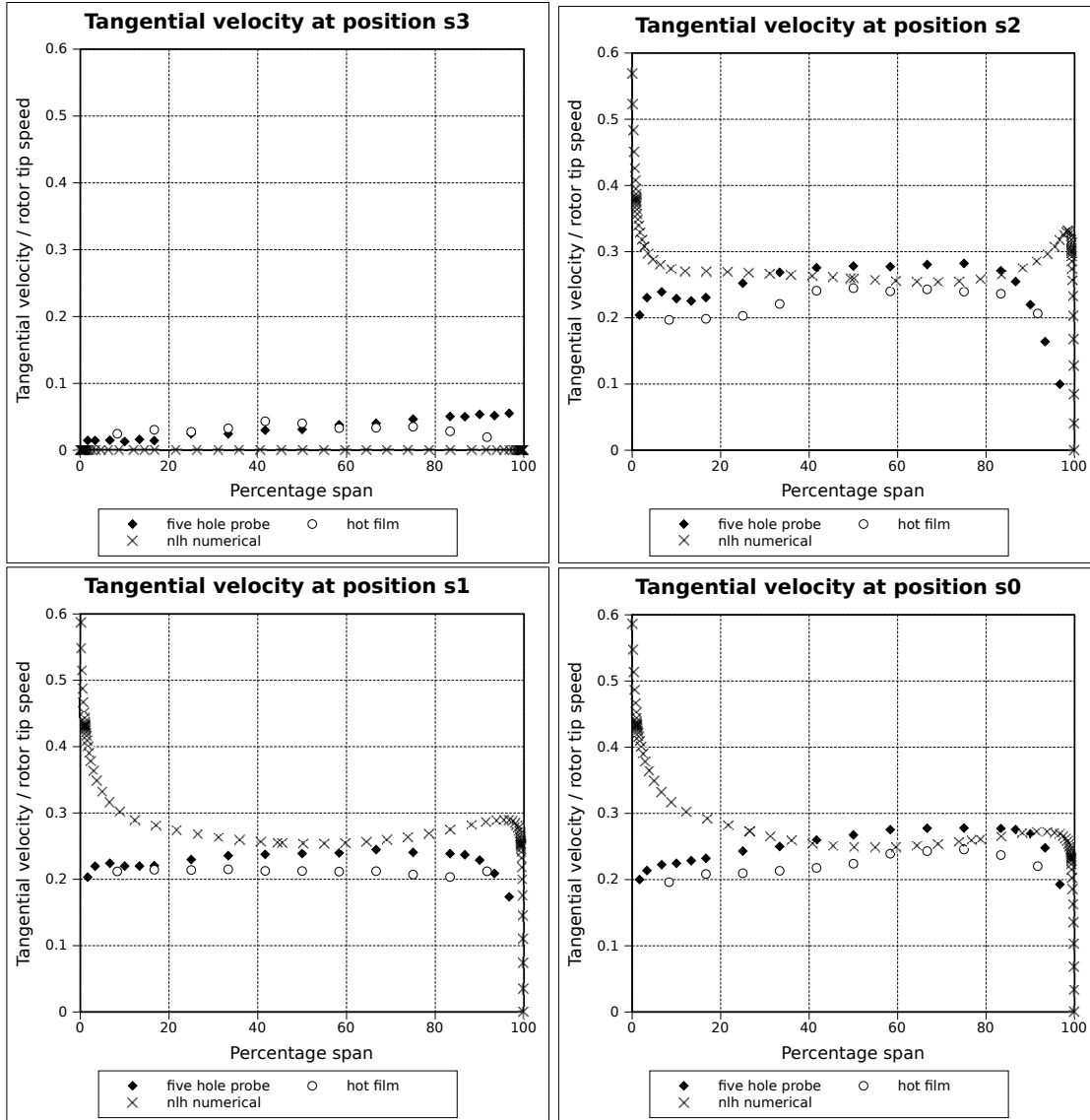


Figure 9.6: Tangential velocity components as a function of radius at $\phi = -0.369$

blades. The vortices will be identified in the numerical results in the next section. The vortices also appear to present at a flow coefficient of -0.369 (figure 9.11). At this last flow coefficient, the second harmonic becomes distinguishable above the background noise (with an amplitude twice that of the noise level) with an amplitude 20 % that of the fundamental at S2 and 25 % of the fundamental at S1. The presence of the second harmonic indicates that the rotor wakes are increasing in sharpness, which suggests that the degree of separation decreases with an increase in flow coefficient.

Figure 9.12 shows a time series of the axial velocity distribution downstream of the first stage stator for a rectangular area corresponding approximately to a single blade passage, for a flow coefficient of -0.220 . The separated region is largest and most pronounced near the shroud; at 20 % of the span the width of the wake is more than 50 % the local blade pitch; in comparison the width is 27 % of the local blade pitch at 80 % of the blade span. Despite the large width of the wake, the velocity in the core of the wake near 20 % of the span (label A) is only 10 % smaller than the mean axial velocity. Cyrus [2004] reported a

CHAPTER 9. THIRD QUADRANT: NEGATIVE ROTATION

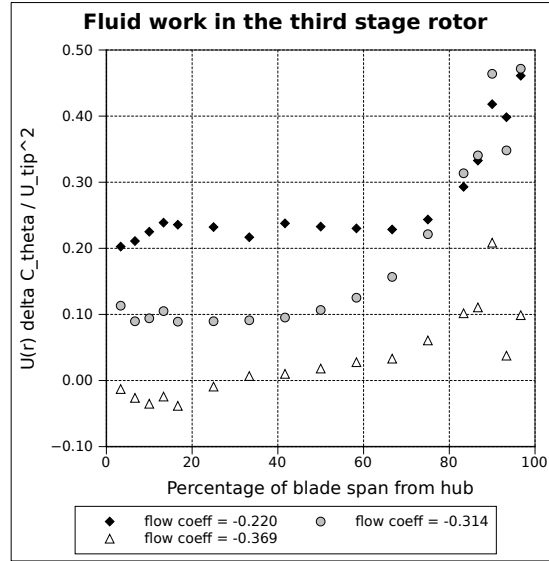


Figure 9.7: Spanwise distribution of work performed on fluid at station S2

slight decrease in the stator loss coefficient from hub to approximately 80 % of full span, beyond which there was a sharp increase in losses near the tip. Assuming that a larger wake equates to a larger loss coefficient, this would appear to agree with the evidence of figure 9.12.

As in rotor rows, most throughflow takes place between midspan and the casing. The maximum axial velocity in the jet is nearly twice the average axial velocity, and occurs at approximately 90 % of span (label B).

Based upon the similarity of velocity distributions downstream of the first and second stage rotor rows (positions S1 and S0) (figures 9.1 and 9.2), it is reasonable to assume that the area downstream of the second stage stator (station R2) exhibits a similar flow structure, in particular a large wake caused by flow separation, at this flow coefficient. Flow downstream of the final stage stator (station R3) will be more ordered and with a much narrower wake, however, due to the lack of any upstream blade rows, and the fact that the trailing edges of the stator, which function as leading edges under reversed flow conditions, are aligned axially.

9.3 Numerical results

Due to the highly separated nature of the flow at a flow coefficient of -0.220, it was not possible to obtain a converged steady-state or time-dependent (non-linear harmonic) numerical solution for this flow coefficient. This is to be expected, as operation at this flow coefficient has been shown to be similar to severely stalled operation in the first quadrant. The difficulties associated with the numerical modelling of compressor operation within the stalled regime, in particular the large computational resources demanded, have already been discussed in chapter 6.

Simulations for flow coefficients of -0.314 and -0.369 (figures 9.3-9.6) yielded reasonable agreement with experimental data, given the separated nature of the flow. Axial velocity varied circumferentially by up to 33 % of the average axial velocity (at 20 % of the span at position S2 for $\phi = -0.369$) due to the separated nature of the flow,

CHAPTER 9. THIRD QUADRANT: NEGATIVE ROTATION

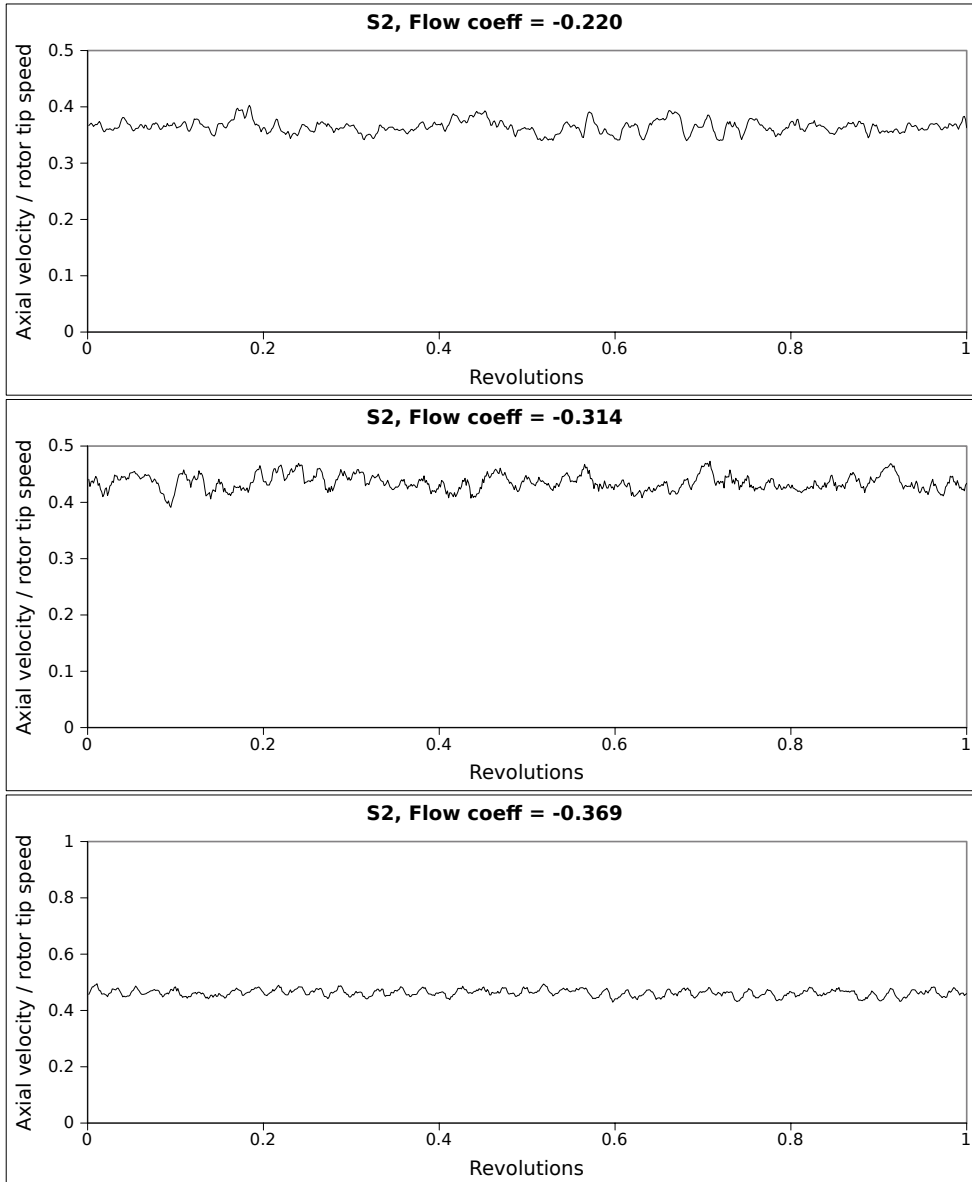


Figure 9.8: Time-traces for axial velocity components at midspan over one revolution

Because experimental data was gathered at one circumferential position, the circumferentially averaged numerical values differed from the experimentally determined values. For this reason, the approximate minimum and maximum numerical values are plotted for position S2 in figure 9.5. From this it is evident that the experimental traverse coincided approximately with the area of maximum velocity between the upstream stator wakes. It will be noted that although the magnitude of the axial velocity component varies by up to 33 % of the average axial velocity across the blade passage, the change in axial velocity from the edge of the hub boundary layer to that of the casing varies by approximately 10 %. This was found to apply for six tangential positions approximately equally spaced within a blade passage at this axial position.

The initial solution assumed was found to be of great importance in obtaining realistic simulation results for third quadrant operation. It was necessary to use the results of the simulation representing the smallest flow coefficient investigated in the second quadrant

CHAPTER 9. THIRD QUADRANT: NEGATIVE ROTATION

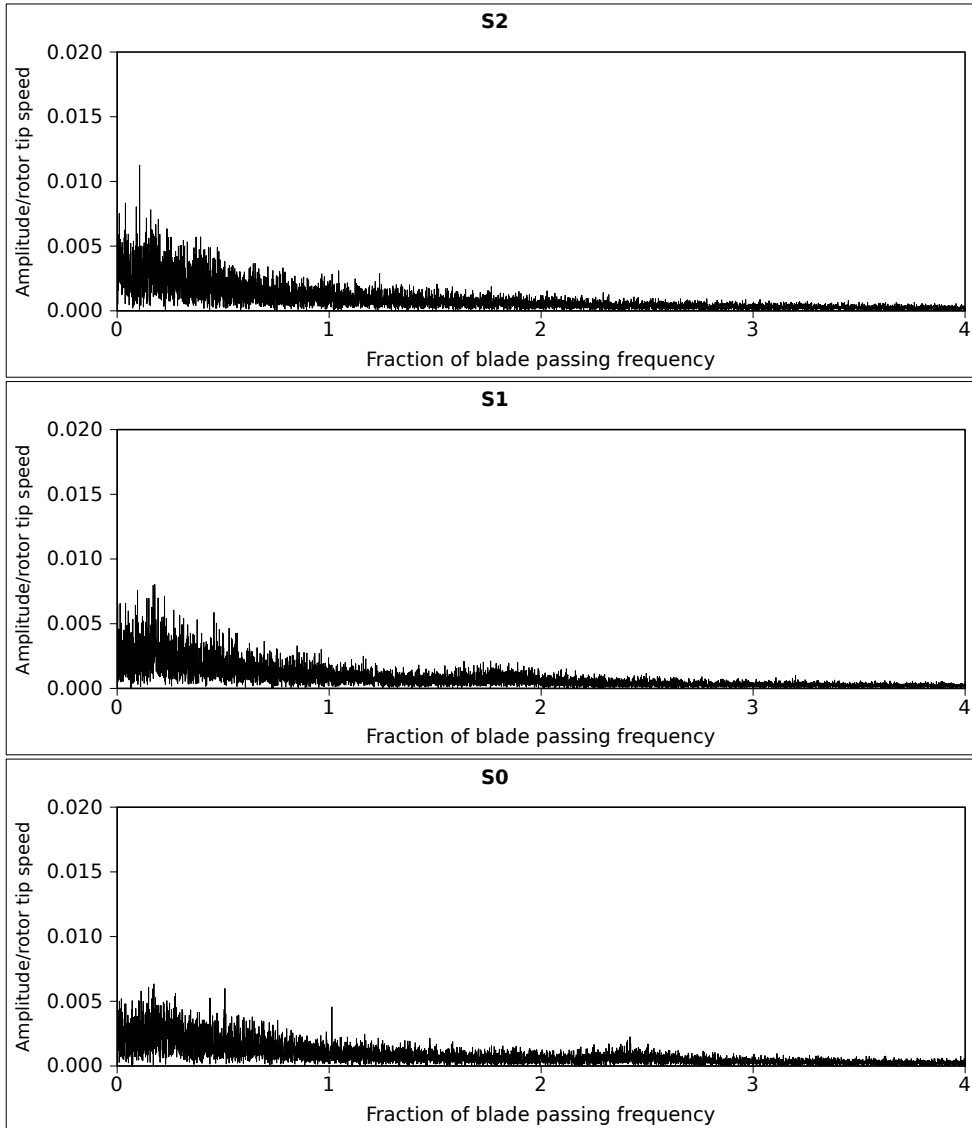


Figure 9.9: Frequency domain of axial velocity component variation at $\phi = -0.220$ at mid-span

for negative rotation ($\phi = -0.482$) to initialise the highest third quadrant flow coefficient ($\phi = -0.369$). The solution of that case could then be used to initialise the simulation of the medium flow coefficient in the third quadrant ($\phi = 0.314$) third quadrant case.

The steady state solutions obtained were highly unrealistic, and have been omitted for this reason. The assumptions implied by the mixing plane approach, specifically that flow is approximately axisymmetric, are clearly severely violated in third quadrant operation due to the large degree of separation on blade surfaces, and the resultant large rotor and stator wakes. The assumption of steady state operation is itself flawed, as flow conditions vary significantly and continuously with time in a cyclical manner due to the movement of the large rotor blade wakes. Finally, the sensitivity of the simulations to the initial condition has already been noted, and no steady state solutions which might serve this purpose were obtained for second quadrant turbine-like operation, as will be explained in chapter 10).

Figure 9.13 shows the entropy distribution at midspan, normalised relative to conditions at the compressor outlet (where flow enters the machine in this mode of operation). In this

CHAPTER 9. THIRD QUADRANT: NEGATIVE ROTATION

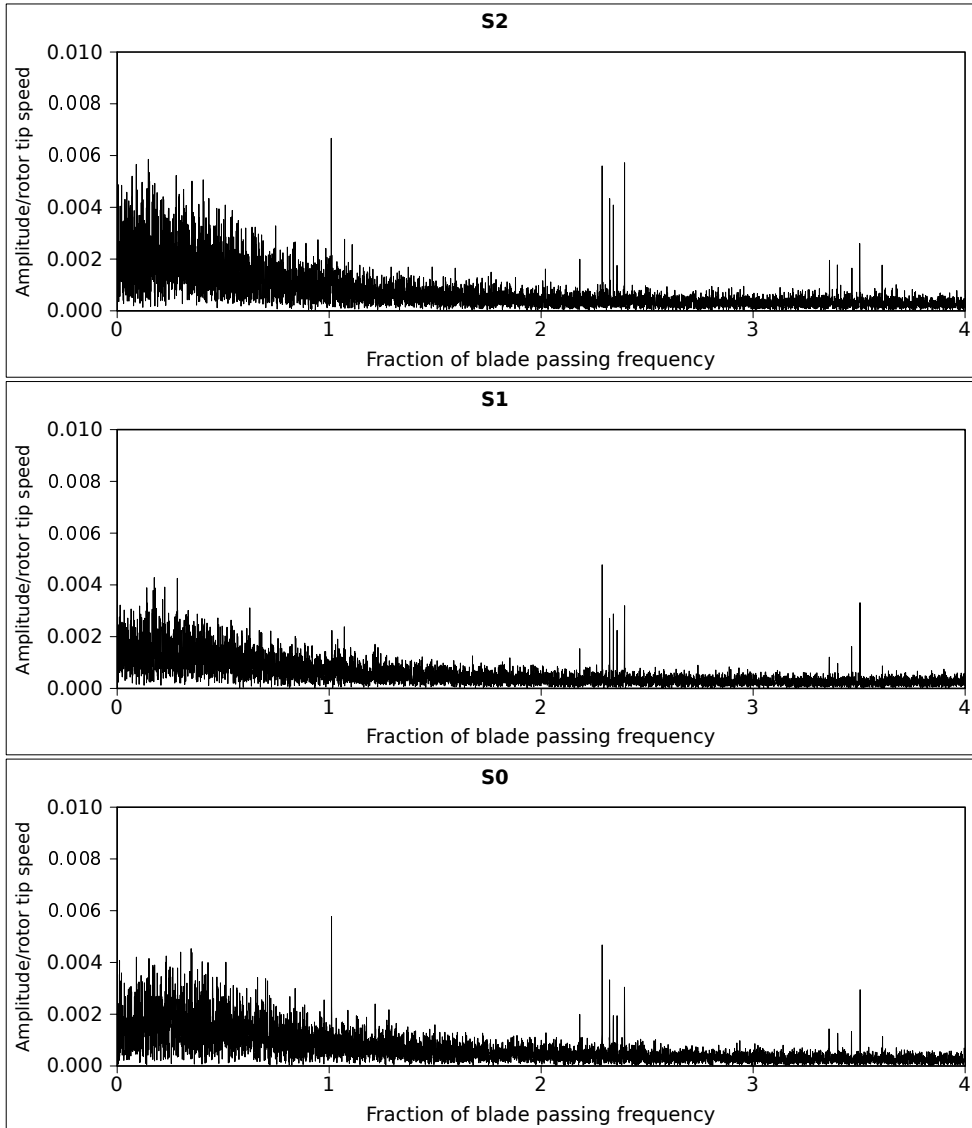


Figure 9.10: Frequency domain of axial velocity component variation at $\phi = -0.314$ at mid-span

and all subsequent figures, the flow direction is from the left to the right, and the blade trailing edges are upstream of the leading edges.

The flow field is dominated by areas of separation on the pressure (concave) surfaces of both rotor and stator blades. There is no separation on the final stage stator (the first blade row to affect the flow entering the machine), as the trailing edge is aligned with the axial direction, and thus this blade row merely turns the flow. At the leading edges of second and first stage stators (which function as trailing edges under reverse flow conditions), however, the separated area is approximately 50 % of the local blade pitch; much larger than the 10 % occurring on second and first stage rotor blades. The separated regions on stator blades decrease by approximately 10 % from the outlet to the inlet.

The flow fields surrounding individual blades will now be examined in more detail. Figure 9.14 shows the flow field surrounding the first and third stage stators at a flow coefficient of -0.314. The difference between the final stage (subfigure (a)) and the second stage (subfigure (b)) is dramatic. The first stage stator is omitted for the sake of brevity; it is very similar to that of subfigure (b). The size and shape of the separated region does not

CHAPTER 9. THIRD QUADRANT: NEGATIVE ROTATION

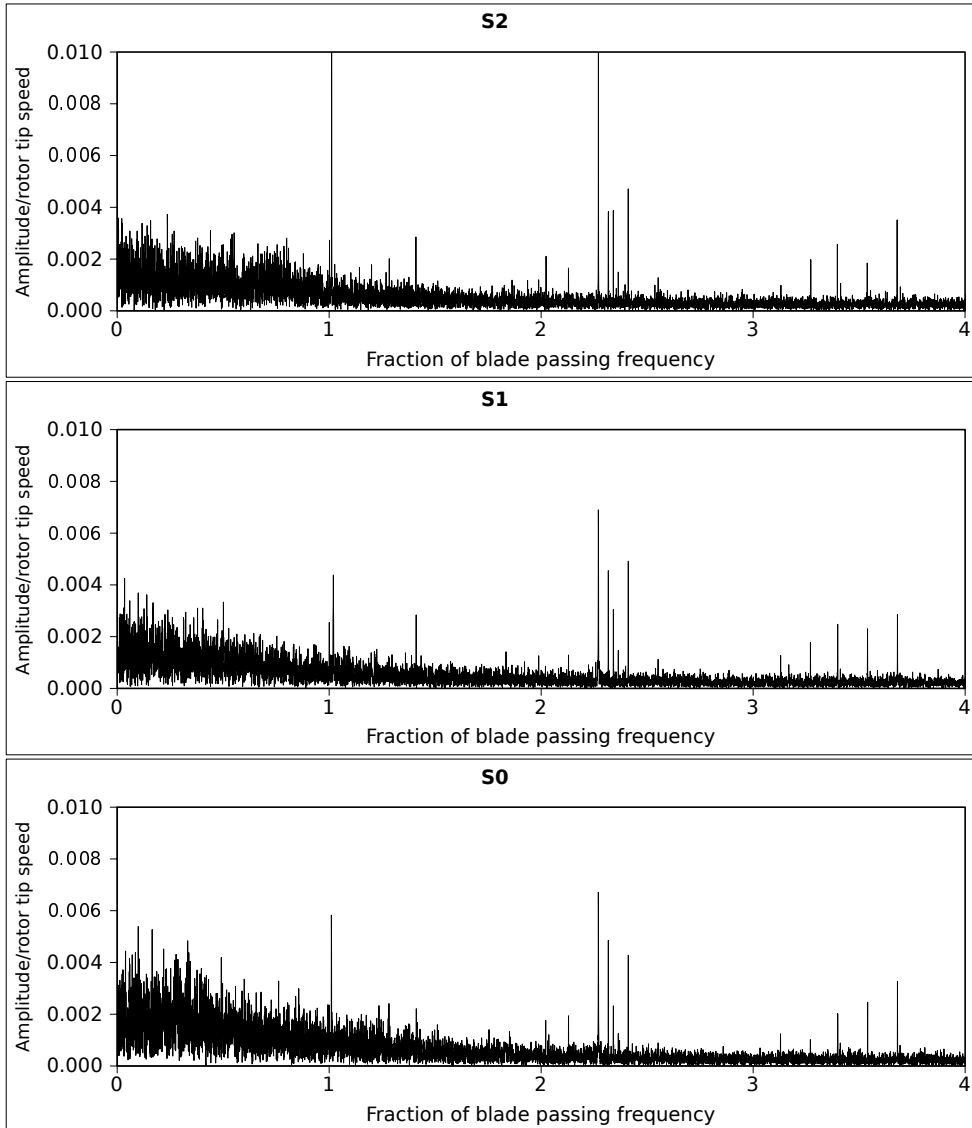


Figure 9.11: Frequency domain of axial velocity component variation at $\phi = -0.369$ at mid-span

vary significantly with span. This was also suggested by the area traverse results (figure 9.12, as the width of the wake varies very little in the spanwise direction. The size of the separated areas attached to the pressure surfaces of the stator blades is also not strongly affected by varying the flow coefficient.

Figure 9.15 shows the flow field surrounding the third stage (subfigure (a)) and first stage (subfigure (b)) rotors at midspan, for a flow coefficient of -0.314. Unusually, the flow field surrounding the first stage rotor is less disordered than that surrounding the third stage rotor, despite the former being downstream of several more blade rows (the flow fields surrounding which are severely separated) than the latter. It would thus appear that the flow angle downstream of the third stage stator is more poorly matched to the blade angles of the third stage rotor. A separation bubble approximately 20 % of the blade pitch in width can be seen on the suction surface near the trailing edge of the third stage rotor in subfigure (a), while there is no evidence of separation in subfigure (b).

The flow field surrounding the rotors was also found to vary with radius. Figure 9.16 shows the streamlines surrounding the rotor at on transparent planes in the hub, tip and

CHAPTER 9. THIRD QUADRANT: NEGATIVE ROTATION

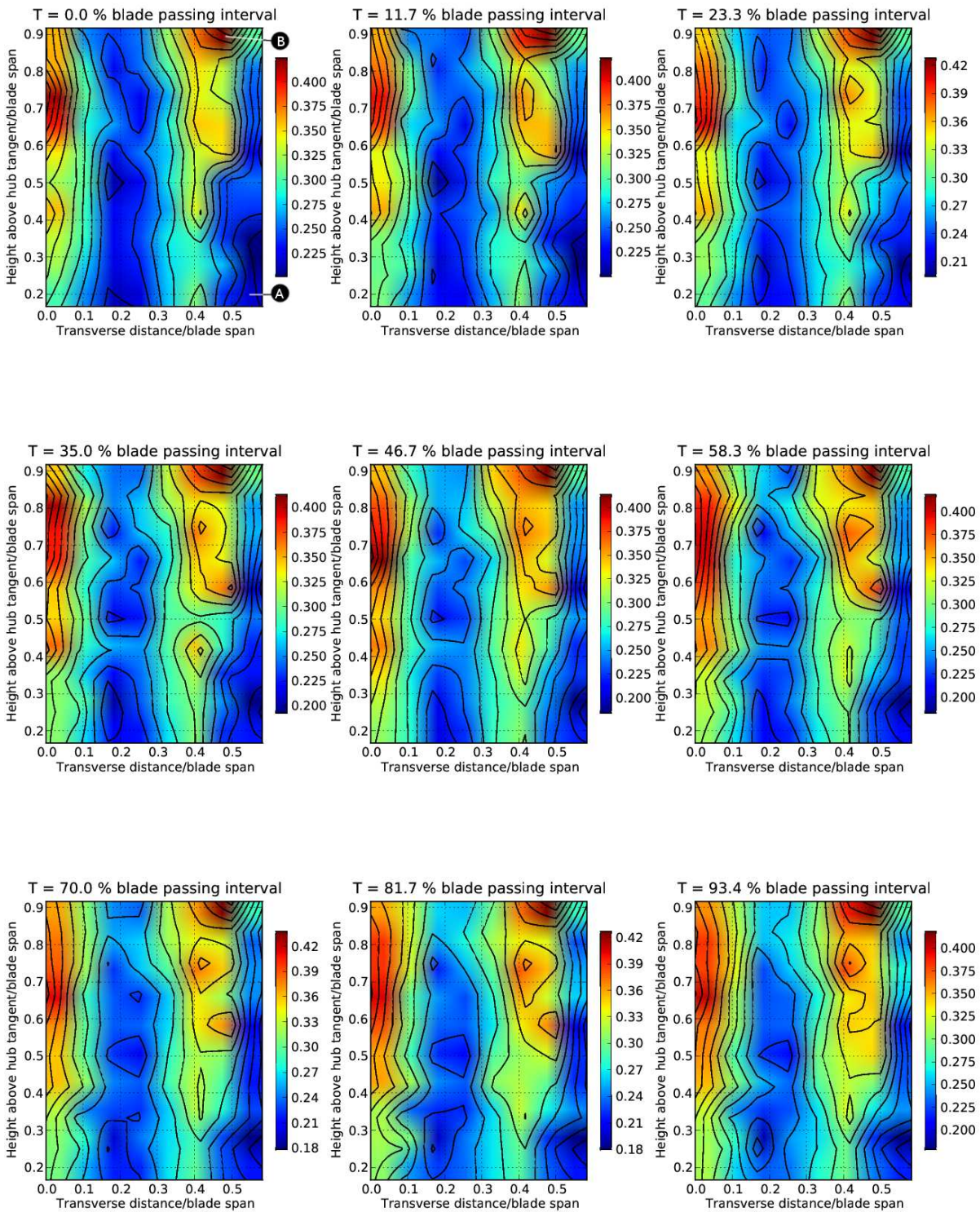


Figure 9.12: Time series of axial velocity contours at position R1 at $\phi = -0.220$

CHAPTER 9. THIRD QUADRANT: NEGATIVE ROTATION

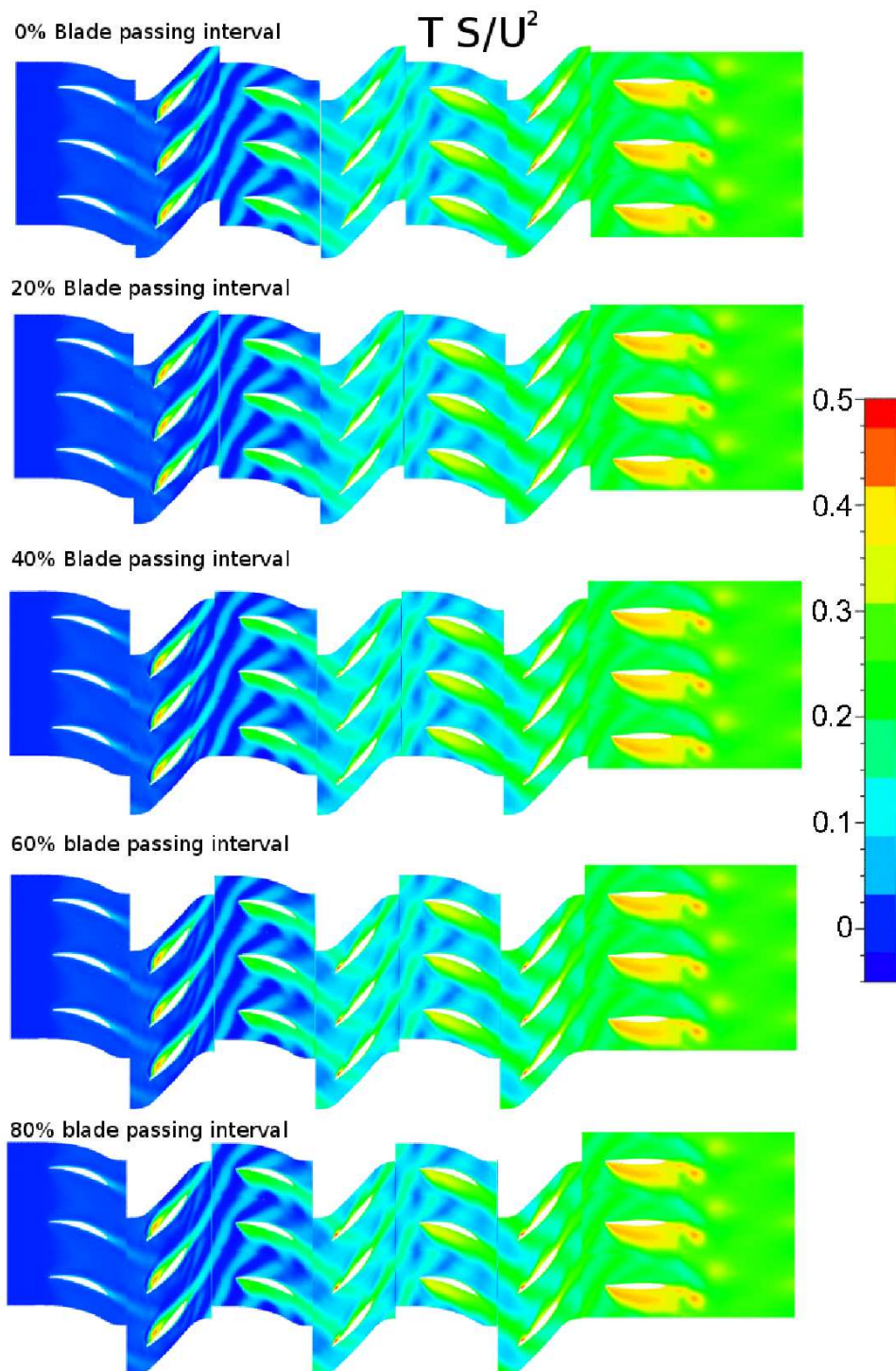


Figure 9.13: Time-series entropy distribution, normalised relative to inlet, on constant radius surface at midspan; $\phi = -0.314$

CHAPTER 9. THIRD QUADRANT: NEGATIVE ROTATION

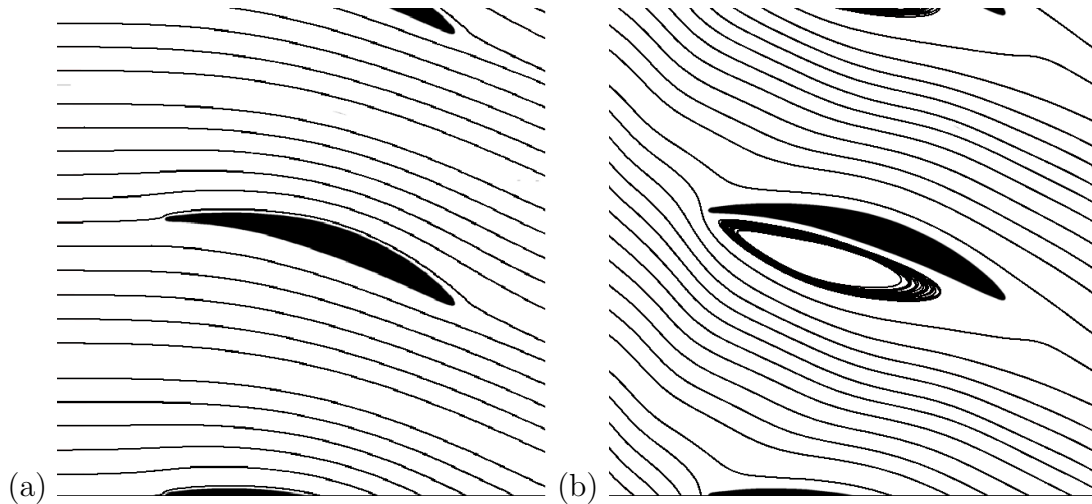


Figure 9.14: Streamlines surrounding stators: (a) third and (b) second stage at 50 % of blade span, $\phi = -0.314$

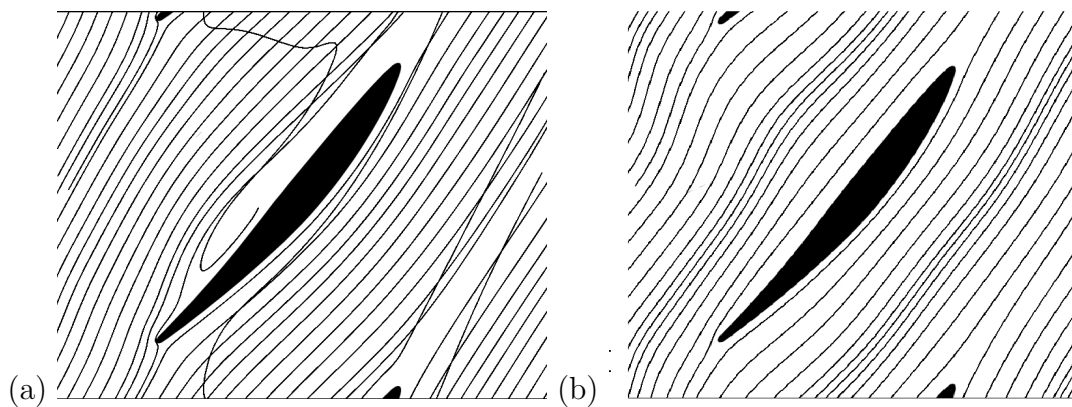


Figure 9.15: Relative velocity streamlines surrounding rotors: (a) third and (b) first stage at 50 % of blade span, $\phi = -0.314$

midspan regions for flow coefficients of -0.314 and -0.369. It will be noted that separation for both flow coefficients is worst near the hub. The presence of crossing streamlines in subfigures (a) and (b) indicate that flow in these regions has a radial component. This appears to be caused by the vortex in the region of separated flow propagating downstream as it moves tipward. These vortices may be the cause of the cyclic disturbance at approximately 225 % of the blade passing frequency that was detected by hot film measurements. The apparent crossing of streamlines in figures (e) and (f) appears to be evidence of a tip-vortex.

Separation is more severe at a flow coefficient of -0.314 than at a flow coefficient of -0.369, and would appear to be worse still at flow coefficients closer to zero, based on the experimental investigation and the non-convergence of the attempted simulation of operation at a flow coefficient of -0.220.

Figure 9.17 shows the radial velocity distribution at midspan for a flow coefficient of -0.314. Although significant radial velocity components were found in the areas of separated flow on pressure surfaces of rotors and stators near the hub, these were weak or absent

CHAPTER 9. THIRD QUADRANT: NEGATIVE ROTATION

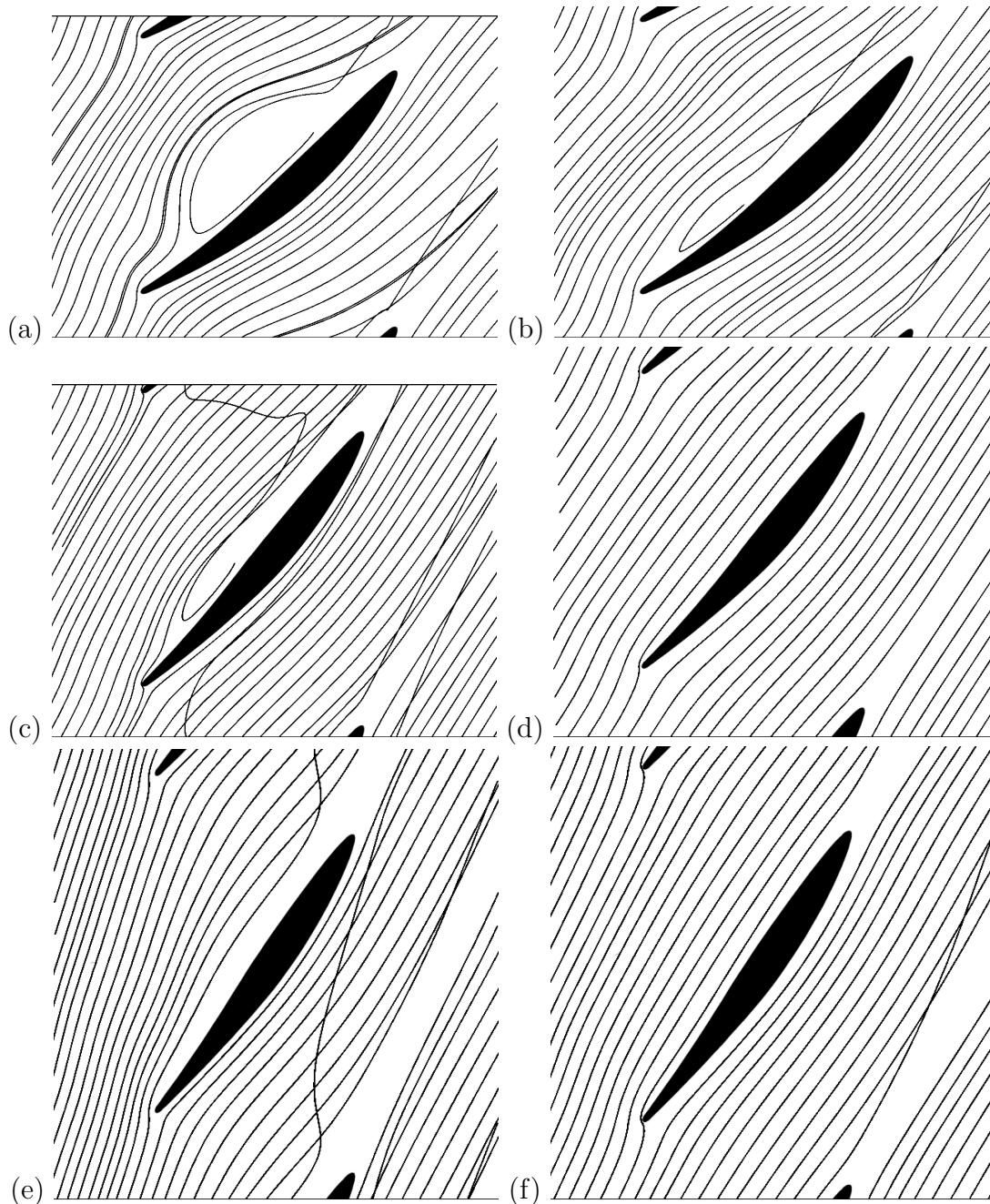


Figure 9.16: Relative velocity streamlines surrounding the third stage rotor blade at: (a) 10 % span, $\phi = -314$ (b) 10 % span, $\phi = -0.369$, (c) 50 % span, $\phi = -314$ (d) 50 % span, $\phi = -0.369$, (e) 90 % span, $\phi = -314$ (f) 90 % span, $\phi = -0.369$

CHAPTER 9. THIRD QUADRANT: NEGATIVE ROTATION

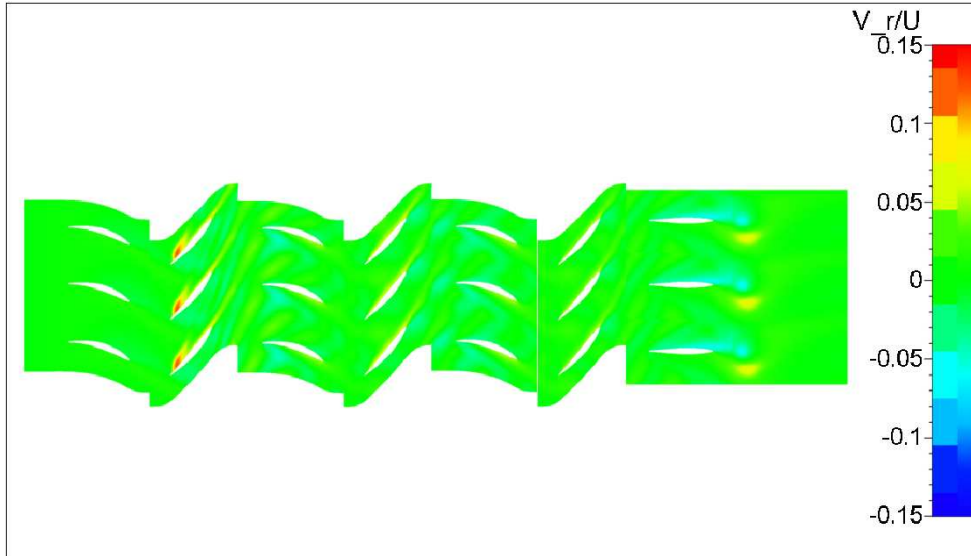


Figure 9.17: Radial velocity distribution on constant radius surface at midspan at $\phi = -0.314$

at midspan, with the exception of a region of high tipward velocity (approximately 15 % of the rotor tip speed, or 49 % of the average absolute flow velocity at station S3), which occurred in the separated region near the trailing edge of the third stage rotor. This was the rotor row for which separation was most severe, and no downstream rotor rows showed any significant separation at midspan. As the tipward flow coincides with the centre of the recirculation zone on the rotor pressure (concave) surface, it may be due to centrifugal acceleration of the low relative-velocity fluid in the recirculation zone, which has a high rotational speed in the absolute frame of reference.

The wakes of downstream blade rows show smaller radial velocity components. These take the form of areas of hubward flows and tipward flows following the wake, alternating in the spanwise direction downstream of the second and third stage rotor rows. The magnitudes of both hubward and tipward flows downstream of the third stage stator are equal at approximately 16 % of the average velocity at station S3. This suggests that these alternating patterns are further evidence of the vortex shed downstream of the blade at midspan, which was detected in hot film measurements and described earlier. There is also evidence of larger areas of hubward low speed radial flow in the separated areas on the suction surfaces of stator rows.

The circumferentially averaged flow field at the same flow coefficient, shown in figure 9.18, shows small undulations in the streamlines nearest the hub, though streamlines near midspan are nearly straight and parallel with one another. This indicates that there are small radial flows in these regions. Flow in the second and first stage stator has a tipward radial component, particularly near the hub.

9.4 Discussion

In order to understand third quadrant operation, a distinction must be drawn between operating points close to the zero flow line, or y-axis of the compressor map ($\phi = -0.220$ represents such a case), and those close to the zero pressure rise line, or x-axis ($\phi = -0.314$ and $\phi = -0.369$). The former has been shown to be analogous to first quadrant stalled

CHAPTER 9. THIRD QUADRANT: NEGATIVE ROTATION

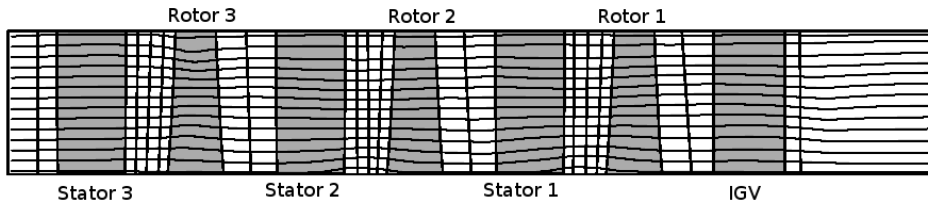


Figure 9.18: Meridional view of the test compressor showing circumferentially averaged flow paths and areas of separation and recirculation on the hub and shroud at $\phi = -0.314$

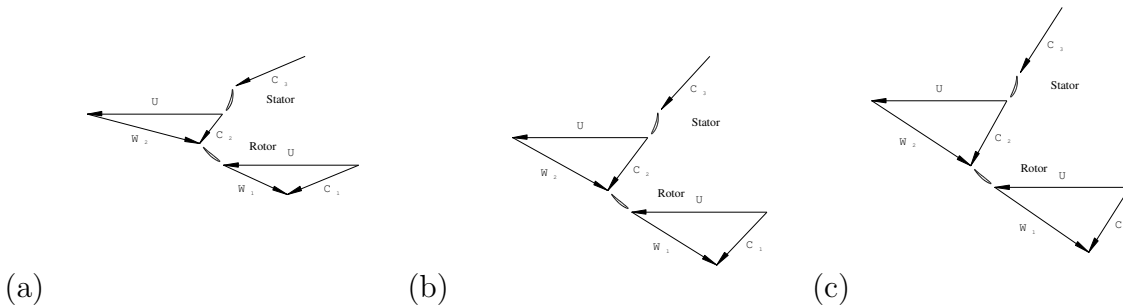


Figure 9.19: Velocity triangles for first stage (stations S1 - S0) at 50 % of blade span: (a) $\phi = -0.220$ (b) $\phi = -0.314$ (c) $\phi = -0.369$

operation. The latter resembles a stalled compressor near the tip, while near the hub, flow conditions resemble those in second quadrant turbine operation, described in the next chapter.

In the former case, flow separation is most severe near the hub in both rotor and stator rows, as therefore axial velocity components are highest near the casing. In addition, in rotor rows, work input to the fluid in rotor rows is highest near the tip at all flow coefficients, thus axial velocities in the tip region downstream of rotor rows are still higher.

In the latter case, the directions of the forces acting on the blade for the compressor-like region near the tip will differ from those in the turbine like region near the hub. Although structural analysis is beyond the scope of this work, the unusual nature of the resultant moment acting on the blade may have serious repercussions in terms of the safety of third quadrant operation, particularly in conjunction with the cyclic nature of blade loading under such conditions with the associated dangers of fatigue failure, particularly in compressors operating at higher speeds and pressure ratios than the test compressor.

Velocity triangles at midspan are shown for the three flow coefficients in figure 9.19. The diagram of the smallest coefficient (subfigure (a)) is based on experimental data, while those for the larger negative flow coefficients (subfigures (b) and (c)) are derived from numerical data. The severe separation on rotor and stator blades at a flow coefficient of -0.220 can be seen to be the result of the very poor match between the flow angles and blade trailing edge metal angles. As the flow coefficient increases, the mismatch between blade metal angles and flow angles becomes less severe.

It will be remembered that blockage of stator blade passages was most severe near the hub, where the wake extended across half the local blade pitch, while high flow velocities occurred in a jet from hub to midspan, while both the fraction of the blade passage blocked

CHAPTER 9. THIRD QUADRANT: NEGATIVE ROTATION

by the recirculating flow in the separated region and the size of the recirculation zone decreased near the tip. Flow entering the stator blade passages must thus move tipward in the blade passage in order to avoid the separated region. In contrast, separation on rotors occurs near the casing at the trailing edge (which functions as the leading edge in reversed flow), and diminishes along the blade chord. Flow leaving the stator flows over the recirculation zone on entering the rotor, then flows hubward as this decreases along the rotor chord.

9.5 Summary

The flow field within the test compressor during third quadrant operation has been investigated. The spanwise distributions of the axial and tangential velocity components downstream of rotor rows vary significantly with the flow coefficient. At a flow coefficient of -0.220, there is a 400 % increase in axial velocity from hub to tip, as blockage due to flow separation is largest near the tip, but is present across the entire blade span. At larger negative flow coefficients, the axial velocity profile becomes more uniform, although the degree of blockage remains higher near the hub than the casing. Axial jets form near the hub. The axial velocity varies by up to 33 % circumferentially downstream of rotor rows, due to the wakes of upstream stator rows. The average tangential velocity decreases as the magnitude of the flow coefficient increases. There is considerably more variation in the tangential velocity profile than that of the axial velocity downstream of the final stage rotor and the second and first stage rotors, which are downstream of the former due to the reversed flow direction. This is due to the lack of separation on the final stage stator.

Radial velocity components up to 49 % of the velocity magnitude at S3 occur in the regions of separated flow in blade passages, particularly near the hub. The circumferential average of radial velocity between rotor and stator rows is close to zero, however, although areas of radial flow of alternating sign occur in and between blade wakes.

Separation occurs on the pressure surface of all blade rows, and is most severe on stators and at small flow coefficients. Blade wakes are large and may occupy half the width of a blade passage due to the large separated areas of flow. The size of the separated areas on stators does not vary significantly with span. The size of the separated regions on rotors, and thus their wakes, vary significantly with span, and are most severe near the hub, occupying up to 50 % of the blade passage at half-chord at a flow coefficient of -0.314, and least severe near the tip, where it is negligible. Vortices appear to be shed from the regions of separated flow on the pressure surfaces of rotor blades from the hub to approximately midspan at a flow coefficients of -0.314 and -0.369. At these flow coefficients, separation is most severe on the final stage rotor.

The wake-jet pattern is approximately sinusoidal at small negative flow coefficients, but the wakes become thinner and sharper at larger negative flow coefficients, as separation on blades becomes less severe. Operation at small negative flow coefficients resembles severe first quadrant stall, and numerical simulation of this operational point was unsuccessful.

Chapter 10

Second quadrant: negative rotation

10.1 Introduction

This chapter describes the flow structures observed under second quadrant operating conditions, for reverse rotation. In this mode of operation, the compressor acts as a turbine, rotating in the reverse of the design direction, and with flow through the machine reversed, and consequently with a pressure drop from the design outlet of the machine to the inlet. Operation at three flow coefficients was investigated, namely -0.482, -0.553 and -0.843, based on the turbine anemometer measurements. Due to the limitations of the auxiliary fans, the compressor rotational speed was reduced to 75 %, 65 % and 40 % of design speed respectively.

In this chapter, as in the second quadrant mode discussed in chapter 8 and third quadrant operation as discussed in chapter 9, a positive axial velocity implies that the velocity has the same direction as the mean flow through the machine, i.e. it is reversed from the normal direction. In the same way, the tangential velocity is defined as positive when swirl occurs in the opposite direction to the movement of the rotor blades under design conditions.

10.2 Experimental results

10.2.1 Time-averaged velocity profiles

Time averaged velocity profiles were obtained by means of a five-hole probe and by time-averaging of hot-film probe velocity measurements. Velocity distributions as a function of radius were obtained at the compressor outlet and downstream of each rotor row (measurement stations S3, S2, S1 and S0 in figure 3.1). These are shown in figures 10.1-10.6.

Radial velocity components as measured by means of the five-hole probe and the inclined hot film sensor were less than 10 % of the absolute velocity magnitude for all of the flow coefficients investigated.

A circumferential velocity component was observed at the machine outlet (station S3), where the flow entered the compressor in this mode of operation. At a flow coefficient of -0.482 (figure 10.2), it was 20 % of the average axial velocity component; while at a flow coefficient of -0.553 (figure 10.4) it had risen to 30 % and at a flow coefficient of -0.843 (figure 10.6) it had increased further to 35 % of the average axial velocity. This represented a flow angle varying between 11.6° and 17.1° . This swirl component was not observed in other reverse flow operational modes. The direction of this velocity component is opposite

CHAPTER 10. SECOND QUADRANT: NEGATIVE ROTATION

that of the swirl components determined at stations S2, S1 and S0 under the same operating conditions. This occurred despite flow straighteners installed approximately 10 chord lengths upstream of station S3, and was demonstrated to be repeatable in presence and magnitude. The swirl component increases with auxiliary fan speed (and thus flow rate). Although this phenomenon may appear to be related to the flow conditions observed at S3 for second quadrant, positive rotation operation (chapter 8, this is unlikely to be the case for three reasons. Firstly, the velocity magnitude and flow angle measurements for this mode of operation were demonstrated to be repeatable for all flow coefficients investigated, which was not the case in chapter 8. Secondly, the five hole probe and hot film measurements agree closely for all cases in this mode, which again was not the case for second quadrant operation for positive rotation. Thirdly, hot film measurements indicated relatively steady flow, which also differs markedly from measurements at this location in the other mode. Turbulence intensity in this region was of the order of 1.7 %. These three facts also appear to indicate that the swirl component is a real phenomenon rather than an erroneous measurement. The possibility that the swirl component is induced by separation in the Venturi meter may be dismissed for the reasons already proposed in chapter 8. In addition, the length to diameter ratio of the passages within the honeycomb flow straighteners is approximately 7.3, which is too large and the cell diameters are too small to allow a swirl component of this magnitude from the auxiliary fan to enter the compressor.

The most probable explanation for the swirl at S3 in this mode of operation is as follows. It will be recalled that there are six struts immediately downstream of S3, which support the rotor drive shaft bearing at the compressor exit. The struts are each approximately two stator pitches from the measuring ports on either side. Examination of the struts showed that the strut closest to the measuring port used for this investigation showed a small angular misalignment relative to the machine axis. The row of measuring ports on the other side of the machine were used for the third quadrant operation, because these ports were better placed between stator wakes under that operating condition. The strut nearest the this other S3 port is more accurately aligned with the machine axis, therefore third quadrant measurements did not show a swirl velocity component.

At flow coefficients of -0.482 and -0.553 the discrepancy between numerically integrated volume flow rate at station S3 (where the flow entered the machine) and that measured by the turbine anemometer was approximately 8 %. The volume flow rate at a coefficient of -0.843 as determined from the turbine anemometer was 15 % lower than that obtained by integrating the velocity profile at station S3. Because the axial velocity profile was used as an inlet boundary condition, this resulted in a discrepancy of 15 % between flow coefficients based on turbine anemometer measurements and those based on area-weighted average axial velocity at station S3 (the outlet under design conditions). These discrepancies and the swirl component at station S3 suggest that some flow distortion occurred in the duct between the auxiliary fan and the compressor outlet. For this reason, the flow coefficients used here are those based upon area-weighted average axial velocity at station S3.

The axial velocity profiles downstream of the rotor rows at a flow coefficient of -0.482 (figure 10.1) are nearly uniform. Near the rotor tips the axial velocities are 8 % higher than at midspan. The velocities near the hub are also somewhat higher than that observed at midspan at stations S1 and S0, although examination of numerical results suggests that this is a non-axisymmetric effect caused by a strong wake-jet pattern near the hub, where the curvature of upstream stator blades is least well aligned with the flow. The boundary layers at hub and casing occupy less than 10 % of the blade span each, and are thus smaller than those observed during first quadrant operation near design point. This is probably

CHAPTER 10. SECOND QUADRANT: NEGATIVE ROTATION

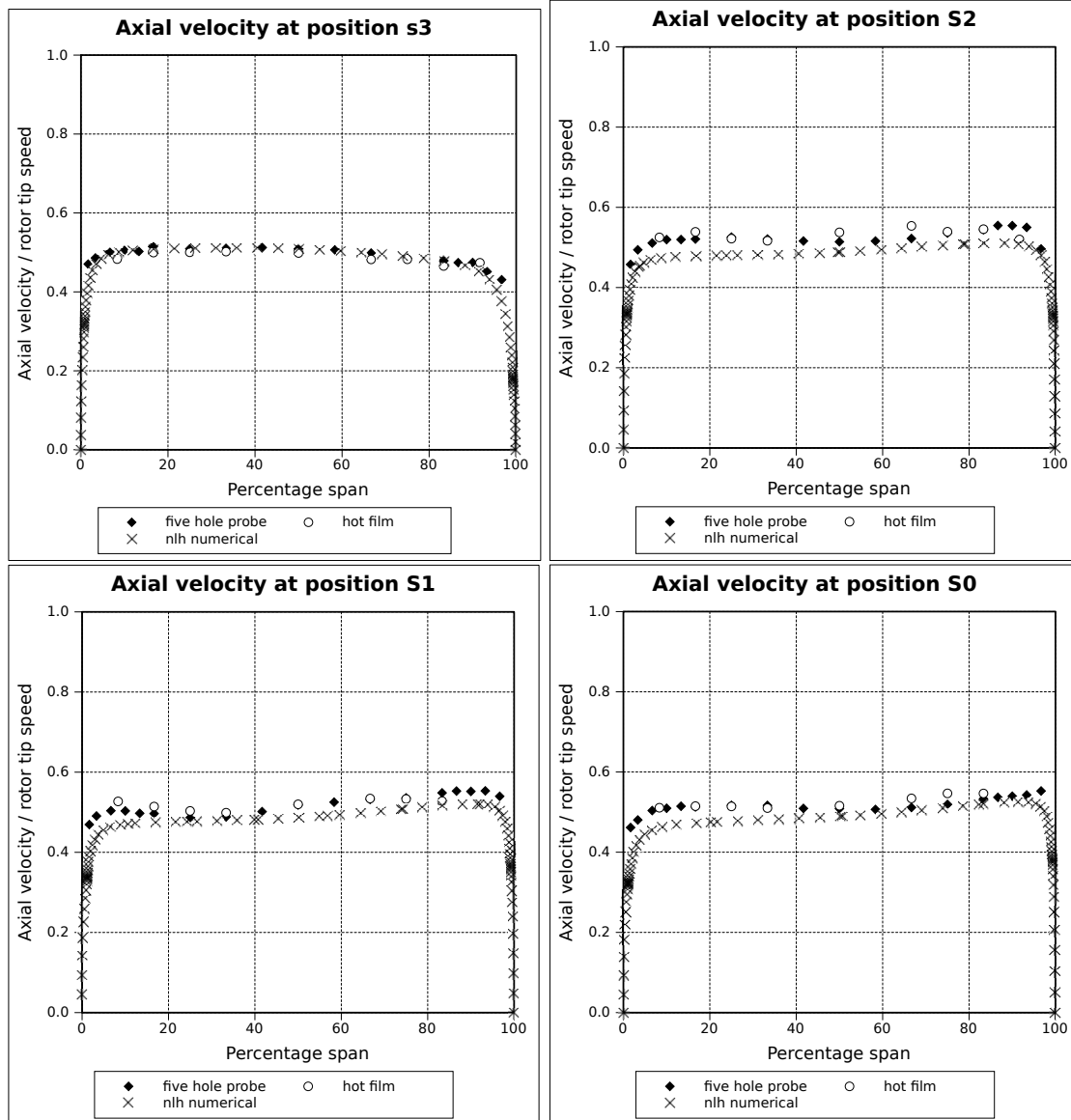


Figure 10.1: Axial velocity components as a function of radius at $\phi = -0.482$

due to the favourable pressure gradient present under this operating condition, contrasted with the adverse pressure gradient at compressor design point. The tangential velocity profiles are also approximately uniform, and similar for all stages, as is shown in figure 10.2. The magnitude of the tangential component decreases by 20 % from hub to 80 % of the span. A highly localised increase in magnitude of the swirl component of approximately 10 % relative to midspan is observable in the last 20 % of span at all stations.

The axial velocity profiles at a flow coefficient of -0.553 (figure 10.3) have similar characteristics to those observed at -0.482 (figure 10.1). There is an increase of 6 % in axial velocity from midspan to tip at station S2, and 10 % at station S0, although the increase from midspan to tip at station S1 is only 2 % of the midspan value. Again, all stages yield similar velocity profiles. The tangential velocity profiles (figure 10.4) are likewise similar to those observed at a flow coefficient of -0.482 (figure 10.2). The magnitude of swirl velocities observed downstream of rotors are smaller at this flow coefficient than those at both a flow coefficient of -0.482 and a flow coefficient of -0.843. This suggests that the blade metal

CHAPTER 10. SECOND QUADRANT: NEGATIVE ROTATION

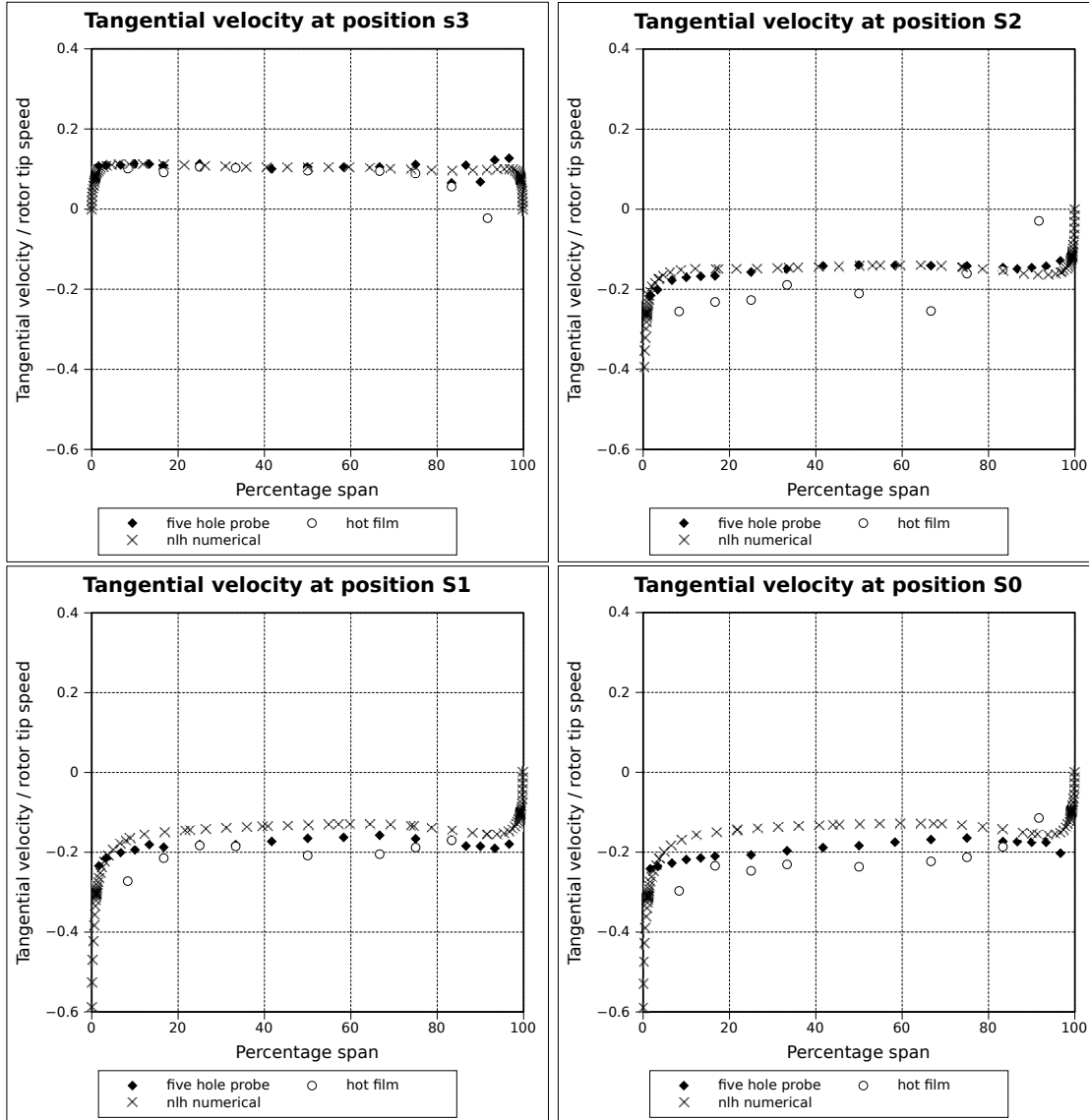


Figure 10.2: Tangential velocity components as a function of radius at $\phi = -0.482$

angles are closer to the flow angles, and thus the compressor is better suited to turbine operation at this flow coefficient than at the lower or higher values. With the exception of the case at a flow coefficient of -0.843, this also continues the trend observed in the third quadrant (chapter 9) that an increase in magnitude of the flow coefficient brings a decrease in average tangential velocity components downstream of rotor blade rows.

The axial velocity profiles observed at a flow coefficient of -0.843 (figure 10.5) differ in several respects from those at flow coefficients of a smaller magnitude. The direction of the velocity gradient downstream of rotor blade rows is reversed, with the highest velocities occurring near the hub, and decreasing by 10 % from hub to tip. The tangential velocity components (figure 10.6) are of interest because they vary between stages. The tangential velocity profile at station S2 is very nearly uniform. At S1 the magnitudes of the velocity at the 15 % of the span closest to the hub is nearly 50 % higher than the average value, and the last 10 % of the span closest to the tip is 13 % higher than the average. The tangential velocity profile at S0 is similar to that of S1 in this regard. The average value

CHAPTER 10. SECOND QUADRANT: NEGATIVE ROTATION

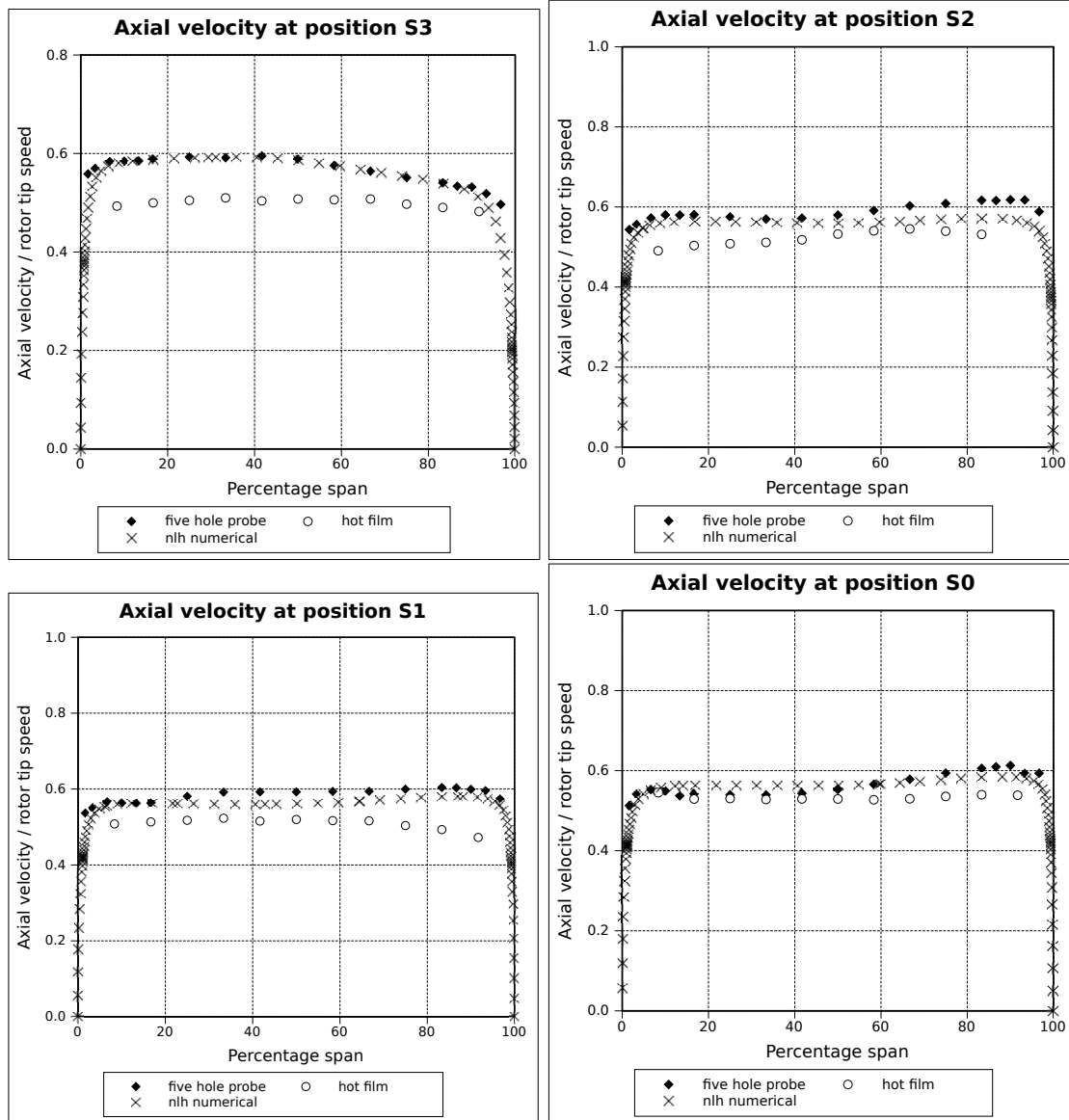


Figure 10.3: Axial velocity components as a function of radius at $\phi = -0.553$

of the tangential velocity component increases with the number of upstream stages, and is twice as large at S0 than at S2. The differences between stages suggest that the flow leaving upstream stages is sufficiently disturbed to disrupt the operation of downstream blade rows. This would appear to indicate the presence of flow separation on at least some blade rows. The average circumferential velocity magnitude is larger for this flow coefficient than for -0.553, and of similar magnitude to that at a flow coefficient of -0.482, with the exception of position S0.

The load coefficient $U(r)\Delta C_\theta(r)/U^2$ is plotted as a function of radius in figure 10.7. The circumferential velocity spanwise profile at station R3 was estimated based on flow angle data for third quadrant operation. This is justified because the flow enters nearly axially, the axial velocities at S3 are similar, and as in chapter 7, deviation angle is not heavily dependent on inlet flow angle for small changes in incidence for either axial flow compressors [Cumpsty, 1989] or axial flow turbines [Dixon, 1978]. Note that for flow coefficients of -0.482 and -0.553 the distribution is virtually identical. This is probably because there

CHAPTER 10. SECOND QUADRANT: NEGATIVE ROTATION

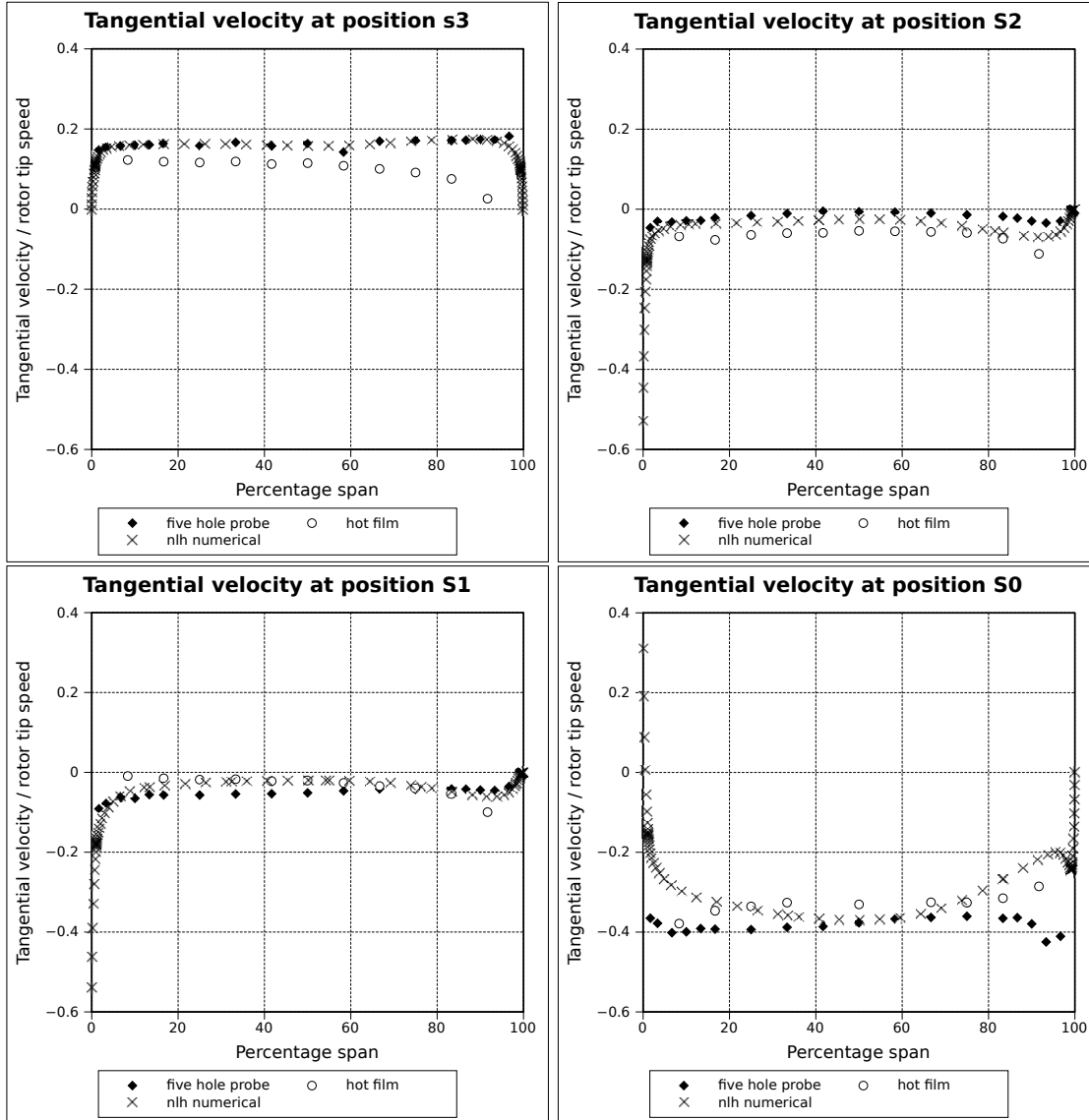


Figure 10.4: Tangential velocity components as a function of radius at $\phi = -0.553$

is only about 12 % difference in between the flow coefficients. The average value at a flow coefficient of -0.843 is approximately double that at the lower flow coefficients. For flow coefficients of -0.482 and -0.553, the work extracted from the flow is approximately constant from the hub to 60 % of the span. Beyond this, the work extracted decreases by approximately 33 % near the hub. Recall that in chapter 9 it was shown that the change from compressor-like to turbine-like operation began near the hub, and extended spanwards as the flow coefficient moved further from the origin. It thus appears that flow angles in the final 40 % of the span are less well matched to the rotor trailing edge blade metal angles than those at lower radii. Nonetheless, the entire blade is extracting flow energy.

At a flow coefficient of -0.740, there is a local maximum in work extracted at approximately 60 % of blade span. The value at the hub is approximately 10 % lower than this maximum, while near the tip the work extracted decreases by about 33 % as for other flow coefficients. The reason for the increase from the hub to 60 % of span is probably that at

CHAPTER 10. SECOND QUADRANT: NEGATIVE ROTATION

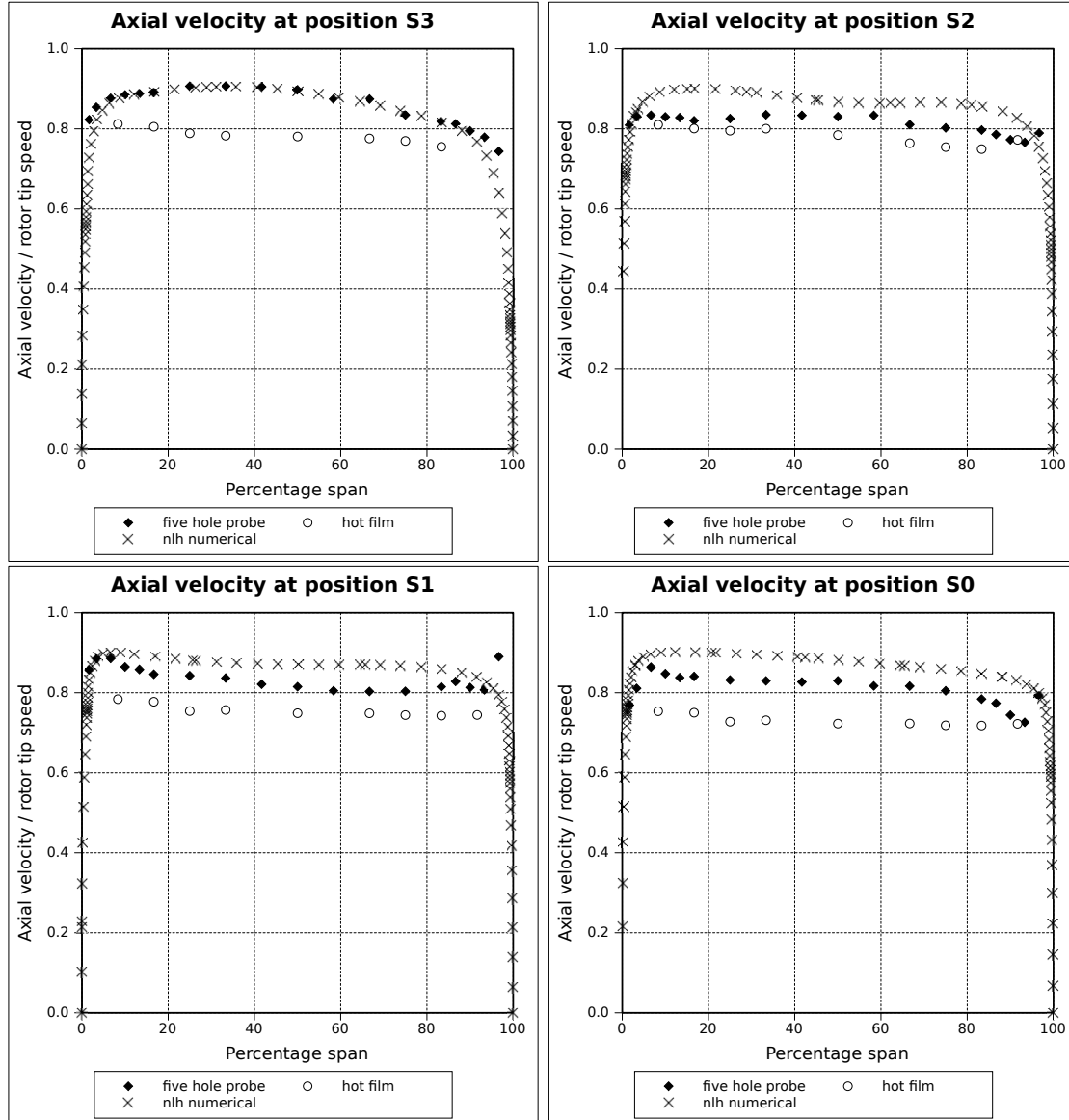


Figure 10.5: Axial velocity components as a function of radius at $\phi = -0.843$

lower radii, the inlet flow angles have begun to exceed the blade metal angles to such a degree that some flow separation occurs on the suction surface. In other words, the blades are beginning to stall near the hub.

10.2.2 Time dependent results

Time dependent velocity data was obtained by means of a single-sensor inclined hot film probe, supplemented by a two-sensor x-probe. Figure 10.8 shows an axial-velocity time-trace downstream of the final rotor row for a single revolution. The wake-jet pattern is clearly visible for the lowest and highest flow coefficient investigated, but less so for a flow coefficient of -0.553 . In all cases, the magnitude of variation of velocity due to passing rotor wakes is approximately 10 % of the time-averaged velocity. The wakes at a flow coefficient of -0.482 are broadest at 50 % of the local blade pitch (approximately 50 % of the time-trace for each blade passing interval is below the time-average), while those at a

CHAPTER 10. SECOND QUADRANT: NEGATIVE ROTATION

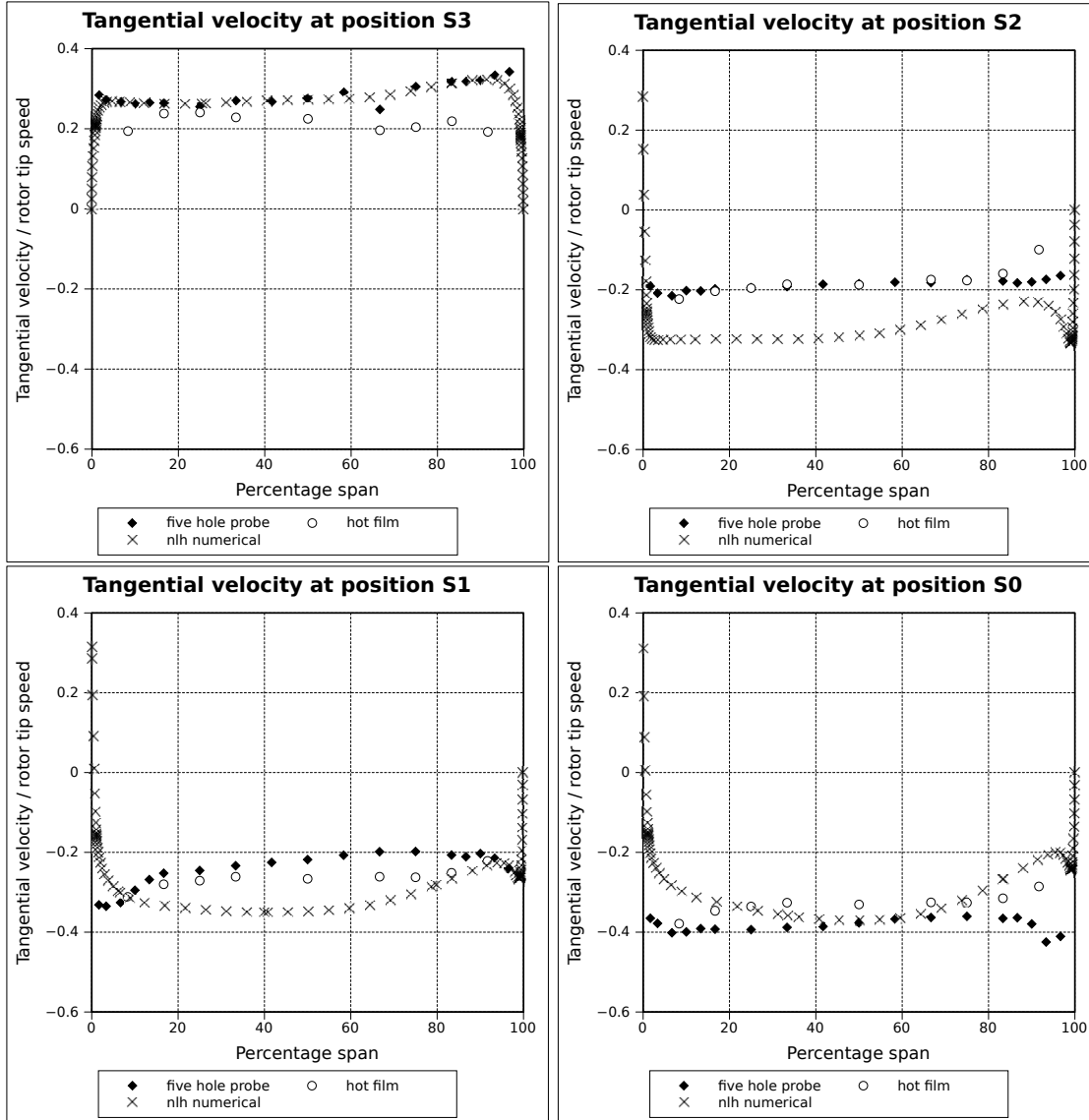


Figure 10.6: Tangential velocity components as a function of radius at $\phi = -0.843$

flow coefficient of -0.553 are approximately 33 % of the the blade pitch. Velocity within the jets between wakes is also more uniform at the two flow coefficients further from the origin. This, combined with the small swirl velocity, suggests that the compressor is better suited to turbine-like operation at this flow coefficient than at the others investigated. The wakes at midspan at a flow coefficient of -0.843 are also approximately 33 % of the local blade pitch.

In the frequency domain, the two smaller flow coefficients are interesting in that the blade passing frequency is of approximately equal size to its harmonics, a state of affairs which was not observed in any other mode of operation. At a flow coefficient of -0.482 (figure 10.9), the second harmonic is 70 % larger than the fundamental, while at a flow coefficient of -0.553 (figure 10.10) the second and third harmonics are approximately the same amplitude as the blade passing frequency component downstream of the second and first stage rotors respectively. This can be explained to some extent by the sharpness of the wakes. However, in cases such as first quadrant design-point operation, in which sharp

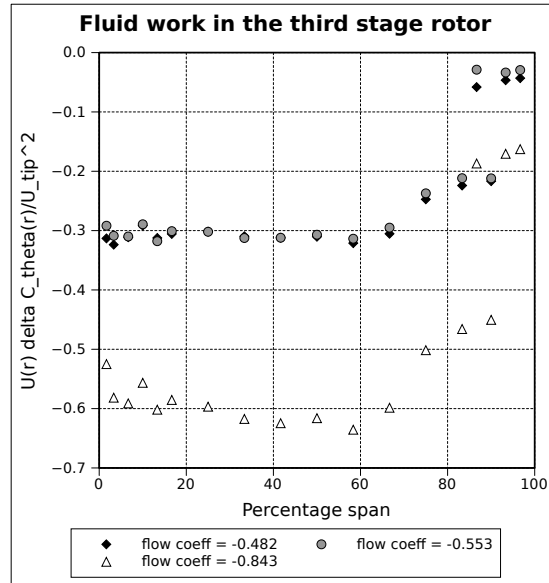


Figure 10.7: Spanwise distribution of local load coefficient at position S2

wakes were also observed, the second harmonics were approximately 20 % at design point, while the third harmonics were only 16 %. A similar tendency to that at design point is observed at the largest flow coefficient of -0.843 (figure 10.11), in which the component at the blade passing frequency dominates all subsequent harmonics.

Figure 10.12 shows a time series of axial velocity contour maps at station R1 downstream of the first stage stator. The wakes of the stator blades are only 25 % of the local blade pitch at their widest point, approximately 20 % of the span from the hub (label A). In contrast, the wakes of the stator blades at design point were 33 % of the local blade pitch at their widest (which occurred at a larger radius). The wakes are most pronounced near the hub, due to the incorrect direction of stator blade twist. The remainder of the flow field is relatively uniform, with maximum velocities occurring in jets near hub and tip, halfway between stator wakes.

10.3 Numerical results

Figures 10.1-10.6 compare the experimental and numerical axial and tangential velocity distributions as a function of percentage span. It can be seen that the numerical results utilising the non-linear harmonic method appear to agree well for axial and tangential velocity profiles, particularly at flow coefficients of -0.482 (figures 10.1 and 10.2) and -0.553 (figures 10.3 and 10.4). There is a small discrepancy between the axial velocity profiles near the hub in figure 10.1, possibly due to a non-axisymmetric flow phenomenon in this region. The numerically determined axial velocity profile at a flow coefficient of -0.843 (figure 10.5) differs with the experimental data by up to 10 %, although the gradient and general form of the profile are captured. In comparison the tangential velocity component agrees relatively poorly with the experimental data in both gradient and profile, particularly at the downstream stations S1 and S0.

As tangential velocities approximately 25 % of the size of the average axial velocity were measured at station S3, these were imposed at the inlet boundary condition. Simulations

CHAPTER 10. SECOND QUADRANT: NEGATIVE ROTATION

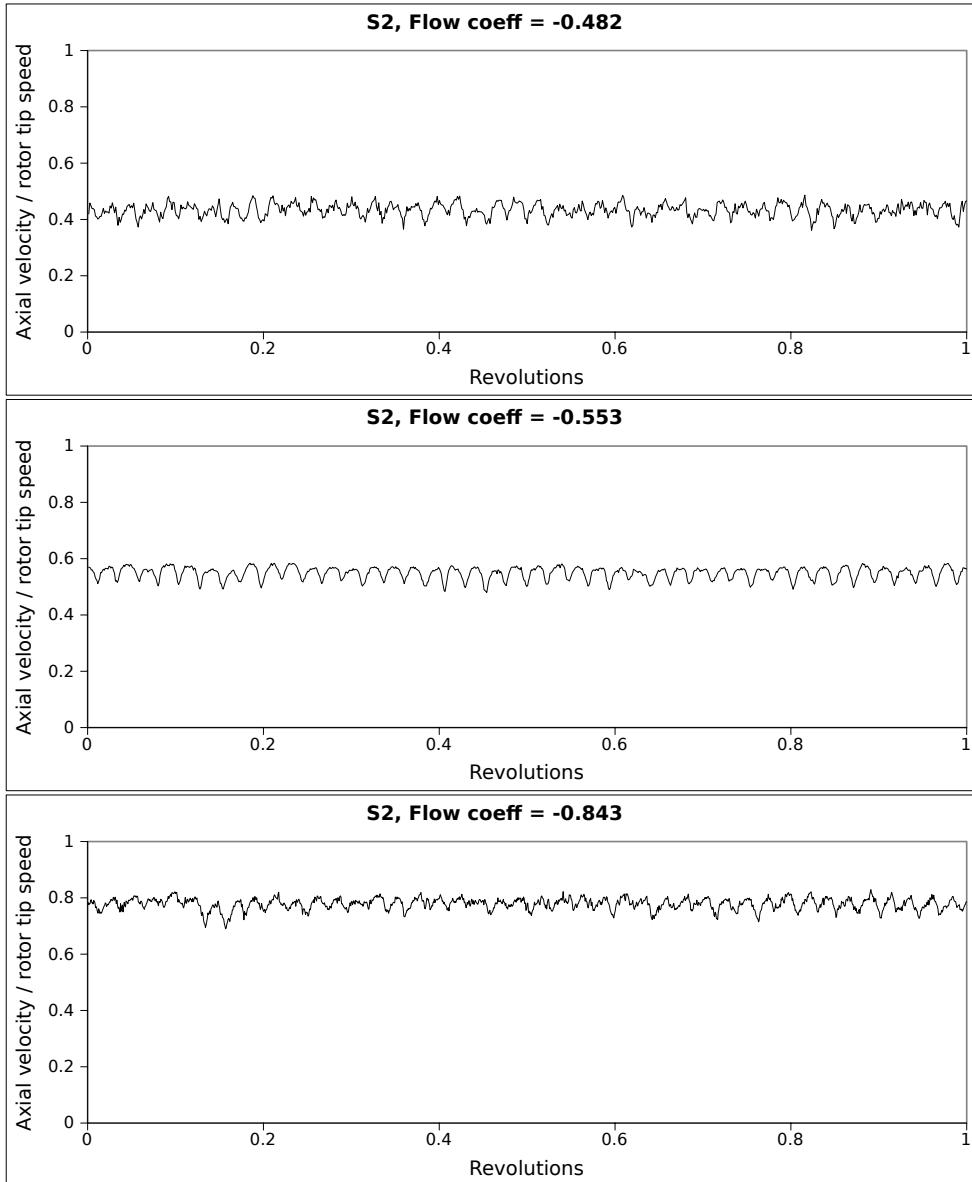


Figure 10.8: Time-traces for axial velocity components at midspan over one revolution

were also run with no tangential velocity imposed at the inlet boundary. The presence of swirl was found to have a large effect on the tangential velocity component downstream of the final rotor row (station S2) as this was the first row to see the flow. The effect became less marked for stages further downstream, although was still detectable at station S0, downstream of the final rotor row.

Steady-state simulation results were attempted but are not presented here, as they differed significantly from both experimental data and the results of the time-dependent simulation. It was found to be necessary to begin by simulating the case representing the highest flow coefficient, for which flow is most ordered, and to use this to initialise the next lowest flow coefficient. The solution for that case was in turn used to initialise the case representing the lowest flow coefficient.

Figure 10.13 shows a time series of entropy contours at mid-span, normalised to the flow inlet. In this and all of the following figures, flow is from left to right of the figure. It

CHAPTER 10. SECOND QUADRANT: NEGATIVE ROTATION

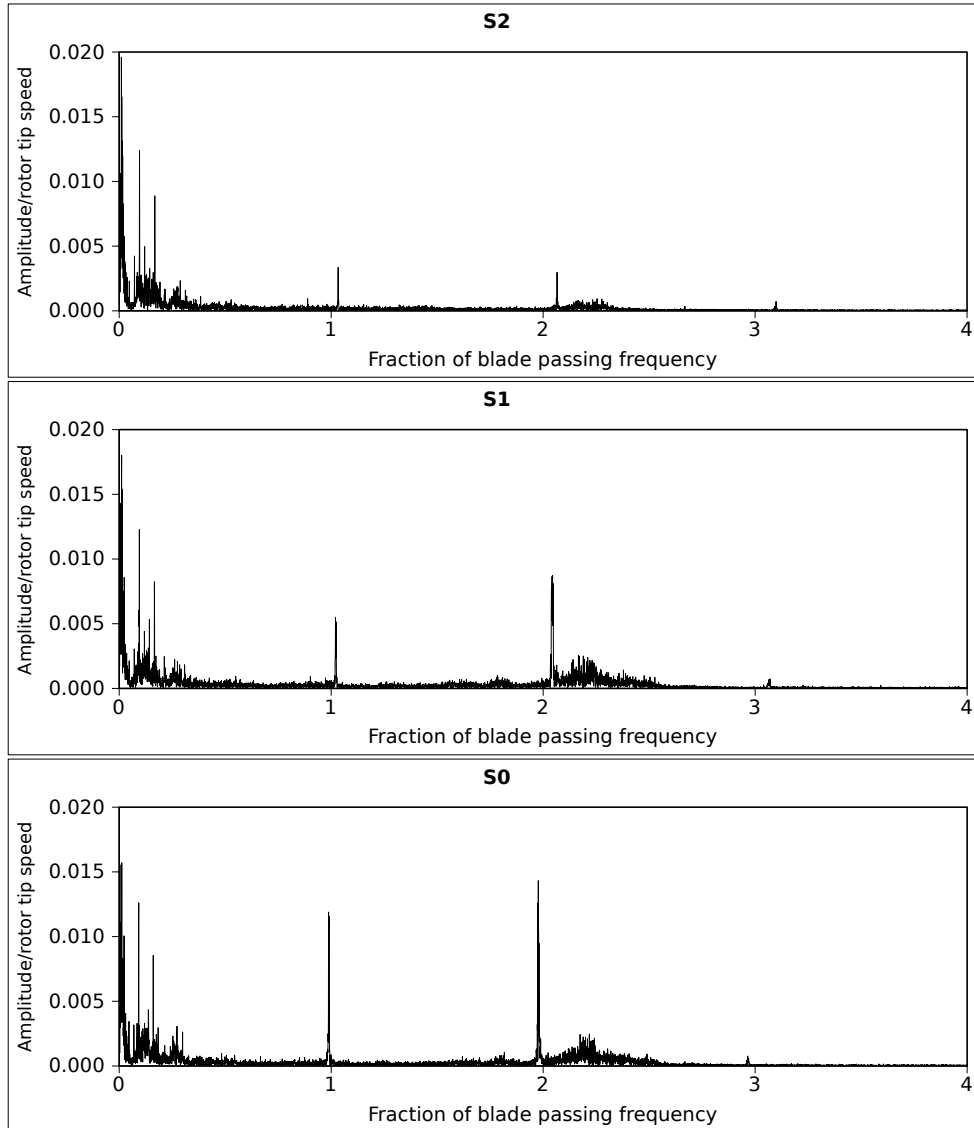


Figure 10.9: Frequency of cooling velocity variation at $\phi = -0.482$ at mid-span

should be remembered that for this mode of operation, both the axial flow direction and rotation direction are reversed relative to design point operation. Thus the leading edges of blades act as trailing edges, and trailing edges act as leading edges. In addition, the movement of rotor blades is in the opposite of the usual direction. However, the pressure and suction surfaces retain their identity. The wakes downstream of rotor and stator rows are each approximately 20 % of the local blade pitch. This is less than the value observed for design point operation. This can be explained by the fact that the pressure gradient is favourable, leading to less mixing. An entropy rise of approximately 50 % the circumferentially averaged value appears to occur in a band across the first stage stator blade passages, possibly indicating the presence of secondary flows within the passage. Entropy rise across each stage is approximately equal.

The area-traverse (figure 10.12) showed the wake downstream of the third stage stator to be largest near the hub. Numerical results show a similar tendency. The flow field around second and third stage stators is shown in figure 10.14, on a constant area surface at 10 % , 50 % and 90 % of the blade span from the hub. A separation bubble can be

CHAPTER 10. SECOND QUADRANT: NEGATIVE ROTATION

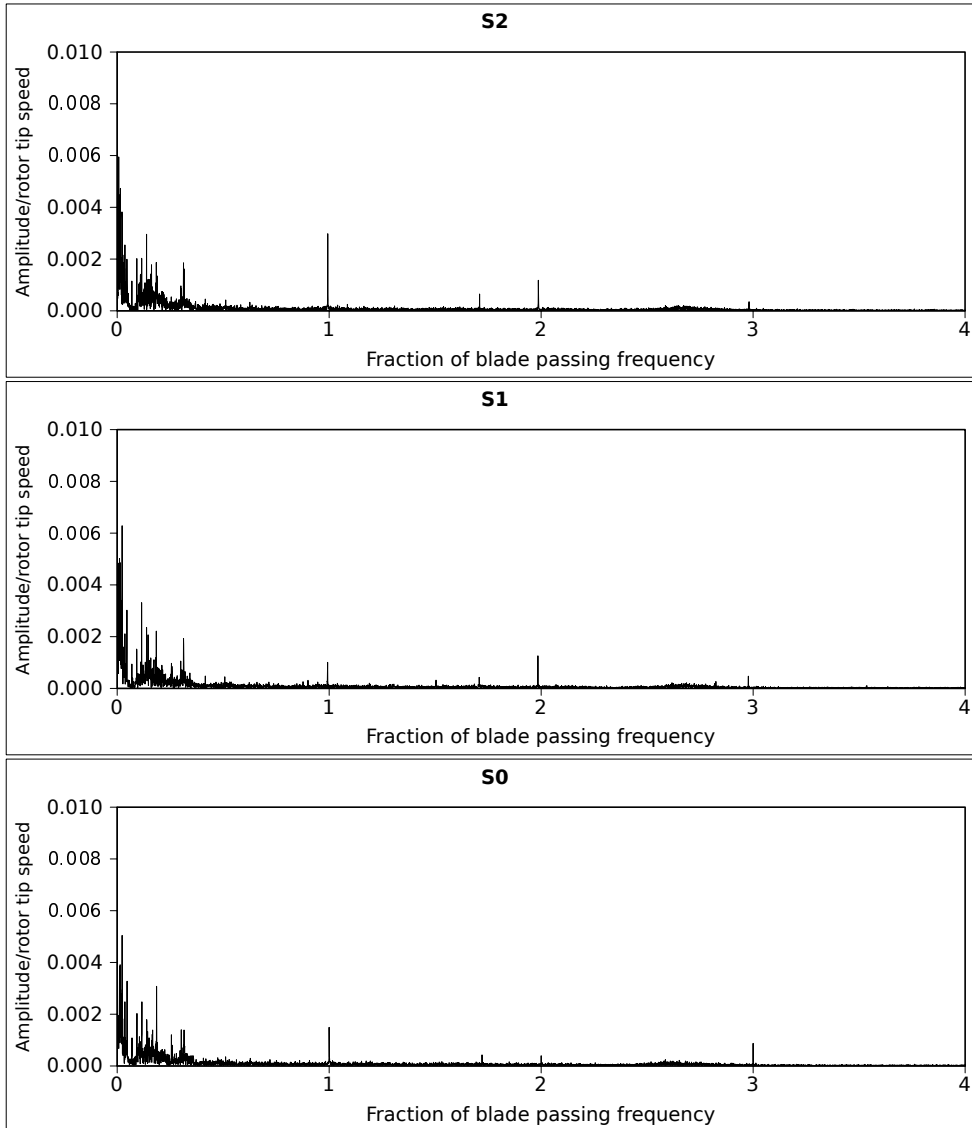


Figure 10.10: Frequency of cooling velocity variation at $\phi = -0.553$ at mid-span

observed on the suction surface of the second stage stator, although none is apparent for the third stage stator at the same radius. This is probably due to the effects of upstream blade passages, which are not present for the final stage stator. It can be seen that the flow field is more uniform at half-span and near the tip (subfigures (c)-(f)), as the blade metal angle in this region is more appropriate. There appears to be a small degree of separation on the suction surface of the second stage rotor at midspan (subfigure (d)) but not in the near tip region (subfigure (f)). There appears to be a small separated region on the third stage stator near the leading edge, in the near tip region (subfigure (e)).

The flow field surrounding rotor blades also differs between stages. Figure 10.15 shows the relative flow fields surrounding third and first stage rotor blades on a constant area surface at 10, 50 and 90 % of the blade span from the hub. The apparent crossing of streamlines observed to the right of the leading edge in subfigure (a) indicates a vortex in this region. This is absent in a downstream stage, as shown in subfigure (b), and flow near the leading edge appears to detach from the suction surface to a small degree. As with the stator, the mid-span (subfigures (c) and (d)) and near-tip regions (subfigures (e) and (f))

CHAPTER 10. SECOND QUADRANT: NEGATIVE ROTATION

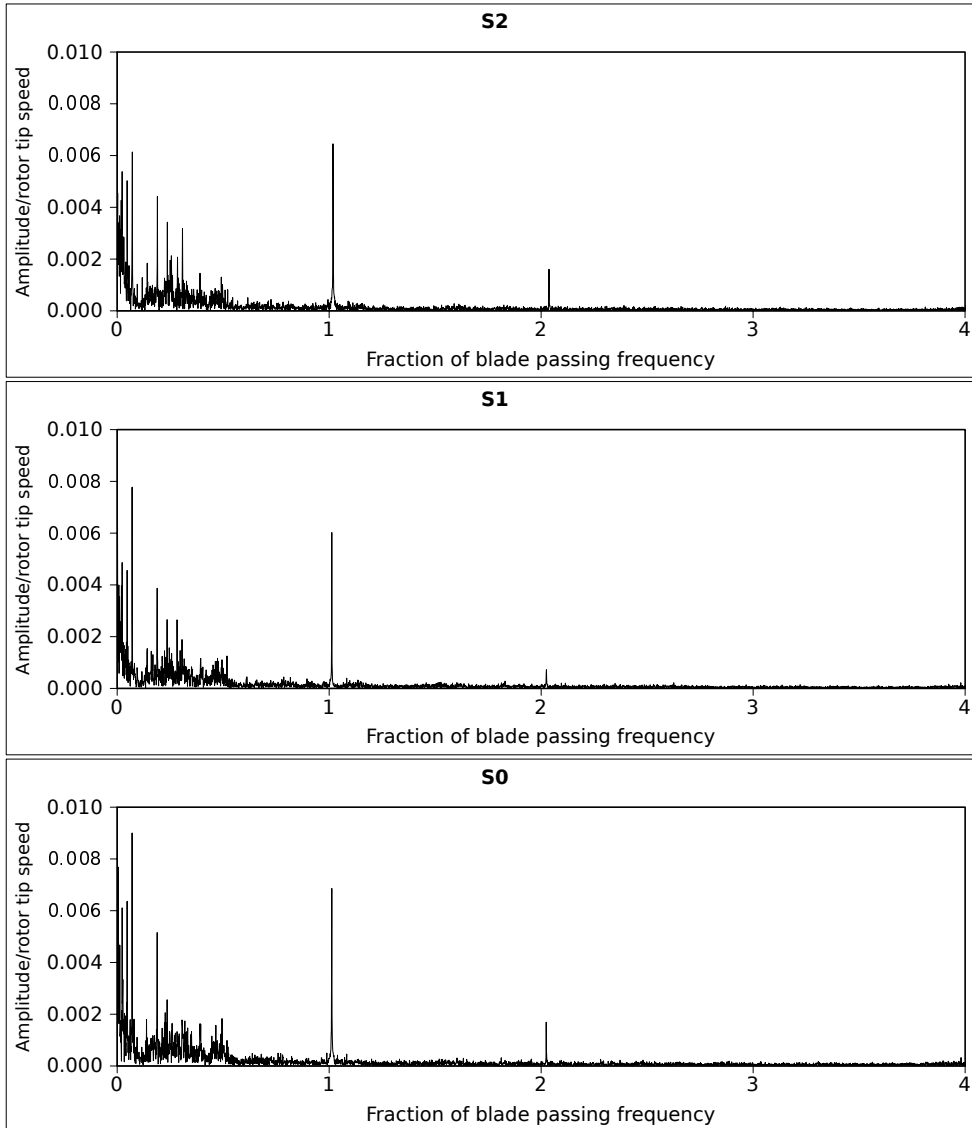


Figure 10.11: Frequency of cooling velocity variation at $\phi = -0.843$ at mid-span

exhibit more orderly flow patterns.

Figure 10.16 shows the radial velocity component at midspan. A positive sign indicates that the flow is in the tipward direction. There appears to be an area of hubwards flow corresponding with the second and first stage stator wakes, with areas of tipward flow between these. The maximum velocity of each is approximately equal, thus the circumferential average radial flow in these regions is approximately zero. The third and second stage rotor wakes do not appear to cause a radial velocity component, but the first stage rotor wake appears to coincide with a hubward radial flow. Tipward radial flows occur on both pressure and suction surfaces of second and first stage rotor blades, but not on those of the third stage. These are balanced by hubward radial flow near the circumferential middle of blade passages. This appears to be further evidence of the vortices which have been found to form downstream of rotor blades.

Thus the circumferentially averaged flow field is shown in figure 10.17 shows no significant radial velocity components.

CHAPTER 10. SECOND QUADRANT: NEGATIVE ROTATION

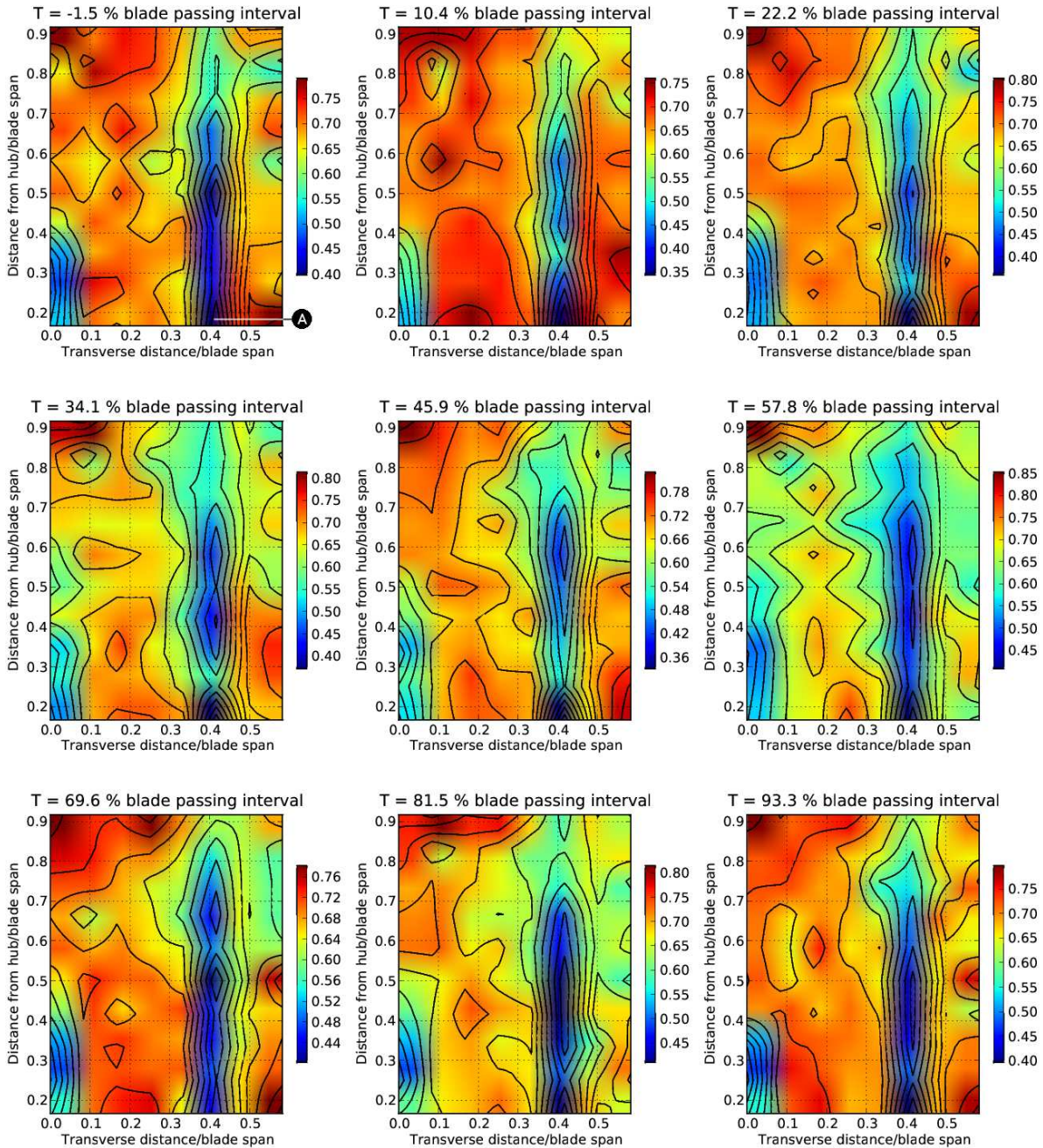


Figure 10.12: Time series of axial velocity contours at position R1 at $\phi = -0.843$

CHAPTER 10. SECOND QUADRANT: NEGATIVE ROTATION

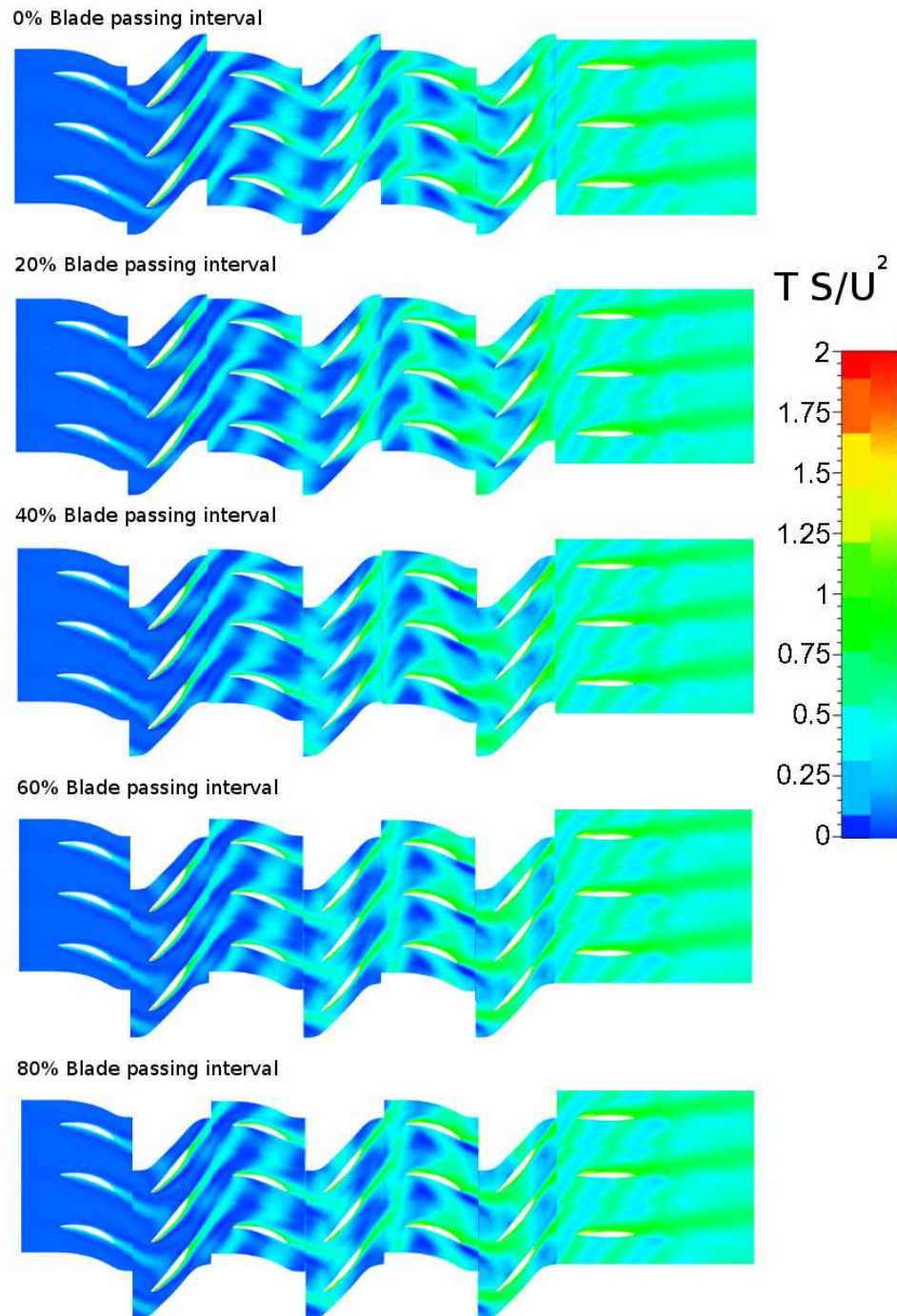


Figure 10.13: Time series entropy distribution, normalised relative to inlet, on constant radius surface at midspan; $\phi = -0.843$

CHAPTER 10. SECOND QUADRANT: NEGATIVE ROTATION

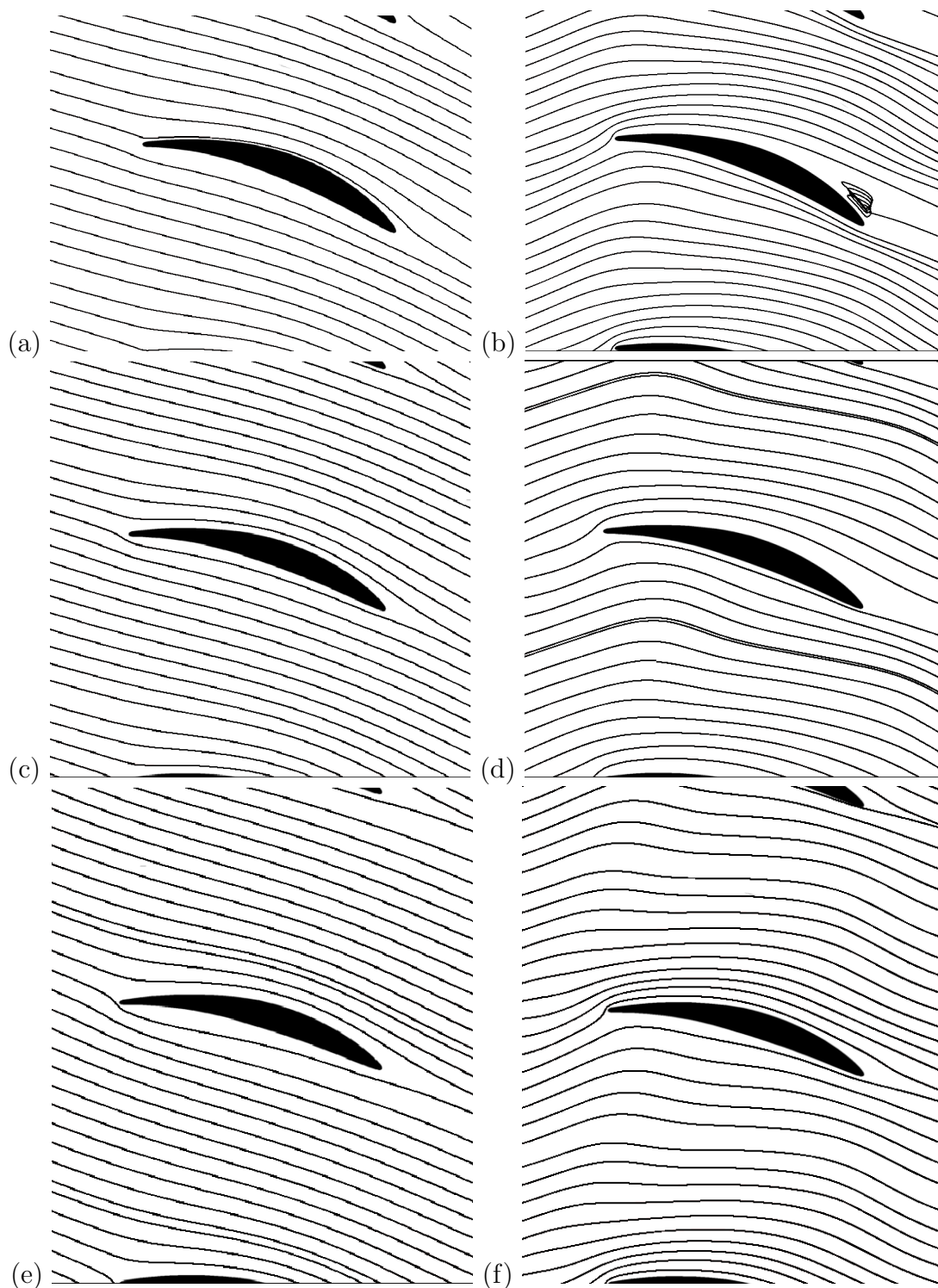


Figure 10.14: Streamlines surrounding stators: (a) third and (b) second stage at 10 %, (c) third and (d) second stage at 50 % and (e) third and (f) second stage at 90 % of blade span; $\phi = -0.843$

CHAPTER 10. SECOND QUADRANT: NEGATIVE ROTATION

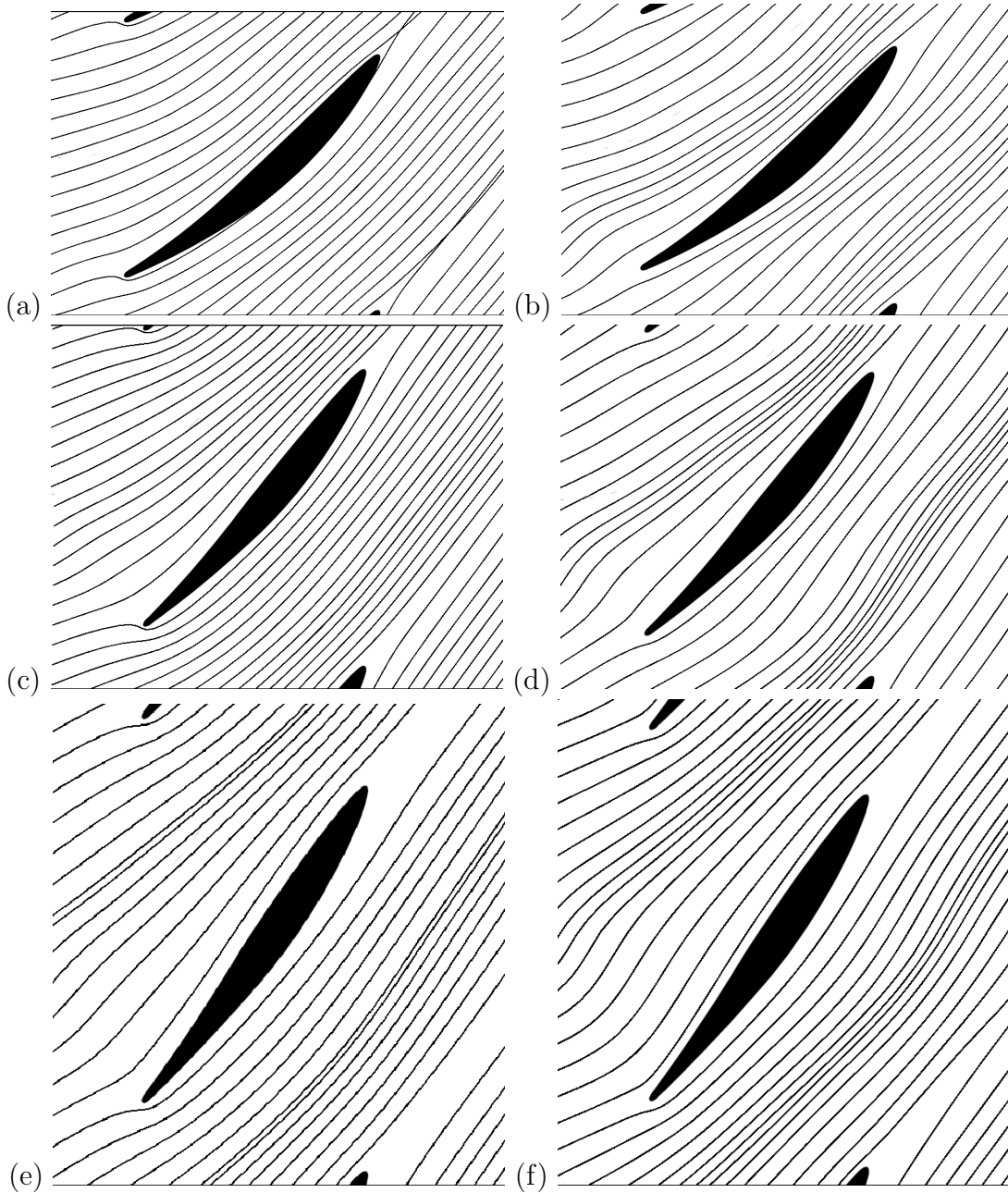


Figure 10.15: Relative velocity streamlines surrounding rotors: (a) third and (b) first stage at 10 % of blade span, (c) third and (d) second stage at 50 % of blade span, (e) third and (f) second stage at 90 % of blade span, ; $\phi = -0.843$

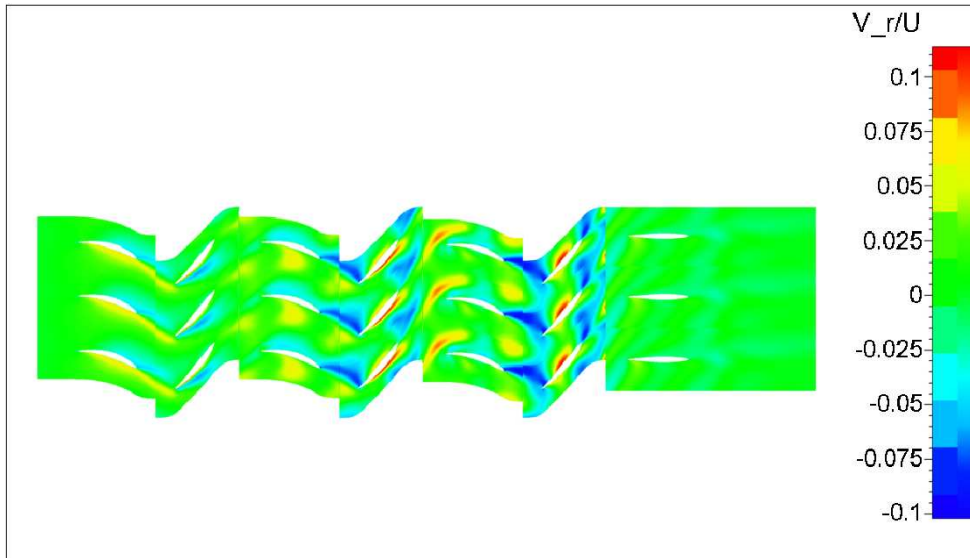


Figure 10.16: Radial velocity distribution on constant radius surface at midspan at $\phi = -0.843$

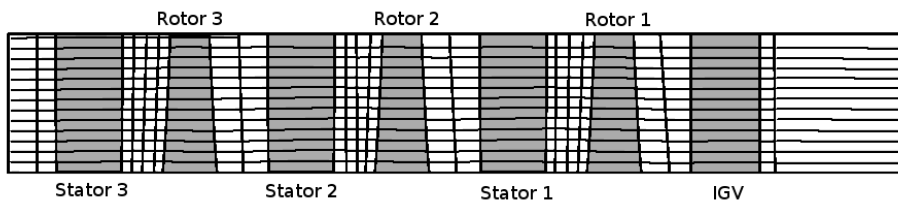


Figure 10.17: Meridional view of the test compressor showing circumferentially averaged flow paths and areas of separation and recirculation on the hub and shroud

10.4 Discussion

The velocity triangles at midspan are shown in figure 10.18 for the three flow coefficients under investigation. In all cases, flow angles and blade metal angles are relatively well matched. The direction of the circumferential velocity component downstream of the rotor blade changes as the flow coefficient increases, as has already been commented upon. This has the effect that at high flow coefficients, there is some danger of separation or blade stall occurring on the suction surface of downstream stators, due to the increase in angle of attack. Based on the evidence of figure 10.14(f), this has not yet occurred to any significant degree at a flow coefficient of -0.843.

10.5 Summary

The flow field within an axial flow compressor operating under turbine-like conditions for reverse flow and rotation has been experimentally and numerically investigated. Operation at three flow coefficients was investigated: $\phi = -0.482$, $\phi = -0.553$ and $\phi = -0.843$.

The axial and tangential velocity profiles downstream of all rotor rows were nearly uniform. A slight increase in axial velocity from hub to tip was observed at the smaller

CHAPTER 10. SECOND QUADRANT: NEGATIVE ROTATION

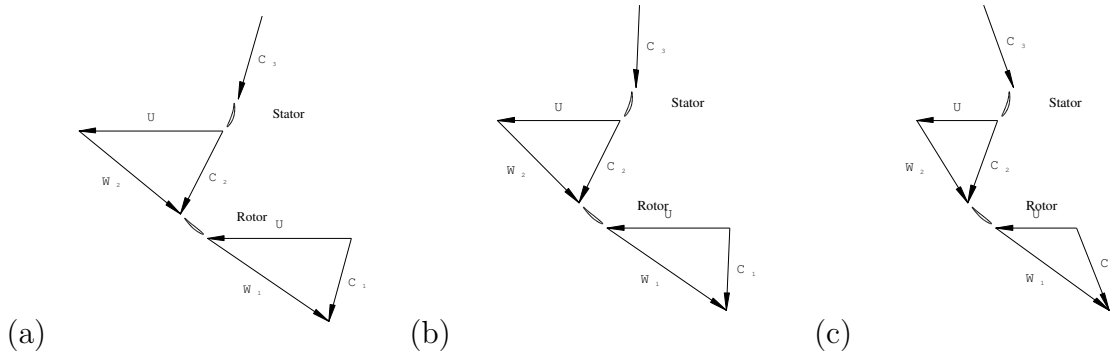


Figure 10.18: Velocity triangles for first stage (stations S1 - S0) at 50 % of blade span: (a) $\phi = -0.482$ (b) $\phi = -0.553$ (c) $\phi = -0.843$

flow coefficients, while at the largest flow coefficient investigated a decrease was observed from hub to tip. Tangential velocities were largest near the hub and casing, and were small in comparison to the axial velocity. Numerical results agree well with experimental results for low flow coefficients, and less well, though still reasonably at the largest flow coefficient.

Rotor and stator wakes were found to be only 20 % of the local blade pitch at midspan. In the frequency domain, the second and third harmonics of the blade passing frequency were detectable above the noise level. For the two smaller flow coefficients, the second harmonic was of a similar amplitude to the blade passing frequency amplitude. The area between stator wakes was of approximately uniform velocity for any given instant, although considerable variation in time was observed, due to the movement of the upstream rotor wake. Small areas of separation on suction surfaces of rotor and stator blades were discovered near the hub.

In simulating second quadrant operation, it was found that for the numerical solver used, the initial solution assumed was most important, particularly at the flow coefficients closer to zero, as poor choice of initial values yielded highly inaccurate results, despite achieving convergence of the iterations. In addition, steady state solutions using the mixing plane approach for second quadrant operation were found to yield highly unrealistic solutions for this solver, and were rejected.

Chapter 11

Fourth quadrant: negative rotation

11.1 Introduction

This chapter describes the flow structures observed under fourth quadrant operating conditions for reversed rotation. In this mode of operation, the compressor rotates in the reverse of the design direction, but the flow through the machine is forced through the machine in the design direction. The pressure drop observed between the machine inlet and outlet rises sharply; at a flow coefficient of 0.165 the non-dimensionalised total to static pressure drop is twice the design point pressure rise. This mode of operation is dissipative: a non-dimensional static temperature rise ($C_p\Delta T/U^2$) of 3.7 was observed in the working fluid across the compressor, which is large compared with the design point value of 0.58. Fourth quadrant negative rotation operation has some similarity to the mode of operation occurring in the second quadrant for positive rotation. However, it is considerably less likely to occur in practice, as it would require multiple failures and/or operator errors in an industrial installation, and it probably could not occur at all in the compressor of a gas turbine engine. For this reason, as well as the steepness of the characteristic in this region (see figures 5.1 and 5.2 in chapter 5), only one operating point was investigated. Tests were conducted at a flow coefficient of 0.165, at 50 % of design speed for reasons of safety and due to the power limitations of the auxiliary fans.

11.2 Experimental results

11.2.1 Time-averaged velocity profiles

Time averaged velocity profiles were obtained by means of a five-hole probe and by time-averaging of hot-film probe velocity measurements. Velocity distributions as a function of radius were obtained at the compressor inlet and downstream of each rotor row (measurement stations S0, R1, R2 and R3 in figure 3.1). These are shown in figures 11.1-11.2.

The axial velocity profile at position R1 (figure 11.1 shows a 50 % decrease in velocity from hub to tip. The axial velocity profiles at axial positions R2 and R3 (figure 11.1) differ from R1, but are similar to one another, with most of the flow occurring near the hub and tip, and nearly none occurring at midspan. Maximum velocities at the hub are 300 % the average value, while those at the tip are 150 %, but at the local minimum at 66.7 % of the span, the axial velocity is approximately 20 % of the average value. Numerical integration of the velocity profile at these points disagrees with the volume flow rate measurements of the turbine anemometer by approximately 3 %.

CHAPTER 11. FOURTH QUADRANT: NEGATIVE ROTATION

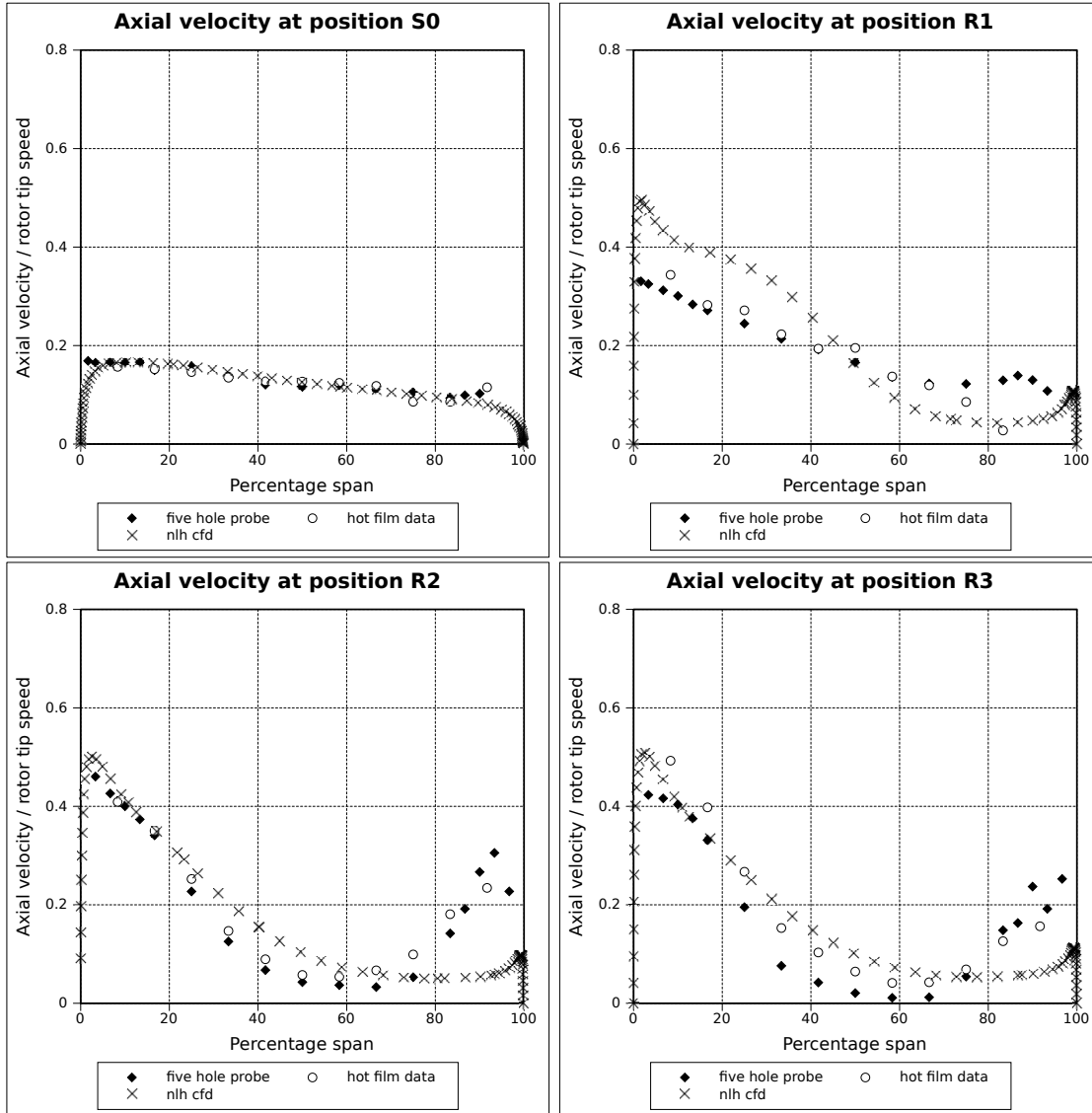


Figure 11.1: Axial velocity components as a function of radius at $\phi = 0.165$

The tangential velocity profiles are shown in figure 11.2. The velocity profiles downstream of the second and third stage rotors (positions R2 and R3) are similar, exhibiting swirl velocity which, at all spans, is approximately 120 % of the rotor tip speed. Swirl velocity magnitudes are highest by approximately 10 % of the average value at midspan. The velocity profile downstream of the first stage rotor (position R1) has an average magnitude of approximately half that of the downstream stages, and decreases by 15 % from hub to tip. The differences are due to the axial direction of flow at the machine inlet, which leads to a smaller relative flow angle upstream of the first stage rotor.

11.2.2 Time dependent results

The time trace of the axial velocity downstream of the first stage rotor as measured by means of the inclined hot film sensor is shown in figure 11.3 at midspan. The average minimum velocity in the wakes is approximately 25 % lower than the average maximum velocity in the jets. The frequency domain of the time trace, shown in figure 11.4, shows

CHAPTER 11. FOURTH QUADRANT: NEGATIVE ROTATION

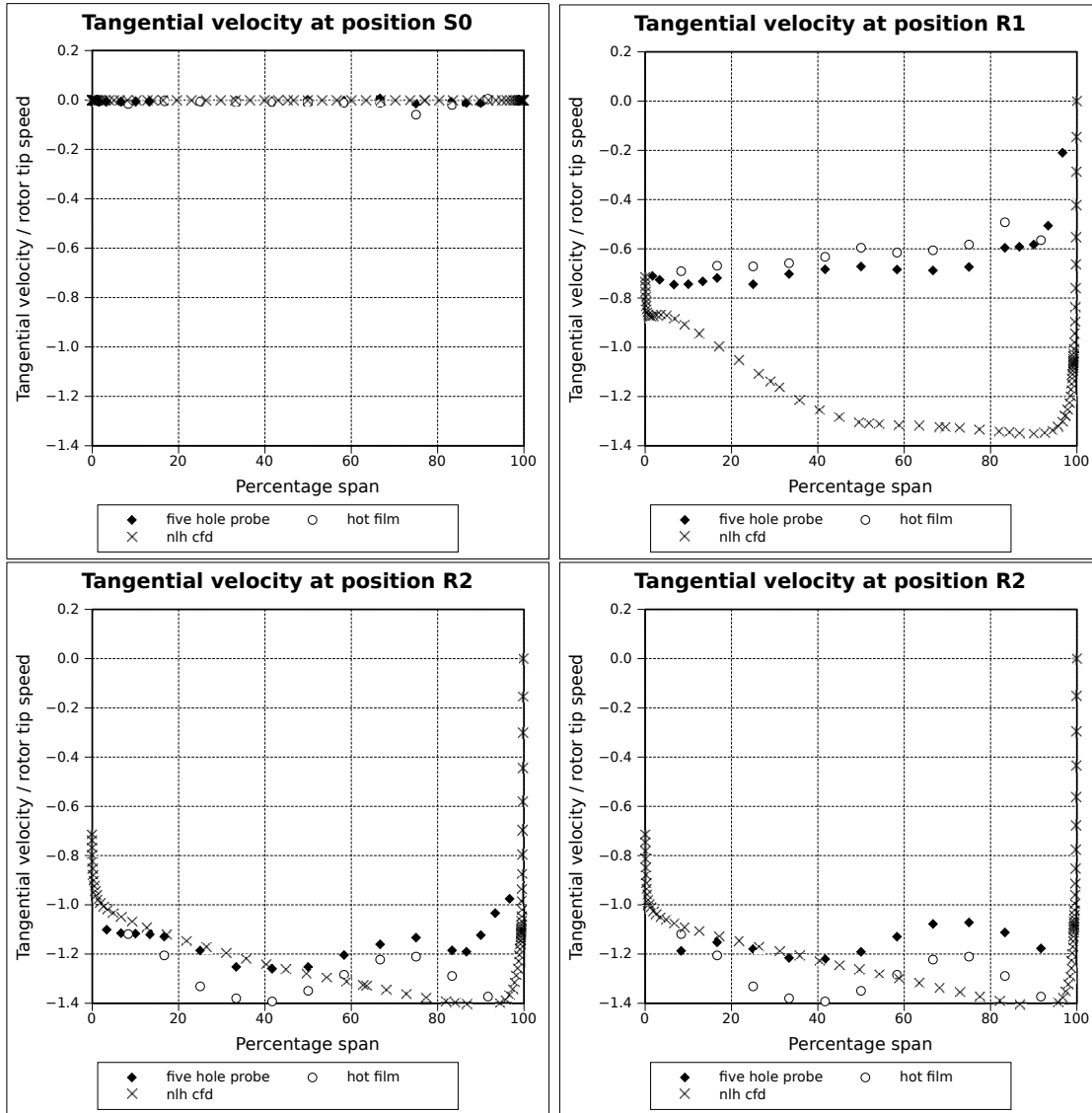


Figure 11.2: Tangential velocity components as a function of radius at $\phi = 0.165$

an equivalent amplitude at the blade passing frequency, with the second harmonic approximately 50 % the amplitude of the fundamental and clearly discernible above background noise. The third harmonic is virtually indistinguishable from background noise, however. The size of the blade passing frequency component amplitude decreases to 67 % of the corresponding amplitude at R1 downstream of the second and third stage rotors (positions R2 and R3). The second harmonic is not distinguishable above background noise at position R2, and is approximately 40 % smaller at R3 than at R1. This suggests that the rotor wakes become increasingly weak and ill-defined further downstream.

A time-series of axial velocity contours for a rectangular area downstream of the first stage stator (axial position S1) is shown in figure 11.5. Two things are immediately evident from the figure. The first is that virtually all the throughflow occurs in an approximately circular region near the casing (label A). This region retains approximately the same size and shape irrespective of the position of upstream rotor blades. The maximum velocity in the centre of this region varies between 530 and 576 % of the average axial velocity. There appears to be one such region per blade passage. The second point is that the

CHAPTER 11. FOURTH QUADRANT: NEGATIVE ROTATION

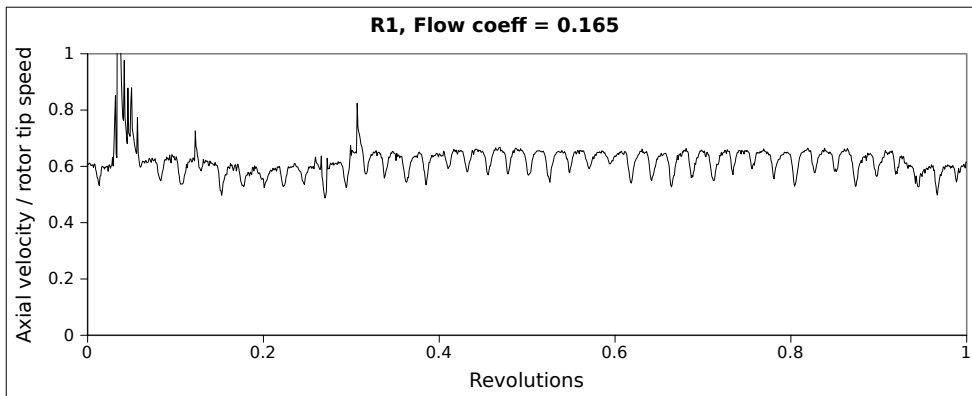


Figure 11.3: Time-traces for axial velocity components at midspan over one revolution

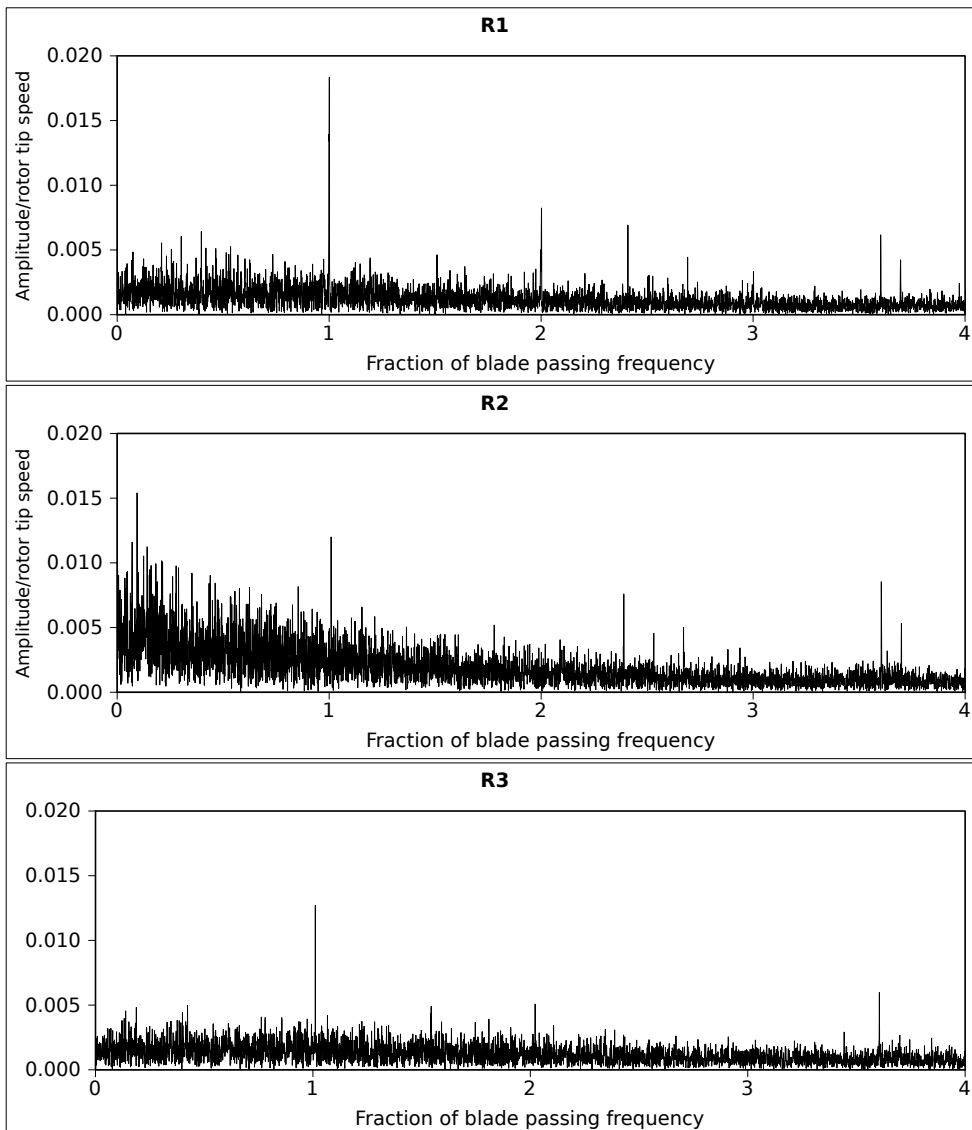


Figure 11.4: Frequency domain of axial velocity component variation at $\phi = 0.165$ at mid-span

CHAPTER 11. FOURTH QUADRANT: NEGATIVE ROTATION

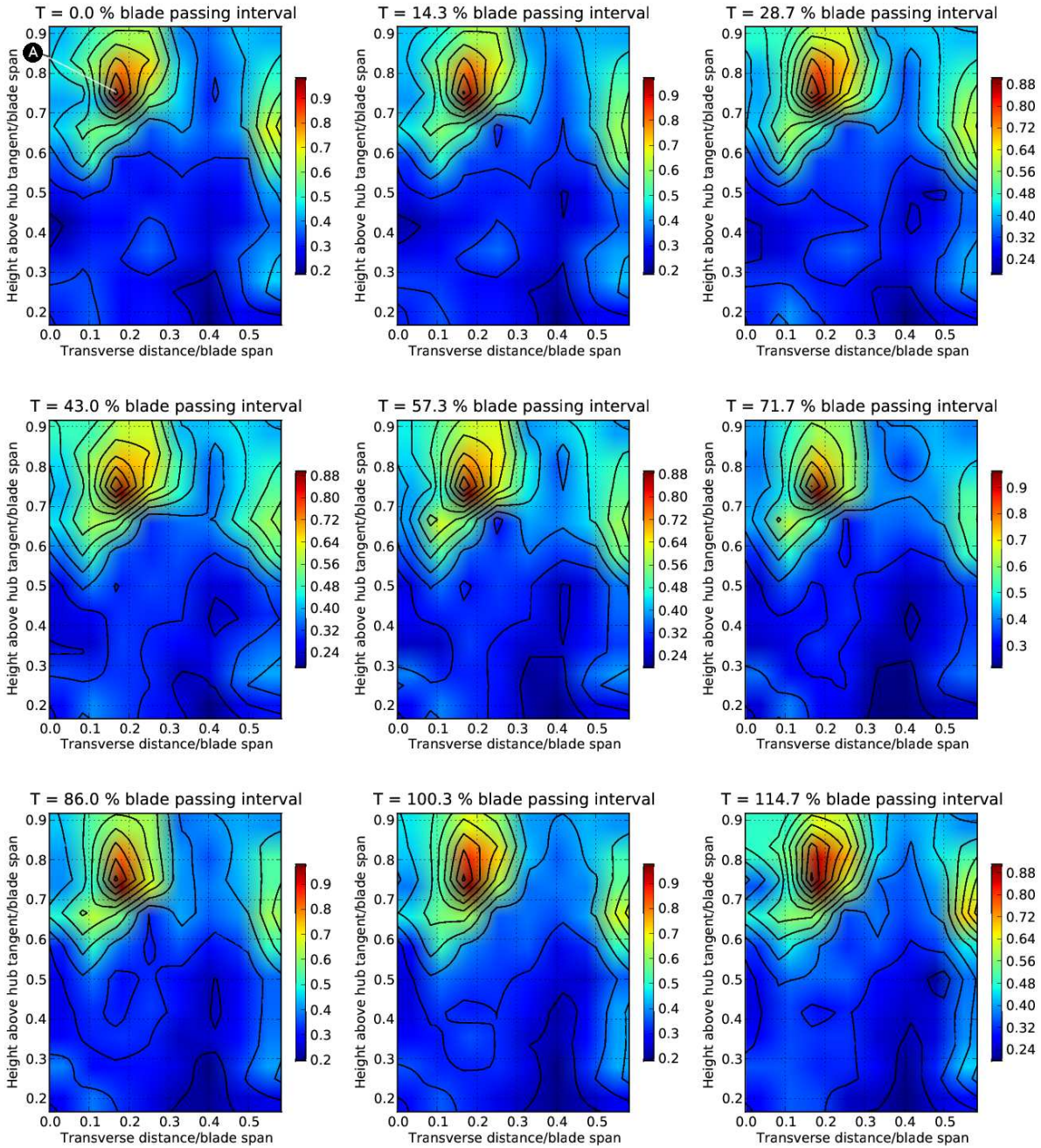


Figure 11.5: Time series of axial velocity contours at position S1 at $\phi = 0.165$

remainder of the flow field, especially the half nearest the hub, is almost entirely uniform. There is no clear evidence of wakes from the upstream stator row, although an area of low velocity does occur at approximately 25 mm from the datum, tangentially between the high-velocity areas, and near the hub, which is suggestive of a wake.

These data, when considered in conjunction with the time-averaged velocity distributions downstream of rotors (figures 11.1 and 11.2) give an indication of the general flow pattern through the compressor for this mode. In rotor rows, throughflow occurs primarily

CHAPTER 11. FOURTH QUADRANT: NEGATIVE ROTATION

near the hub, and to a lesser but extent near the casing. The rest of the inter-blade row flow field is dominated by the swirl component, and blockage to axial flow occurs due to large separated areas with widths of up to 80 % of the blade pitch at midspan. In stator rows, flow occurs primarily near the tip, while the rest of the flow field is subject to blockage due to flow separation.

11.3 Numerical results

Figures 11.1 and 11.2 compare experimentally and numerically determined axial and tangential velocity profiles. Agreement at position R1 is poorest, particularly for the circumferential velocity profile (figure 11.2). However, for both R2 and R3, agreement is relatively good for the region from the hub to approximately midspan. The numerical model does not capture the flow structure near the blade tips, however, as experimental data indicates that velocities in this region increase relative to those at midspan. The large recirculation zone at the outlet may be at fault

Figure 11.6 shows the entropy distribution on a mid-span surface. The low axial velocities present near midspan have a curious effect: the wakes of upstream rotor blades are virtually non-existent. This was also observed in the experimental area traverse downstream of the first stage stator row (figure 11.5). The steady increase in entropy generated and the lack of circumferential variation in the flow field indicates that mixing occurs this mode of operation.

Because the entropy increase per stage is very close to uniform in the circumferential direction, the method of Longley [2007] would be appropriate for numerical simulation of this mode of operation. This is beyond the scope of this dissertation, as has already been stated. However, equation 2.4, which, it will be recalled, related entropy generation to blockage, may be used, in conjunction with a number of simplifying assumptions, to estimate blockage. The equation is restated here for convenience:

$$\rho T \frac{DS}{Dt} = \left(\frac{u|\bar{u}|}{\frac{1}{2}s} \right) \frac{1}{2} \rho (b-1) \bar{\mathbf{u}}^2 \quad (11.1)$$

The entropy generation term may be approximated in the following manner:

$$\frac{DS}{Dt} \approx \frac{\Delta S}{\Delta z} \cdot \frac{\Delta z}{\Delta t} \approx \frac{\Delta S}{\Delta z} \cdot u \quad (11.2)$$

as it seems reasonable to assume that the entropy increase across the stage ΔS must occur during the time which any parcel of fluid spends in the blade row, Δt , traversing the axial distance Δz at axial speed $\Delta z/\Delta t = u = C_z$.

Using this assumption, the blockage may be estimated by the following formula:

$$b = T \frac{\Delta S}{\Delta z} \cdot \frac{s}{C_z} \cdot \frac{1}{C^2} + 1 \quad (11.3)$$

For the first stage stator at midspan, assuming that C_z remains constant across the blade row, and using an average between outlet and inlet velocity magnitudes for C , this results in a blockage factor of 2.45, resulting in a jet wake of approximately 40.8 % the blade pitch. Based on numerical results, this under-predicts blockage by approximately 20 % of the blade pitch. This is probably due to the simplifying assumptions made, as well as the assumption of inviscid flow.

CHAPTER 11. FOURTH QUADRANT: NEGATIVE ROTATION

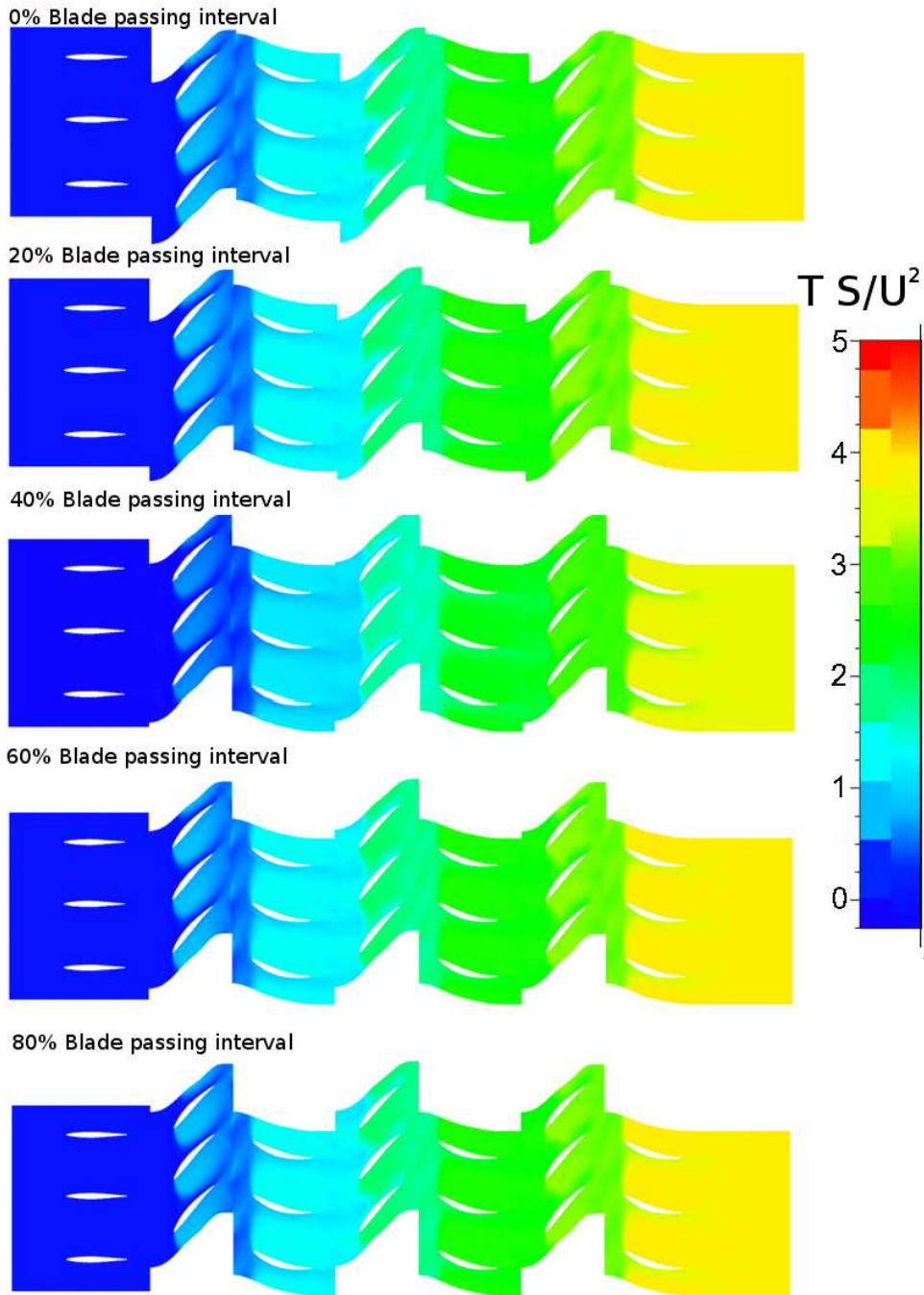


Figure 11.6: Time-series entropy distribution, normalised relative to inlet, on constant radius surface at midspan; $\phi = 0.165$

CHAPTER 11. FOURTH QUADRANT: NEGATIVE ROTATION

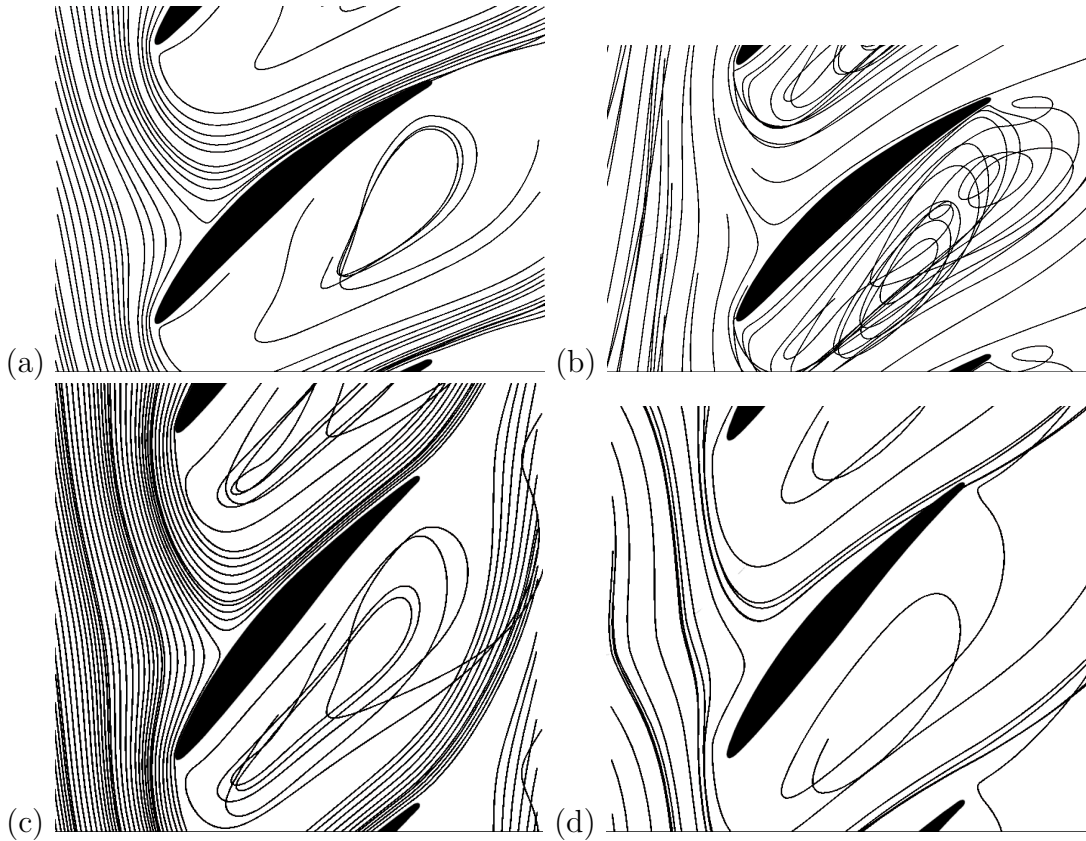


Figure 11.7: Relative velocity streamlines surrounding rotors: (a) first and (b) third stage at 10 % of blade span, (c) first and (d) third stage at 50 % of blade span ; $\phi = 0.165$

The flow field surrounding the first and third stage rotor blades at 10 % and 50 % of full span are shown in figure 11.7. The flow field near the blade tip is not shown due to the large discrepancies between experimental and numerical results in that region. Separation is severe for both first and third stage rotors at all radii. The flow field surrounding the first stage rotor (subfigures (a) and (c)) is marginally more orderly, due to the absence of upstream blade rows. The crossing streamlines indicate radial velocity components in the blade passages and blade wakes. The massive separated areas on the pressure surfaces dominate the flow field, and the only throughflow occurs in a thin layer attached to the suction surfaces of the rotor blades. The flow structure resembles a jet impinging on a slightly curved baffle. The thin layer of throughflow in turn forms a jet which impinges on the downstream stator row. Blockage is more severe at midspan (subfigures (c) and (d)) than near the hub.

The flow field surrounding the stator blades is shown in figure 11.8. The main points of interest are similar to those observed for figure 11.7, namely the large separated area attached to the pressure surface occupying at least 80 % of the blade pitch and the thin layer of throughflow attached to the suction surface, again resembling a jet impinging on a baffle. The crossing streamlines again indicate radial flows at all radii. Unlike the rotors, however, the separated area within stator blade passages appears to take the form of a somewhat more orderly vortex.

It will be recalled from chapter 8 that in second quadrant operation, in the MIT compressor, the arrangement of the areas of separation occurring near hub and shroud between

CHAPTER 11. FOURTH QUADRANT: NEGATIVE ROTATION

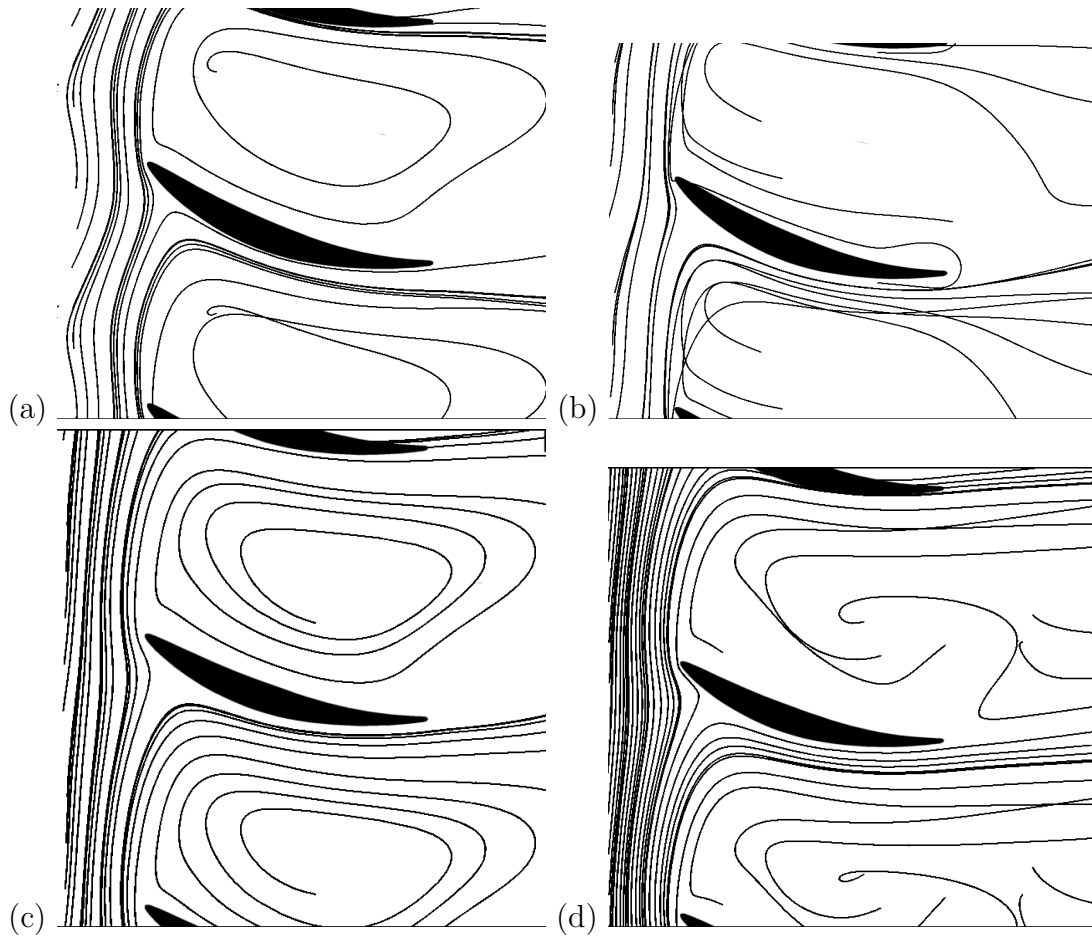


Figure 11.8: Streamlines surrounding stators: (a) first and (b) third stage at 10 % of blade span, (c) first and (d) third stage at 50 % of blade span ; $\phi = 0.165$

rotor and stator caused flow through rotor rows to move in a tipward direction, while flow through stator rows moved hubward. As there are strong similarities between fourth quadrant, negative rotation and second quadrant, positive rotation operation, it is reasonable to expect that similar flow structures would exist for this mode as well. The meridional view of the circumferentially averaged flow paths is shown in figure 11.9. Large areas of separation appear to occur near the trailing edges of stator rows, near the hub. These correspond with the very low axial velocities measured in this region in the area traverse downstream of the first stage stator (figure 11.5). The result is that flow appears to move in a hubward direction within rotor blade passages, and tipward in stator passages, the opposite of what occurs in second quadrant operation (chapter 8). Smaller separated regions appear to occur near the trailing edge rotor tips. It should be remembered, however, that there is disagreement between numerical and experimental data near the shroud. For this reason, the existence of areas of recirculating flow near rotor tips is treated with caution. It is conjectured that the discrepancy may result from the inability of the model to accurately represent the interaction of rotor tip gap leakage jets and the end-wall separation in this region, due to insufficient grid refinement.

It should also be noted that the pattern of recirculating flows near blade hubs and tips resemble those observed in numerical studies of the flow field within rotating mixers, particularly those of Shekhar and Jayanti [2002] and Khopkar et al. [2006], particularly

CHAPTER 11. FOURTH QUADRANT: NEGATIVE ROTATION

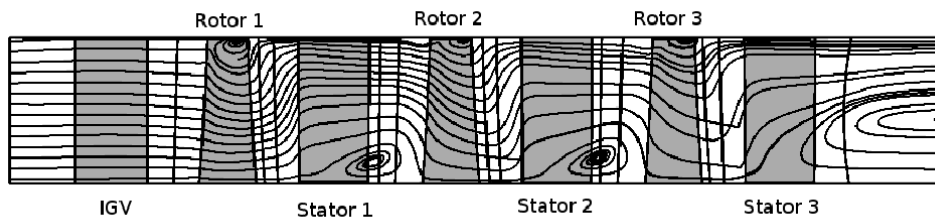


Figure 11.9: Meridional view of the test compressor showing circumferentially averaged flow paths and areas of separation and recirculation on the hub and shroud

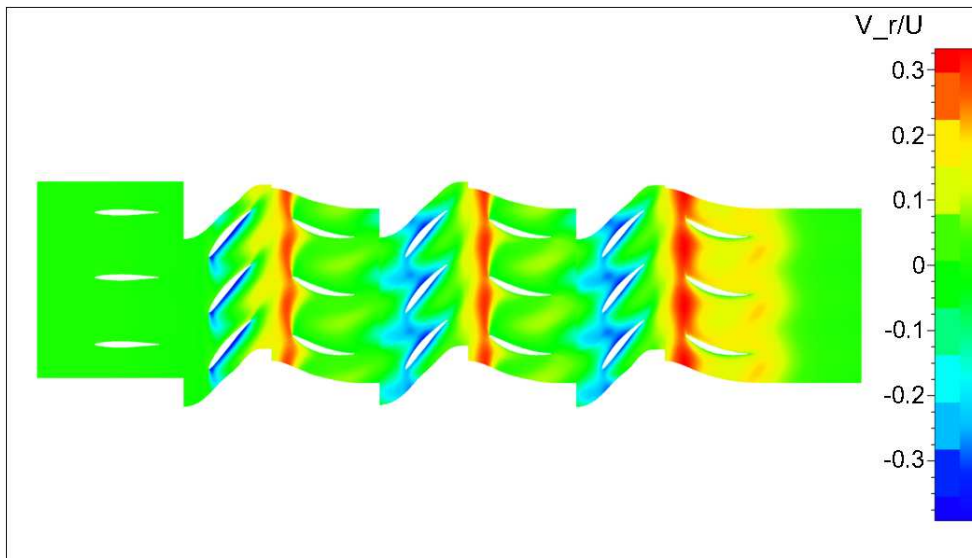


Figure 11.10: Radial velocity distribution on constant radius surface at midspan

when the effect of the net axial flow through the compressor is taken into account, as this is usually absent in the mixers used in those studies.

The radial velocity distribution at midspan is shown in figure 11.10. This illustrates the radial flows already identified in figure 11.9, and shows how these flows vary circumferentially. Large tipward radial velocity components, as much as 30 % of the rotor tip speed, are observed immediately upstream and at the leading edges of the stator rows. The flow moves tipward in stator rows to avoid the separation bubbles extending from hub to midspan, as seen in figure 11.5. Hubward radial velocity components of a similar magnitude are observed on suction surfaces of rotor blades near the leading edges. The recirculating regions in both rotor and stator blade passages do not have discernible radial velocity components, however.

11.4 Summary

Fourth quadrant compressor operation for negative rotation has been investigated. The flow field appears to be almost uniform circumferentially. This is due to the large degree of turbulent mixing resulting from the large degree of separation on the pressure surfaces of

CHAPTER 11. FOURTH QUADRANT: NEGATIVE ROTATION

all rotor and stator blades. As a result, the axial velocity component in the central portion of the rotor blade span is very small, with virtually all axial flow occurring near the hub and tip downstream of the rotor. Downstream of stator rows, the only significant axial flow is found in isolated areas near the tip, occurring once per blade passage, where it is over 500 % higher than the average flow for the rest of the flow field. The flow field near the suction surfaces of both rotor and stator blades resemble a jet impinging on a baffle. The separated areas on the pressure surfaces are dominated by areas of recirculating flow. Hubward radial flows occur at the leading edges of rotors, while tipward flows occur at the leading edges of stators, where the flow "climbs over" the recirculation zone near the hub. In both cases, radial velocity components may be as much as 30 % of the rotor tip speed. Rotor rows generate small wakes, but these are almost non-existent downstream of stator rows. Numerical modelling of fourth quadrant operation appears to agree with the experimentally determined flow field downstream of rotors from the hub to approximately midspan, but does not capture the increase in axial velocity near the blade tips.

Chapter 12

Conclusions

12.1 Summary of results

The compressor performance map relating non-dimensionalised pressure rise or torque to flow coefficient has four quadrants, although only the first quadrant is usually considered. Six modes of operation have been identified in the four quadrants. Three modes can occur when the rotor rotates in the design direction, and three when rotation occurs in the opposite direction. When the compressor rotor is locked in a stationary position and flow is forced through it, the characteristic of the pressure change across the compressor as a function of the flow through it takes the form of an S-shaped curve passing through the origin, and dividing the second and fourth quadrants in two. Because of this, the second and fourth quadrants contain two possible modes of operation each; one for rotation of the rotor in the design direction, and one for rotation in the opposite direction.

Forward rotation operation was investigated at flow coefficients ranging from -0.340 to 1.024, with total to static pressure coefficients varying between approximately 2.0 and -6.9 respectively. Reverse rotation operation was investigated at flow coefficients ranging from -0.740 to 0.165, with a corresponding range of total to static pressure coefficients between approximately -3.6 and 3.6. Some of the more significant findings are summarised below in Table 12.1. Figure 12.1 shows the meridional streamline distributions and typical velocity triangles characteristic of the six modes of four-quadrant compressor operation with the approximate operating points of each. A more detailed description of the principle flow features follows.

The first quadrant is that in which the design point occurs. First quadrant operation may be stalled or unstalled. Unstalled first quadrant operation is the usual and desired state of an axial flow compressor when running. Under these conditions, the degree of separation on rotor and stator blades is small, indeed it is negligible near the design point. Consequently, blade wakes are narrow and sharp, and decay quickly. A velocity time-trace downstream of a rotor at midspan exhibited a variation of only 10 % of the mean velocity in the test compressor. There is very little difference between steady-state simulations utilising a mixing-plane approach and unsteady simulations under these conditions. Under stalled operation, the flow separates from the suction surfaces of some of the compressor blades, leading to the formation of one or more stall cells. The stall cell rotates around the compressor circumferentially at a different rate to the rotor rotational speed. In the test compressor, a single stall cell was detected rotating at 40 % of the rotor rotational speed. Simulating stalled operation numerically requires fully unsteady simulation on a very fine mesh, and is beyond the scope of this dissertation.

CHAPTER 12. CONCLUSIONS

Table 12.1: Summary of findings for four quadrant operation

Quad	Running condition	Description	Efficiency	Flow turning	Separation	
					On rotors	On stators
1st	F+P+R+T+W+	Compressor (near-design) Compressor (stalled)	high	follows blade curvature low	None suction surface	None suction surface
4th	F+P-R+T+W-	Turbine-like (windmilling)	low	small, opposite blade curvature	pressure surface	Pressure surface, worst near hub
2nd	F-P+R+T+W+	Mixer-like (dissipative)	N/A	follows blade curvature but dominated by recirculating flows	Suction surface on hub near leading edge	Pressure surface on casing near leading edge
3rd	F-P-R-T-W+	Compressor-like, reversed from design condition	low	small, opposite blade curvature	Pressure surface	Pressure surface, worst near hub
2nd	F-P+R-T+W-	Turbine-like, reversed from design condition	high	follows blade curvature	Pressure surface near hub at flow coefficients close to origin Suction surface near hub at flow coefficients further from origin	Suction surface near tip at flow coefficients close to origin, Suction surface near tip at flow coefficients further from origin
4th	F+P-R-T-W+	Mixer-like (dissipative)	N/A	follows blade curvature but dominated by recirculating flows	suction surface, midspan	suction surface, midspan on hub near trailing edge

CHAPTER 12. CONCLUSIONS

If the flow coefficient is increased until the pressure rise across the compressor changes sign from the design condition, then the compressor is operating in the fourth quadrant. The performance characteristic curves between the first and fourth quadrants are continuous. In fourth quadrant operation, flow separates from the pressure surface of the blade. The compressor then acts as a turbine, a condition known as windmilling. The turbine efficiency of the compressor is low (30 % or less) due to the mismatch between flow angles and the blade metal angles, as the flow is turned in the opposite direction of the curvature of the blading. A larger blade camber angle increases the size of the separation bubble, as does an increase in flow coefficient. In the test compressor, this meant that separation was much more severe on stators than on rotors. The wakes of stators were consequently broader and less well defined than those of the rotors. In numerical simulations of the test compressor, separation was most severe near the hub on rotor blades, and near the tip on stator blades, although there was less variation in the size of the separated area with span for stators than rotors. Smaller regions of recirculating flow downstream of the main separation bubble on stator rows suggested that vortex shedding was occurring. Despite the recirculation zone near the hub in rotor blade passages, axial velocities are highest near the hub downstream of rotor rows by approximately 25 % in some cases, as more flow energy is extracted near the tip. The transition between first and fourth quadrant operation in rotors begins near the casing and extends hubward as flow coefficient increases. Radial flows occurred within blade passages, and increase in magnitude with stage number. Circumferentially averaged flow in stator blade passages has a hubward component which has a maximum magnitude of 40 % the blade tip speed in the final stage, while a tipward component is present in rotor rows, which reaches half the blade tip speed in the final stage. These radial components are caused by the blockage near the casing in stator rows and the hub in rotor rows. The blockage also causes higher local velocities downstream of rotor rows at the casing, and stator rows near the hub, leading to a higher local flow coefficient for the blade passage downstream, which exacerbates flow separation in that row. This causes the increase in radial velocities with stage number observed.

At high flow coefficients (150 % design flow coefficient or more), it is necessary to perform an unsteady numerical simulation in order to accurately capture the details of the flow field, as the broad wakes violate the assumptions of a steady-state mixing-plane approach.

If the direction of flow through the compressor is reversed, the compressor operates in the second quadrant. There is a discontinuity in the performance characteristic curves for first and second quadrant operation. The discontinuity is caused by the significant difference in flow structures occurring at low positive and negative flow coefficients, and the rapid change between these states. One important feature of second quadrant operation was the presence of periodic flow structures occurring across two blade passages. This was also reported by Gamache and Greitzer [1990]. For this reason, numerical simulation of a single blade passage in this mode of operation in the test compressor yielded results which agreed poorly with experimental data. A more successful simulation was performed of a single blade passage of the compressor used by Gamache and Greitzer [1990] at a negative flow coefficient further from the compressor map origin, where the "every-second-blade passage" flow-phenomena did not occur for that compressor. The results agreed relatively well with the experimental data of Gamache and Greitzer [1990] and also confirmed the presence of tipward radial flows within rotor rows, and hubward radial flows within stator rows. The former appear to be caused by large areas of recirculating flow occurring near the hub in upstream stator rows, while the latter are caused by similar recirculating flows near the

CHAPTER 12. CONCLUSIONS

casing in upstream rotor rows. Downstream of the first stage stator, a series of moving jets corresponding to the "every-second-blade passage" pattern of the upstream rotor was observed between the hub and midspan, while near the casing evidence for a recirculation zone in the meridional plane was observed. Due to this recirculating flow structure, at some points the flow angle exceeded the acceptance angle of the hot film probe used for this measurement, so that the flow velocity and direction could not be resolved.

Due to the dissipative nature of this mode, much of the energy applied to the compressor drive shaft is dissipated as heat in the working fluid. For the test compressor, the non-dimensionalised temperature increase measured in the working fluid was 25 times larger than that at design point.

If the compressor is driven in the reverse of the design direction, and the pressure rise across the machine and the net flow direction are both negative, then the compressor is operating within the third quadrant. Under this condition, the compressor operates as a compressor, but in reverse. The direction of blade curvature and twist are highly inappropriate to the flow direction and turning under this mode of operation, and consequently a large degree of separation occurs on the pressure surface of all blades. The result is that the compressor operates in a condition not unlike severe first quadrant stall. The numerical simulations attempted fail for small negative flow coefficients (-0.220). Successful numerical simulation would probably require similar treatment to stalled first quadrant operation. The degree of separation lessens as the flow coefficient assumes an increasingly large negative value. In the test compressor, separation on compressor blading is less severe near the blade tips than the hub, and at small negative flow coefficients, there is considerable blockage near the hub as a result. The stator wakes are particularly broad, occupying at least half of each blade passage. At larger negative flow coefficients, the degree of separation decreases, and vortices begin to form on rotor blades from hub to midspan, and propagate downstream. At the transition between third quadrant and second quadrant operation for negative rotation, the area of the rotor blades nearest the hub are the first portion to begin operating in a turbine-like mode (that is, extracting energy from the flow). As the flow coefficient becomes more negative, (moves further from the origin), the turbine-like region extends towards the tip.

The initial solution used for numerical simulations was found to be important for simulating third quadrant operation. It was found that an inappropriate choice of initial conditions could result in a converged solution which disagreed significantly with measured conditions within the compressor.

If the magnitude of the reversed flow through the machine becomes larger, the pressure rise across the compressor becomes positive once more, and the compressor begins to operate in the second of the second quadrant modes. Under this condition, the compressor operates as a turbine. The blade angles are well matched to the flow angles under this condition, and the direction of curvature of the blades agree with the direction of flow turning. Consequently, a high turbine efficiency is achievable in this mode of operation. The performance characteristic curves for second and third quadrant operation are continuous with one another. Some separation was observed near the hub of the test compressor downstream of rotor blades, as the blades are twisted in the wrong direction from hub to tip, relative to the flow. Blade wakes are narrow and sharply defined, but are slightly broader near the hub due to the afore-mentioned separation in this region. Vortices, such as those observed at large negative flow coefficients in third quadrant operation, are shed downstream of rotor blades in the region from hub to midspan. The vortices appear stronger than those discovered in the third quadrant. Numerical simulations yielded good

CHAPTER 12. CONCLUSIONS

agreement with measured results. As with the third quadrant, however, the choice of initial conditions had a significant effect on the solution towards which the model converged.

Finally, if the compressor rotates in the opposite direction to that for which it was designed, but flow is forced through it in the design direction, then the compressor operates in the second of the two modes possible in the fourth quadrant. Under this mode of operation, the pressure difference across the compressor has the opposite sign to design conditions, as the outlet pressure is lower than the inlet. The performance characteristic curves for this mode of operation are not continuous with third quadrant operation, just as a discontinuity exists between the characteristic for second quadrant with positive rotation and first quadrant operation. This mode of operation has considerable similarities with second quadrant operation with positive rotation. Like that mode, flow within the compressor is similar to that encountered in a mixer: flow in the test compressor was dominated by the circumferential velocity component, and areas of recirculating flow occur downstream of each stator blade row, giving rise to large radial velocity components, which are evident even after circumferential averaging: tipward flow occurs in stators, while hubward flow occurs in rotors. Virtually all throughflow occurs in the hub and tip regions downstream of rotors, and in the tip region exclusively downstream of stators. At midspan, very large separation bubbles containing recirculating flow patterns are attached to the pressure surfaces of rotor and stator blades, almost entirely blocking flow through the blade passages. The small amount of throughflow occurring within the blade passages at this span takes the form of a thin jet attached to the suction surface. This jet impinges on the suction surface of downstream blades, influencing the formation for the jet of the downstream blade row.

12.2 Further work

This thesis has attempted to identify all modes of operation possible in all four quadrants for an axial flow compressor, determine the performance characteristics in these modes, and provide a description of the flow structures found in the test compressor when operating under these various modes. Some of the potential difficulties in numerically modelling some of the operational modes have also been identified. However, there is considerable scope for further experimental and numerical investigation of four quadrant compressor operation.

The following have not been addressed in the present experimental program and should be considered for future work:

- Multiple compressor builds should be investigated, to determine the effects of blade geometry, reaction ratio, and similar parameters. The effects of rotor and stator blade clocking, both for four quadrant operation and locked-rotor (S-curve) operation should be investigated.
- A similar investigation should be performed for a compressor capable of higher Mach number operation.
- Future investigations should utilise laser Doppler velocimetry, particle image velocimetry, hub and blade-mounted rotating hot wire or hot film sensors and fast response aerodynamic probes if these are available.

There are a number of possibilities for future work in numerical simulation of four quadrant axial flow compressor operation:

CHAPTER 12. CONCLUSIONS

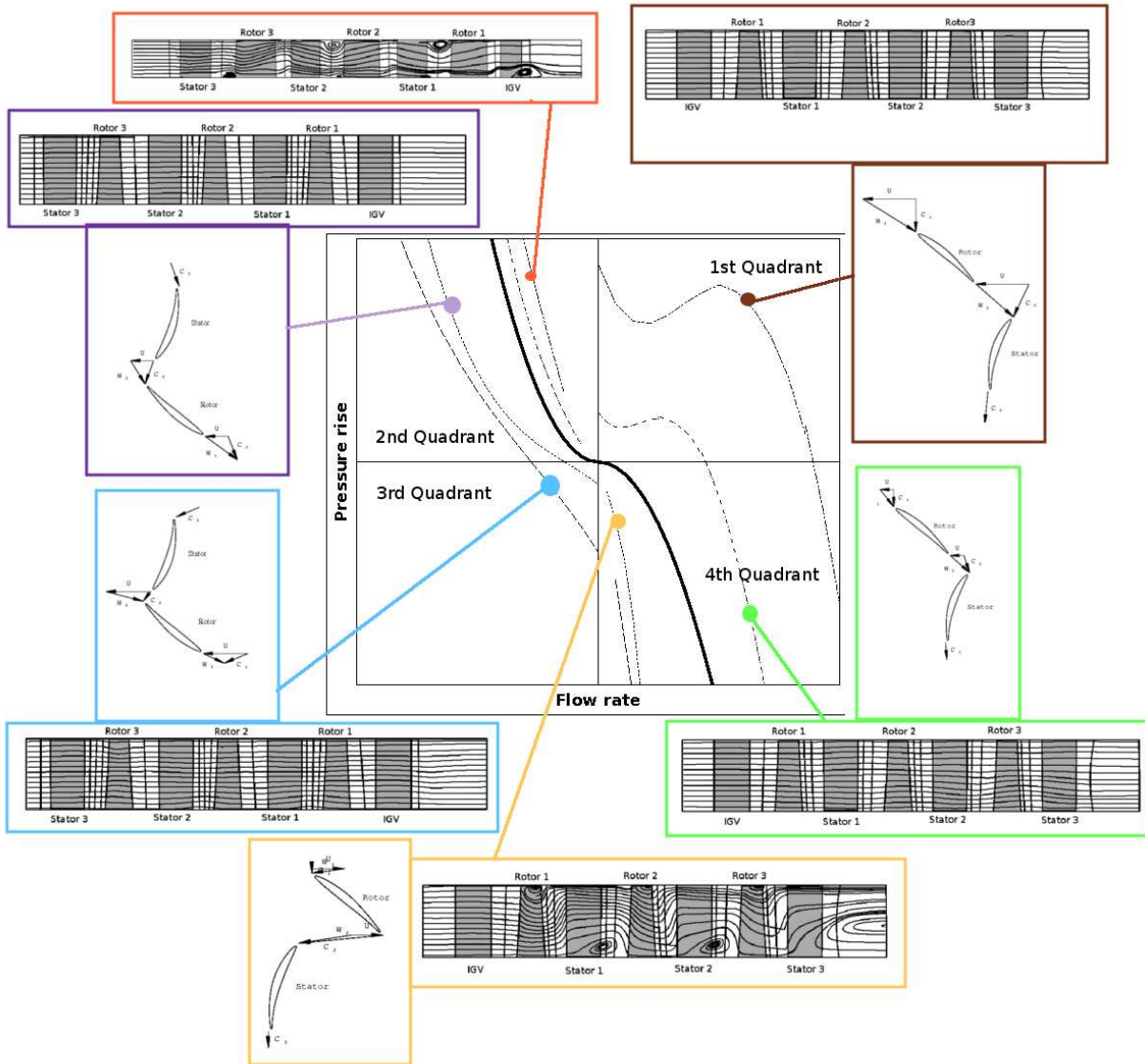


Figure 12.1: A visual summary of the six modes of four-quadrant compressor operation, showing typical stage velocity triangles and meridional streamline distributions for each mode.

CHAPTER 12. CONCLUSIONS

- The method of Longley [2007] should be applied to second quadrant operation for positive rotation and fourth quadrant operation for negative rotation for the test compressor.
- Simulation on a finer grid with a larger number of cells should be attempted to obtain better agreement with experimental data for some cases.
- Fully unsteady simulations using a time-marching approach should be performed.
- Simulation of an entire compressor stage, instead of a single blade passage, should be performed, as this would allow the observation of phenomena affecting more than one blade passage to be simulated.
- A direct numerical simulation (DNS) approach should be applied to some operating conditions, such as stalled first quadrant or third quadrant operation.

List of References

- B. Baldwin and H. Lomax. Thin layer approximation and algebraic model for separated turbulent flows. *AIAA Journal*, 1978.
- K. Bammert and P. Zehner. Measurements of the performance of an air turbine stage at positive and negative mass flow and rotational speed (four-quadrant characteristics). *ASME Journal of Turbomachinery*, pages 22–29, 1978.
- K. Bammert and P. Zehner. Measurements of the four-quadrant characteristics on a multi-stage turbine. *ASME Journal of Turbomachinery*, pages 316–321, 1980.
- J.G. Bernadé. The development of an impulse-type compressor blade cascade. Master's project, University of Stellenbosch, Faculty of Engineering, October 1986.
- R. E. Budinger and A. R. Thompson. Investigation of a 10-stage subsonic axial-flow compressor; II—preliminary analysis of overall performance. NACA Research Memorandum RME52C04, NACA, Washington DC, 1952.
- T. R. Camp and I. J. Day. A study of spike and modal stall phenomena in a low-speed axial compressor. *ASME Journal of Turbomachinery*, 120:393–401, 1998.
- A. Celić and E.H. Hirschel. Comparison of eddy-viscosity turbulence models in flows with adverse pressure gradient. *AIAA Journal*, 44(10):2156–2169, 2006.
- Y. H. Choi and C. L. Merkle. The application of precondition in viscous flows. *Journal of Computational Physics*, 105:207–223, 1993.
- S. H. Chue. Pressure probes for fluid measurement. *Prog. Aerospace Sci*, 16(2):200–201, 1975.
- N. A. Cumpsty. *Compressor Aerodynamics*. Longman, 1989.
- Vaclav Cyrus. The turbine regime of a rear axial compressor stage. *ASME Gas Turbine and Aeroengine Congress and Exposition, Brussels, Belgium*, pages 1–8, 11-14 June 1990.
- Vaclav Cyrus. Axial fan at reverse flow. *Proceedings of ASME Turbo Expo 2004: Power for Land, Sea and Air*, pages 437–446, 14-17 June 2004.
- I. J. Day. Stall inception in axial flow compressors. *ASME Journal of Turbomachinery*, 115:1–9, 1993.
- I. J. Day. Axial compressor performance during surge. *Journal of Propulsion and Power*, 10, 1994.

CHAPTER 12. CONCLUSIONS

- J. D. Denton. Some limitations of turbomachinery cfd. *Proceedings of ASME Turbo Expo 2010: Power for Land, Sea and Air*, 14-18 June 2010.
- S. L. Dixon. *Thermodynamics of Turbomachines*. Pergamon Press, Oxford, 1978.
- L. Gallar, I. Tzagarakis, V. Pachidis, and R. Singh. Compressor performance 2d modelling at reverse flow conditions. *ASME TURBO EXPO proceedings*, June 2010.
- R. N. Gamache and E. M. Greitzer. Reverse flow in multistage axial compressors. *International Journal of Turbo and Jet Engines*, 6:461–473, 1990.
- R.N. Gamache. *Axial Compressor Reverse-Flow Performance*. Ph.d. dissertation, Massachusetts Inst. of Technology, Cambridge, MA., May 1985.
- A. J. Gannon, G.V. Hobson, and W.L. Davis. Axial transonic rotor and stage behaviour near the stability limit. *ASME TURBO EXPO proceedings*, June 2010.
- A. Gill, T. W. von Backström, and T. M. Harms. Fundamentals of four quadrant axial flow compressor maps. *Proceedings of the IMechE part A: Journal of Power and Energy*, 221(A7):1001–1010, 2007a.
- A. Gill, T. W. von Backström, and T. M. Harms. Four quadrant total to static characteristics of an axial flow compressor. *Proceedings of the Fifth International Conference on Heat Transfer, Fluid Mechanics, and Thermodynamics, HEFAT2007*, (GA1), 2007b.
- A. Gill, T. W. von Backström, and T. M. Harms. The flow field within an axial flow compressor at extremely high flow coefficients. *ASME TURBO EXPO proceedings*, (GT2010-22894), June 2010.
- L. He and W. Ning. Efficient approach for analysis of unsteady viscous flows in turbomachines. *AIAA Journal*, 36:2005–2012, 1998.
- T. Houghton and I.J. Day. Stability enhancement by casing grooves: the importance of stall inception mechanism and solidity. *ASME TURBO EXPO proceedings*, June 2010.
- A. R. Khopkar, G. R. Kasat, A. B. Pandit, and V. V. Ranade. Cfd simulation of mixing in tall gas-liquid stirred vessel: Role of local flow patterns. *Elsevier Journal of Chemical Engineering Science*, 61:2921–2929, 2006.
- C. F. Kirstein. Flow through a solar chimney power plant collector-to-chimney transition section. Master’s thesis, University of Stellenbosch, Faculty of Engineering, December 2004.
- S. G. Koff. Stalled flow characteristics for axial flow compressors. Master’s thesis, Massachusetts Institute of Technology, 1983.
- K. Kovach and D. M. Sandercock. Experimental investigation of a five-stage axial-flow compressor with transonic rotors in all stages; II—compressor overall performance. NACA Research Memorandum RME54G01, NACA, Washington DC, 1954.
- N. Laubscher. Axial flow compressor. Undergraduate final year project, Faculty of Engineering, University of Stellenbosch, November 2008.

CHAPTER 12. CONCLUSIONS

- Lekakis. Measurement of velocity vectors with orthogonal and non-orthogonal triple-sensor probes. *Experiments in Fluids*, Springer-Verlag, 7:228–240, 1989.
- K.L. Lewis. Prediction of stall inception in an axial flow compressor. Master’s project, University of Witwatersrand, Faculty of Engineering, July 1989.
- S. Lieblein. Loss and stall analysis of compressor cascades. *ASME Journal of Basic Engineering, Series D*, 81:387–397, 1959.
- J. P. Longley. Calculating stall and surge transients. *ASME TURBO EXPO proceedings*, (GT2007-27378), 2007.
- N. M. McDougall, N. A. Cumpsty, and T. P. Hynes. Stall inception in axial compressors. *ASME Journal of Turbomachinery*, 112:116–124, 1990.
- NUMECA. *User Manual Fine/Turbo v.8a*. NUMECA International, 5 Avenue Franklin Roosevelt 1050 Brussels Belgium, October 2007.
- T.H. Roos. A prediction method for flow in axial flow compressors. Master’s project, University of Stellenbosch, Department of Mechanical Engineering, Faculty of Engineering, March 1995.
- S. Russ and T. W. Simon. On the rotating, slanted hot-wire technique. *Experiments in Fluids*, Springer-Verlag, 12:76–80, 1991.
- S. M. Shekhar and S. Jayanti. Cfd study of power and mixing time for paddle mixing in unbaffled vessels. *Transactions of IChemE, part A*, 80, 2002.
- P. R. Spalart and S. R. Allmaras. A one-equation turbulence model for aerodynamic flows. *AIAA 30th Aerospace Sciences Meeting & Exhibit*, January 1992.
- P. R. Spalart and C. L. Rumsey. Turbulence model behaviour in low reynolds number regions of aerodynamic flowfields. *AIAA 38th Aerospace Sciences Meeting & Exhibit*, June 2008.
- Kenneth L. Suder, Patricia C. Prahst, and Scott A. Thorpe. Results of an advanced fan stage operating over a wide range of speed and bypass ratio-part i:fan stage design and experimental results. *ASME TURBO EXPO proceedings*, June 2010.
- G. N. Vanderplaats. *Numerical Optimisation Techniques for Engineering Design*. Vanderplaats Research & Development, Inc., 2001.
- F. M. White. *Viscous Fluid Flow*. McGraw-Hill International Editions, second edition edition, 1991.
- I. Wilke and H.P. Kau. A numerical investigation of the flow mechanisms in a high pressure compressor front stage with axial slots. *ASME Journal of Turbomachinery*, 126(3):339–349, 2004.

Appendix A

Instrument calibrations curves

This chapter provides representative samples of the calibration data for all instruments used in the experimental investigations.

A.1 Pressure transducers

All pressure transducers were calibrated by means of a Betz micromanometer with a range of 5000 Pa. The zero-reading were monitored for signs of drift, and pressure transducers were recalibrated when this became excessive. Pressure transducers 1 to 5 were used for the five hole probe, while 7 and 8 were used to measure inlet conditions and the compressor pressure rise.

A.2 Turbine anemometer

A.3 Torque load cell

The torque transducer was calibrated for torque in both directions by hanging masspieces of varying mass on notches in arms extending from the motor to either side of the machine.

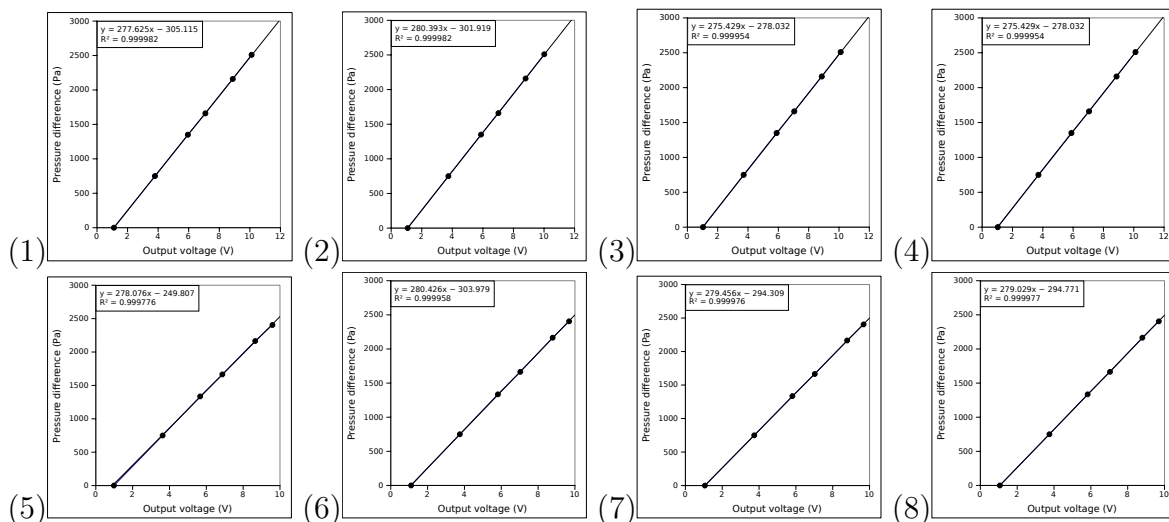


Figure A.1: Calibration data and curve fits for pressure transducers 1 to 8

APPENDIX A. INSTRUMENT CALIBRATIONS CURVES

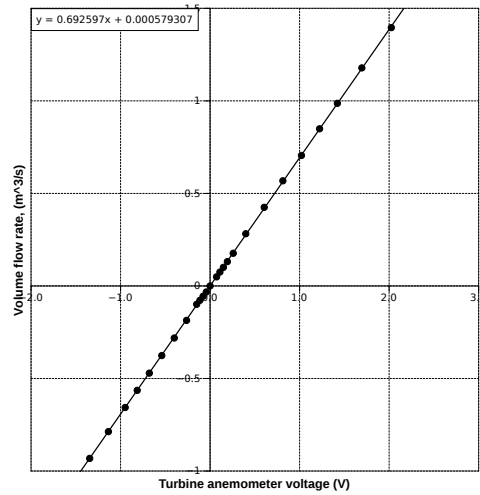


Figure A.2: Turbine anemometer calibration data and curve fit

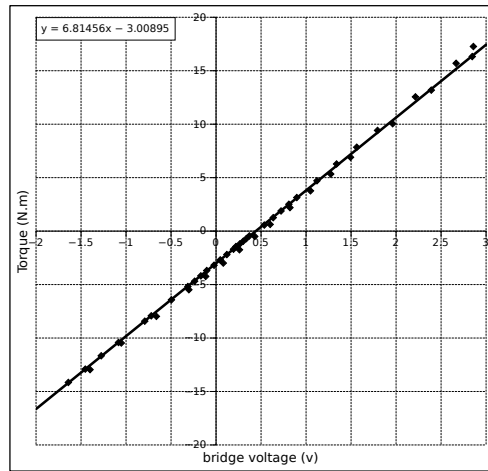


Figure A.3: Torque transducer calibration data and curve fit

The notches are exactly 0.254 m (10 in) from the axis of the machine.

A.4 Inclined single sensor hot film probe

The velocity sensitivity and pitch and yaw-angle sensitivity for the single sensor probe are presented below. From this data, the value of the transverse coefficients $k = 0.34035$ and $h = 1.1$ were determined. The cooling velocity equation determined was:

$$Q_1 = 6.7869v^3 - 9.1725v^2 - 7.3963v + 10.3552 \quad (\text{A.1})$$

A.5 Two-sensor hot film X-probe

The velocity sensitivity and yaw angle sensitivity were determined, and the data used to simultaneously extract the calibration curve for cooling velocities (Q_1 and Q_2) and yaw

APPENDIX A. INSTRUMENT CALIBRATIONS CURVES

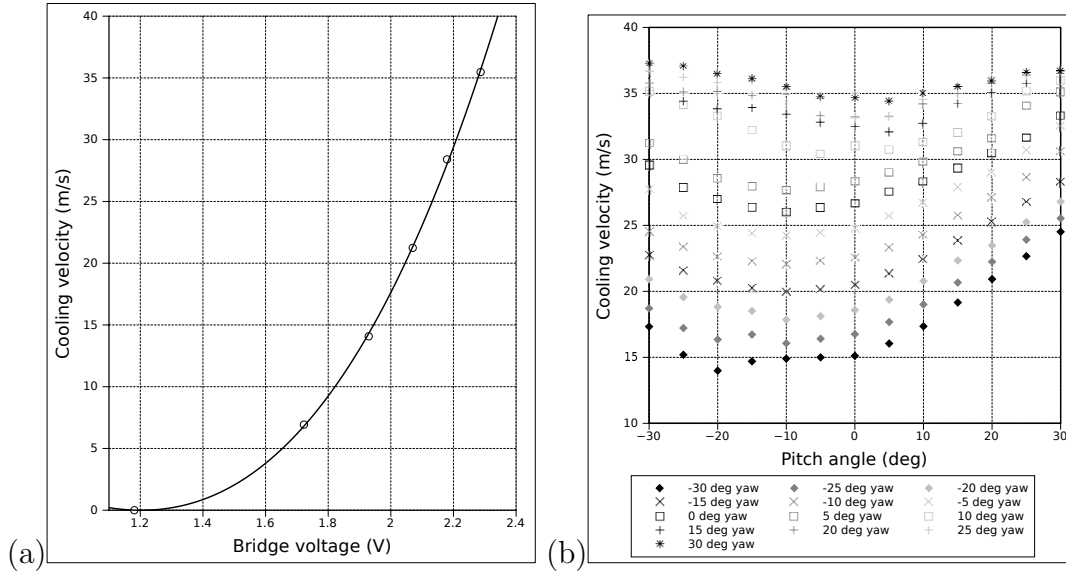


Figure A.4: Inclined cylindrical hot film probe sensitivity: (a) velocity, (b) pitch and yaw angle

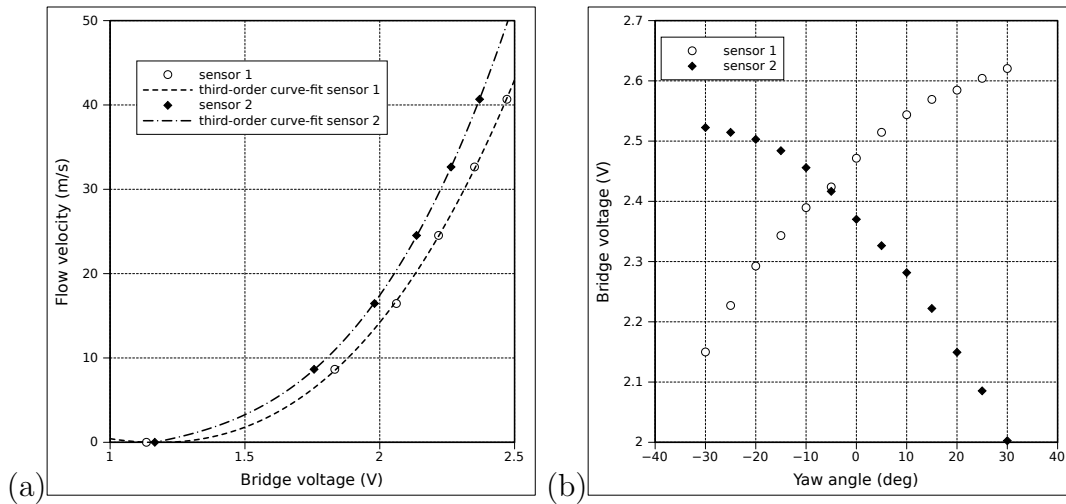


Figure A.5: X-probe sensitivity: (a) velocity, (b) yaw angle

coefficients (k_1 and k_2) by iteratively estimating values and minimisation of errors.

The cooling velocity equations determined were:

$$Q_1 = 5.22955852v^3 - 7.11972449v^2 - 5.01234495v + 7.21890084 \quad (\text{A.2})$$

$$Q_2 = 10.38564749v^3 - 32.5011749v^2 + 38.02273053v - 16.60840202 \quad (\text{A.3})$$

The yaw coefficients determined were:

$$k_1 = 0.319066991856 \quad (\text{A.4})$$

$$k_2 = 0.175088336831 \quad (\text{A.5})$$

Appendix B

Solution method for hot film X-probe velocity vector

This appendix gives the derivation of the method used for the determination of the velocity components from the two sensors of a two-sensor "x" hot wire or cylindrical hot film probe. The method is a two-dimensional simplification of the three-dimensional method of Lekakis [1989]

Jorgensten's equations for the cooling velocity of the first and second hot wire sensors (Q_1 and Q_2 respectively) in a two-dimensional flow are shown in equations B.1 and B.2:

$$Q_1^2 = U^2 \left(\cos^2(\theta + \delta_1) + k_1^2 \sin^2(\theta + \delta_1) \right) \quad (\text{B.1})$$

$$Q_2^2 = U^2 \left(\cos^2(\theta - \delta_2) + k_2^2 \sin^2(\theta - \delta_2) \right) \quad (\text{B.2})$$

Where U is the actual velocity magnitude, θ is the angle between the flow velocity and the probe datum, δ is the absolute value of angle between the sensor and the probe datum, and k is the yaw coefficient for the sensor.

Expanding equation B.1 and grouping like terms yields:

$$\begin{aligned} Q_1^2 &= U^2 \left(\cos^2 \theta (\cos^2 \delta_1 + k_1^2 \sin^2 \delta_1) \right. \\ &\quad + (k_1^2 - 1) (2 \sin \delta_1 \cos \delta_1) (\sin \theta \cos \theta) \\ &\quad \left. + \sin^2 \theta (\sin^2 \delta_1 + k_1^2 \cos^2 \delta_1) \right) \end{aligned} \quad (\text{B.3})$$

and similarly equation B.2 yields:

$$\begin{aligned} Q_2^2 &= U^2 \left(\cos^2 \theta (\cos^2 \delta_2 + k_2^2 \sin^2 \delta_2) \right. \\ &\quad + (1 - k_2^2) (2 \sin \delta_2 \cos \delta_2) (\sin \theta \cos \theta) \\ &\quad \left. + \sin^2 \theta (\sin^2 \delta_2 + k_2^2 \cos^2 \delta_2) \right) \end{aligned} \quad (\text{B.4})$$

let $R = Q_1^2/Q_2^2$, and substitute in equations B.3 and B.4 to eliminate U , yielding:

$$R = \frac{\cos^2 \theta (\cos^2 \delta_1 + k_1^2 \sin^2 \delta_1) + (k_1^2 - 1) (2 \sin \delta_1 \cos \delta_1) (\sin \theta \cos \theta) + \sin^2 \theta (\sin^2 \delta_1 + k_1^2 \cos^2 \delta_1)}{\cos^2 \theta (\cos^2 \delta_2 + k_2^2 \sin^2 \delta_2) + (1 - k_2^2) (2 \sin \delta_2 \cos \delta_2) (\sin \theta \cos \theta) + \sin^2 \theta (\sin^2 \delta_2 + k_2^2 \cos^2 \delta_2)} \quad (\text{B.5})$$

APPENDIX B. SOLUTION METHOD FOR HOT FILM X-PROBE VELOCITY VECTOR

Multiplying both sides by the denominator of the right side of the equation, and grouping like terms in θ yields:

$$\begin{aligned}
0 &= \cos^2 \theta \left(R(\cos^2 \delta_2 + k_2^2 \sin^2 \delta_2) - (\cos^2 \delta_1 + k_1^2 \sin^2 \delta_1) \right) \\
&+ \sin \theta \cos \theta \left(R(1 - k_2^2)(2 \sin \delta_2 \cos \delta_2) - (k_1^2 - 1)(2 \sin \delta_1 \cos \delta_1) \right) \\
&+ \sin^2 \theta \left(R(\sin^2 \delta_2 + k_2^2 \cos^2 \delta_2) - (\sin^2 \delta_1 + k_1^2 \cos^2 \delta_1) \right)
\end{aligned} \tag{B.6}$$

Dividing equation B.6 by $\cos^2 \theta$ yields:

$$\begin{aligned}
0 &= \left(R(\cos^2 \delta_2 + k_2^2 \sin^2 \delta_2) - (\cos^2 \delta_1 + k_1^2 \sin^2 \delta_1) \right) \\
&+ \tan \theta \left(R(1 - k_2^2)(2 \sin \delta_2 \cos \delta_2) + (1 - k_1^2)(2 \sin \delta_1 \cos \delta_1) \right) \\
&+ \tan^2 \theta \left(R(\sin^2 \delta_2 + k_2^2 \cos^2 \delta_2) - (\sin^2 \delta_1 + k_1^2 \cos^2 \delta_1) \right)
\end{aligned} \tag{B.7}$$

which is a quadratic equation in $\tan \theta$. There are thus two roots of the equation, corresponding to two possible angles. Only one falls within the range of acceptance angles of the probe, however, and the other is discarded. The velocity magnitude U may then be calculated by substituting the value for θ into equation B.1 or B.2.

The above assumes that $\cos \theta \neq 0$. This is a safe assumption, as $\cos \theta = 0$ implies that $\theta = \pi/2$ or $\theta = -\pi/2$, neither which fall within the angle of acceptance of a x-probe if the datum bisects the angle between the sensors.

Appendix C

Testing procedure checklist

The following generalised testing procedure was followed for all experimental investigations

1. Inspect compressor for damage
2. If necessary, mount auxiliary fans on Venturi outlet
3. Mount probe traverse on compressor
4. Ensure that probe cannot touch rotor or hub.
5. Check probe alignment
6. Check instrumentation wiring
7. Check pressure transducer and probe piping
8. Check DAQ software settings
9. Zero-reading
10. Lock compressor motor
11. Set compressor rotation direction
12. Connect power cable
13. Connect compressed air hose
14. If necessary, connect auxiliary fans to power supply
15. Run compressor and set speed and mass flow rate
16. If necessary, adjust speed of auxiliary fans
17. Unlock motor if torque measurements are required
18. Position probe at midspan and offset for yaw
19. Perform traverse
20. Shut down compressor
21. If necessary, shut down auxiliary fans
22. Remove probe and traverse

Appendix D

CFD convergence, grid sensitivity and turbulence model sensitivity

D.1 Grid convergence and turbulence model sensitivity

A sample of grid convergence data for the mesh used for all forward flow simulations is provided here. As discussed in chapter 4, the three meshes correspond to the three multigrid levels used in the finest mesh. The reverse flow mesh yielded similar results, being very similar in structure, and is omitted here for the sake of brevity. The simulation represents a first-quadrant operating point at a flow coefficient of 0.568; somewhat above design point. The effect of grid coarseness on the shape of the wake of a first stage rotor blade (position R1) at midspan is shown in figure D.1.

The tangential position of the wake can be seen not to vary significantly between the different grids. However, the wake shape differs considerably between the coarsest and

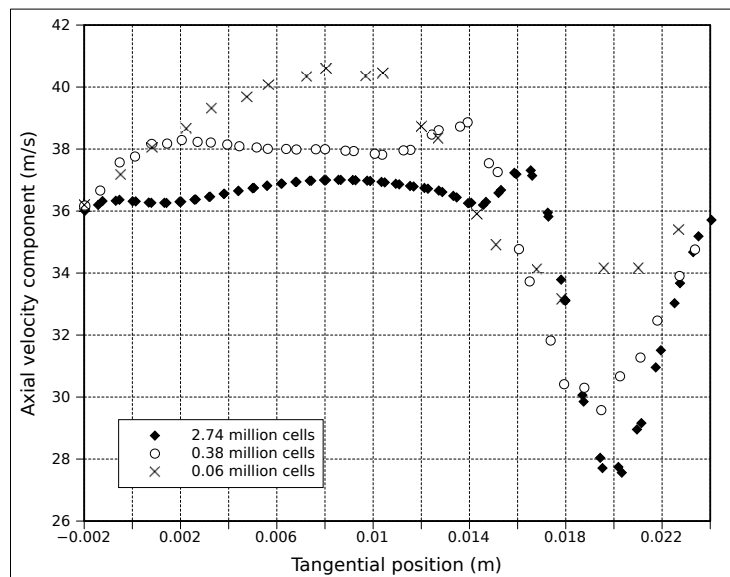


Figure D.1: Plot of axial velocity as a function of tangential position at position R1, midspan, for meshes of varying coarseness

APPENDIX D. CFD CONVERGENCE, GRID SENSITIVITY AND TURBULENCE MODEL SENSITIVITY

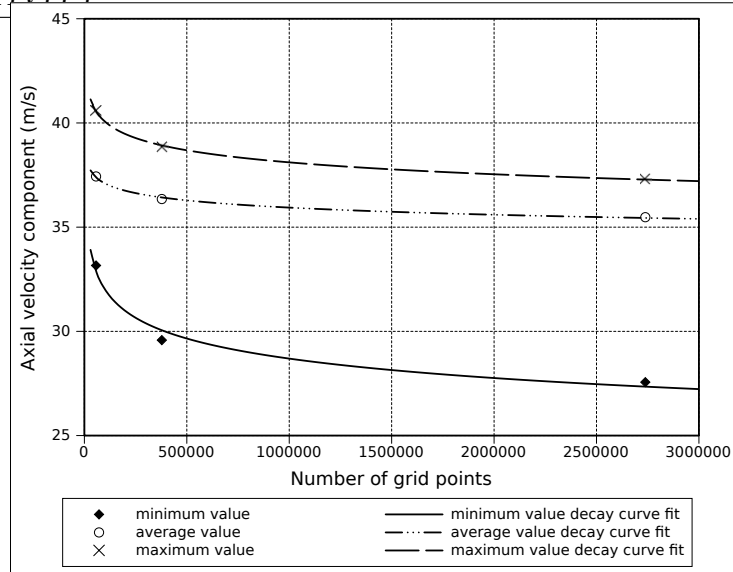


Figure D.2: Plot of minimum, maximum and average axial velocity values at midspan at position R1 as a function of number of cells

finest grids. As the maximum velocities occur in the inter-wake jets, and the minimum velocities in the wakes, comparison of these values yields a good indication of the variation of the wake shape with grid refinement. The average value across the blade passage is also included. Finally, an exponential decay curve was fitted to the data as an indication of the degree of grid convergence attained. This is shown in figure D.2.

D.2 Convergence of the iterations

Convergence curves for design-point operation for inlet and outlet mass flow rate, total to total pressure ratio, shaft torque and compressor efficiency are shown in figures D.3, D.4, D.5 and D.6 respectively.

D.3 Turbulence model sensitivity

Figure D.7 shows the sensitivity of the solution to the choice of turbulence model, with simplified boundary conditions. SA is the Spalart-Allmaras model, KW is the $K - \omega$ SST model, and KE is Chien's formulation of the $K - \epsilon$ model. The digits 000, 111 and 222 refer to the multi-grid level, where 000 is the finest mesh, and 222 the coarsest, thus giving additional information on grid-convergence.

Figure D.8 shows comparison of the solutions using Spalart-Allmaras $K - \omega$ SST models with the final choice of boundary conditions as used for this dissertation, again for near-design point operation ($\phi = 0.508$).

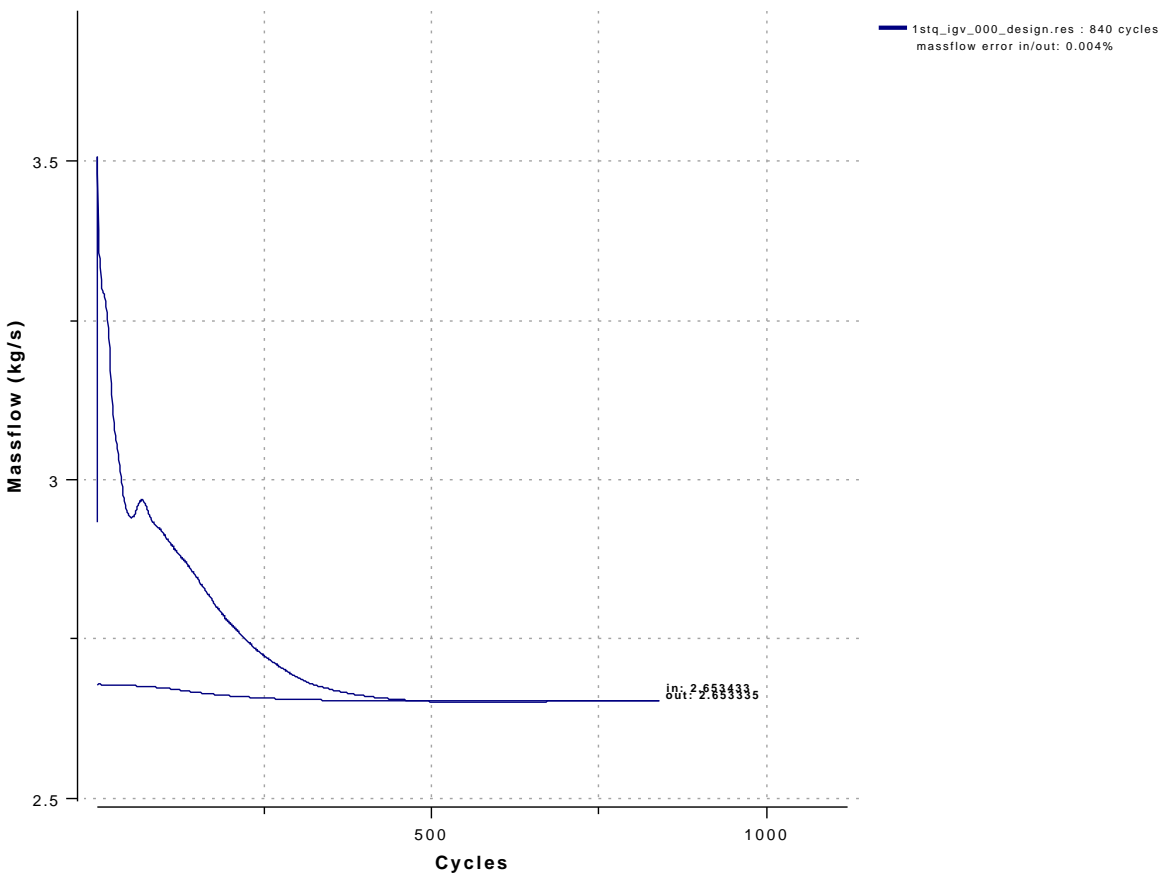


Figure D.3: Convergence of inlet and outlet mass flow rate

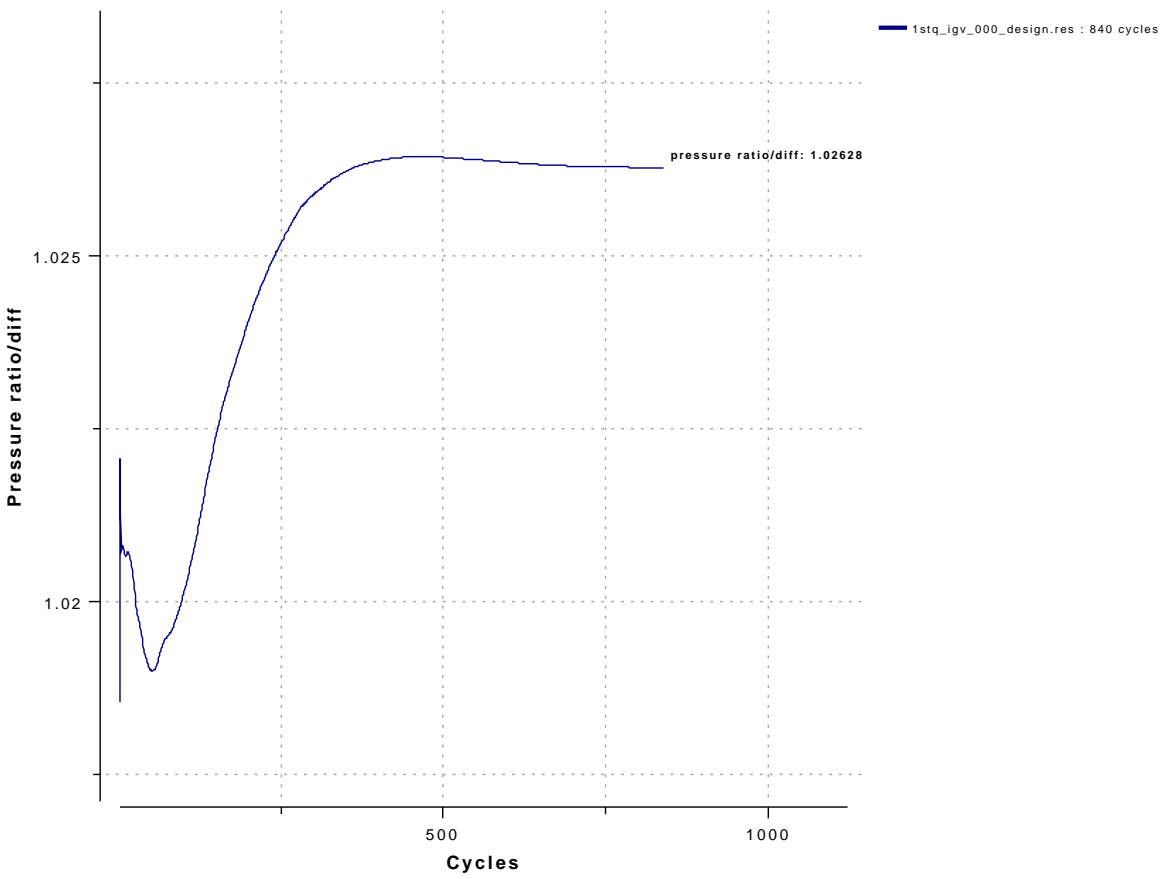


Figure D.4: Convergence of total to total pressure ratio

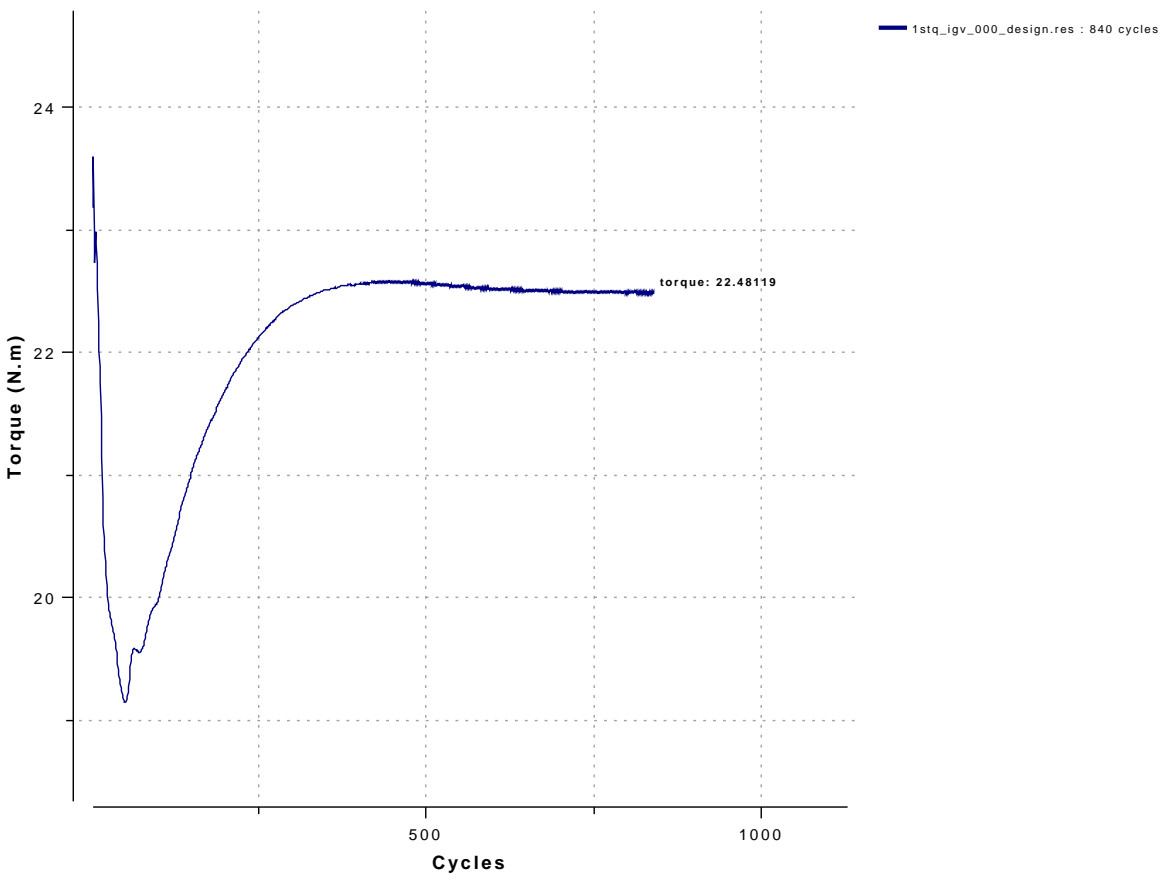


Figure D.5: Convergence of compressor shaft torque

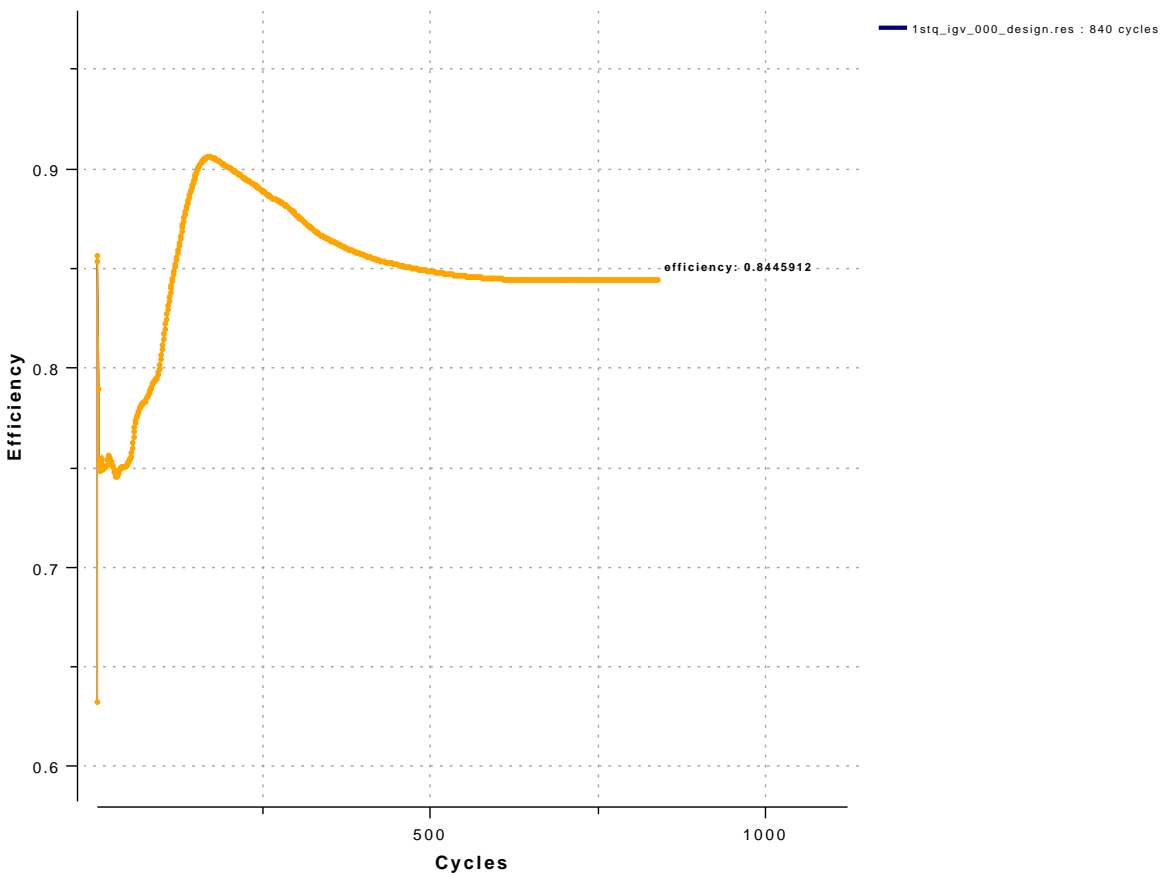


Figure D.6: Convergence of compressor efficiency

APPENDIX D. CFD CONVERGENCE, GRID SENSITIVITY AND TURBULENCE MODEL SENSITIVITY

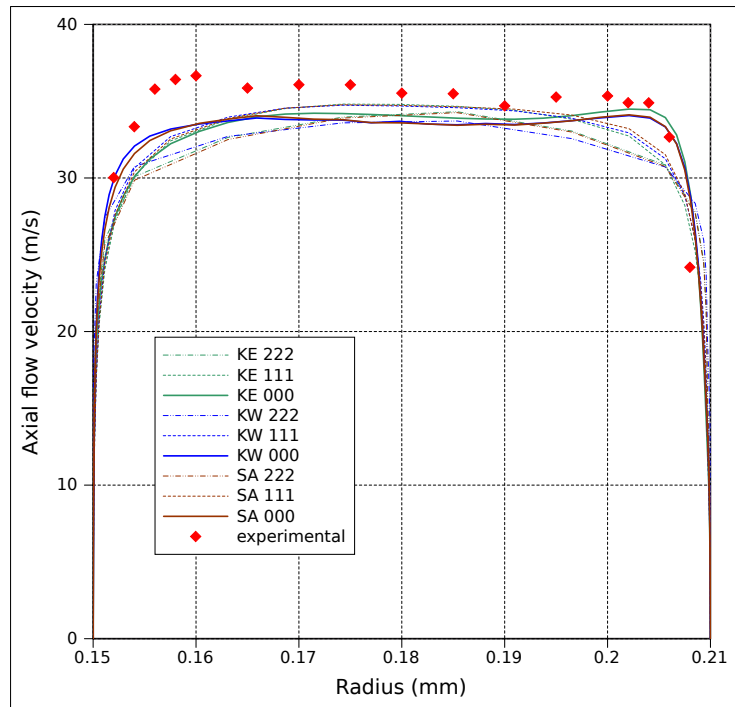


Figure D.7: Turbulence model sensitivity study for near-design point operation

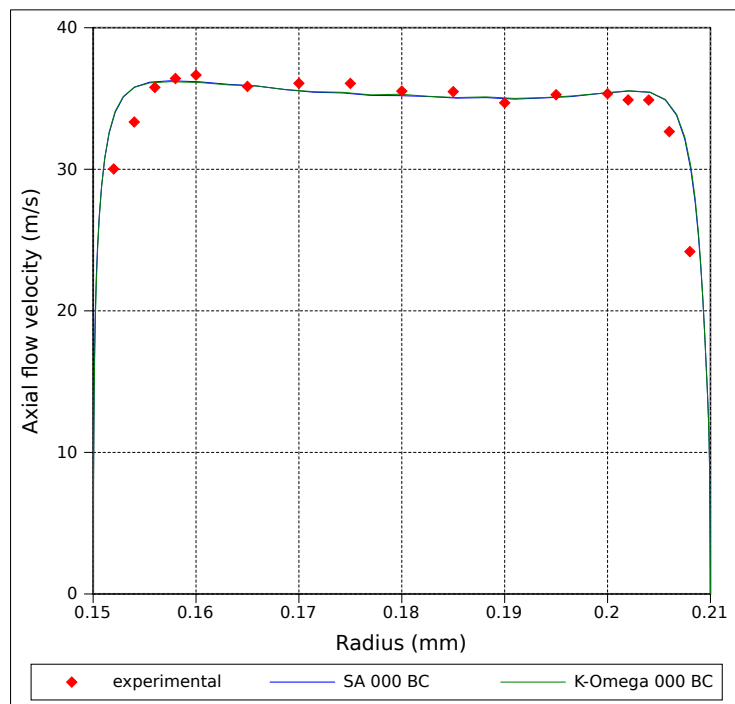


Figure D.8: Turbulence model sensitivity study for fourth quadrant operation

Appendix E

CFD grid quality

E.1 Design flow direction mesh

***** AUTOGRID version 8.4-3 REPORT FILE *****

PROJECT : 1stq_igv
 TEMPLATE FILE : /home/agill/cfd/1stq_igv/_mesh/1stq_igv.trb

NI_BEGIN PROJECT_INFO
 NUMECA Int.- AUTOGRID - PROJECT INFO

NUMBER OF POINTS 2738277
 NUMBER OF ROWS 7

ROW NAME: igv
 NUMBER OF MAIN BLADES 36
 NUMBER OF SPLITTER BLADES 0
 NUMBER OF POINTS 291525
 NUMBER OF LAYERS 69
 BLADE TO BLADE TOPOLOGY Default

ROW NAME: rotor1
 NUMBER OF MAIN BLADES 43
 NUMBER OF SPLITTER BLADES 0
 NUMBER OF POINTS 407792
 NUMBER OF LAYERS 69
 BLADE TO BLADE TOPOLOGY Default

ROW NAME: stator1
 NUMBER OF MAIN BLADES 41
 NUMBER OF SPLITTER BLADES 0
 NUMBER OF POINTS 407792
 NUMBER OF LAYERS 69
 BLADE TO BLADE TOPOLOGY Default

ROW NAME: rotor2
 NUMBER OF MAIN BLADES 43
 NUMBER OF SPLITTER BLADES 0

APPENDIX E. CFD GRID QUALITY

```

        NUMBER OF POINTS                407792
        NUMBER OF LAYERS                 69
        BLADE TO BLADE TOPOLOGY        Default
ROW NAME: stator2
        NUMBER OF MAIN BLADES           41
        NUMBER OF SPLITTER BLADES      0
        NUMBER OF POINTS                407792
        NUMBER OF LAYERS                 69
        BLADE TO BLADE TOPOLOGY        Default
ROW NAME: rotor3
        NUMBER OF MAIN BLADES           43
        NUMBER OF SPLITTER BLADES      0
        NUMBER OF POINTS                407792
        NUMBER OF LAYERS                 69
        BLADE TO BLADE TOPOLOGY        Default
ROW NAME: stator3
        NUMBER OF MAIN BLADES           41
        NUMBER OF SPLITTER BLADES      0
        NUMBER OF POINTS                407792
        NUMBER OF LAYERS                 69
        BLADE TO BLADE TOPOLOGY        Default

```

```

NI_END PROJECT_INFO
NI_BEGIN PERSONNAL_INFO
NI_END PERSONNAL_INFO
NI_END INFO

```

```

*****
*****  GRID QUALITY REPORT  *****
*****

```

```

Generation Date : Wed Nov 05 17:21 2008
Generation Time : 00:20:56
Mesh Validity   : OK (No Overlapping Cells Generated)

```

Entire Mesh Quality

```

No Negative Cell
Number of Points 2738277
Multigrid Level 3
Minimal Skewness Angle: 19.811
Maximal Skewness Angle: 90
Average Skewness Angle: 77.5532
Minimal Spanwise Skewness Angle: 172.955
Maximal Spanwise Skewness Angle: 180
Average Spanwise Skewness Angle: 179.939
Minimal Spanwise Expansion Ratio: 1
Maximal Spanwise Expansion Ratio: 1.42307
Average Spanwise Expansion Ratio: 1.24361

```

APPENDIX E. CFD GRID QUALITY

Minimal Aspect Ratio: 1
 Maximal Aspect Ratio: 447.381
 Average Aspect Ratio: 500
 Minimal Expansion Ratio: 1
 Maximal Expansion Ratio: 3.001
 Average Expansion Ratio: 1.40011
 Minimal wall Distance : 0.0097382
 Maximal wall Distance : 0.0175779
 Average wall Distance : 0.0109139

igv Quality

No Negative Cell
 Number of Points 291525
 Multigrid Level 3
 Minimal Skewness Angle: 55.806
 Maximal Skewness Angle: 90
 Average Skewness Angle: 80.9824
 Minimal Spanwise Skewness Angle: 179.824
 Maximal Spanwise Skewness Angle: 180
 Average Spanwise Skewness Angle: 179.993
 Minimal Spanwise Expansion Ratio: 1
 Maximal Spanwise Expansion Ratio: 1.25972
 Average Spanwise Expansion Ratio: 1.17829
 Minimal Aspect Ratio: 1
 Maximal Aspect Ratio: 204.965
 Average Aspect Ratio: 500
 Minimal Expansion Ratio: 1
 Maximal Expansion Ratio: 1.677
 Average Expansion Ratio: 1.4
 Minimal wall Distance : 0.00999439
 Maximal wall Distance : 0.0147614
 Average wall Distance : 0.0113709
 Max Location wall Distance : igv_flux_1_Main_Blade_skin I,J,K:1,68,18

rotor1 Quality

No Negative Cell
 Number of Points 407792
 Multigrid Level 3
 Minimal Skewness Angle: 22.496
 Maximal Skewness Angle: 90
 Average Skewness Angle: 75.277
 Minimal Spanwise Skewness Angle: 179.086
 Maximal Spanwise Skewness Angle: 180
 Average Spanwise Skewness Angle: 179.934
 Minimal Spanwise Expansion Ratio: 1
 Maximal Spanwise Expansion Ratio: 1.36725

APPENDIX E. CFD GRID QUALITY

Average Spanwise Expansion Ratio: 1.24221
 Minimal Aspect Ratio: 1
 Maximal Aspect Ratio: 254.936
 Average Aspect Ratio: 500
 Minimal Expansion Ratio: 1
 Maximal Expansion Ratio: 2.834
 Average Expansion Ratio: 1.40015
 Minimal wall Distance : 0.00997512
 Maximal wall Distance : 0.016983
 Average wall Distance : 0.0109777
 Max Location wall Distance : rotor1_flux_1_Main_Blade_skin I,J,K:1,18,80

stator1 Quality

No Negative Cell
 Number of Points 407792
 Multigrid Level 3
 Minimal Skewness Angle: 32.071
 Maximal Skewness Angle: 90
 Average Skewness Angle: 78.9508
 Minimal Spanwise Skewness Angle: 178.514
 Maximal Spanwise Skewness Angle: 180
 Average Spanwise Skewness Angle: 179.947
 Minimal Spanwise Expansion Ratio: 1
 Maximal Spanwise Expansion Ratio: 1.42307
 Average Spanwise Expansion Ratio: 1.27857
 Minimal Aspect Ratio: 1
 Maximal Aspect Ratio: 258.189
 Average Aspect Ratio: 500
 Minimal Expansion Ratio: 1
 Maximal Expansion Ratio: 2.355
 Average Expansion Ratio: 1.40011
 Minimal wall Distance : 0.00998637
 Maximal wall Distance : 0.0169932
 Average wall Distance : 0.0107861
 Max Location wall Distance : stator1_flux_1_Main_Blade_skin I,J,K:1,16,41

rotor2 Quality

No Negative Cell
 Number of Points 407792
 Multigrid Level 3
 Minimal Skewness Angle: 23.093
 Maximal Skewness Angle: 90
 Average Skewness Angle: 75.325
 Minimal Spanwise Skewness Angle: 178.946
 Maximal Spanwise Skewness Angle: 180
 Average Spanwise Skewness Angle: 179.933

APPENDIX E. CFD GRID QUALITY

Minimal Spanwise Expansion Ratio: 1
 Maximal Spanwise Expansion Ratio: 1.36736
 Average Spanwise Expansion Ratio: 1.23781
 Minimal Aspect Ratio: 1
 Maximal Aspect Ratio: 257.609
 Average Aspect Ratio: 500
 Minimal Expansion Ratio: 1
 Maximal Expansion Ratio: 2.774
 Average Expansion Ratio: 1.40018
 Minimal wall Distance : 0.00997195
 Maximal wall Distance : 0.0175779
 Average wall Distance : 0.0110669
 Max Location wall Distance : rotor2_flux_1_Main_Blade_skin I,J,K:1,18,80

stator2 Quality

No Negative Cell
 Number of Points 407792
 Multigrid Level 3
 Minimal Skewness Angle: 29.19
 Maximal Skewness Angle: 90
 Average Skewness Angle: 78.8117
 Minimal Spanwise Skewness Angle: 178.516
 Maximal Spanwise Skewness Angle: 180
 Average Spanwise Skewness Angle: 179.947
 Minimal Spanwise Expansion Ratio: 1
 Maximal Spanwise Expansion Ratio: 1.36716
 Average Spanwise Expansion Ratio: 1.26325
 Minimal Aspect Ratio: 1
 Maximal Aspect Ratio: 263.634
 Average Aspect Ratio: 500
 Minimal Expansion Ratio: 1
 Maximal Expansion Ratio: 2.501
 Average Expansion Ratio: 1.40011
 Minimal wall Distance : 0.00998631
 Maximal wall Distance : 0.0167962
 Average wall Distance : 0.0107382
 Max Location wall Distance : stator2_flux_1_Main_Blade_skin I,J,K:1,50,19

rotor3 Quality

No Negative Cell
 Number of Points 407792
 Multigrid Level 3
 Minimal Skewness Angle: 19.811
 Maximal Skewness Angle: 90
 Average Skewness Angle: 75.2004
 Minimal Spanwise Skewness Angle: 178.525

APPENDIX E. CFD GRID QUALITY

Maximal Spanwise Skewness Angle: 180
Average Spanwise Skewness Angle: 179.932
Minimal Spanwise Expansion Ratio: 1
Maximal Spanwise Expansion Ratio: 1.36744
Average Spanwise Expansion Ratio: 1.2281
Minimal Aspect Ratio: 1
Maximal Aspect Ratio: 255.279
Average Aspect Ratio: 500
Minimal Expansion Ratio: 1
Maximal Expansion Ratio: 3.001
Average Expansion Ratio: 1.4002
Minimal wall Distance : 0.00996859
Maximal wall Distance : 0.0169762
Average wall Distance : 0.0109805
Max Location wall Distance : rotor3_flux_1_Main_Blade_skin I,J,K:1,21,80

stator3 Quality

No Negative Cell
Number of Points 407792
Multigrid Level 3
Minimal Skewness Angle: 33.697
Maximal Skewness Angle: 90
Average Skewness Angle: 79.3029
Minimal Spanwise Skewness Angle: 172.955
Maximal Spanwise Skewness Angle: 180
Average Spanwise Skewness Angle: 179.901
Minimal Spanwise Expansion Ratio: 1
Maximal Spanwise Expansion Ratio: 1.3726
Average Spanwise Expansion Ratio: 1.25844
Minimal Aspect Ratio: 1
Maximal Aspect Ratio: 447.381
Average Aspect Ratio: 500
Minimal Expansion Ratio: 1
Maximal Expansion Ratio: 1.879
Average Expansion Ratio: 1.40001
Minimal wall Distance : 0.0097382
Maximal wall Distance : 0.0168433
Average wall Distance : 0.0106073
Max Location wall Distance : stator3_flux_1_Main_Blade_skin I,J,K:1,16,41

APPENDIX E. CFD GRID QUALITY

E.2 Reversed flow direction mesh

***** AUTOGRID version 8.7-2 REPORT FILE *****

PROJECT : reverse_flow
 TEMPLATE FILE : /home/agill/cfd/thirdq_2010/_mesh/reverse_flow.trb

NI_BEGIN PROJECT_INFO
 NUMECA Int.- AUTOGRID - PROJECT INFO

NUMBER OF POINTS 2922143
 NUMBER OF ROWS 7

ROW NAME: stator3
 NUMBER OF MAIN BLADES 41
 NUMBER OF SPLITTER BLADES 0
 NUMBER OF POINTS 494601
 NUMBER OF LAYERS 73
 BLADE TO BLADE TOPOLOGY Default

ROW NAME: rotor3
 NUMBER OF MAIN BLADES 43
 NUMBER OF SPLITTER BLADES 0
 NUMBER OF POINTS 419776
 NUMBER OF LAYERS 73
 BLADE TO BLADE TOPOLOGY Default

ROW NAME: stator2
 NUMBER OF MAIN BLADES 41
 NUMBER OF SPLITTER BLADES 0
 NUMBER OF POINTS 419776
 NUMBER OF LAYERS 73
 BLADE TO BLADE TOPOLOGY Default

ROW NAME: rotor2
 NUMBER OF MAIN BLADES 43
 NUMBER OF SPLITTER BLADES 0
 NUMBER OF POINTS 419776
 NUMBER OF LAYERS 73
 BLADE TO BLADE TOPOLOGY Default

ROW NAME: stator1
 NUMBER OF MAIN BLADES 41
 NUMBER OF SPLITTER BLADES 0
 NUMBER OF POINTS 419776
 NUMBER OF LAYERS 73
 BLADE TO BLADE TOPOLOGY Default

ROW NAME: rotor1
 NUMBER OF MAIN BLADES 43
 NUMBER OF SPLITTER BLADES 0
 NUMBER OF POINTS 419776

APPENDIX E. CFD GRID QUALITY

```

NUMBER OF LAYERS                73
BLADE TO BLADE TOPOLOGY        Default
ROW NAME: igv
NUMBER OF MAIN BLADES           36
NUMBER OF SPLITTER BLADES      0
NUMBER OF POINTS                 328662
NUMBER OF LAYERS                 57
BLADE TO BLADE TOPOLOGY        Default

```

```

NI_END PROJECT_INFO
NI_BEGIN PERSONNAL_INFO
NI_END PERSONNAL_INFO
NI_END INFO

```

```

*****
*****  GRID QUALITY REPORT  *****
*****

```

```

Generation Date : Tue Mar 16 2010 15:14
Generation Time : 00:19:55
Mesh Validity   : OK (No Overlapping Cells Generated)

```

Entire Mesh Quality

```

No Negative Cell
Number of Points 2922143
Multigrid Level 3
Minimal Skewness Angle: 20.306
Maximal Skewness Angle: 90
Average Skewness Angle: 77.9228
Minimal Spanwise Skewness Angle: 168.464
Maximal Spanwise Skewness Angle: 180
Average Spanwise Skewness Angle: 179.942
Minimal Spanwise Expansion Ratio: 1
Maximal Spanwise Expansion Ratio: 1.8152
Average Spanwise Expansion Ratio: 1.32363
Minimal Aspect Ratio: 1
Maximal Aspect Ratio: 657.306
Average Aspect Ratio: 500
Minimal Expansion Ratio: 1
Maximal Expansion Ratio: 2.108
Average Expansion Ratio: 1.41066
Minimal wall Distance : 0.00962397
Maximal wall Distance : 0.0121069
Average wall Distance : 0.0101115

```

stator3 Quality

```

No Negative Cell

```

APPENDIX E. CFD GRID QUALITY

Number of Points 494601
 Multigrid Level 3
 Minimal Skewness Angle: 25.236
 Maximal Skewness Angle: 90
 Average Skewness Angle: 79.3539
 Minimal Spanwise Skewness Angle: 178.456
 Maximal Spanwise Skewness Angle: 180
 Average Spanwise Skewness Angle: 179.946
 Minimal Spanwise Expansion Ratio: 1
 Maximal Spanwise Expansion Ratio: 1.65236
 Average Spanwise Expansion Ratio: 1.32335
 Minimal Aspect Ratio: 1
 Maximal Aspect Ratio: 290.837
 Average Aspect Ratio: 500
 Minimal Expansion Ratio: 1
 Maximal Expansion Ratio: 2.108
 Average Expansion Ratio: 1.40046
 Minimal wall Distance : 0.00962397
 Maximal wall Distance : 0.011753
 Average wall Distance : 0.0101082
 Max Location wall Distance : stator3_flux_1_Main_Blade_skin I,J,K:1,12,104

rotor3 Quality

No Negative Cell
 Number of Points 419776
 Multigrid Level 3
 Minimal Skewness Angle: 20.667
 Maximal Skewness Angle: 90
 Average Skewness Angle: 75.9889
 Minimal Spanwise Skewness Angle: 173.935
 Maximal Spanwise Skewness Angle: 180
 Average Spanwise Skewness Angle: 179.921
 Minimal Spanwise Expansion Ratio: 1
 Maximal Spanwise Expansion Ratio: 1.69891
 Average Spanwise Expansion Ratio: 1.31711
 Minimal Aspect Ratio: 1
 Maximal Aspect Ratio: 289.922
 Average Aspect Ratio: 500
 Minimal Expansion Ratio: 1
 Maximal Expansion Ratio: 2.062
 Average Expansion Ratio: 1.40048
 Minimal wall Distance : 0.00967784
 Maximal wall Distance : 0.0119105
 Average wall Distance : 0.0101033
 Max Location wall Distance : rotor3_flux_1_Main_Blade_skin I,J,K:1,60,76

stator2 Quality

APPENDIX E. CFD GRID QUALITY

No Negative Cell
Number of Points 419776
Multigrid Level 3
Minimal Skewness Angle: 26.578
Maximal Skewness Angle: 90
Average Skewness Angle: 79.2244
Minimal Spanwise Skewness Angle: 178.253
Maximal Spanwise Skewness Angle: 180
Average Spanwise Skewness Angle: 179.948
Minimal Spanwise Expansion Ratio: 1
Maximal Spanwise Expansion Ratio: 1.69898
Average Spanwise Expansion Ratio: 1.33241
Minimal Aspect Ratio: 1
Maximal Aspect Ratio: 290.416
Average Aspect Ratio: 500
Minimal Expansion Ratio: 1
Maximal Expansion Ratio: 2.108
Average Expansion Ratio: 1.40054
Minimal wall Distance : 0.00963511
Maximal wall Distance : 0.0115252
Average wall Distance : 0.0101181
Max Location wall Distance : stator2_flux_1_Main_Blade_skin I,J,K:1,12,104

rotor2 Quality

No Negative Cell
Number of Points 419776
Multigrid Level 3
Minimal Skewness Angle: 20.621
Maximal Skewness Angle: 89.999
Average Skewness Angle: 76.011
Minimal Spanwise Skewness Angle: 177.111
Maximal Spanwise Skewness Angle: 180
Average Spanwise Skewness Angle: 179.926
Minimal Spanwise Expansion Ratio: 1
Maximal Spanwise Expansion Ratio: 1.81513
Average Spanwise Expansion Ratio: 1.33531
Minimal Aspect Ratio: 1
Maximal Aspect Ratio: 289.509
Average Aspect Ratio: 500
Minimal Expansion Ratio: 1
Maximal Expansion Ratio: 2.062
Average Expansion Ratio: 1.40249
Minimal wall Distance : 0.00967801
Maximal wall Distance : 0.0119129
Average wall Distance : 0.0101031
Max Location wall Distance : rotor2_flux_1_Main_Blade_skin I,J,K:1,60,76

APPENDIX E. CFD GRID QUALITY

stator1 Quality

No Negative Cell
Number of Points 419776
Multigrid Level 3
Minimal Skewness Angle: 23.738
Maximal Skewness Angle: 90
Average Skewness Angle: 79.1118
Minimal Spanwise Skewness Angle: 178.256
Maximal Spanwise Skewness Angle: 180
Average Spanwise Skewness Angle: 179.95
Minimal Spanwise Expansion Ratio: 1
Maximal Spanwise Expansion Ratio: 1.81519
Average Spanwise Expansion Ratio: 1.35697
Minimal Aspect Ratio: 1
Maximal Aspect Ratio: 289.408
Average Aspect Ratio: 500
Minimal Expansion Ratio: 1
Maximal Expansion Ratio: 2.106
Average Expansion Ratio: 1.44181
Minimal wall Distance : 0.00964381
Maximal wall Distance : 0.0121069
Average wall Distance : 0.0101139
Max Location wall Distance : stator1_flux_1_Main_Blade_skin I,J,K:1,12,104

rotor1 Quality

No Negative Cell
Number of Points 419776
Multigrid Level 3
Minimal Skewness Angle: 20.306
Maximal Skewness Angle: 90
Average Skewness Angle: 75.9973
Minimal Spanwise Skewness Angle: 168.464
Maximal Spanwise Skewness Angle: 180
Average Spanwise Skewness Angle: 179.915
Minimal Spanwise Expansion Ratio: 1
Maximal Spanwise Expansion Ratio: 1.8152
Average Spanwise Expansion Ratio: 1.34745
Minimal Aspect Ratio: 1
Maximal Aspect Ratio: 288.605
Average Aspect Ratio: 500
Minimal Expansion Ratio: 1
Maximal Expansion Ratio: 2.062
Average Expansion Ratio: 1.4281
Minimal wall Distance : 0.0096779
Maximal wall Distance : 0.0119017

APPENDIX E. CFD GRID QUALITY

Average wall Distance : 0.0101045
Max Location wall Distance : rotor1_flux_1_Main_Blade_skin I,J,K:1,60,76

igv Quality

No Negative Cell
Number of Points 328662
Multigrid Level 3
Minimal Skewness Angle: 39.245
Maximal Skewness Angle: 90
Average Skewness Angle: 79.9593
Minimal Spanwise Skewness Angle: 179.84
Maximal Spanwise Skewness Angle: 180
Average Spanwise Skewness Angle: 179.996
Minimal Spanwise Expansion Ratio: 1
Maximal Spanwise Expansion Ratio: 1.33769
Average Spanwise Expansion Ratio: 1.23324
Minimal Aspect Ratio: 1
Maximal Aspect Ratio: 657.306
Average Aspect Ratio: 500
Minimal Expansion Ratio: 1
Maximal Expansion Ratio: 1.9
Average Expansion Ratio: 1.40033
Minimal wall Distance : 0.00979876
Maximal wall Distance : 0.0116899
Average wall Distance : 0.0101348
Max Location wall Distance : igv_flux_1_Main_Blade_skin I,J,K:1,42,15

Appendix F

MIT compressor geometry reconstruction data

The camber and stagger angles for each blade row, obtained from the free-vortex design reconstruction of the MIT compressor [Gamache and Greitzer, 1990] are tabulated below. Blade chord length was assumed to be equal to that at midspan for all radii. Inter-blade row spacing was assumed to be equal to the chord length of the IGVs at midspan. Both assumptions were based on drawings and photographs in Gamache and Greitzer [1990] and Gamache [1985]. Naca 65 aerofoil thickness profiles on circular arc camberlines were assumed for blades.

APPENDIX F. MIT COMPRESSOR GEOMETRY RECONSTRUCTION DATA

Table F.1: Blade profile data for the MIT compressor

Blade row	Radius (m)	Camber angle (deg)	Stagger angle (deg)
IGV	0.273	11.000	9.000
	0.282	11.000	9.000
	0.291	11.000	8.000
	0.301	11.000	8.000
	0.310	11.000	7.000
Rotor 1	0.273	20.624	34.807
	0.282	19.474	35.998
	0.291	18.435	37.082
	0.301	17.494	38.072
	0.310	16.639	38.979
Stator 1	0.273	27.955	22.306
	0.282	27.471	21.637
	0.291	27.000	21.000
	0.301	26.542	20.393
	0.310	26.098	19.815
Rotor 2	0.273	21.811	35.548
	0.282	20.604	36.697
	0.291	19.514	37.743
	0.301	18.526	38.698
	0.310	17.628	39.573
Stator 2	0.273	25.826	24.392
	0.282	25.409	23.679
	0.291	25.000	23.000
	0.301	24.601	22.353
	0.310	24.211	21.736
Rotor 3	0.273	24.175	36.692
	0.282	22.857	37.778
	0.291	21.665	38.768
	0.301	20.584	39.671
	0.310	19.601	40.499
Stator 3	0.273	54.965	16.402
	0.282	53.965	15.943
	0.291	53.000	15.500
	0.301	52.070	15.072
	0.310	51.173	14.658

Appendix G

Brief explanation of non-linear harmonic method

Consider a relative velocity flow field in a perfect fluid, for a rotating reference frame. Let U represent the conservative flow variables, as defined in equation G.1:

$$U = (\rho, \rho\vec{v}, \rho E) \quad (\text{G.1})$$

where ρ is the fluid density, \vec{v} is a vector representing the three dimensional velocity:

$$\vec{v} = (v_x, v_y, v_z) \quad (\text{G.2})$$

and E is the total energy, that is, the sum of the internal and kinetic energy.

The conservative variables are separated into time-averaged values and unsteady fluctuations. The unsteady fluctuation of each is assumed to be periodic in nature, and occur at the blade passing frequency and its harmonics. It may thus be expressed as a Fourier series, as in equation G.3:

$$U = \bar{U}(t) + \sum_{k=-\infty}^{\infty} U_k \cdot e^{j\omega_k t} \quad (\text{G.3})$$

The quantity ω_k represent the upstream and downstream blade passing frequencies and their harmonics

In equation G.3, the terms $U_{-k} \cdot e^{j\omega_{-k}t}$ and $U_k \cdot e^{j\omega_k t}$ are complex conjugates of each other, thus in the final summation, there are no imaginary quantities and all the conservative variables are real. Of course, in a practical computation, k cannot include all the integers from $-\infty$ to ∞ , thus the series is truncated to N terms (from $k = 0$ to $k = N$, for the real components, as the imaginary portions of the series terms for the negative values of k are conjugates of the equivalent positive values of k , and thus cancel out in summation of the series).

Using this definition of U , the continuity and momentum equations may be formulated similarly to the Reynolds-averaged Navier-Stokes equation. Expressed in finite volume form, these take the form of equation G.4

$$V_i \frac{d\bar{U}_i}{dt_i} = - \sum_{\text{cellfaces}} \bar{F}_c \cdot \vec{S} + \sum_{\text{cellfaces}} \bar{F}_v \cdot \vec{S} + V_i \cdot \bar{Q}_i \quad (\text{G.4})$$

V_i is the volume of control-volume or cell i , \bar{F}_c represents the convective fluxes at each cell face, \bar{F}_v represents the viscous fluxes at each cell face, \vec{S}_i is the vector normal to each cell face and Q represents source terms relating to Coriolis and centrifugal effects.

APPENDIX G. BRIEF EXPLANATION OF NON-LINEAR HARMONIC METHOD

The convective flux terms $\overline{F}_c \cdot \vec{S}$ are given in expanded form in equation G.5:

$$\overline{F}_c \cdot \vec{S} = \begin{bmatrix} \rho\vec{v} \cdot \vec{S} \\ (\rho\vec{v} \cdot \vec{S}) \vec{v}_x + \bar{p}S_x \\ (\rho\vec{v} \cdot \vec{S}) \vec{v}_y + \bar{p}S_y \\ (\rho\vec{v} \cdot \vec{S}) \vec{v}_z + \bar{p}S_z \\ (\rho\vec{v} \cdot \vec{S}) \bar{H} \end{bmatrix} + \begin{bmatrix} 0 \\ \frac{v'_x ((\rho\vec{v}) \cdot \vec{S})}{v'_y ((\rho\vec{v}) \cdot \vec{S})} \\ \frac{v'_y ((\rho\vec{v}) \cdot \vec{S})}{v'_z ((\rho\vec{v}) \cdot \vec{S})} \\ \frac{v'_z ((\rho\vec{v}) \cdot \vec{S})}{H' ((\rho\vec{v}) \cdot \vec{S})} \end{bmatrix} \quad (\text{G.5})$$

in which H is the internal energy.

The viscous flux terms $\overline{F}_v \cdot \vec{S}$ are given in expanded form in equation G.6:

$$\overline{F}_v \cdot \vec{S} = \begin{bmatrix} 0 \\ \begin{bmatrix} \tau_{xx} & \tau_{xy} & \tau_{xz} \\ \tau_{yx} & \tau_{yy} & \tau_{yz} \\ \tau_{zx} & \tau_{zy} & \tau_{zz} \end{bmatrix} \cdot \vec{S} \\ \left(\begin{bmatrix} \tau_{xx} & \tau_{xy} & \tau_{xz} \\ \tau_{yx} & \tau_{yy} & \tau_{yz} \\ \tau_{zx} & \tau_{zy} & \tau_{zz} \end{bmatrix} \cdot \vec{v} \right) \cdot \vec{S} + \bar{q} \end{bmatrix} + \begin{bmatrix} 0 \\ 0 \\ 0 \\ 0 \\ \left(\begin{bmatrix} \tau_{xx} & \tau_{xy} & \tau_{xz} \\ \tau_{yx} & \tau_{yy} & \tau_{yz} \\ \tau_{zx} & \tau_{zy} & \tau_{zz} \end{bmatrix} \cdot \vec{v} \right) \cdot \vec{S} \end{bmatrix} \quad (\text{G.6})$$

in which the τ_{ij} terms represent the fluid stress tensor.

The unsteady cyclic perturbations are dealt with by considering the linearised conservation equations for each of the first N terms U_k in the truncated fourier series U' in the frequency domain. This results in a series of conservation equations. The equations are written in pseudo-time dependent form, in order to allow them to tend towards a cyclically steady operation. The finite volume form of the conservation equations for a single control-volume or cell (cell number i) is similar to equation G.4, and is shown in equation G.7:

$$V_i \frac{dU_{k,i}}{d\zeta_i} = - \sum_{\text{cellfaces}} F_{ck} \cdot \vec{S} + \sum_{\text{cellfaces}} F_{vk} \cdot \vec{S} + V_i \cdot \bar{Q}_{ki} \quad (\text{G.7})$$

in which ζ is pseudo-time, F_{ck} are the convective terms of the conservation equation for the cyclic components for each term k in the series, shown in equation G.8:

$$F_{ck} \cdot \vec{S} = \begin{bmatrix} (\rho\vec{v})_k \cdot \vec{S} \\ (\overline{\rho\vec{v}} \cdot \vec{S}) \vec{v}_{xk} + ((\rho\vec{v})_k \cdot \vec{S}) \bar{v}_x + p_k S_x \\ (\overline{\rho\vec{v}} \cdot \vec{S}) \vec{v}_{yk} + ((\rho\vec{v})_k \cdot \vec{S}) \bar{v}_y + p_k S_y \\ (\overline{\rho\vec{v}} \cdot \vec{S}) \vec{v}_{zk} + ((\rho\vec{v})_k \cdot \vec{S}) \bar{v}_z + p_k S_z \\ (\overline{\rho\vec{v}} \cdot \vec{S}) \bar{H} + ((\rho\vec{v})_k \cdot \vec{S}) \bar{H} \end{bmatrix} + \begin{bmatrix} 0 \\ \frac{v'_x ((\rho\vec{v}) \cdot \vec{S})}{v'_y ((\rho\vec{v}) \cdot \vec{S})} \\ \frac{v'_y ((\rho\vec{v}) \cdot \vec{S})}{v'_z ((\rho\vec{v}) \cdot \vec{S})} \\ \frac{v'_z ((\rho\vec{v}) \cdot \vec{S})}{H' ((\rho\vec{v}) \cdot \vec{S})} \end{bmatrix} \quad (\text{G.8})$$

and F_{vk} are the viscous terms in the conservation equation for the cyclic components, shown in equation G.9:

$$F_{vk} \cdot \vec{S} = \begin{bmatrix} 0 \\ \begin{bmatrix} \tau_{xx} & \tau_{xy} & \tau_{xz} \\ \tau_{yx} & \tau_{yy} & \tau_{yz} \\ \tau_{zx} & \tau_{zy} & \tau_{zz} \end{bmatrix}_k \cdot \vec{S} \\ \left(\begin{bmatrix} \tau_{xx} & \tau_{xy} & \tau_{xz} \\ \tau_{yx} & \tau_{yy} & \tau_{yz} \\ \tau_{zx} & \tau_{zy} & \tau_{zz} \end{bmatrix} \cdot \vec{v}_k \right) \cdot \vec{S} + \left(\begin{bmatrix} \tau_{xx} & \tau_{xy} & \tau_{xz} \\ \tau_{yx} & \tau_{yy} & \tau_{yz} \\ \tau_{zx} & \tau_{zy} & \tau_{zz} \end{bmatrix} \cdot \vec{v} \right) \cdot \vec{S} + q_k \end{bmatrix} \quad (\text{G.9})$$

APPENDIX G. BRIEF EXPLANATION OF NON-LINEAR HARMONIC METHOD

Because the equation is in the frequency domain, the source term q_k contains the complex term $-j\omega_k U_k$ in addition to terms representing the Coriolis and centrifugal effects.

Turbulence models are restricted to one equation models, namely Spalart-Allmaras or Baldwin-Lomax. Turbulent eddy viscosity μ_t is assumed not to be affected by the cyclic components. Thus the viscous stress tensor

$$\begin{bmatrix} \tau_{xx} & \tau_{xy} & \tau_{xz} \\ \tau_{yx} & \tau_{yy} & \tau_{yz} \\ \tau_{zx} & \tau_{zy} & \tau_{zz} \end{bmatrix}$$

including turbulent viscosity effects, may be expressed as follows:

$$\bar{\tau}_{ij} = (\mu + \mu_t) \left(\frac{\partial \bar{v}_i}{\partial x_j} + \frac{\partial \bar{v}_j}{\partial x_i} - \frac{2}{3} (\nabla \cdot \bar{\mathbf{v}} \delta_{ij}) \right) \quad (\text{G.10})$$

and the unsteady stress term τ_k expressed as below:

$$\tau_{kij} = (\mu + \mu_t) \left(\frac{\partial v_{ik}}{\partial x_j} + \frac{\partial v_{jk}}{\partial x_i} - \frac{2}{3} (\nabla \cdot \bar{\mathbf{v}}_k \delta_{ij}) \right) \quad (\text{G.11})$$

Once the time-averaged and cyclic perturbation equations have been solved, a time-series solution may be reconstructed by substituting appropriate values of \bar{U} , U_k and t into the truncated form of equation G.3